Novel Methodology and its Applications to Intermolecular Interaction Studies Using Two-Dimensional Correlation Spectroscopy

A Thesis for the Degree

Of

Doctor of Science

Submitted to

School of Science and Technology

Kwansei-Gakuin University

By

Anqi He

Supervisor: Prof. Yukihiro Ozaki

in Dec.2017

Contents

Abstract

The thesis has two parts. The first part is a novel methodology and its applications to intermolecular interaction studies using two-dimensional correlation spectroscopy. In orthogonal sample design (OSD) and related techniques used in two-dimensional correlation spectroscopy (2DCOS), the cross peaks can reliably reflect intermolecular interaction between two solutes dissolved in the same solvent. Subtle changes of the absorption peaks of the two solutes can be revealed by characteristic patterns of cross peaks in 2D correlation spectra generated via OSD and relevant techniques. It can help us to understand on the nature of intermolecular interaction.

When weak intermolecular interaction is investigated, the cross peaks are quite vulnerable to noise. Thus, improving signal-to-noise level of 2DCOS spectrum used in such investigation is important. In order to solve the problem, a new approach is proposed to construct 2D asynchronous spectrum without subtracting a reference spectrum. This approach is effective in enhance the intensities of cross peaks. Under investigation on weak intermolecular interaction, in some cases, enhancing the intensities of the cross peaks alone is not enough, and some additional step should be taken to suppress the effect of noise. Butterworth filter is used to reduce the standard deviation of noise. A new strategy is proposed to reduce the noise on one hand and control signal distortion on the other hand. Another current issue is that application of 2DCOS spectra using the OSD techniques have not been extensively exploited. Convincing illustrative example of the utility and merit of this technique must be presented. 2D asynchronous spectrum is applied to investigate intermolecular interaction between berberine and β-CyD. The occurrence of cross peaks around (420 nm, 420 nm) in 2D asynchronous spectrum reveals that intermolecular interaction indeed exists between berberine and β-CyD. The behaviors of cross peaks demonstrate that berberine enter the hydrophobic cavity of β-CyD. The above spectral results are helpful in understanding why the solubility of berberine is enhanced by β-CyD.

Moreover, the doubly asynchronous DAOSD approach is adopted to study intermolecular interaction between two solutes dissolved in the same solution. In the system, one solute occurs in two exchangeable states. In this case, cross peaks in 2D asynchronous spectra may still reflect intermolecular interaction reliably. However, it should also be noted that certain cross peaks can still be produced even if intermolecular interaction do not bring about any changes on the characteristic peaks of solutes. These cross peaks are related to the variations of chemical systems caused by intermolecular interaction at a network level.

The second part of the thesis is the preparation and characterization of lanthanum carbonate octahydrate for the treatment of hyperphosphatemia. Lanthanum carbonate is an ideal phosphate binder. It can be utilized as phosphate binder for renal failure patients. A new approach is proposed to prepare lanthanum carbonate via reactions between lanthanum chloride and $NaHCO_3$. In the reaction, small amount of $NaHCO_3$ solution was firstly added into the acidic solution of lanthanum chloride to generate lanthanum carbonate nuclei and then $NaHCO_3$ is added into the lanthanum chloride at a constant speed. This approach makes both precipitation reaction and neutralization

reaction take place simultaneously. Consequently, lanthanum carbonate is produced at low pH environment (the pH value is below 4.5) so that the risk of generating lanthanum carbonate hydroxide is reduced.

Preface

This thesis consists of two parts: the first part is novel methodology study and its application to intermolecular interaction studies of two-dimension correlation spectroscopy (2DCOS). The second part is on the preparation and characterization of lanthanum carbonate octahydrate for the treatment of hyperphosphatemia.

In the first part, the thesis is mainly focused on development of the methodology of 2DCOS to study weak intermolecular interactions between two solutes dissolved in the same solutions. The 2DCOS is a very powerful analytical technique. It has been applied in many fields. In many cases, only weak intermolecular interaction occurs and the relevant cross peaks are quite weak in the resultant 2D correlation spectra. Consequently, noise in 2D correlation spectra often brings about significant interference on the identification of weak cross peaks that are related to weak intermolecular interactions. The author addressed the problem from the aspects of enhancing the intensities of cross peaks and reduction of noise by using novel approach to construct 2D spectra and Butterworth filter.

In some systems, a solute that take part in intermolecular interaction may occur in two exchangeable states such as conformational changes, etc. This situation may bring about additional complexity in the resultant 2D asynchronous spectrum. The author investigate the spectral behavior of a pair of 2D asynchronous spectra, which extend the application of 2D correlation spectroscopy to much broader applications.

Berberine is a Chinese traditional medicine, which has many new pharmaceutical functions in medical researches. Unfortunately, the low solubility of berberine poses a limitation to the broader application in medical practice. An effective way to increase its solubility is to introduce suitable excipient. The author investigated the interaction between berberine and β-cyclodextrin (β-CyD) by using 2DCOS. The spectral behavior from cross peaks in 2D asynchronous spectrum is helpful in understanding why the solubility of berberine is enhanced by β-CyD. The result support that 2DCOS may become a new method to selecting the optimized excipients.

In the second part of the thesis, the author developed an approach to produce lanthanum carbonate that can be used in the treatment of hyperphosphatemia of renal failure patients.

The novelty of this thesis can be described as follows:

In chapter 1, the author proposed a new approach to construct 2D asynchronous spectrum without subtraction of a reference spectrum. This approach is effective in enhance the intensities of cross peaks.

In chapter 2, the author proposed to use the Butterworth filter to reduce the standard deviation of noise. A new strategy is proposed to reduce the noise on one hand and control signal distortion on the other hand.

In chapter 3, the author applied 2D asynchronous spectrum to investigate intermolecular interaction between berberine and β-CyD. The occurrence of cross peaks around (420 nm, 420 nm) in 2D asynchronous spectrum reveals that specific intermolecular interaction indeed exists between berberine chloride and β-CyD. The behaviors of cross peaks demonstrate that berberine enter the hydrophobic cavity of β-

CyD. The above spectral behavior is helpful in understanding why the solubility of berberine is enhanced by β-CyD.

In chapter 4, the author adopted the DAOSD approach to study intermolecular interaction between two solutes dissolved in the same solution. In the system, one solute occurs in two exchangeable states. In this case, cross peaks in 2D asynchronous spectra can still reflect intermolecular interaction reliably. It should be noted that cross peaks can still be produced even if intermolecular interaction do not bring about any changes on the characteristic peaks of solutes. These cross peaks are related to the variations of chemical systems caused by intermolecular interaction at a network level.

In the second part of the thesis, a new approach is proposed to prepare lanthanum carbonate via reactions between lanthanum chloride and $NaHCO_3$. In the reaction, small amount of $NaHCO_3$ solution was firstly added into the acidic solution of lanthanum chloride to generate lanthanum carbonate nuclei and then $NaHCO_3$ is added into the lanthanum chloride at a constant speed. This approach makes both precipitation reaction and neutralization reaction take place simultaneously. Consequently, lanthanum carbonate is produced at low pH environment (the pH value is below 4.5) so that the risk of generating lanthanum carbonate hydroxide is reduced.

1. Background of Two–Dimensional Correlation Spectroscopy

A novel idea was put forward in the field of NMR spectroscopy about 40 years ago that, by spreading spectral peaks over the second dimension, one can simplify the visualization of complex spectra consisting of many overlapped peaks.[1-5] It became possible for the spectral intensity to be obtained as a function of two independent spectral variables. Two-dimensional (2D) NMR has greatly expanded the scope of application, especially in the solution of protein and other biological macromolecules. Following this conceptual breakthrough, an impressive amount of progress has been made in the branch of science now known as 2D spectroscopy.

2D NMR technology provides a good support for the representation of complex systems. Unfortunately, the technology cannot be applied to other common optical spectroscopic techniques. The common optical spectroscopy techniques, such as IR, Raman, and ultraviolet–visible (UV–vis) are governed by physical phenomena having time scales which are very different from those of NMR.[5] The characteristic time scale of molecular vibrations observed in IR absorption spectroscopy is on the order of picosecond, compared to the micro to millisecond ranges usually encountered in NMR.[5]

In NMR, a set of time-domain data collected after double Fourier transformed under multiple-pulse excitations generates 2D spectra.[1-5] Direct adaptations of such a procedure based on pulsed excitations to conventional vibrational spectroscopy was rather difficult several decades ago. Nowadays, it has become possible to conduct certain experiments based on ultrafast femtosecond optical pulses in a fashion analogous to pulse-based 2D NMR experiments.[6-11] However, such measurements are still in their infancy. The commercial IR spectrometers cannot adequately provide rapid excitation and detection of vibrational relaxation responses to carry out such measurements. Thus, the specific experimental procedure of 2D NMR had to be fundamentally modified before being applied to practical optical spectroscopy.[5]

The basic concept of perturbation-based 2D IR correlation spectra was proposed first by Noda in 1986.[12-14] Noda considered the multiple-pulse excitations in 2D NMR spectroscopy as a perturbation to the system. Therefore, a simple cross-correlation analysis was applied to sinusoidally varying dynamic IR signals to obtain a set of 2D IR correlation spectra. This 2D IR correlation spectroscopy has been successful in the study of samples stimulated by a small-amplitude mechanical or electrical perturbation.[5]

The major shortcomings of the above 2DCOS approach was that the small-amplitude perturbation must be sinusoidal to effectively employ the original data analysis scheme. To overcome this limitation, Noda proposed generalized 2DCOS in 1993.[5, 15] The mathematical procedure to yield 2DCOS spectra was modified to handle an arbitrary form of variable dependence much more complex than simple sinusoidally varying time-dependent spectral signals. The generalized 2DCOS scheme lifted the constraint of the perturbations and excitation types. As a result, perturbations can be a variety of physical origins, such as mechanical, electrical, temperature, pH, concentration, biological, etc..[16-63] The type of spectral signals analyzed by the newly proposed 2D correlation method became virtually limitless, which broaden possible applications to various fields among IR, Raman, X-ray, UV–vis, fluorescence, even to fields outside of spectroscopy.[16, 20, 23-27, 29-31, 33-37, 39-43, 45, 48-56, 58-60, 62, 64-98] At the same time, hetero-spectral correlation can be constructed by 2DCOS, among different spectroscopic techniques, such as 2D-IR-Raman correlation spectra, 2D-XRD-Raman correlation spectra.[24, 33, 39, 42, 45, 48, 62] Therefore, 2DCOS is truly revolutionized in the field of vibrational spectroscopy.

2. Construction of Two–Dimensional Correlation Spectra

Figure 1-1 shows the general scheme for constructing 2DCOS spectra.[15]

In 2DCOS, an additional external perturbation is applied to the system during the spectroscopic measurement. This external perturbation stimulates the system to cause some selective changes in the state, order, surroundings, etc. of system constituents. The response of the stimulated system to the applied external perturbation leads to distinctive changes in the spectrum. This spectral variation induced by an applied perturbation is called a dynamic spectrum.[5]

The dynamic spectrum of a system is defined as:

$$\tilde{y}(v, t) = \begin{cases} y(v, t) - \bar{y}(v) & \text{for: } T_{\min} \le t \le T_{\max} \\ 0 & \text{otherwise} \end{cases} \quad (1\text{-}1)$$

where $y(v, t)$ is a perturbation-induced variation of a spectral intensity during a fixed interval of some external variable t between $T_{\min}$ and $T_{\max}$. The external variable t in many cases is not only the chronological time, but also can be any other reasonable measure of a physical quantity, such as temperature, concentration, voltage, etc.. The variable v can be any appropriate spectral index used in the field of spectroscopy. $\bar{y}(v)$ is the reference spectrum.[5] It is customary to set $\bar{y}(v)$ to be the averaged spectrum given by:

$$\bar{y}(v) = \frac{1}{T_{\max} - T_{\min}} \int_{T_{\min}}^{T_{\max}} y(v, t)\mathrm{dt} \tag{1-2}$$

The generalized 2DCOS function given below

$$\boldsymbol{\Phi}(v_1, v_2) + i\boldsymbol{\Psi}(v_1, v_2) = \frac{1}{\pi(T_{\max} - T_{\min})} \int_0^\infty \tilde{Y}_1(\omega) \cdot \tilde{Y}_2^*(\omega)\mathrm{d}\omega \tag{1-3}$$

where the real part $\boldsymbol{\Phi}(v_1, v_2)$ and the imaginary part $\boldsymbol{\Psi}(v_1, v_2)$ are the synchronous correlation spectra and asynchronous correlation spectra, respectively. The term $\tilde{Y}_1(\omega)$ is the forward Fourier transform of the spectral intensity variations $\tilde{y}(v_1, t)$ observed at a given spectral variable v_1 with respect to the external variable t. The conjugate of the Fourier transform $\tilde{Y}_2^*(\omega)$ of the spectral intensity variation $\tilde{y}(v_2, t)$ is observed at another spectral variable v_2.[5]

By applying the well-known Wiener–Khintchine theory,[99] the synchronous 2DCOS spectrum can be directly computed as:

$$\boldsymbol{\Phi}(v_1, v_2) = \frac{1}{T_{\max} - T_{\min}} \int_{T_{\min}}^{T_{\max}} \tilde{y}(v_1, t) \cdot \tilde{y}(v_2, t)\mathrm{dt} \tag{1-4}$$

The manipulation of a classical cross-correlation function of dynamic spectra constructs only a synchronous 2DCOS spectrum. In order to circumvent the use of the Fourier transformation of dynamic spectra, Noda developed provides a reasonable estimate of an asynchronous 2D correlation spectrum in 2000.[5, 100] He introduced the time-domain Hilbert transform into the calculation of asynchronous correlation spectra. The asynchronous correlation spectrum is shown as

$$\boldsymbol{\Psi}(v_1, v_2) = \frac{1}{T_{\max} - T_{\min}} \int_{T_{\min}}^{T_{\max}} \tilde{y}(v_1, t) \cdot \tilde{z}(v_2, t)\mathrm{dt} \tag{1-5}$$

where $\tilde{z}(v_2, t)$ is the time-domain Hilbert transform of the dynamic spectrum $\tilde{y}(v_2, t)$ shown as:

$$\tilde{z}(v_2, t) = \frac{1}{\pi}\mathrm{pv} \int_{-\infty}^{+\infty} \frac{\tilde{y}(v_2, t')}{t' - t}\mathrm{dt}' \tag{1-6}$$

The practical numerical computation methods for synchronous and asynchronous 2DCOS spectra.[5, 15, 100, 101] It can be written as:

$$\boldsymbol{\Phi}(v_1, v_2) = \frac{1}{m - 1}\tilde{y}(v_1)^{\mathrm{T}}\tilde{y}(v_2)$$

$$\boldsymbol{\Psi}(v_1, v_2) = \frac{1}{m - 1}\tilde{y}(v_1)^{\mathrm{T}}\mathbf{N}\tilde{y}(v_2) \tag{1-7}$$

where m is the number of 1D spectra to construct the 2DCOS spectrum, $\tilde{y}(v_n)$ is the dynamic spectra, T is transpose, and $\mathbf{N}$ is the m order Hilbert-Noda matrix[100] as follows:

$$N_{ij} = \frac{1}{\pi} \begin{bmatrix} 0 & 1 & \frac{1}{2} & \frac{1}{3} & ... \\ -1 & 0 & 1 & \frac{1}{2} & ... \\ -\frac{1}{2} & -1 & 0 & 1 & ... \\ -\frac{1}{3} & -\frac{1}{2} & -1 & 0 & ... \\ ... & ... & ... & ... & ... \end{bmatrix}_m \qquad (1\text{-}8)$$

Figure 1-2A shows a typical synchronous 2DCOS spectrum.[5, 14] A synchronous spectrum is a symmetric spectrum with respect to a diagonal line corresponding to coordinates. Correlation peaks appear at both diagonal and off-diagonal positions. The intensity of peaks located at diagonal positions mathematically corresponds to the autocorrelation function of spectral intensity variations observed. Therefore, the diagonal peaks are referred to as autopeaks, which is always positive. The magnitude of an autopeak intensity represents the overall extent of spectral intensity variation observed at the specific spectral variable v during the observation interval between T_{min} and T_{max}. Thus, any region of a spectrum which changes intensity to a great extent under a given perturbation will show strong autopeaks.

Cross peaks located at the off-diagonal positions of a synchronous 2D spectrum represent simultaneous or coincidental changes of spectral intensities observed at two different spectral variables v_1 and v_2. The sign of cross peaks can be either positive or negative. Such a synchronized change, in turn, suggests the possible existence of a coupled or related origin of the spectral intensity variations. It is often useful to construct a correlation square joining the pair of cross peaks located at opposite sides of a diagonal line drawn through the corresponding autopeaks to show the existence of coherent variation of spectral intensities at these spectral variables.

Figure 1-2B shows an example of an asynchronous 2DCOS spectrum.[5, 14] The asynchronous spectrum is antisymmetric with respect to the diagonal line. Autopeak occurs on a 2D asynchronous spectrum. That is to say, 2D asynchronous spectrum consists exclusively of cross peaks located at off-diagonal positions. The cross peaks in an asynchronous spectrum develop only if the intensities of two spectral features change out of phase with each other (i.e., delayed or accelerated if time is the external variable). This property is especially useful in differentiating overlapped bands arising from spectral signals of different origins.

3. The development of Orthogonal Sample Design (OSD) and Related Techniques

This thesis is based on orthogonal sample design (OSD) and related techniques, which were introduced by Xu et al.[20, 26, 37, 40, 72, 79, 80, 93, 102-120] Herein we give a brief introduction of OSD approach and its development.

Intermolecular interactions, which occur ubiquitously in nature, have been the focus of extensive research interests, as they lie at the center of many physical, chemical,

and biological processes including molecular recognition and molecular catalysis. Over the past several decades, various methods have been utilized to characterize intermolecular interactions.[121-125] Among those approaches, molecular spectroscopic methods possess great potential. For example, the variation in frequency and bandwidth of OH/NH stretching bands in infrared (IR) and Raman spectra provides a sensitive probe to monitor the formation and change of hydrogen bonds.[126-137] However, many intermolecular interactions, such as dipole–dipole interaction, albeit quite strong, can induce only subtle spectral changes that are often buried within complex spectral profiles. Consequently, it is quite difficult to investigate these intermolecular interactions directly by using conventional spectroscopic methods.

The advent of two-dimensional (2D) correlation spectroscopy provides a new avenue to study intermolecular interactions. Two-dimensional correlation spectroscopy is a powerful spectral analysis technique based on the analysis of a set of spectral data, which are sequentially obtained under some form of perturbation applied to the sample. Many important spectral features that are not readily accessible in the original set of one-dimensional spectra can be clearly visualized in the 2D spectra.

For example, the cross-peaks in a 2D synchronous spectrum can be used to characterize intermolecular interactions. A system containing two substances is considered here. The two substances are denoted as P and Q. The spectral coordinate of a characteristic peak from P is given by X_P, and that from Q is X_Q. The occurrence of a cross-peak at (X_P, X_Q) in the 2D synchronous spectrum indicates that the responses of spectral intensities at X_P and X_Q vary in a synchronous or coordinated manner under the external perturbation. In principle, this synchronous behavior of spectral intensities may sometimes suggest the presence of intermolecular interaction between P and Q. However, interfering cross peaks due to other sources of synchronicity, such as concentration variations of solutes, also arise. Consequently, cross peak may appear at (X_P, X_Q) in the corresponding 2D synchronous spectrum even if there is no intermolecular interaction between P and Q. This problem makes it difficult to directly use the cross-peaks in a 2D synchronous spectrum as a reliable criterion to judge whether intermolecular interaction actually occurs or not.

The work of Yu is quite heuristic to address the problem. In his work, Yu and his co-worker demonstrated that intermolecular interaction can be reflected by the spectral signals that are systematic deviated from the Beer-Lambert law.[121] This work conferred a solid physical basis to use 2D correlation spectra to study intermolecular interaction.

Inspired by Yu's work, Xu and his co-worker proposed an orthogonal sample design (OSD) scheme to reflect intermolecular interaction using cross peaks in 2D synchronous spectrum is a reliable manner.

Xu and his coworker study intermolecular interaction between two solutes (denoted as P and Q) dissolved by the same solvents. They use concentration of P and Q as external perturbations. The advantage of this selection is two folds: 1) The relationship between the perturbation and dynamic data becomes simple and can be expressed mathematically in a straightforward manner. 2) The spectral behavior is controllable. This approach provides an opportunity to tailor the dynamic data by designing suitable concentration series to control the information content of the 2D

synchronous spectra.

Xu et al. used a model system to express the idea of the OSD approach. To investigate intermolecular interaction between P and Q, a series of solution containing different amount of P and Q are prepared and the spectra of these solutions are recorded. Then a 2D synchronous spectrum is generated via the obtained spectra.

In the obtained spectra, Xu et al assumed that: (1) No spectral overlapping occurs between the characteristic peak of P at X_P and the characteristic peak of Q at X_Q. (2) Solvent has no spectral contribution to the characteristic peak of P and that of Q.

When P and Q co-exist in the same solution and intermolecular interaction occur between P and Q. The absorbance at X_P and X_Q can be express as:

$$A_P^i(X_P) = \varepsilon_P L C_P^i - \delta_P^i\left(X_P, C_P^i, C_Q^i\right)$$

$$A_Q^i\left(X_Q\right) = \varepsilon_Q L C_Q^i - \delta_Q^i\left(X_Q, C_P^i, C_Q^i\right) \tag{1-9}$$

where ε_P is the molar absorptivity of P at X_P, while ε_Q is that of Q at X_Q. L is the path length of the solution, and C_P^i and C_Q^i are the concentrations of P and Q in the ith spectrum, respectively. $\delta_P^i\left(X_P, C_P^i, C_Q^i\right)$ and $\delta_Q^i\left(X_Q, C_P^i, C_Q^i\right)$ are the deviation terms that can be used to characterize the intermolecular interactions between P and Q.

Then, the series of spectra were used to construct a 2D synchronous spectrum and the expression of 2D synchronous spectrum at (x,y) is composed of two parts:

$$\Phi(X_P, X_Q) = \frac{1}{m-1}\left[\mathbf{M}(X_P, X_Q) + \mathbf{N}(X_P, X_Q)\right] \tag{1-10}$$

Where

$$\mathbf{M}\left(X_P, X_Q\right) = -\sum_{i=1}^{m}\left[\varepsilon_P L \tilde{C}_P^i \tilde{\delta}_Q^i\left(X_Q, C_P^i, C_Q^i\right) + \varepsilon_Q L \tilde{C}_Q^i \tilde{\delta}_P^i\left(X_P, C_P^i, C_Q^i\right)\right.$$

$$\left. - \tilde{\delta}_P^i\left(X_P, C_P^i, C_Q^i\right)\tilde{\delta}_Q^i\left(X_Q, C_P^i, C_Q^i\right)\right] \tag{1-11}$$

$$\mathbf{N}(x, y) = \varepsilon_P \varepsilon_Q L^2 \sum_{i=1}^{m} \tilde{C}_P^i \tilde{C}_Q^i$$

The first term $\mathbf{M}(X_P, X_Q)$ contains the excess terms, $\tilde{\delta}_P^i\left(X_P, C_P^i, C_Q^i\right)$ and $\tilde{\delta}_Q^i\left(X_Q, C_P^i, C_Q^i\right)$, which can be nonzero when intermolecular interactions exist between P and Q. That is to say, $\mathbf{M}(X_P, X_Q)$ reflects intermolecular interaction in the form of the deviation from the Beer–Lambert law. The second term $\mathbf{N}(X_P, X_Q)$ is just related to the concentration of the solutes and has nothing to do with intermolecular interaction between the two solutes.

If no intermolecular interactions occur between P and Q, then both $\tilde{\delta}_P^i\left(X_P, C_P^i, C_Q^i\right)$ and $\tilde{\delta}_Q^i\left(X_Q, C_P^i, C_Q^i\right)$ become zero, and we have

$$\mathbf{M}(x,y)=0 \tag{1-12}$$

Combining eq. 1-10 and 1-12, we obtain

$$\Phi(x,y)= \mathbf{N}(x,y) \tag{1-13}$$

For a 2D synchronous spectrum that is designed to reflect intermolecular interactions properly, it is desirable for Φ (X_P, X_Q) to be zero when there is no interaction between P and Q. Thus, $\mathbf{N}(X_P, X_Q)$ has to be zero.

From eq. 1-11, it is quite clear that $\mathbf{N}(X_P, X_Q)$ may be nonzero if the concentrations of P and Q are selected arbitrarily. Thus, something should be done on the design of the concentration series of P and Q to make the value of $\mathbf{N}(X_P, X_Q)$ to be zero.

Xu et al. noticed that $\mathbf{N}(X_P, X_Q)$ could be written as a dot product of two vectors $\vec{\mathbf{C}}_P^{(init)}$ and $\vec{\mathbf{C}}_Q^{(init)}$.

$$\mathbf{N}(X_P, X_Q) = \varepsilon_P \varepsilon_Q L^2 \vec{\mathbf{C}}_P^{(init)} \cdot \vec{\mathbf{C}}_Q^{(init)}. \tag{1-14}$$

According to the basic properties of a vector dot product, a feasible way to make the value of $\mathbf{N}(X_P, X_Q)$ be zero is that the vector $\vec{\mathbf{C}}_P^{(init)}$ is orthogonal to the vector $\vec{\mathbf{C}}_Q^{(init)}$.

$$(\vec{\mathbf{C}}_P^{(init)})^T \vec{\mathbf{C}}_Q^{(init)} = 0 \tag{1-15}$$

Table 1-1 provide an example of concentration series of P and Q that satisfies eq. 1-15.

This is the basic idea of the OSD approach.

Xu and his coworkers have used the OSD approach on a couple of chemical system. For example, they investigated weak coordination between Pr^{3+} and carbonyl group of butanone.[40] Cross peaks indeed appear in the 2D synchronous spectrum generated using the OSD approach (**Figure 1-3A**). For comparison, they performed a negative control experiment (**Figure 1-3B**). In this experiment, Pr^{3+} and butanone are spatially separated, thereby excluding the possibility interaction occur between Pr^{3+} and butanone. Spectra of Pr^{3+} and butanone are recorded separated. Afterward, the spectra of Pr^{3+} and butanone added to "synthesized" spectra of Pr^{3+}/butanone mixture. The obtained "synthesis" spectra are used to generate 2D synchronous spectrum via the OSD approach. In this case cross peak does not appear, demonstrating the effectiveness of the OSD approach.

Nowadays, multiple dimensional NMR have been extensively used. The key point in the approach is designing of suitable pulse sequences. Via this way, irrelevant signals are removed so that physicochemical features that the users are concerned appear as cross peaks in multiple dimensional NMR spectra.

In 2DCOS, Xu and his co-worker adopted a strategy: Construction of 2D correlation spectra via designing of concentration series. They hope this approach is helpful to enhance the understanding on intermolecular interaction.

However, the OSD approach has limitation.

Based on Mathematical analysis, Li and Xu demonstrated that it is not practically feasible to remove interference portion completely from 2D synchronous spectrum when the characteristic peaks of P and Q are overlapped.[114]

To a considerable extent, this limitation restricts the extensive application of the OSD approach in real chemical systems. To solve the problem, Xu and his co-worker developed <u>A</u>synchronous <u>O</u>rthogonal <u>S</u>ample <u>D</u>esign (AOSD) approach.[114]

In this approach, cross peaks in 2D asynchronous spectrum rather than 2D synchronous spectrum are used to reflect intermolecular interaction between two solutes (P and Q) dissolved in the same solution.

Li and Xu demonstrated that interference part that are difficult to be completely removed in 2D synchronous spectrum can be completely eliminated using the basic mathematical properties of the Hilbert-Noda matrix. As a result, cross peaks in 2D asynchronous spectrum are still reliable probe to reflect intermolecular interaction even if the characteristic peaks of P and Q are overlapped. In their paper, they use two model systems to show the effectiveness of the AOSD approach.

In the two model systems, interaction between two solutes (P and Q) are investigated. The characteristic peak of P and Q are overlapped. In the first system, intermolecular interaction is present between P and Q while no intermolecular interaction occurs between P and Q in the second system. The description of the two model system in detail can be found in ref. 114.

The spectra of a typical solution of the first solution and the second solution are shown in **Figure 1-4**. No observable difference is found between the two spectra. When 2D asynchronous spectra are generated using the AOSD approach (**Figure 1-5**), dramatically difference are found between the two systems. In the 2D asynchronous spectrum of the first system (**Figure 1-5A**), cross peak are present while no cross peaks are found in the 2D asynchronous spectrum of the second system (**Figure 1-5B**). The results clearly demonstrate that intermolecular interaction between two solutes dissolved in the same solutions can be accurately reflected by 2D asynchronous spectrum generated via the AOSD approach even if the characteristic peaks of the two solutes are overlapped.

P and Q co-exist in the same solution and interaction occur between P and Q, the intermolecular interaction can also be described by the following model:

Under the interaction, a small fraction of P undergoes subtle structural variation and converts into another form, denoted as U. A small fraction of Q changes into V. In 1D spectra, the peak parameters, including peak position, bandwidth, and absorptivity of U, are quite closed to those of P. Hence, the peak of P and that of U are severely overlapped. Moreover, weak interaction only converts very small fraction of P into U. Thus, the concentration of is usually overwhelmingly stronger than that of U. In a spectroscopic experiment, what we can observe is the summation of the signal from P and U. From this summation, it is almost impossible to differentiate the signal from P and that of U. Similar problem occur between the characteristic peaks of Q and V. That, revealing subtle spectral changes is a challenge.

In another paper, Zhang and Xu designed a concentration series of P and Q.[119] Using this concentration series, interference part from both 2D synchronous spectrum

and 2D asynchronous spectrum can be completely removed. Thus, cross peaks in both 2D synchronous spectrum and 2D asynchronous spectrum can be used to reflect intermolecular interaction between P and Q. The approach is called double orthogonal sample design (DOSD) scheme.

Zhang and Xu defined $\Delta X_P, \Delta X_Q, \Delta W_P, \Delta W_Q, \Delta\varepsilon_P, \Delta\varepsilon_Q$ as follows:

$$\Delta X_P = X_U - X_P$$
$$\Delta X_Q = X_V - X_Q$$
$$\Delta W_P = W_U - W_P$$
$$\Delta W_Q = W_V - W_Q \tag{1-16}$$
$$\Delta\varepsilon_P = \varepsilon_U - \varepsilon_P$$
$$\Delta\varepsilon_Q = \varepsilon_V - \varepsilon_Q$$

The patterns of cross peaks in both 2D synchronous spectrum and 2D asynchronous spectrum generated using the DOSD approach provided a comprehensive information that is helpful in revealing subtle changes in peak position, bandwidth, and absorptivity.

In the first example, the peak parameters of P, Q, U and V are summarized in **Table 1-2**. In comparison with the characteristic peak of P, the peak of U undergoes a slight shift. As a result, the peak of P and U are highly overlapped. From a solution containing P, Q, U and V, the overlapping between the peaks of P and U are so severe that the characteristic peak of U cannot be observed even if second derivative spectra method is used. However, 2D synchronous spectrum and 2D asynchronous spectrum (**Figure 1-6A**) generated via the DOSD approach managed to reveal the occurrence of U even if the characteristic peak of P and U are severely overlapped. For example, around (150,350) in 2D synchronous spectrum, a group of cross peaks that is composed of one positive cross peak and a negative cross peak can be observed. In 2D asynchronous spectrum, two groups of cross peaks are relevant to the subtle band-shift. The first group of cross peaks appear around (150, 350). The first group of cross peaks is also composed of one positive cross peak and a negative cross peak. The second group of cross peaks locate near the diagonal. This group of cross peaks is composed of two cross peak that are antisymmetric about the diagonal.

In the second example, the peak parameters of P, Q, U and V are summarized in **Table 1-3**. In this case, the peak positions of the characteristic peak of P and U are the same. However, the bandwidth of the two peaks are different. To our knowledge, there is no other method available to differentiate the two overlapped peaks whose peaks positions are the same. However, both 2D synchronous and asynchronous spectra (**Figure 1-6B**) generated using the DOSD approach can reveal the existence of U via the characteristic patterns. Around (150, 350) in 2D synchronous spectrum, a group of cross peaks is produced. The group of cross peaks is composed of two peaks whose sign and absolute intensity are the same. Two groups of cross peaks are present in 2D asynchronous spectrum. The first group of cross peaks occur around (150,350). The pattern of this group of cross peaks are roughly the same as that in 2D synchronous spectrum. The second group of cross peaks is composed of two horizontal cross peaks and two vertical cross peaks that form a diamond pattern. The absolute intensities of the four cross peaks are the same. The sign of two horizontal cross peaks are the same

and the sign of the two vertical cross peaks are the same. However, signs of the horizontal cross peaks are different from that of the two vertical cross peaks.

In the third example, the peak parameters of P, Q, U and V are listed in **Table 1-4**. In this case, both peak position and bandwidth of the characteristic peak of P are the same as those of U. However, the absorptivity of characteristic peak of P and U are different. That is to say, the characteristic peaks of P and U are completely overlapped. In spite of the severe overlapping, 2D correlation spectra (**Figure 1-6C**) generated using the DOSD approach can be used to reveal the existence of U that is completely covered by the peak of P. In both 2D synchronous spectrum and 2D asynchronous spectrum, single cross peaks appear at (150, 350).

The above results demonstrate that characteristic pattern of cross peaks in 2D synchronous spectrum and 2D asynchronous spectra become a powerful resolution enhancement tool that can be used to differentiate highly overlapping peaks.

In the further work, Xu and his colleagues found that the pattern of cross peaks in 2D correlation spectra constructed via the DOSD approach cannot reveal what happens when peak position, bandwidth and absorptivity change simultaneously.

To enhance understanding on the physical-chemical nature of intermolecular interaction, a new approach called double asynchronous orthogonal sample design (DAOSD) scheme is developed by Chen and Xu.[103]

In the DAOSD approach, two groups of solutions are prepared. In the first group of solutions, the initial concentrations of P are constant, while the initial concentrations of Q can be selected arbitrarily. In the second group solution, the initial concentrations of Q are constant, while the initial concentration of P can be selected arbitrarily. Spectra of the two groups of solutions are recorded. Subsequently, a 2D asynchronous spectrum is generated from the first group of solution and the resultant 2D asynchronous spectrum is called $\Psi_P(x, y)$. Similarly, the spectra of the second group of solutions are used to construct 2D asynchronous spectrum and the resultant 2D asynchronous spectrum is called $\Psi_Q(x, y)$. [103]

Chen and Xu used a model system to show the spectral behavior of the pair of 2D asynchronous spectrum ($\Psi_P(x, y)$ and $\Psi_Q(x, y)$) generated via the DAOSD approach. In the model system, the characteristic peaks of P occur at XP and the characteristic peak of Q occur at X_Q. The pattern of $\Psi_P(x, y)$ and $\Psi_Q(x, y)$ are illustrated in **Scheme 1-1**. There are three groups of cross peaks in $\Psi_P(x, y)$. The first group of cross peaks appears around (X_Q, X_Q). The second and third groups of cross peaks occur around (X_P, X_Q) and (X_Q, X_P), respectively. Mathematical analysis demonstrated that the cross peaks around (X_Q, X_Q) reflect the difference on peak position and bandwidth between the characteristic peak of Q and V. The relationship between the sign of ΔX_Q and ΔW_Q and the pattern of cross peaks are summarized in **Figure 1-7**. The second and the third groups of cross peaks in $\Psi_P(x, y)$ are antisymmetric about the diagonal and only the second group of cross peaks are discussed. Mathematical analysis indicates that the second group of cross peaks is composed of two parts. The first part is related to the difference on peak position and bandwidth between the characteristic peak of P and U, and the second part is relevant to the difference on absorptivity between the characteristic peak of P and U. The relationship between the sign of ΔX_P and ΔW_P and

the pattern of the first part of second group of the cross peaks is shown in **Figure 1-8**. In addition, the relationship between the sign of $\Delta \varepsilon_P$ and the pattern of the second part of second group of the cross peaks is shown in **Figure 1-8**.

Similarly, there are three groups of cross peaks in $\Psi_Q(x, y)$. The first group of cross peaks appears around (X_P, X_P). The second and third groups of cross peaks occur around (X_P, X_Q) and (X_Q, X_P), respectively. The cross peaks around (X_P, X_P) reflect the difference on peak position and bandwidth between the characteristic peak of P and U. The relationship between the sign of ΔX_P and ΔW_P are similar to **Figure 1-7**. The second and the third groups of cross peaks are antisymmetric about the diagonal and only the second group of cross peaks are discussed. The second group of cross peaks is composed of two parts. The first part is related to the difference on peak position and bandwidth between the characteristic peak of Q and V and the second part is relevant to the difference on absorptivity between the characteristic peak of Q and V.

The above spectral properties of the cross peaks make it possible to deduce ΔX_P, ΔX_Q, ΔW_P, ΔW_Q, $\Delta \varepsilon_P$ and $\Delta \varepsilon_Q$ via the patterns of cross peaks in the pair of 2D asynchronous spectra generated via the DAOSD approach.

An example of analysis of ΔX_P, ΔW_P, $\Delta \varepsilon_P$, ΔX_Q, ΔW_Q and $\Delta \varepsilon_Q$ on a model system by using the DAOSD approach is shown in **Figure 1-9**

First, a 2D asynchronous spectrum generated by using the AOSD approach is shown on the left part of **Figure 1-9**. Although interference part that has nothing to do with intermolecular interaction has been completely removed, the patterns of cross peaks are still quite complex. It is difficult to deduce what happen on the characteristic peak of P and Q upon intermolecular interaction.

When the DASOSD approach is utilized, 2D asynchronous spectrum generated by using the AOSD approach can be split into $\Psi_P(x, y)$ and $\Psi_Q(x, y)$. According to the pattern of cross peak around (300, 300) in $\Psi_P(x, y)$, we learn that the bandwidth of Q decreases upon interaction with P. Based on the pattern of cross peaks around (100, 100) in $\Psi_Q(x, y)$, it can be deduced that $\Delta X_P > 0$ and $\Delta W_P > 0$.

Based on the above results, we simulate cross peaks around (100, 300) in Ψ_P. After comparing the simulated cross peak with cross peaks around (100, 300) in Ψ_P, a negative single cross peak appears at (100, 300) in Ψ_P. Based on this result, we get a conclusion that $\Delta \varepsilon_P$ is negative under interaction. Similarly, we simulate cross peak around (300, 100) in Ψ_Q. After comparing the simulated cross peak with cross peaks around (300, 100) in Ψ_Q, we find a positive single cross peak occur at (100, 300) in Ψ_P. Thus, $\Delta \varepsilon_P$ should be positive.

The peak parameters for P, Q, U and V are shown in **Table 1-5**. The signs of ΔX_P, ΔW_P, $\Delta \varepsilon_P$, ΔX_Q, ΔW_Q and $\Delta \varepsilon_Q$ are the same as those deduced from the pattern of cross peaks from $\Psi_P(x, y)$ and $\Psi_Q(x, y)$.

4. Other Developments in Two-Dimensional Correlation Spectroscopy

In recent years, numerous significant new concepts of 2DCOS have been reported with the development of 2DCOS theory[138]. For example, chemometrics-combined two-

dimensional correlation spectroscopy,[30, 139-147] moving-window two-dimensional analysis (MW2D),[34-36, 49-55, 58-60, 71, 87, 90, 148-150] quadrature orthogonal signal corrected two-dimensional correlation spectroscopy (QOSC),[151, 152] projection two-dimensional,[153] two-dimensional codistribution spectroscopy (2DCDS)[154] have been developed. A brief introduction about chemometrics-combined two-dimensional correlation spectroscopy and moving-window two-dimensional analysis is provided in the section.

4.1. Chemometrics-Combined Two-Dimensional Correlation Spectroscopy

2DCOS and chemometric techniques are very popular in spectral analyzes in many research fields. The combination of 2DCOS and chemometric generally provides more useful information to explain the subtle spectral changes of the system, which are hardly detectable in conventional 2DCOS.[30, 138-144]

Jung et al. firstly reported the real combination of 2DCOS and principal component analysis (PCA), which is called PCA-2DCOS. In this technology, PCA is an essential part of PCA-2DCOS.[138, 139, 144] It is a very powerful technique for eliminating the noise contribution in the spectrum and extract useful information. Jung also reported on a new concept of *eigenvalue manipulation transform* (EMT) for PCA-2DCOS, which can emphasize weak but important contribution.[30, 138, 141-143]

Here we will briefly introduce background of PCA-2DCOS and EMT.[30, 138, 141-143] The original spectral data matrix $\mathbf{A}$ is an $n \times m$ matrix with n spectra and m data points in each spectrum. In PCA, the significant part of the data matrix $\mathbf{A}^*$ can be expressed as the product of score and loading matrices.

$$\mathbf{A}^* = \mathbf{WV}^T + \mathbf{E} = \mathbf{A}^* + \mathbf{E} \qquad (1\text{-}17)$$

where $\mathbf{W}$ and $\mathbf{V}$ are the loading matrix ($m \times r$) and score matrix ($n \times r$), respectively, and $\mathbf{E}$ is the residual matrix often related with pure noise. The matrix product $\mathbf{A}^*$ is the reconstructed data matrix of the original data $\mathbf{A}$ without noise contribution.[30, 138, 141-143]

$$\mathbf{A}^* = \mathbf{WV}^T \qquad (1\text{-}18)$$

In PCA-2DCOS, this *reconstructed data matrix* $\mathbf{A}^*$ from a few selected significant scores and loading vectors of PCA is used instead of the original data matrix. PCA-2DCOS highlights the most important features of synchronization and asynchrony with noise-free contribution.

This PCA-reconstructed data matrix $\mathbf{A}^*$ can be also expressed as a singular value decomposition:

$$\mathbf{A}^* = \mathbf{USV}^T \qquad (1\text{-}19)$$

and

$$\mathbf{S} = \mathbf{L}^{1/2} \qquad (1\text{-}20)$$

where $\mathbf{U}$ and $\mathbf{S}$ are the orthonormal score matrix and diagonal matrix containing the singular value, respectively.

$\mathbf{L} = \mathbf{W'W}$ is a diagonal matrix where each diagonal element corresponds to the eigenvalue of principal component (PC). The scoring matrix $\mathbf{W}$ is expressed as $\mathbf{W} = \mathbf{US}$ and can be obtained directly from $\mathbf{W} = \mathbf{AV}$.

By manipulating and replacing the eigenvalues of **A***, a new transformed data matrix **A*** can be obtained.

$$\mathbf{A^{**}=US^{**}V^T} \tag{1-21}$$

where **S*** is given by varying the corresponding eigenvalues in **S** by raising them to the power of m.

$$\mathbf{S^{**}=S^m} \tag{1-22}$$

In this technique, the specific information content in 2D correlation spectroscopy is amplified by using a transformation of the data set.[30, 138, 141-143]

Jung et al. investigate the impact of the new reconstructed data matrix on 2D correlation spectra by using the time-dependent FT-IR spectra of a mixture of methyl ethyl ketone, deuterated toluene, and polystyrene system as an example.[141] The experiment details can be found in ref. 100.

Jung et al. inject artificial noise to the 1D spectra and set the value of the power parameter m, as $m = 2$. **Figure 1-10A** displays a synchronous 2D correlation spectrum from the EMT-reconstructed data matrix A** obtained by replacing the original eigenvalues by varying the value of the power parameter m, as $m=2$. In comparison, the original synchronous 2D correlation spectrum is shown in **Figure 1-10B**. The corresponding asynchronous 2D correlation spectra are depicted in **Figure 1-11**.[141]

For $m=2$, this operation will diminish the contribution of smaller eigenvalues much more rapidly. The net result is that minor factors representing the noise component are effectively eliminated.

The most noticeable benefit of EMT operation is a gradual noise reduction process based on more flexible fine-tuning operation compared to the abrupt truncation of noise (and spectral information) performed by the PCA-2D correlation analysis. As eq 1-21and 1-22, the transformation of spectral data via a simple manipulation of eigenvalues to enhance spectral selectivity shows promising flexibility and potential, especially when coupled with 2D correlation analysis.

4.2. Moving-Window Two-Dimensional Analysis (MW2D)

The interpretation of 2DCOS based on a large set of spectral data sometimes becomes difficult, due to the inclusion of too many underlying processes influencing the spectral changes. In order to solve this problem, Thomas et al. introduced the concept of moving window into the 2DCOS.[90] A spectrum data matrix $y(v, p)$ is consisted of rows along the spectral variable and columns along the perturbation variable. A submatrix of the data is constructed by choosing only $2m+1$ rows around the jth row of the data.[149, 150] That j and J are correspond to the index of a window and that of a spectrum within the window, respectively. Generalized 2D correlation spectra are then calculated from the individual submatrix, and a certain characteristic one-dimensional (1D) spectrum (a diagonal line spectrum, a slice spectrum, etc.) is extracted from the 2D spectrum. Finally, the set of 1D spectra thus collected are aligned along the perturbation axis by incrementally shifting the position of the window to obtain a MW2D correlation spectrum.[5]

PCMW2D analysis is a variant form of the MW2D analysis introduced by Morita et al..[138, 148] In PCMW2D analysis, the spectral intensity variation within a chosen window is correlated synchronously and asynchronously with the perturbation variable itself. The resulting waterfall plots as functions of wavenumber and perturbation variable roughly correspond to the first and second derivatives of spectral intensities with respect to the perturbation variable. PCMW2D technique has been recently applied for identification of a specific zone along the perturbation variable axis containing distinct variations of spectral intensities. Once such zones of interest are identified, then traditional 2D correlation analysis is applied only to those localized zones. The combination of PCMW2D and standard 2D correlation analysis yields unambiguous correlation results by avoiding the inclusion of multiplicity of spectral intensity variation responses. This approach is often preferred over the simple segmentation of data set into arbitrary blocks, as PCMW2D provides good estimates for both location and width of perturbation variable interval to be used for 2D correlation analysis.[34-36, 49-55, 58-60, 138, 148]

Morita et al. proposed that the synchronous ($\mathbf{\Pi_\Phi}$) and asynchronous ($\mathbf{\Pi_\Psi}$) PCMW2D correlation spectra are calculated as follows:[148]

$$\mathbf{\Pi}_{\Phi,j}(v, p_j) = \frac{1}{2m} \sum_{J=j-m}^{j+m} \tilde{y}(v, p_J) \cdot \tilde{p}_J$$

$$\mathbf{\Pi}_{\Psi,j}(v, p_j) = \frac{1}{2m} \sum_{J=j-m}^{j+m} \tilde{y}(v, p_J) \cdot \sum_{K=j-m}^{j+m} \mathbf{N} \cdot \tilde{p}_K \tag{1-23}$$

In addition, they find an important rule that the synchronous and asynchronous PCMW2D correlation spectra are similar to the first derivative and second derivative of the spectral intensity variation along the perturbation direction (eq 1-24). **Table 1-6** summarized the rules of PCMW2D correlation spectra.[148]

$$\mathbf{\Pi}_{\Phi,j}(v, p) \sim \left[\frac{\partial y(v, p)}{\partial p} \right]_v$$

$$\mathbf{\Pi}_{\Psi,j}(v, p) \sim - \left[\frac{\partial^2 y(v, p)}{\partial p^2} \right]_v \tag{1-24}$$

The authors used an example to elucidate spectral features of the PCMW2D correlation analysis. In the example, the PCMW2D technique was applied to a set of simulated spectra as shown in **Figure 1-12**. Each spectrum possesses two peaks (a and b). The intensity of each peak changes as a function of the perturbation variable p.[148]

Figure 1-13A and **1-13B** are both the synchronous and asynchronous correlation spectra shown in a form of a birds-eye view and generated from the simulated spectra (**Figure 1-12**).[148]

Figure 1-14A shows a slice spectrum at v=300 of the original simulated spectra. **Figure 1-14B** and **Figure 1-14C** are the slice spectra of the synchronous (**Figure 1-13A**) and asynchronous (**Figure 1-13B**) PCMW2D correlation spectra at v=300, respectively.[148]

17

The variation of the intensities of the original spectra versus perturbation variable can be described by a sine function. The slice spectrum at v=300 in the synchronous PCMW2D spectrum can be roughly described by a cosine function, the first derivative of the sine function. The slice spectrum at v=300 in the asynchronous PCMW2D spectrum can be roughly described by a sine function, the second derivative of the sine function. The behavior on the simulated system supporting the author's conclusion, i.e., the synchronous and asynchronous PCMW2D correlation spectra are similar to the first derivative and second derivative of the spectral intensity variation along the perturbation direction.[148]

5. Applications of Two-Dimensional Correlation Spectroscopy

It has been reported that 2DCOS has significant experiments in many fields, including the types of analytical probes employed, various external perturbations used in the experiments, and various materials and systems for 2DCOS studies. To investigate the properties of the system, 2DCOS was applied to spectra measured by different types of modern analytical probes such as IR,[23, 25, 27, 30, 31, 33-36, 40-42, 45, 49-55, 58-60, 62, 71, 87, 90, 94] NIR,[27, 68, 89, 91, 96] Raman,[29, 39, 67, 76, 77, 81, 88, 95, 98] vibrational optical activity(VOA),[16, 43, 65, 66, 84] UV-Vis,[20, 26, 29, 37, 56, 72, 79, 80, 92, 97] fluorescence,[69, 73, 74, 93] X-ray[24, 29, 33, 39, 48, 75, 82, 83] and NMR.[42, 64, 70, 78, 85, 86] Among the external perturbations applied, such as mechanical,[45-47, 62] electrical,[18, 28, 39, 57] thermal,[19, 24, 30, 31, 33-36, 41, 44, 48-55, 58-60, 62] chemical,[16, 20, 23, 25-27, 29, 32, 33, 37, 38, 40, 42, 43, 56, 63] biological,[17, 21, 22, 61] etc., temperature is the most commonly used application in 2DCOS. 2DCOS has been utilized to investigate various materials and systems such as polymers,[24, 28, 30, 31, 33, 34, 36, 42, 46, 48, 50-54, 56, 58-60, 62, 69, 76, 81, 88, 94, 96, 155-158] proteins and peptides,[16, 29, 32, 43, 44, 65, 159, 160] nanomaterials and composites,[38, 47, 89, 92, 161-164] medicine,[26, 45, 165-167] nucleic acids,[22, 74, 161, 168] food,[97, 169-174] natural materials[17, 61, 175-177] and environmental[178-181] by using 2DCOS.

A very attractive advantage in 2DCOS applications is the hetero-correlation analysis, such as hetero-spectral correlation,[24, 33, 39, 42, 45, 48] hetero-perturbation (or hybrid) correlation,[33, 62] and hetero-sample correlation.[25, 182] Among them, 2D heterogeneous correlation is the most frequently used, and it is possible to compare two systems of completely different types of spectral data obtained under similar external perturbations. In the 2D hetero-spectral correlation analysis, the correlation between different spectral signals under the same perturbation can be detected. 2D heterogeneous spectral analysis can be applied to correlations not only between closely related spectroscopic measurements such as IR and Raman spectroscopy, but also between completely different types of spectroscopic or physical techniques such as IR and X-ray spectroscopy.

6. Outline of Each Chapter

The outline of each chapter for the present thesis will be described as follows.
This thesis consists of five chapters.
Chapter 1: this chapter describes a novel approach to generate 2DCOS spectra, in order to enhance the intensity of cross peaks relevant to intermolecular interaction.

We investigate intermolecular interaction between two solutes (denoted as P and Q, where P has a characteristic peak at X_P) dissolved in the same solvent via the near diagonal cross peaks around the coordinate (X_P, X_P) in a two-dimensional (2D) asynchronous spectrum of generalized spectroscopy. Because of physical constrains in many cases, the variation ranges of the initial concentrations of P or Q must be kept very narrow, leading to very weak cross peak intensities. The weak cross peaks vulnerable to noise bring about difficulty in the investigation of subtle intermolecular interaction. Herein, we propose a new of way constructing a 2D asynchronous spectrum without the subtraction of the average spectrum often used as a reference spectrum. Mathematical analysis and computer simulation demonstrate that the near diagonal cross peaks around the coordinate (X_P, X_P) in the 2D asynchronous spectrum using the new approach possess two characteristics: 1) they can still reflect an intermolecular interaction reliably; 2) the absolute intensities of the cross peaks are significantly stronger than those generated by the conventional method. We incorporate the novel method with the DAOSD (Double Asynchronous Orthogonal Sample Design Scheme) approach and applied the modified DAOSD approach to study hydrogen bonding behavior in diethyl either/methanol/THF system. The new approach made the weak cross peaks, which are not observable in 2D asynchronous spectrum generated using conventional approach, become observable. The appearance of the cross peak demonstrate that: When a small amount of THF is introduced into diethyl solution containing low amount of methanol, THF breaks the methanol-diethyl ether complex and forms methanol-THF complex via new hydrogen bond. This process takes place in spite of the fact that the content of diethyl ether is overwhelmingly larger than that of THF. The above result demonstrates that the new approach is applicable to enhance intensity of cross peaks in real chemical systems.

Chapter 2: this chapter describes the behavior of noise in asynchronous 2DCOS spectra and a new approach to improve a signal-to-noise ratio of 2DCOS spectra by a Butterworth filter. Mathematical analysis on the noise of 2D spectra and computer simulation on a model system show that the fluctuation of noise in a 2D asynchronous spectrum can be characterized by the standard deviation of noise in 1D spectra. Furthermore, a new approach to improve a signal-to-noise ratio of 2D asynchronous spectrum by a Butterworth filter is developed. A strategy to determine the optimal conditions is proposed. Computer simulation on a model system indicates that the noise of 2D asynchronous spectrum can be significantly suppressed using the Butterworth filtering. In addition, we have tested the approach to a real chemical system where interaction between berberine and β-CyD is investigated using 2D UV-vis asynchronous spectra. When artificial noise is added, cross peaks that reflect intermolecular interaction between berberine and β-CyD are completely masked by noise. After the method described in this article is utilized, noise is effectively suppressed and cross peaks are faithfully recovered. The above result demonstrates that the approach described in this article is applicable in real chemical systems.

Chapter 3: this chapter describes interaction between berberine chloride and β-CyD by using 2DCOS spectra. The occurrence of cross peaks around (420 nm, 420 nm) in 2D asynchronous spectrum reveals that specific intermolecular interaction indeed

exists between berberine chloride and β-CyD. In spite of the difficulty caused by overlaping of cross peaks, we manage to confirm that the 420 nm band of berberine undergoes red-shift and its its bandwidth decrease under interaction with β-CyD. The red-shift of the 420 nm band that can be assigned to n-π* transition indicates the environment of berberine become more hydrophobic. The above spectral behavior is helpful in understanding why the solubility of berberine is enhanced by β-CyD.

Chapter 4: this chapter describes a particular system: there has intermolecular interaction between two solutes (P and Q) in the solution and P occurs in two exchangeable states. In this particular system, P occurs in two exchangeable states when it is dissolved in the solutions. Results on mathematical analysis and computer simulation demonstrated that interference unrelated to the intermolecular interaction can be completely removed. Hence, the resultant 2D asynchronous spectra generated by using the DAOSD approach can reflect intermolecular interaction reliably. Moreover, properties of cross peaks in different regions of the pair of asynchronous spectra are discussed. In our previous works, cross peaks generated by using the DAOSD and relevant techniques reflect variations on peak position, bandwidth or absorptivity of the characteristic peaks of solutes caused by intermolecular interaction. However, we find that cross peak can still be produced even if intermolecular interaction do not bring about any changes on the characteristic peaks of solutes. Mathematical analysis demonstrates that cross peaks are related to the variations of chemical systems caused by intermolecular interaction at a network level.

Chapter 5: this chapter describes a new approach to prepare lanthanum carbonate via reactions between lanthanum chloride and $NaHCO_3$. In the reaction, small amount of $NaHCO_3$ solution was firstly added into the acidic lanthanum chloride solution to generate lanthanum carbonate nuclei and then $NaHCO_3$ is added into the lanthanum chloride at a constant speed. This approach makes both precipitation reaction and neutralization reaction take place simultaneously. Consequently, lanthanum carbonate is produced at low pH environment (pH below 4.5) so that the risk of generating lanthanum carbonate hydroxide is reduced. The product of the above reaction is validated by EDTA titration, elemental analysis and XRD characterization. In addition, we established a FTIR spectroscopic method to identify $La(OH)CO_3$ from $La_2(CO_3)_2 \cdot 8H_2O$. Lanthanum carbonate exhibits considerable ability to bind phosphate.

References

1. Aue, W.; Bartholdi, E.; Ernst, R. R. Two-Dimensional Spectroscopy. Application to Nuclear Magnetic Resonance. *J. Chem. Phys.* **1976,** *64*, 2229-2246.
2. Bax, A., *Two-Dimensional Nuclear Magnetic Resonance in Liquids*. D. Reidal Publishing Company: Dordrecht, Holland, 1981.
3. Ernst, R. R.; Bodenhausen, G.; Wokaun, A., *Principles of Nuclear Magnetic Resonance in one and Two Dimensions*. Clarendon Press: Oxford, U.K., 1987.
4. Sanders, J. K. M.; Hunter, B. K., *Modern NMR Spectroscopy, a Guide for Chemists*. Oxford University Press: Oxford, U.K., 1987.

5. Noda, I.; Ozaki, Y., *Two-Dimensional Correlation Spectroscopy: Applications in Vibrational and Optical Spectroscopy*. John Wiley & Sons: Chichester, U.K., 2004.

6. Steffen, T.; Duppen, K. Femtosecond Two-Dimensional Spectroscopy of Molecular Motion in Liquids. *Phys. Rev. Lett.* **1996,** *76*, 1224.

7. Tanimura, Y.; Mukamel, S. Two-Dimensional Femtosecond Vibrational Spectroscopy of Liquids. *J. Chem. Phys.* **1993,** *99*, 9496-9511.

8. Tokmakoff, A.; Lang, M.; Larsen, D.; Fleming, G.; Chernyak, V.; Mukamel, S. Two-Dimensional Raman Spectroscopy Of Vibrational Interactions in Liquids. *Phys. Rev. Lett.* **1997,** *79*, 2702.

9. Tominaga, K.; Yoshihara, K. Fifth Order Optical Response of Liquid CS_2 Observed by Ultrafast Nonresonant Six-Wave Mixing. *Phys. Rev. Lett.* **1995,** *74*, 3061.

10. Zanni, M. T.; Ge, N.-H.; Kim, Y. S.; Hochstrasser, R. M. Two-Dimensional Ir Spectroscopy Can Be Designed to Eliminate the Diagonal Peaks and Expose only the Crosspeaks Needed for Structure Determination. *Proc. Natl. Acad. Sci. U. S. A.* **2001,** *98*, 11265-11270.

11. Zhao, W.; Wright, J. C. Measurement of χ (3) for Doubly Vibrationally Enhanced Four Wave Mixing Spectroscopy. *Phys. Rev. Lett.* **1999,** *83*, 1950-1953.

12. Noda, I. Two-Dimensional Infrared (2D IR) Spectroscopy of Synthetic and Biopolymers. *Bull. Am. Phys. Soc.* **1986,** *31*, 520.

13. Noda, I. Two-Dimensional Infrared-Spectroscopy. *J. Am. Chem. Soc.* **1989,** *111*, 8116-8118.

14. Noda, I. 2-Dimensional Infrared (2D IR) Spectroscopy - Theory and Applications. *Appl. Spectrosc.* **1990,** *44*, 550-561.

15. Noda, I. Generalized 2-Dimensional Correlation Method Applicable to Infrared, Raman, and Other Types of Spectroscopy. *Appl. Spectrosc.* **1993,** *47*, 1329-1336.

16. Ashton, L.; Johannessen, C.; Goodacre, R. The Importance of Protonation in the Investigation of Protein Phosphorylation Using Raman Spectroscopy and Raman Optical Activity. *Anal. Chem.* **2011,** *83*, 7978-7983.

17. Ashton, L.; Xu, Y.; Brewster, V. L.; Cowcher, D. P.; Sellick, C. A.; Dickson, A. J.; Stephens, G. M.; Goodacre, R. The challenge of applying Raman Spectroscopy to Monitor Recombinant Antibody Production. *Analyst* **2013,** *138*, 6977-6985.

18. Bae, J.; Chae, B.; Seo, H.; Jung, Y. M.; Lee, S. W. Structural Characterization of Triphenylamine (TPA)-Based Polymers during the Oxidative Reaction by Two-Dimensional (2D) Infrared Correlation Study. *J. Mol. Struct.* **2014,** *1069*, 200-204.

19. Bai, B. L.; Wei, J.; Spegazzini, N.; Wu, Y. Q.; Wang, H. T.; Li, M.; Ozaki, Y. Two-Dimensional Correlation Infrared Spectroscopy Studies on the thermal-Induced Mesophase of 4-Nitrobenzohydrazide Derivative. *Vib. Spectrosc.* **2014,** *70*, 115-119.

20. Bi, Q.; Chen, J.; Li, X. P.; Shi, J. J.; Wang, X. M.; Zhang, J.; Gao, D. Q.; Zhai, Y. J.; Zhao, Y.; Weng, S. F., et al. Investigation on the Dipole-Dipole Interactions

between Tetramethylurea and Acetonitrile by Two-Dimensional Asynchronous Spectroscopy. *J. Mol. Struct.* **2014,** *1069*, 264-271.

21. Carmona, P.; Molina, M.; Calero, M.; Bermejo-Pareja, F.; Martinez-Martin, P.; Toledanog, A. Discrimination Analysis of Blood Plasma Associated with Alzheimer's Disease Using Vibrational Spectroscopy. *Journal of Alzheimers Disease* **2013,** *34*, 911-920.

22. Chandra, G. K.; Eklouh-Molinier, C.; Fere, M.; Angiboust, J. F.; Gobinet, C.; Van-Gulick, L.; Jeannesson, P.; Piot, O. Probing in Vitro Ribose Induced DNA-Glycation Using Raman Microspectroscopy. *Anal. Chem.* **2015,** *87*, 2655-2664.

23. Chen, Y.; Cao, Y. Y.; Yan, C. Y.; Zhang, Y. W.; Mu, T. C. The Dynamic Process of Atmospheric Water Sorption in [BMIN][Ac]: Quantifying Bulk versus Surface Sorption and Utilizing Atmospheric Water as a Structure Probe. *J. Phys. Chem. B* **2014,** *118*, 6896-6907.

24. Choi, H. C.; Ryu, S. R.; Ji, H.; Kim, S. B.; Noda, I.; Jung, Y. M. Two-Dimensional Heterospectral Correlation Analysis of X-Ray Photoelectron Spectra and Infrared Spectra for Spin-Coated Films of Biodegradable Poly(3-hydroxybutyrate-co-3-hydroxyhexanoate) Copolymers. *J. Phys. Chem. B* **2010,** *114*, 10979-10985.

25. Czarnik-Matusewicz, B.; Bin Kim, S.; Jung, Y. M. A Study of Urea-dependent Denaturation of beta-Lactoglobulin by Principal Component Analysis and Two-dimensional Correlation Spectroscopy. *J. Phys. Chem. B* **2009,** *113*, 559-566.

26. Gao, Y. L.; Li, D.; Shi, J. J.; Wang, X. M.; Kang, T. G.; Weng, S. F.; Xu, Y. Z.; Noda, I.; Wu, J. G. Coordination between Lanthanide (III) Ions and Organic Ligands of Natural Pharmaceutical Containing Lactone Group Probed by DAOSD Approach. *Biomed. Spectrosc. Imaging* **2015,** *4*, 129-137.

27. Genkawa, T.; Watari, M.; Nishii, T.; Suzuki, M.; Ozaki, Y. Two-Dimensional Heterospectral Correlation Analysis of Water and Liquid Oleic Acid Using an Online Near-Infrared/Mid-Infrared Dual-Region Spectrometer. *Appl. Spectrosc.* **2013,** *67*, 724-730.

28. Grzeszczuk, M.; Granska, A.; Szostak, R. Raman Spectroelectrochemistry of Polyaniline Synthesized Using Different Electrolytic Regimes - Multivariate Analysis. *Int. J. Electrochem. Sci.* **2013,** *8*, 8951-8965.

29. Haas, S.; Plivelic, T. S.; Dicko, C. Combined SAXS/UV-vis/Raman as a Diagnostic and Structure Resolving Tool in Materials and Life Sciences Applications. *J. Phys. Chem. B* **2014,** *118*, 2264-2273.

30. Jung, Y. M.; Kim, H. J.; Ryu, D. Y.; Bin Kim, S.; Kim, J. K. Application of Principal Component Analysis-Based Two-Dimensional Correlation Spectroscopy to Characterization of Order-Disorder Transition of Polystyrene-Block-Poly(n-Pentyl Methacrylate) Copolymer. *J. Mol. Struct.* **2006,** *799*, 96-101.

31. Jung, Y. M.; Shin, H. S.; Kim, S. B.; Noda, I. Two-Dimensional Gradient Mapping Technique Useful for Detailed Spectral Analysis of Polymer Transition Temperatures. *J. Phys. Chem. B* **2008,** *112*, 3611-3616.

32. Kang, D.; Ryu, S. R.; Park, Y.; Czarnik-Matusewicz, B.; Jung, Y. M. pH-Induced

Structural Changes of Ovalbumin Studied by 2D Correlation IR Spectroscopy. *J. Mol. Struct.* **2014,** *1069*, 299-304.

33. Kim, H. J.; Bin Kim, S.; Kim, J. K.; Jung, Y. M. Two-Dimensional Heterospectral Correlation Analysis of Wide-Angle X-ray Scattering and infrared Spectroscopy for Specific Chemical Interactions in Weakly Interacting Block Copolymers. *J. Phys. Chem. B* **2006,** *110*, 23123-23129.

34. Lai, H. J.; Wu, P. Y. A Infrared Spectroscopic Study on the Mechanism of Temperature-Induced Phase Transition of Concentrated Aqueous Solutions of Poly(N-Isopropylacrylamide) and N-Isopropylpropionamide. *Polymer* **2010,** *51*, 1404-1412.

35. Li, W.; Sun, B. J.; Wu, P. Y. Study on Hydrogen Bonds of Carboxymethyl Cellulose Sodium Film with Two-Dimensional Correlation Infrared Spectroscopy. *Carbohydr. Polym.* **2009,** *78*, 454-461.

36. Li, W. Z.; Wu, P. Y. Study on the Crystalline Structure Transition of Syndiotactic Polystyrene Film During Heat Treatment by Two-Dimensional Infrared Correlation Spectroscopy. *Appl. Spectrosc.* **2009,** *63*, 926-931.

37. Liu, Y. H.; Shi, J. J.; Gao, D. Q.; Gao, Y. L.; Guo, R.; Ling, X. F.; Weng, S. F.; Xu, Y. Z.; Noda, I.; Wu, J. G. Interactions between Pyridinium and Nd^{3+}. *Chin. Chem. Lett.* **2015,** *26*, 182-186.

38. Mao, Z.; Song, W.; Xue, X. X.; Ji, W.; Chen, L.; Lombardi, J. R.; Zhao, B. Multiphonon Resonant Raman Scattering and Photoinduced Charge-Transfer Effects at ZnO-Molecule Interfaces. *J. Phys. Chem. C* **2012,** *116*, 26908-26918.

39. Park, Y.; Kim, N. H.; Choi, H. C.; Lee, S. M.; Hwang, H.; Jeong, Y. U.; Jung, Y. M. Two-Dimensional Hetero-Spectral Raman/XAS Correlation Analysis of $Li[Ni_{0.45}Co_{0.18}Mn_{0.25}Al_{0.12}]O^-_2$ Cathode in the Overcharged State. *Vib. Spectrosc.* **2012,** *60*, 226-230.

40. Qi, J.; Li, H. Z.; Huang, K.; Chen, H. H.; Liu, S. X.; Yang, L. M.; Zhao, Y.; Zhang, C. F.; Li, W. H.; Wu, J. G., et al. Orthogonal Sample Design Scheme for Two-Dimensional Synchronous Spectroscopy and its Application in Probing Intermolecular Interactions. *Appl. Spectrosc.* **2007,** *61*, 1359-1365.

41. Quaroni, L.; Zlateva, T. Real-Time Metabolic Analysis of Living Cancer Cells with Correlated Cellular Spectro-microscopy. *Anal. Chem.* **2014,** *86*, 6887-6895.

42. Ryu, S. R.; Bae, W. M.; Hong, W. J.; Ihn, K. J.; Jung, Y. M. Characterization of Chain Transfer Reaction during Radical Polymerization of Silver Nanocomposite Polyvinylpyrrolidone by using 2D Hetero-Spectral IR/NMR Correlation Spectroscopy. *Vib. Spectrosc..* **2012,** *60*, 168-172.

43. Ryu, S. R.; Czarnik-Matusewicz, B.; Dukor, R. K.; Nafie, L. A.; Jung, Y. M. Analysis of the Molten Globule State of Bovine Alpha-Lactalbumin by using Vibrational Circular Dichroism. *Vib. Spectrosc.* **2012,** *60*, 68-72.

44. Schwaighofer, A.; Kotlowski, C.; Araman, C.; Chu, N.; Mastrogiacomo, R.; Becker, C.; Pelosi, P.; Knoll, W.; Larisika, M.; Nowak, C. Honey Bee Odorant-Binding Protein 14: Effects on Thermal Stability upon Odorant Binding Revealed by FT-IR Spectroscopy and CD Measurements. *Eur. Biophys. J.* **2014,** *43*, 105-112.

45. Shinzawa, H.; Awa, K.; Ozaki, Y. Compression Effect on Sustained-Release and Water Absorption Properties of Cellulose Tablets Studied by Heterospectral Two-Dimensional (2D) Correlation Analysis. *Anal. Methods* **2012,** *4*, 1530-1537.

46. Shinzawa, H.; Kanematsu, W.; Noda, I. Rheo-Optical Near-Infrared (NIR) Spectroscopy Study of Low-Density Polyethylene (LDPE) in Conjunction with Projection Two-Dimensional (2D) Correlation Analysis. *Vib. Spectrosc.* **2014,** *70*, 53-57.

47. Shinzawa, H.; Kanematsu, W.; Noda, I. Tensile Deformation of Isotactic Polypropylene (iPP) and iPP-Nanocomposite Studied by Rheo-Optical Near-Infrared (NIR) Spectroscopy. *Vib. Spectrosc.* **2015,** *78*, 34-38.

48. Smirnova, D. S.; Kornfield, J. A.; Lohse, D. J. Morphology Development in Model Polyethylene via Two-Dimensional Correlation Analysis. *Macromolecules* **2011,** *44*, 6836-6848.

49. Sun, B. J.; Wu, P. Y. Trace of the Thermally Induced Evolution Mechanism of Interactions Between Water and Ionic Liquids. *J. Phys. Chem. B* **2010,** *114*, 9209-9219.

50. Sun, S. T.; Hu, J.; Tang, H.; Wu, P. Y. Chain Collapse and Revival Thermodynamics of Poly(N-isopropylacrylamide) Hydrogel. *J. Phys. Chem. B* **2010,** *114*, 9761-9770.

51. Sun, S. T.; Tang, H.; Wu, P. Y. Interpretation of Carbonyl Band Splitting Phenomenon of a Novel Thermotropic Liquid Crystalline Polymer without Conventional Mesogens: Combination Method of Spectral Analysis and Molecular Simulation. *J. Phys. Chem. B* **2010,** *114*, 3439-3448.

52. Sun, S. T.; Tang, H.; Wu, P. Y.; Wan, X. H. Supramolecular Self-Assembly Nature of a Novel Thermotropic Liquid Crystalline Polymer Containing no Conventional Mesogens. *PCCP* **2009,** *11*, 9861-9870.

53. Sun, S. T.; Wu, P. Y. Role of Water/Methanol Clustering Dynamics on Thermosensitivity of Poly(N-isopropylacrylamide) from Spectral and Calorimetric Insights. *Macromolecules* **2010,** *43*, 9501-9510.

54. Sun, S. T.; Wu, P. Y. Infrared Spectroscopic Insight into Hydration Behavior of Poly(N-vinylcaprolactam) in Water. *J. Phys. Chem. B* **2011,** *115*, 11609-11618.

55. Sun, S. T.; Wu, P. Y. Spectral insights into gelation microdynamics of N-octyl-D-gluconamide in water. *Soft Matter* **2011,** *7*, 6451-6456.

56. Tarver, J.; Loo, Y. L. Manipulating Structure and Enhancing Conductivity of Polymer Acid Doped Polyaniline by Exploiting Redox Chemistry. *Thin Solid Films* **2013,** *539*, 303-308.

57. Uchida, T.; Osawa, M.; Lipkowski, J. SEIRAS Studies of Water Structure at the Gold Electrode Surface in the Presence of Supported Lipid Bilayer. *J. Electroanal. Chem.* **2014,** *716*, 112-119.

58. Unger, M.; Morita, S.; Sato, H.; Ozaki, Y.; Siesler, H. W. Variable-Temperature Fourier Transform Infrared Spectroscopic Investigations of Poly(3-Hydroxyalkanoates) and Perturbation-Correlation Moving-Window Two-Dimensional Correlation Analysis. Part II: Study of Poly(epsilon-Caprolactone) Homopolymer and a Poly(3-Hydroxybutyrate)-Poly(epsilon-Caprolactone)

Blend. *Appl. Spectrosc.* **2009,** *63*, 1034-1040.

59. Unger, M.; Morita, S.; Sato, H.; Ozaki, Y.; Siesler, H. W. Variable-Temperature Fourier Transform Infrared Spectroscopic Investigations of Poly(3-Hydroxyalkanoates) and Perturbation-Correlation Moving-Window Two-Dimensional Correlation Analysis. Part I: Study of Non-Annealed and Annealed Poly(3-Hydroxybutyrate) Homopolymer. *Appl. Spectrosc.* **2009,** *63*, 1027-1033.

60. Wang, M. Y.; Sun, S. T.; Wu, P. Y. Spectral Insight into Intensity Variations in Phase-Transition Processes Using Two-Dimensional Correlation Analysis. *Appl. Spectrosc.* **2010,** *64*, 1396-1406.

61. Weselucha-Birczynska, A.; Kozicki, M.; Czepiel, J.; Labanowska, M.; Nowak, P.; Kowalczyk, G.; Kurdziel, M.; Birczynska, M.; Biesiada, G.; Mach, T., et al. Human Erythrocytes Analyzed by Generalized 2D RAMAN CORRELATION Spectroscopy. *J. Mol. Struct.* **2014,** *1069*, 305-312.

62. Wu, Y. Q.; Meersman, F.; Ozaki, Y. A Novel Application of Hybrid Two-Dimensional Correlation Infrared Spectroscopy: Exploration of the Reversibility of the Pressure- and Temperature-Induced Phase Separation of Poly(N-Isopropylacrylamide) and Poly(N-Isopropylmethacrylamide) in Aqueous Solution. *Macromolecules* **2006,** *39*, 1182-1188.

63. Zhou, Y.; Zheng, Y. Z.; Sun, H. Y.; Deng, G.; Yu, Z. W. Hydrogen Bonding Interactions in Ethanol and Acetonitrile Binary System: A Near and Mid-Infrared Spectroscopic Study. *J. Mol. Struct.* **2014,** *1069*, 251-257.

64. Abdulla, H. A. N.; Minor, E. C.; Dias, R. F.; Hatcher, P. G. Transformations of the Chemical Compositions of High Molecular Weight DOM Along a salinity Transect: Using Two Dimensional Correlation Spectroscopy and Principal Component Analysis Approaches. *Geochim. Cosmochim. Acta* **2013,** *118*, 231-246.

65. Ashton, L.; Boguslawa, C. M. B.; Blanch, E. W. Application of Two-Dimensional Correlation Analysis to Raman Optical Activity. *J. Mol. Struct.* **2006,** *799*, 61-71.

66. Ashtony, L.; Barronz, L. D.; Czarnik-Matusewicz, B.; Hecht, L.; Hyde, J.; Blanch, E. W. Two-dimensional Correlation Analysis of Raman Optical Activity Data on the Alpha-Helix-To-Beta-Sheet Transition in Poly(L-lysine). *Mol. Phys.* **2006,** *104*, 1429-1445.

67. Bai, B. L.; Wei, J.; Kummetha, R. R.; Ozaki, Y.; Wang, H. T.; Li, M. Study of the Hydrogen Bonding of 1,4-Bis[(3,4,5-Trihexyloxyphenyl)Hydrazide]Phenylene in Crystalline and Liquid Crystalline Phases using Infrared, Raman, and Two-Dimensional Correlation Spectroscopy. *Vib. Spectrosc.* **2014,** *73*, 150-157.

68. Chen, Y. J.; Ozaki, Y.; Czarnecki, M. A. Molecular Structure And Hydrogen Bonding in Pure Liquid Ethylene Glycol and Ethylene Glycol-Water Mixtures Studied using NIR Spectroscopy. *PCCP* **2013,** *15*, 18694-18701.

69. Ding, C. C.; Zhang, M.; Wu, K.; Li, G. Y. The response of collagen molecules in acid solution to temperature. *Polymer* **2014,** *55*, 5751-5759.

70. Eads, C. D.; Noda, I. Generalized Correlation NMR Spectroscopy. *J. Am. Chem. Soc.* **2002,** *124*, 1111-1118.

71. Elmore, D. L.; Dluhy, R. A. Beta Nu-Correlation Analysis: A Modified Two-Dimensional Infrared Correlation Method for Determining Relative Rates of Intensity Change. *J. Phys. Chem. B* **2001,** *105*, 11377-11386.

72. He, A. Q.; Kang, X. Y.; Xu, Y. Z.; Noda, I.; Ozaki, Y.; Wu, J. G. Investigation on Intermolecular Interaction between Berberine and Beta-Cyclodextrin by 2D UV-Vis Asynchronous Spectra. *Spectrochim. Acta, Part A* **2017,** *185*, 343-348.

73. Ishii, K.; Tahara, T. Two-Dimensional Fluorescence Lifetime Correlation Spectroscopy. 1. Principle. *J. Phys. Chem. B* **2013,** *117*, 11414-11422.

74. Ishii, K.; Tahara, T. Two-Dimensional Fluorescence Lifetime Correlation Spectroscopy. 2. Application. *J. Phys. Chem. B* **2013,** *117*, 11423-11432.

75. Jheng, J. B.; Chuang, W. T.; Hong, P. D.; Huang, Y. C.; Jeng, U. S.; Su, C. J.; Pan, G. R. Formation of Mesomorphic Domains Associated with Dimer Aggregates of Phenyl Rings in Cold Crystallization of Poly(Trimethylene Terephthalate). *Polymer* **2013,** *54*, 6242-6252.

76. Kim, S.; Shinzawa, H.; Chung, H.; Ozaki, Y. Measurement of Polyethylene Pellets Near the Glass Transition Temperature to Enhance Raman Spectral Selectivity among Samples and Improve Accuracy for Density Determination. *Analyst* **2015,** *140*, 1906-1912.

77. Kwasniewicz, M.; Czarnecki, M. A. MIR and NIR Group Spectra of n-Alkanes and 1-Chloroalkanes. *Spectrochim. Acta, Part A* **2015,** *143*, 165-171.

78. Lin, E. C.; Opella, S. J. Covariance Spectroscopy in High-Resolution Multi-Dimensional Solid-State NMR. *J. Magn. Reson.* **2014,** *239*, 57-60.

79. Liu, J.; Gao, Y. L.; Zheng, L. R.; Gao, D. Q.; He, A. Q.; Liu, Y. H.; Weng, S. F.; Zhao, Y.; Yang, Z. L.; Yang, L. M., et al. Coordination between Cobalt (II) Ion and Carbonyl Group in Acetone Probed by using DAOSD Approach. *J. Mol. Struct.* **2014,** *1069*, 217-222.

80. Liu, Y.; Zhang, C.; Liu, S.; Zhao, Y.; Wang, D.; Wu, J.; Xu, Y.; Nodac, I. Modified Orthogonal Sample Design Scheme to Probe Intermolecular Interactions. *J. Mol. Struct.* **2008,** *883*, 124-128.

81. Noda, I. Vibrational Spectroscopy in the Development of Surface Hydrophilic Elastomer Latex (SHEL). *Vib. Spectrosc.* **2014,** *71*, 70-75.

82. Park, Y.; Kim, N. H.; Kim, J. M.; Kim, Y. C.; Jeong, Y. U.; Lee, S. M.; Choi, H. C.; Jung, Y. M. Surface Reaction of $LiCoO_2$/Li System under High-Voltage Conditions by X-ray Spectroscopy and Two-Dimensional Correlation Spectroscopy (2D-COS). *Appl. Spectrosc.* **2011,** *65*, 320-325.

83. Park, Y.; Kim, N. H.; Kim, J. Y.; Eom, I. Y.; Jeong, Y. U.; Kim, M. S.; Lee, S. M.; Choi, H. C.; Jung, Y. M. Surface Characterization of the High Voltage $LiCoO_2$/Li Cell by X-ray Photoelectron Spectroscopy and 2D Correlation Analysis. *Vib. Spectrosc.* **2010,** *53*, 60-63.

84. Pazderka, T.; Kopecky, V. Two-Dimensional Correlation Analysis of Raman Optical Activity - Basic Rules and Data Treatment. *Vib. Spectrosc.* **2012,** *60*, 193-199.

85. Qian, Y.; Shen, M.; Amoureux, P.; Noda, I.; Hu, B. W. The Dependence of Signal-to-Noise Ratio on Number of Scans in Covariance Spectroscopy. *Solid*

State Nucl. Magn. Reson. **2014,** *59-60*, 31-33.

86. Rudd, T. R.; Macchi, E.; Muzi, L.; Ferro, M.; Gaudesi, D.; Torri, G.; Casu, B.; Guerrini, M.; Yates, E. A. Unravelling Structural Information from Complex Mixtures Utilizing Correlation Spectroscopy Applied to HSQC Spectra. *Anal. Chem.* **2013,** *85*, 7487-7493.

87. Shanmukh, S.; Dluhy, R. A. kv Correlation analysis. A Quantitative two-Dimensional IR Correlation Method for Analysis of Rate Processes with Exponential Functions. *J. Phys. Chem. A* **2004,** *108*, 5625-5634.

88. Shinzawa, H.; Hashimoto, K.; Sato, H.; Kanematsu, W.; Noda, I. Multiple-Perturbation Two-Dimensional (2D) Correlation Analysis for Spectroscopic Imaging Data. *J. Mol. Struct.* **2014,** *1069*, 176-182.

89. Shinzawa, H.; Murakami, T. N.; Nishida, M.; Kanematsu, W.; Noda, I. Near-Infrared (NIR) Imaging Analysis of Polylactic Acid (PLA) Nanocomposite by Multiple-Perturbation Two-Dimensional (2D) Correlation Spectroscopy. *J. Mol. Struct.* **2014,** *1069*, 171-175.

90. Thomas, M.; Richardson, H. H. Two-Dimensional FT-IR Correlation Analysis of the Phase Transitions in a Liquid Crystal, 4 '-n-Octyl-4-Cyanobiphenyl (8CB). *Vib. Spectrosc.* **2000,** *24*, 137-146.

91. Unger, M.; Ozaki, Y.; Pfeifer, F.; Siesler, H. W. 2DCOS and PCMW2D Analyses of MIR/ATR and FT-NIR Spectra Monitoring the Deuterium/Hydrogen Exchange in Liquid D_2O. *J. Mol. Struct.* **2014,** *1069*, 258-263.

92. Wang, J.; Xu, W. Q.; Zhang, J. J.; Xu, S. P. Ag Nanoparticles Decorated Small-Sized AgTCNQF(4) Nanorod: Synthesis in Aqueous Solution and Its Photoinduced Charge Transfer Reactions. *J. Phys. Chem. C* **2014,** *118*, 24752-24760.

93. Wang, J. D.; He, A. Q.; Guo, R.; Wei, Y. J.; Feng, J.; Xu, Y. Z.; Noda, I.; Wu, J. G. Investigation on the Spectral Properties of 2D Asynchronous Fluorescence Spectra Generated by using Variable Excitation Wavelengths as a Perturbation. *J. Mol. Struct.* **2016,** *1124*, 221-227.

94. Wang, Q. W.; Tang, H.; Wu, P. Y. Aqueous Solutions of Poly(ethylene oxide)-Poly(N-isopropylacrylamide): Thermosensitive Behavior and Distinct Multiple Assembly Processes. *Langmuir* **2015,** *31*, 6497-6506.

95. Wang, W. B.; Paliwal, J. A Multimodal Spectrometer for Raman Scattering and Near-Infrared Absorption Measurement. *Vib. Spectrosc.* **2014,** *74*, 13-19.

96. Yamasaki, H.; Morita, S. Identification of the Epoxy Curing Mechanism under Isothermal Conditions by Thermal Analysis and Infrared Spectroscopy. *J. Mol. Struct.* **2014,** *1069*, 164-170.

97. Zhang, J.; Zhao, Z.; Wang, L.; Zhu, X.; Shen, L.; Yu, Y. Two-Dimensional UV Absorption Correlation Spectroscopy as a Method for the Detection of Thiamethoxam Residue in Tea. *Appl. Spectrosc.* **2015,** *82*, 311-315.

98. Zou, C. J.; Larisika, M.; Nagy, G.; Srajer, J.; Oostenbrink, C.; Chen, X. D.; Knoll, W.; Liedberg, B.; Nowak, C. Two-Dimensional Heterospectral Correlation Analysis of the Redox-Induced Conformational Transition in Cytochrome c Using Surface-Enhanced Raman and Infrared Absorption Spectroscopies on a

Two-Layer Gold Surface. *J. Phys. Chem. B* **2013,** *117*, 9606-9614.

99. Jennison, R. C., *Fourier transforms: and convolutions for the experimentalist*. Pergamon Press: New York, U.S.A., 1961.

100. Noda, I. Determination of Two-Dimensional Correlation Spectra using the Hilbert Transform. *Appl. Spectrosc.* **2000,** *54*, 994-999.

101. Noda, I.; Dowrey, A. E.; Marcott, C.; Story, G. M.; Ozaki, Y. Generalized two-dimensional correlation spectroscopy. *Appl. Spectrosc.* **2000,** *54*, 236A-248A.

102. Bi, Q.; Chen, J.; Li, X. P.; Shi, J. J.; Guo, R.; Zhai, Y. J.; Xu, Y. Z.; Noda, I.; Wu, J. G. A Method Based on the DAOSD Approach to Estimate the Variation of the Peak Position and Bandwidth Caused by Intermolecular Interactions. *J. Mol. Struct.* **2014,** *1069*, 211-216.

103. Chen, J.; Bi, Q.; Liu, S. X.; Li, X. P.; Liu, Y. H.; Zhai, Y. J.; Zhao, Y.; Yang, L. M.; Xu, Y. Z.; Noda, I., et al. Double Asynchronous Orthogonal Sample Design Scheme for Probing Intermolecular Interactions. *J. Phys. Chem. A* **2012,** *116*, 10904-10916.

104. Chen, J.; Zhang, C.; Li, H.; Liu, Y.; Li, W.; Xu, Y.; Wu, J.; Noda, I. Patterns of Cross Peaks in 2D Synchronous Spectrum Generated by using orthogonal Sample Design Scheme. *J. Mol. Struct.* **2008,** *883-884*, 129-136.

105. Chen, M.; Guo, R.; Zhao, Y.; Weng, S. F.; Xu, Y. Z.; Noda, I.; Wu, J. G. Investigation on the Intermolecular Interaction between Diethyl Ether and Dichloromethane in Gaseous Phase by using the DAOSD Approach. *J. Mol. Struct.* **2016,** *1124*, 244-248.

106. Gao, D. Q.; Li, X. P.; Shi, J. J.; Kang, X. Y.; Kang, T. G.; Xia, J. M.; Ling, X. F.; Weng, S. F.; Xu, Y. Z.; Noda, I., et al. Two-Dimensional Correlation Spectroscopic Studies on Coordination between Carbonyl Group of Butanone and Metal Ions. *Chin. Chem. Lett.* **2015,** *26*, 177-181.

107. Gao, Y. L.; Liu, J.; Liu, Y. H.; Shi, J. J.; Weng, S. F.; Yang, L. M.; Wen, X. D.; Kang, T. G.; Xu, Y. Z.; Noda, I., et al. Characterization of the Coordination between Nd^{3+} and Ester Groups by using Double Asynchronous Orthogonal Sample Design Approach. *J. Mol. Struct.* **2014,** *1069*, 205-210.

108. Kang, X. Y.; He, A. Q.; Guo, R.; Chen, J.; Zhai, Y. J.; Xu, Y. Z.; Noda, I.; Wu, J. G. Investigation on Intermolecular Interaction between Two Solutes where One Solute Occurs in Two States. *J. Mol. Struct.* **2016,** *1124*, 228-237.

109. Kang, X. Y.; He, A. Q.; Guo, R.; Zhai, Y. J.; Xu, Y. Z.; Noda, I.; Wu, J. G. A Simplified Concentration Series to Produce a Pair of 2D Asynchronous Spectra Based on the DAOSD Approach. *J. Mol. Struct.* **2016,** *1124*, 151-158.

110. Li, H. Z.; Tao, D. L.; Qi, J.; Wu, J. G.; Xu, Y. Z.; Noda, I. Dipole-dipole Interactions in Solution Mixtures Probed by Two-Dimensional Synchronous Spectroscopy Based on Orthogonal Sample Design Scheme. *Spectrochim. Acta, Part A* **2014,** *124*, 697-702.

111. Li, X. P.; Bi, Q.; Liu, S. X.; Chen, J.; Yue, S. J.; Wei, Y. J.; Huang, K.; Zhao, Y.; Liu, H. Z.; Zhai, Y. J., et al. Improvement of the Sensitivity of the Two-Dimensional Asynchronous Spectroscopy Based on the AOSD Approach by using a Modified Reference Spectrum. *J. Mol. Struct.* **2013,** *1034*, 101-111.

112. Li, X. P.; Fan, X. K.; Huang, K.; Liu, H. Z.; Zhao, Y.; Wei, Y. J.; Liu, C. G.; Xu, Y. Z.; Noda, I.; Wu, J. G. Characterization of Intermolecular Interaction between Two Substances when One Substance Does not Possess any Characteristic Peak. *J. Mol. Struct.* **2014,** *1069*, 127-132.

113. Li, X. P.; He, A. Q.; Huang, K.; Liu, H. Z.; Zhao, Y.; Wei, Y. J.; Xu, Y. Z.; Noda, I.; Wu, J. G. Two-Dimensional Asynchronous Spectrum with Auxiliary Cross Peaks in Probing Intermolecular Interactions. *RSC Adv.* **2015,** *5*, 87739-87749.

114. Li, X. P.; Liu, S. X.; Chen, J.; Yue, S. J.; Liu, C. G.; Wei, Y. J.; Huang, K.; Zhao, Y.; Xu, Y. Z.; Noda, I., et al. The influence of Changing the Sequence of Concentration Series on the 2D Asynchronous Spectroscopy Generated by the Asynchronous Orthogonal Sample Design (AOSD) Approach. *Vib. Spectrosc.* **2012,** *60*, 212-216.

115. Li, X. P.; Pan, Q. H.; Chen, J.; Liu, S. X.; He, A. Q.; Liu, C. G.; Wei, Y. J.; Huang, K.; Yang, L. M.; Feng, J., et al. Asynchronous Orthogonal Sample Design Scheme for Two-Dimensional Correlation Spectroscopy (2D-COS) and Its Application in Probing Intermolecular Interactions from Overlapping Infrared (IR) Bands. *Appl. Spectrosc.* **2011,** *65*, 901-917.

116. Qi, J.; Gao, X. X.; Chen, H. H.; Huang, K.; Liu, S. X.; Zhao, Y.; Yang, L. M.; Weng, S. F.; Xu, Y. Z.; Xu, D. F., et al. Studies on Coordination and Hydrogen Bond Intermolecular Interaction Using 1D & 2D FTIR Spectroscopy. *Spectroscopy and Spectral Analysis* **2008,** *28*, 538-542.

117. Qi, J.; Huang, K.; Gao, X. X.; Li, H. Z.; Liu, S. X.; Zhao, Y.; Xu, Y. Z.; Wu, J. G.; Noda, I. Orthogonal Sample Design Scheme for Two-Dimensional Synchronous Spectroscopy: Application in Probing Lanthanide Ions Interactions with Organic Ligands in Solution Mixtures. *J. Mol. Struct.* **2008,** *883*, 116-123.

118. Shi, J. J.; Liu, Y. H.; Guo, R.; Li, X. P.; He, A. Q.; Gao, Y. L.; Wei, Y. J.; Liu, C. G.; Zhao, Y.; Xu, Y. Z., et al. Design of a New Concentration Series for the Orthogonal Sample Design Approach and Estimation of the Number of Reactions in Chemical Systems. *Appl. Spectrosc.* **2015,** *69*, 1229-1242.

119. Zhang, C. F.; Huang, K.; Li, H. Z.; Chen, J.; Liu, S. X.; Zhao, Y.; Wang, D. J.; Xu, Y. Z.; Wu, J. G.; Noda, I., et al. Double Orthogonal Sample Design Scheme and Corresponding Basic Patterns in Two-Dimensional Correlation Spectra for Probing Subtle Spectral Variations Caused by Intermolecular Interactions. *J. Phys. Chem. A* **2009,** *113*, 12142-12156.

120. Zhang, J.; Guo, R.; He, A.; Weng, S. F.; Gao, X. X.; Xu, Y. Z.; Noda, I.; Wu, J. Q. Investigation on the Relationship between Solubility of Artemisinin and Polyvinylpyrroli Done Addition by using DAOSD Approach. *Spectrochim. Acta, Part A* **2017,** *182*, 136-142.

121. Yu, Z. W.; Chen, L.; Sun, S. Q.; Noda, I. Determination of Selective Molecular Interactions using Two-Dimensional Correlation FT-IR Spectroscopy. *J. Phys. Chem. A* **2002,** *106*, 6683-6687.

122. Bernardi, A.; Arosio, D.; Potenza, D.; Sanchez-Medina, I.; Mari, S.; Canada, F. J.; Jimenez-Barbero, J. Intramolecular Carbohydrate-Aromatic Interactions and Intermolecular Van Der Waals Interactions Enhance the Molecular Recognition

Ability of GMI Glycomimetics for Cholera Toxin. *Chem-Eur J* **2004,** *10*, 4395-4406.

123. Huang, B. Q.; Hirst, A. R.; Smith, D. K.; Castelletto, V.; Hamley, I. W. A Direct Comparison of one- and two-Component Dendritic Self-Assembled Materials: Elucidating Molecular Recognition Pathways. *J. Am. Chem. Soc.* **2005,** *127*, 7130-7139.

124. Kitamura, N.; Suzuki, Y.; Ishizaka, S. A Spectroscopic and Photophysical Study on Molecular Recognition via Hydrogen-Bonding and pi-pi Stacking Interactions. *Photoch Photobio Sci* **2005,** *4*, 135-142.

125. Moreau, J. J. E.; Pichon, B. P.; Arrachart, G.; Man, M. W. C.; Bied, C. Nanostructuring Organo-Silicas: Combination of Intermolecular Interactions and Molecular Recognition Properties to Generate Self-Assembled Hybrids with Phenylene or Adenine Center Dot Center Dot Center Dot Thymine Bridging Units. *New J. Chem.* **2005,** *29*, 653-658.

126. Imamura, K.; Sakaura, K.; Ohyama, K.; Fukushima, A.; Imanaka, H.; Sakiyama, T.; Nakanishi, K. Temperature Scanning FTIR Analysis of Hydrogen Bonding States of Various Saccharides in Amorphous Matrixes Below and Above their Glass Transition Temperatures. *J. Phys. Chem. B* **2006,** *110*, 15094-15099.

127. Mikhaylova, Y.; Adam, G.; Haussler, L.; Eichhorn, K. J.; Voit, B. Temperature-Dependent FTIR Spectroscopic and Thermoanalytic Studies of Hydrogen Bonding of Hydroxyl (Phenolic Group) Terminated Hyperbranched Aromatic Polyesters. *J. Mol. Struct.* **2006,** *788*, 80-88.

128. Thompson, M. G. K.; Lewars, E. G.; Parnis, J. M. Observation of the pi Center Dot Center Dot Center Dot H hydrogen-Bonded Ternary Complex, $(C_2H_4)(_2)H_2O$, using Matrix Isolation Infrared Spectroscopy. *J. Phys. Chem. A* **2005,** *109*, 9499-9506.

129. Munoz, M. A.; Sama, O.; Galan, M.; Guardado, P.; Carmona, C.; Balon, M. Interactions between Betacarboline and Benzenoid pi Bases: FTIR Evidence for the Formation of NH-pi Hydrogen Bonds. *J. Phys. Chem. B* **1999,** *103*, 8794-8798.

130. Kaczmarczyk, B. FTIR Study of Hydrogen Bonds in Aliphatic Polyesteramides. *Polymer* **1998,** *39*, 5853-5860.

131. Langner, R.; Zundel, G. FT-IR Investigation of OH Center Dot Center Dot Center Dot N Reversible Arrow O-Center Dot Center Dot Center Dot H+N Hydrogen Bonds with Large Proton Polarizability in Phosphinic Acid Plus N-Base Systems in the Middle and Far Infrared Region. *J. Phys. Chem. A* **1998,** *102*, 6635-6642.

132. Alia, J. M.; Edwards, H. G. M.; Kiernan, B. M. Raman Spectroscopic Study of Hydrogen Bonding in Benzenesulfonic Acid/Acrylonitrile Solutions. *Spectrochim. Acta, Part A* **2005,** *61*, 2939-2945.

133. Alia, J. M.; Edwards, H. G. M.; Kiernan, B. M. Hydrogen Bonding in Benzenesulfonic and 4-Toluenesulfonic Acids Dissolved in N,N '-Dimethylformamide: an FT-Raman Study. *Journal of Raman Spectroscopy* **2004,** *35*, 111-118.

134. Markarian, S. A.; Zatikyan, A. L.; Bonora, S.; Fagnano, C. Raman and FT IR ATR Study of Diethylsulfoxide/Water Mixtures. *J. Mol. Struct.* **2003,** *655*, 285-292.

135. Salzmann, C. G.; Kohl, I.; Loerting, T.; Mayer, E.; Hallbrucker, A. Raman Spectroscopic Study on Hydrogen Bonding in Recovered Ice IV. *J. Phys. Chem. B* **2003,** *107*, 2802-2807.

136. Lalanne, P.; Tassaing, T.; Danten, Y.; Besnard, M. Raman and Infrared Studies of Hydrogen-Bonding in Supercritical Ethanol. *J. Mol. Liq.* **2002,** *98-9*, 201-212.

137. Goncharov, A. F.; Struzhkin, V. V.; Mao, H. K.; Hemley, R. J. Raman Spectroscopy of Dense H_2O and the Transition to Symmetric Hydrogen Bonds. *Phys. Rev. Lett.* **1999,** *83*, 1998-2001.

138. Xu, Y.; Ozaki, Y.; Noda, I.; Jung, Y. M., *Molecular and laser spectroscopy: advances and applications*. Elsevier: Amsterdam, Netherlands, 2017.

139. Jung, Y. M.; Shin, H. S.; Bin Kim, S.; Noda, I. New Approach to Generalized Two-Dimensional Correlation Spectroscopy. 1: Combination of Principal Component Analysis and Two-Dimensional Correlation Spectroscopy. *Appl. Spectrosc.* **2002,** *56*, 1562-1567.

140. Jung, Y. M.; Kim, S. B.; Noda, I. Application of Two-Dimensional Correlation Spectroscopy to Chemometrics: Self-Modeling Curve Resolution Analysis of Spectral Data Sets. *Appl. Spectrosc.* **2003,** *57*, 1376-1380.

141. Jung, Y. M.; Kim, S. B.; Noda, I. New Approach to Generalized Two-Dimensional Correlation Spectroscopy. II: Eigenvalue Manipulation Transformation (EMT) for Noise Suppression. *Appl. Spectrosc.* **2003,** *57*, 557-563.

142. Jung, Y. M.; Kim, S. B.; Noda, I. New Approach to Generalized Two-Dimensional Correlation Spectroscopy. III: Eigenvalue (EMT) for Spectral Selectivity Manipulation Transformation Enhancement. *Appl. Spectrosc.* **2003,** *57*, 564-570.

143. Jung, Y. M.; Bin Kim, S.; Noda, I. New Approach to Generalized Two-Dimensional Correlation Spectroscopy. IV: Eigenvalue Manipulation Transformation (EMT) for Partial Attenuation of Dominant Factors. *Appl. Spectrosc.* **2003,** *57*, 850-857.

144. Jung, Y. M. Principal Component Analysis Based Two-Dimensional Correlation Spectroscopy for Noise Filtering Effect. *Vib. Spectrosc.* **2004,** *36*, 267-270.

145. Ryu, S. R.; Noda, I.; Jung, Y. M. What is the Origin of Positional Fluctuation of Spectral Features: True Frequency Shift or Relative Intensity Changes of Two Overlapped Bands? *Appl. Spectrosc.* **2010,** *64*, 1017-1021.

146. Ryu, S. R.; Noda, I.; Jung, Y. M. Moving Window Principal Component Analysis for Detecting Positional Fluctuation of Spectral Changes. *Bull. Korean Chem. Soc.* **2011,** *32*, 2332-2338.

147. Ryu, S. R.; Noda, I.; Lee, C. H.; Lee, P. H.; Hwang, H.; Jung, Y. M. Two-Dimensional Correlation Analysis and Waterfall Plots for Detecting Positional Fluctuations of Spectral Changes. *Appl. Spectrosc.* **2011,** *65*, 359-368.

148. Morita, S.; Shinzawa, H.; Noda, I.; Ozaki, Y. Perturbation-Correlation Moving-

Window Two-Dimensional Correlation Spectroscopy. *Appl. Spectrosc.* **2006,** *60*, 398-406.

149. Izawa, K.; Ogasawara, T.; Masuda, H.; Okabayashi, H.; O'Connor, C. J.; Noda, I. Two-Dimensional Correlation Gel Permeation Chromatography (2D GPC) Study of 1H, 1H, 2H, 2H-Perfluorooctyltriethoxysilane Sol− Gel Polymerization Process. *J. Phys. Chem. B* **2002,** *106*, 2867-2874.

150. Ren, Y.; Murakami, T.; Nishioka, T.; Nakashima, K.; Noda, I.; Ozaki, Y. Two-Dimensional Fourier Transform Raman Correlation Spectroscopy Studies of Polymer Blends: Conformational Changes and Specific Interactions in Blends of Atactic Polystyrene and Poly (2, 6-Dimethyl-1, 4-Phenylene Ether). *Macromolecules* **1999,** *32*, 6307-6318.

151. Wu, Y. Q.; Noda, I. Quadrature Orthogonal Signal Corrected Two-Dimensional Correlation Spectroscopy. *Appl. Spectrosc.* **2006,** *60*, 605-610.

152. Wu, Y.; Noda, I.; Meersman, F.; Ozaki, Y. Orthogonal signal Corrected Two-Dimensional (OSC 2D) Correlation Infrared Spectroscopy. *J. Mol. Struct.* **2006,** *799*, 121-127.

153. Noda, I. Projection Two-Dimensional Correlation Analysis. *J. Mol. Struct.* **2010,** *974*, 116-126.

154. Noda, I. Two-Dimensional Codistribution Spectroscopy to Determine the Sequential Order of Distributed Presence of Species. *J. Mol. Struct.* **2014,** *1069*, 50-59.

155. Chen, Y.; Sun, X. F.; Yan, C. Y.; Cao, Y. Y.; Mu, T. C. The Dynamic Process of Atmospheric Water Sorption in [EMIM][Ac] and Mixtures of [EMIM][Ac] with Biopolymers and CO_2 Capture in These Systems. *J. Phys. Chem. B* **2014,** *118*, 11523-11536.

156. Meiners, F.; Ahlers, M.; Brand, I.; Wittstock, G. Impact of Temperature and Electrical Potentials on the Stability and Structure of Collagen Adsorbed on the Gold Electrode. *Surf. Sci.* **2015,** *631*, 220-228.

157. Nishikawa, Y.; Nakano, T.; Noda, I. Molecular Interaction of Polyimide Films Probed by using Soft-Pulse Dynamic Compression ATR Time-Resolved Infrared and Double Fourier-Transform Based 2D-IR Spectroscopy. *Vib. Spectrosc.* **2014,** *72*, 79-89.

158. Park, Y.; Hashimoto, C.; Hashimoto, T.; Hirokawa, Y.; Jung, Y. M.; Ozaki, Y. Reaction-Induced Self-Assembly of Gel Structure: A New Insight into Chemical Gelation Process of N-Isopropylacrylamide as Studied by Two-Dimensional Infrared Correlation Spectroscopy. *Macromolecules* **2013,** *46*, 3587-3602.

159. Ashton, L.; Pudney, P. D. A.; Blanch, E. W.; Yakubov, G. E. Understanding Glycoprotein Behaviours using Raman and Raman Optical Activity Spectroscopies: Characterising the Entanglement Induced Conformational Changes in Oligosaccharide Chains of Mucin. *Adv. Colloid Interface Sci.* **2013,** *199*, 66-77.

160. Lu, R.; Li, W. W.; Katzir, A.; Raichlin, Y.; Yu, H. Q.; Mizaikoff, B. Probing the Secondary Structure of Bovine Serum Albumin During Heat-Induced Denaturation using Mid-Infrared Fiberoptic Sensors. *Analyst* **2015,** *140*, 765-

770.

161. El-Khoury, P. Z.; Hess, W. P. Vibronic Raman Scattering at the Quantum Limit of Plasmons. *Nano Lett.* **2014,** *14*, 4114-4118.

162. Hou, L.; Ma, K.; An, Z. S.; Wu, P. Y. Exploring the Volume Phase Transition Behavior of POEGA- and PNIPAM-Based Core-Shell Nanogels from Infrared-Spectral Insights. *Macromolecules* **2014,** *47*, 1144-1154.

163. Hou, L.; Wu, P. Y. The Effect of added Gold Nanoparticles on the Volume Phase Transition Behavior for PVCL-Based Microgels. *RSC Adv.* **2014,** *4*, 39231-39241.

164. Zhang, D. L.; Ju, X.; Li, L. H.; Kang, Y.; Gong, X. L.; Li, B. J.; Zhang, S. An Efficient Multiple Healing Conductive Composite via Host-Guest Inclusion. *Chem. Commun.* **2015,** *51*, 6377-6380.

165. Adib, A. M.; Jamaludin, F.; Kiong, L. S.; Hashim, N.; Abdullah, Z. Two-Dimensional Correlation Infrared Spectroscopy Applied to Analyzing and Identifying the Extracts of Baeckea Frutescens Medicinal Materials. *J. Pharm. Biomed. Anal.* **2014,** *96*, 104-110.

166. Feng, K.; Hou, L.; Schoener, C. A.; Wu, P. Y.; Gao, H. Exploring the Drug Migration Process through Ethyl Cellulose-Based Films From Infrared-Spectral Insights. *Eur. J. Pharm. Biopharm.* **2015,** *93*, 46-51.

167. Momose, W.; Katz, J. M.; Drennen, J. K.; Anderson, C. A. Development of NIR Methods for Blend Analysis Using Small Quantities of Materials. *Journal of Pharmaceutical Innovation* **2015,** *10*, 36-46.

168. Carmona, P.; Molina, M. Interactions of Protein and Nucleic Acid Components of Hepatitis C Virus As Revealed by Fourier Transform Infrared Spectroscopy. *Biochemistry* **2010,** *49*, 4724-4731.

169. Chen, G. Y.; Sun, X.; Huang, Y. P.; Chen, K. J. Tracking the Dehydration Process of Raw Honey by Synchronous Two-Dimensional Near Infrared Correlation Spectroscopy. *J. Mol. Struct.* **2014,** *1076*, 42-48.

170. Lu, C. X.; Chen, L. J.; Yang, Z. L.; Liu, X.; Han, L. J. Visual Recognition of Fishmeal and Meat and Bone Meal Using Temperature-Dependent Two-Dimensional Correlation Near-Infrared Spectroscopy. *Appl. Spectrosc.* **2013,** *67*, 1390-1394.

171. Lu, C. X.; Chen, L. J.; Yang, Z. L.; Liu, X.; Han, L. J. Two-Dimensional Correlation Spectroscopy (2D-COS) Variable Selection for Near-Infrared Microscopy Discrimination of Meat and Bone Meal in Compound Feed. *Appl. Spectrosc.* **2014,** *68*, 844-851.

172. Xiao, Q.; Tong, Q. Y.; Lim, L. T. Drying Process of Pullulan Edible Films Forming Solutions Studied by ATR-FTIR with Two-Dimensional Correlation Spectroscopy. *Food Chem.* **2014,** *150*, 267-273.

173. Yang, R. J.; Liu, R.; Xu, K. X.; Yang, Y. R. Discrimination of Adulterated Milk Based on Two-Dimensional Correlation Spectroscopy (2D-COS) Combined with Kernel Orthogonal Projection to Latent Structure (K-OPLS). *Appl. Spectrosc.* **2013,** *67*, 1363-1367.

174. Yang, R. J.; Liu, R.; Xu, K. X.; Yang, Y. R.; Dong, G. M.; Zhang, W. Y.

Classification of Adulterated Milk with the Parameterization of 2D Correlation Spectroscopy and Least Squares Support Vector Machines. *Anal. Methods* **2013,** *5*, 5949-5953.

175. Li, M. H.; Wang, J. S.; Lu, Z. G.; Wei, D. D.; Yang, M. H.; Kong, L. Y. NMR-Based Metabolomics Approach to Study the Toxicity of Lambda-Cyhalothrin To Goldfish (Carassius auratus). *Aquat. Toxicol.* **2014,** *146*, 82-92.

176. Popescu, C. M.; Popescu, M. C. A Near Infrared Spectroscopic Study of the Structural Modifications of Lime (Tilia cordata Mill.) Wood During Hydro-Thermal Treatment. *Spectrochim. Acta, Part A* **2013,** *115*, 227-233.

177. Ren, F.; Zheng, Y. F.; Liu, X. M.; Yue, X. Y.; Ma, L.; Li, W. G.; Lai, F.; Liu, J. L.; Guan, W. L. An Investigation of the Oxidation Mechanism of Abietic Acid using Two-Dimensional Infrared Correlation Spectroscopy. *J. Mol. Struct.* **2015,** *1084*, 236-243.

178. Gu, C. Y.; Tang, Q. Q.; Xiang, B. R.; Xu, J. P. Determination of Fenitrothion in Water by Near Infrared Spectroscopy and Chemometric Analysis. *Anal. Lett.* **2015,** *48*, 1481-1493.

179. Li, X. M.; Shen, Q. R.; Zhang, D. Q.; Mei, X. L.; Ran, W.; Xu, Y. C.; Yu, G. H. Functional Groups Determine Biochar Properties (pH and EC) as Studied by Two-Dimensional C-13 NMR Correlation Spectroscopy. *Plos One* **2013,** *8*, e65949.

180. Mecozzi, M.; Pietroletti, M.; Trifiro, G.; Nisini, L. Two-Dimensional Correlation Analysis and Multivariate Time Series Analysis as Innovative Tools for the Study and the Comparison of the Hydrocarbon Distributions in Marine Antarctic Cores. *Mar. Chem.* **2014,** *159*, 9-18.

181. Xu, H. C.; Zhong, J. C.; Yu, G. H.; Wu, J.; Jiang, H. L.; Yang, L. Y. Further Insights into Metal-DOM Interaction: Consideration of Both Fluorescent and Non-Fluorescent Substances. *Plos One* **2014,** *9*, e112272.

182. Pi, F. W.; Shinzawa, H.; Czarnecki, M. A.; Iwahashi, M.; Suzuki, M.; Ozaki, Y. Self-Assembling of Oleic Acid (cis-9-octadecenoic acid) and Linoleic Acid (cis-9, cis-12-octadecadienoic acid) in Ethanol Studied by Time-Dependent Attenuated Total Reflectance (ATR) Infrared (IR) and Two-Dimensional (2D) Correlation Spectroscopy. *J. Mol. Struct.* **2010,** *974*, 40-45.

Table 1-1 An Example of Concentration Series of P and Q that Satisfies OSD Approach.

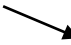| $C_P^{(init)}$	$C_Q^{(init)}$	$\tilde{C}_P^{(init)}$	$\tilde{C}_Q^{(init)}$
5	4	1	0
4	5	0	1
3	4	-1	0
4	3	0	-1

Table 1-2 Peak Parameters for the Model Systems that is Analyzed by using the DOSD Approach shown in **Figure 1-6A**.[119]
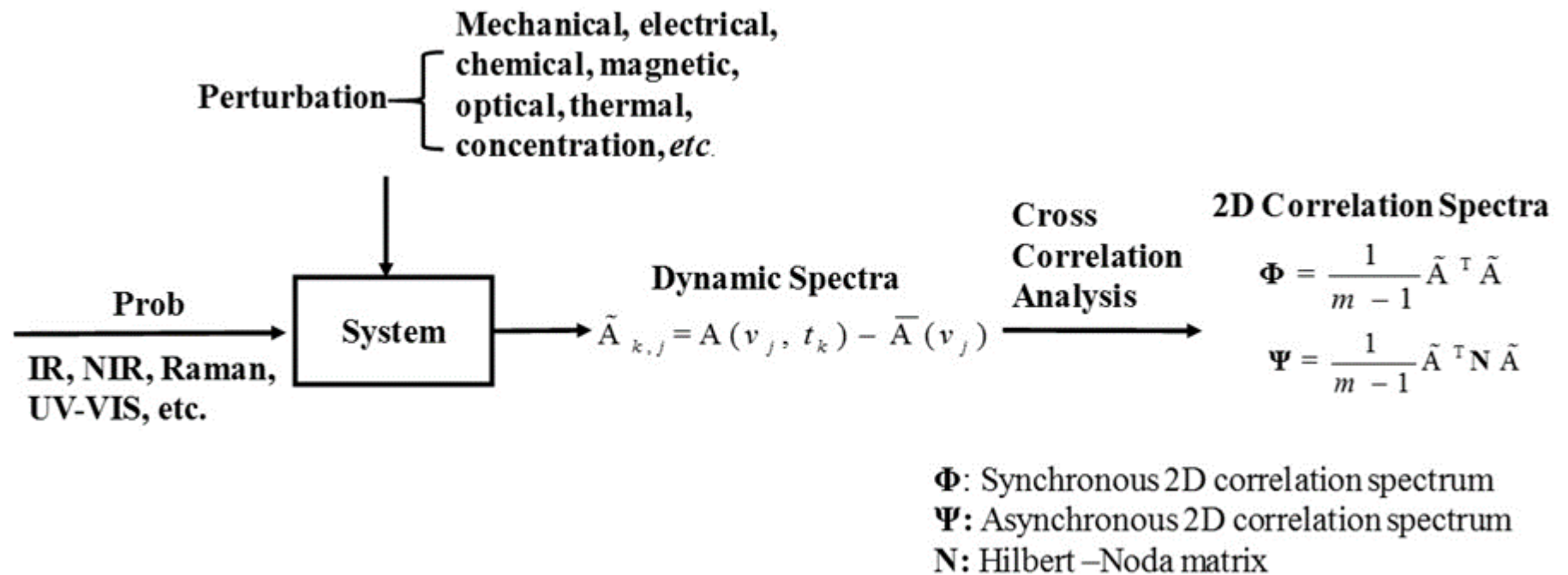
	P	U	Q	V
Peak position(X)/cm^{-1}	150	152	350	350
Bandwidth(W) /cm^{-1}	20	20	20	20
Absorptivity(ε)	1.00	1.00	1.00	1.00

Table 1-3 Peak Parameters for the Model Systems that is Analyzed by using the DOSD Approach shown in **Figure 1-6B**.[119]

	P	U	Q	V
Peak position(X)/cm^{-1}	150	150	350	350
Bandwidth(W) /cm^{-1}	20	22	20	20
Absorptivity(ε)	1.00	1.00	1.00	1.00
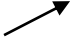
Table 1-4 Peak Parameters for the Model Systems that is Analyzed by using the DAOSD Approach Shown in **Figure 1-6C**.[119]

	P	U	Q	V
Peak position(X)/cm^{-1}	150	150	350	350
Bandwidth(W) /cm^{-1}	20	20	20	20
Absorptivity(ε)	1.00	1.10	1.00	1.00

Table 1-5 Peak Parameters for the Model Systems that is Analyzed by using the DAOSD Approach Shown in **Figure 1-9**.[109]

	P	U	Q	V
Peak position(X)/cm^{-1}	100	101	300	300
Bandwidth(W) /cm^{-1}	20	21	20	19
Absorptivity(ε)	1.00	0.95	1.00	1.05

Table 1-6. Rules of PCMW2D Correlation Spectroscopy (in the case of Linear Increment Perturbation).[148]

Synchronous	Asynchronous	Spectral Change	
+	+	Convex increment	
+	0	Linear increment	
+	-	Concave increment	
0	+	Convex top	
0	0	Constant	
0	-	Concave bottom	
-	+	Convex decrement	
-	0	Linear decrement	
-	-	Concave decrement	

Figure content:

Perturbation — Mechanical, electrical, chemical, magnetic, optical, thermal, concentration, *etc.*

Prob

IR, NIR, Raman, UV-VIS, etc.

System

Dynamic Spectra

$$\tilde{A}_{k,j} = A(v_j, t_k) - \overline{A}(v_j)$$

Cross Correlation Analysis

2D Correlation Spectra

$$\Phi = \frac{1}{m-1} \tilde{A}^{\mathrm{T}} \tilde{A}$$

$$\Psi = \frac{1}{m-1} \tilde{A}^{\mathrm{T}} N \tilde{A}$$

Φ: Synchronous 2D correlation spectrum
Ψ: Asynchronous 2D correlation spectrum
N: Hilbert –Noda matrix

Figure 1-1. General Scheme for Obtaining Perturbation-Based 2DCOS Spectra. [5, 15, 138]
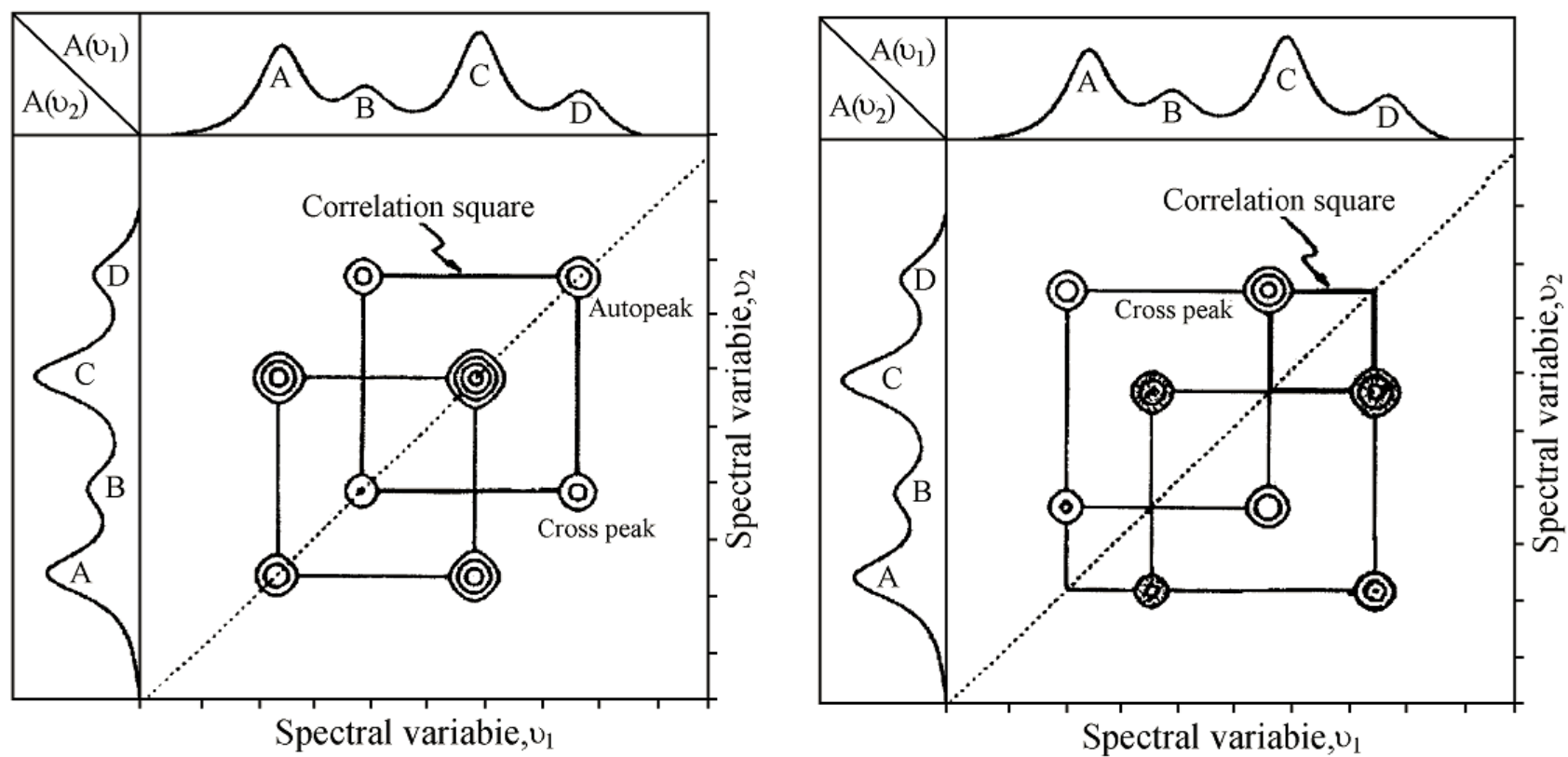
Figure 1-2. The Typical Synchronous (A) and Asynchronous (B) 2DCOS Spectra.[5, 15]
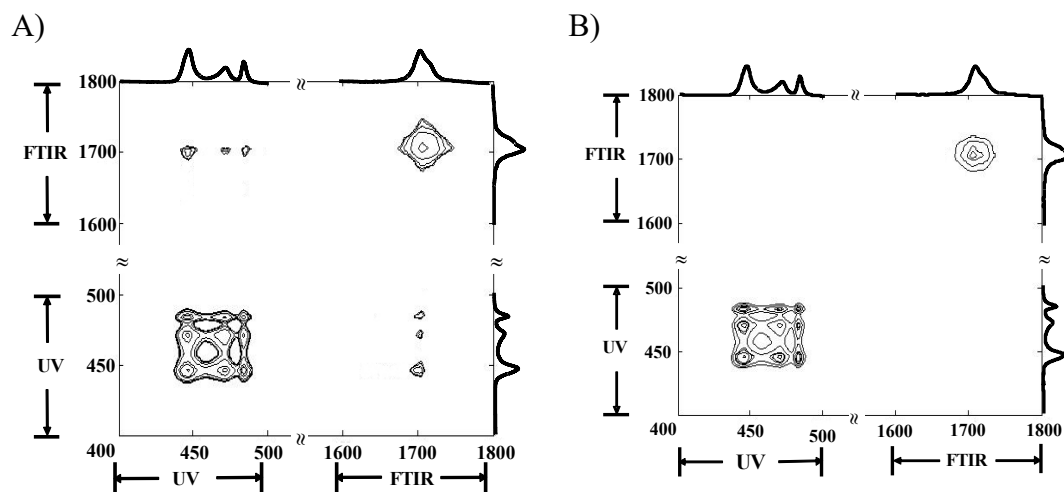
Figure 1-3 The Synchronous Spectra of Weak Coordination between Pr^{3+} and Carbonyl Group of Butanone. A) 2D Synchronous Spectrum is Generated using the OSD Approach. B) A Negative Control Experiment is used for Comparison.[40]
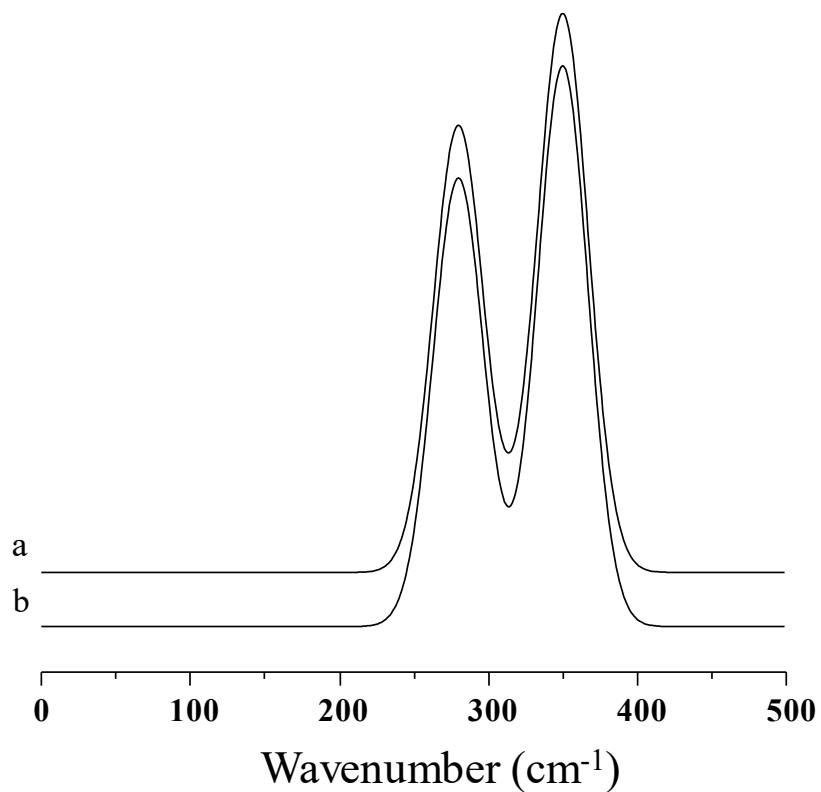
Figure 1-4. 1D Spectra of the Model System: (a) Mixture of P, Q, U, and V when only Bandwidth Variations Are Allowed due to Intermolecular Interaction; (b) no Intermolecular Interaction between P and Q Achieved by Setting the Equilibrium Constant K to zero.[115]
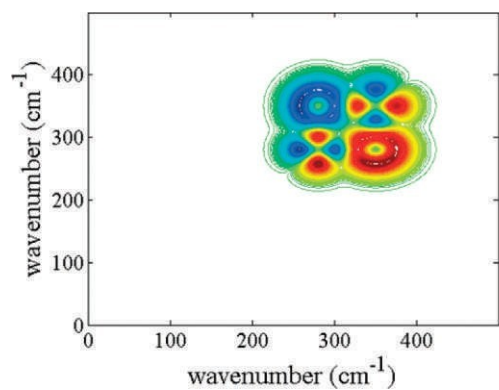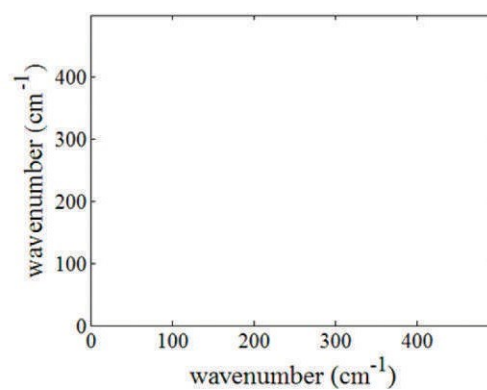
Figure 1-5. 2D Asynchronous Spectrum: A) Only Bandwidth Variations Are Allowed to Change due to Intermolecular Interaction; B) There Is No Intermolecular Interaction between P and Q.[115]

2D synchronous spectra　　　　**2D asynchronous spectra**

A)

B)

C)
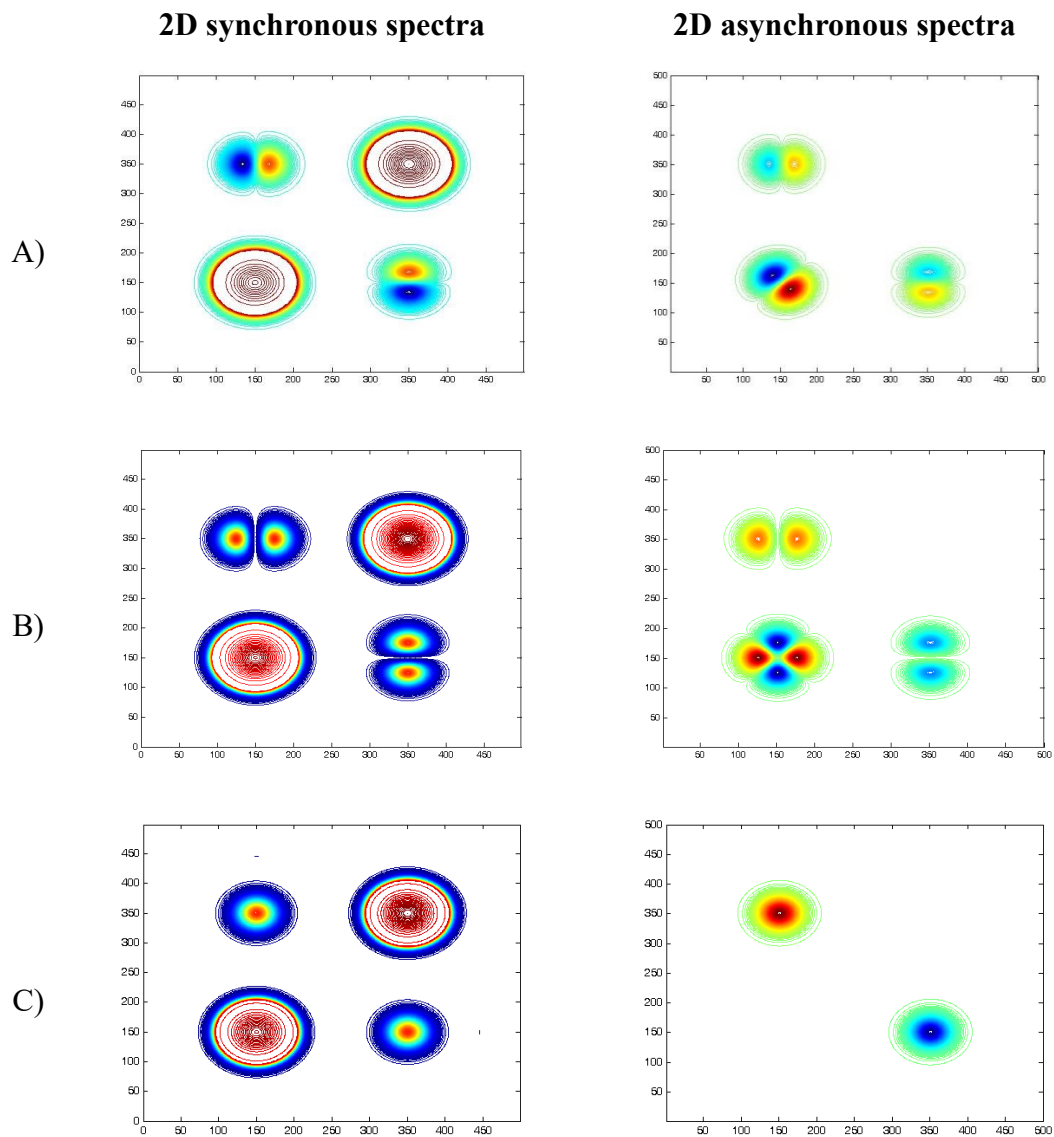
Figure 1-6. 2D Synchronous Spectra and asynchronous Spectra of the Model System Obtained as a Consequence of Peak Position and Bandwidth Variations, respectively.[119]

$\Delta X_Q<0, \Delta W_Q<0$	$\Delta X_Q<0, \Delta W_Q=0$	$\Delta X_Q<0, \Delta W_Q>0$
$\Delta X_Q=0, \Delta W_Q<0$	$\Delta X_P=0, \Delta W_Q=0$	$\Delta X_Q=0, \Delta W_Q>0$
$\Delta X_Q>0, \Delta W_Q<0$	$\Delta X_Q>0, \Delta W_Q=0$	$\Delta X_Q>0, \Delta W_Q>0$
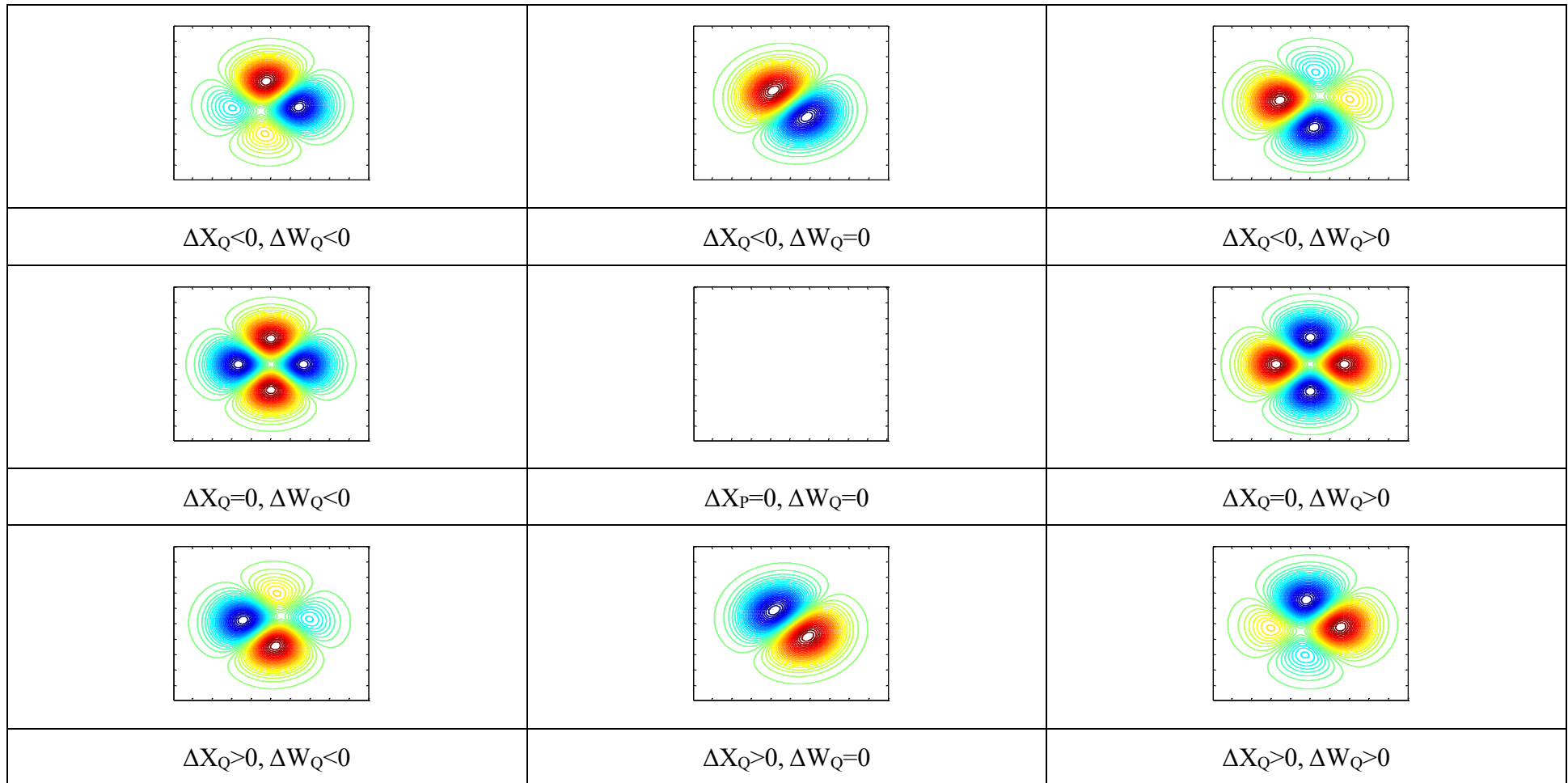
Figure. 1-7 The Relationship between the Pattern of Cross Peaks around (X_Q, X_Q) in $\Psi_P(x, y)$ and the Signs of ΔX_Q and ΔW_Q.[109]

$\Delta X_P=0, \Delta W_P=0, \Delta\varepsilon_P<0$	$\Delta X_P<0, \Delta W_P<0, \Delta\varepsilon_P=0$	$\Delta X_P<0, \Delta W_P=0, \Delta\varepsilon_P=0$	$\Delta X_P<0, \Delta W_P>0, \Delta\varepsilon_P=0$
$\Delta X_P=0, \Delta W_P=0, \Delta\varepsilon_P=0$	$\Delta X_P=0, \Delta W_P<0, \Delta\varepsilon_P=0$	$\Delta X_P=0, \Delta W_P=0, \Delta\varepsilon_P=0$	$\Delta X_P=0, \Delta W_P>0, \Delta\varepsilon_P=0$
$\Delta X_P=0, \Delta W_P=0, \Delta\varepsilon_P>0$	$\Delta X_P>0, \Delta W_P<0, \Delta\varepsilon_P=0$	$\Delta X_P>0, \Delta W_P=0, \Delta\varepsilon_P=0$	$\Delta X_P>0, \Delta W_P>0, \Delta\varepsilon_P=0$
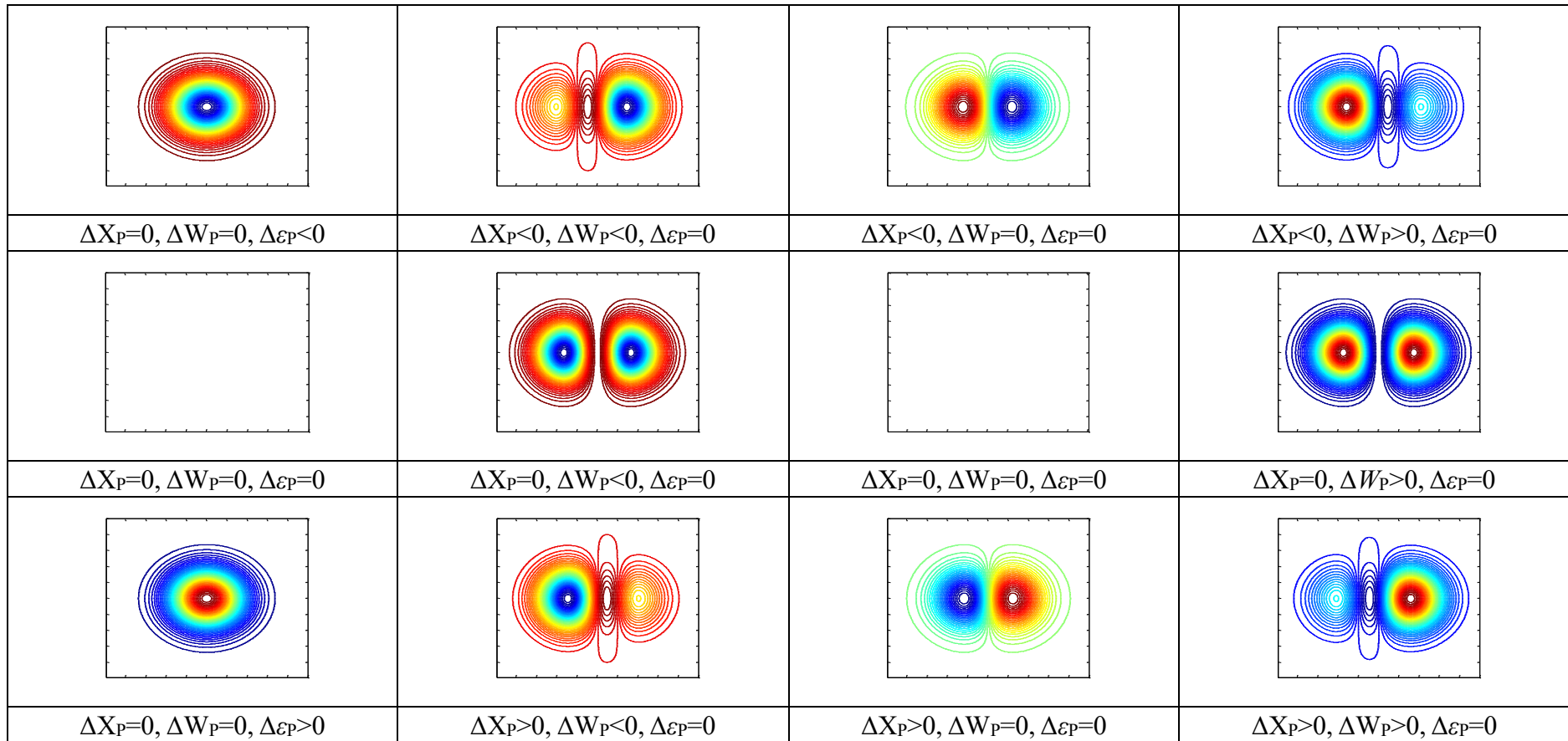
Figure 1-8 The Relationship between the Pattern of Cross Peaks around (X_P, X_Q) in $\mathbf{\Psi}_P(x, y)$ and the Signs of ΔX_P, ΔW_P and $\Delta\varepsilon_P$.[109]
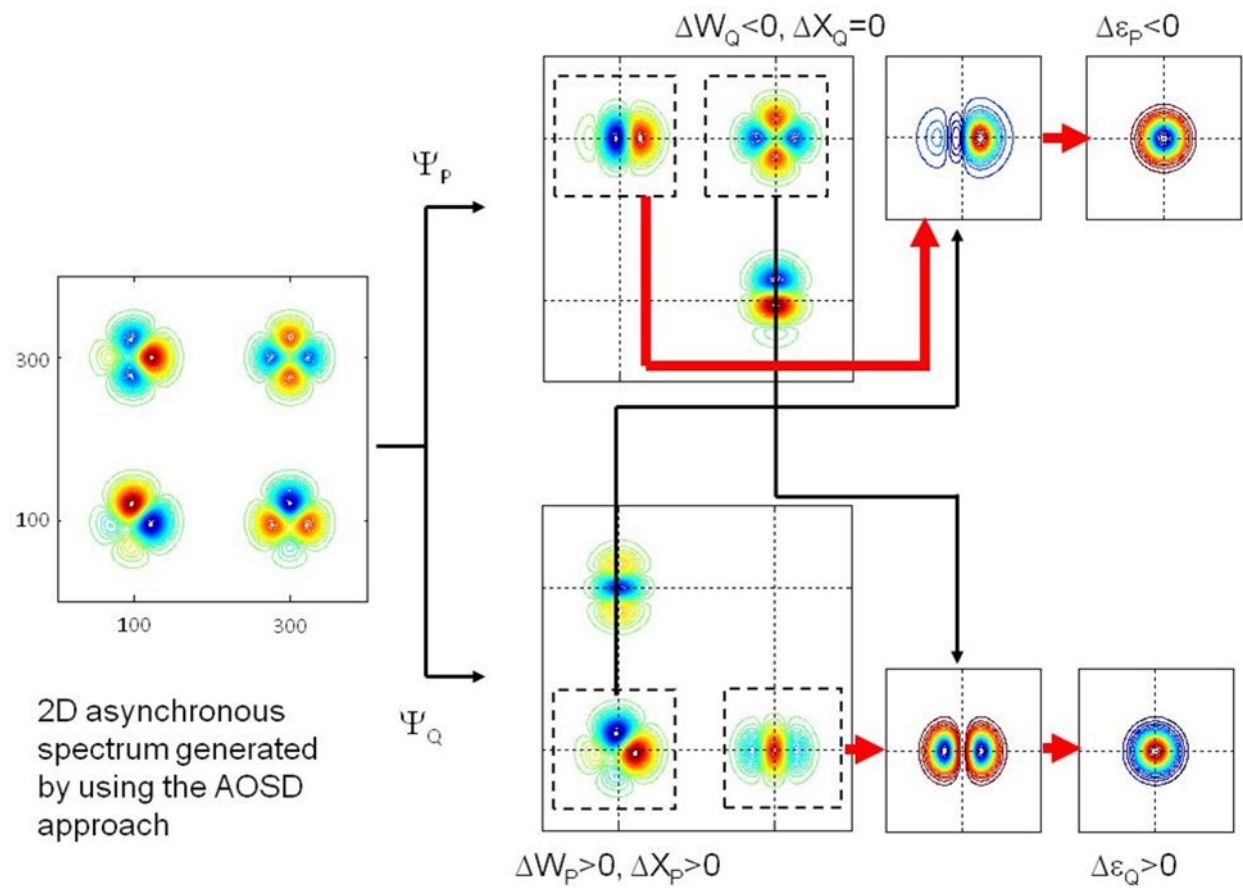
Figure 1-9. An Example of Analyzing the Signs of ΔX_P, ΔW_P, $\Delta \varepsilon_P$, ΔX_Q, ΔW_Q and $\Delta \varepsilon_Q$ Based on the Pattern of Cross Peaks from a pair of 2D Asynchronous Spectra Generated by using the DAOSD Approach. [109]
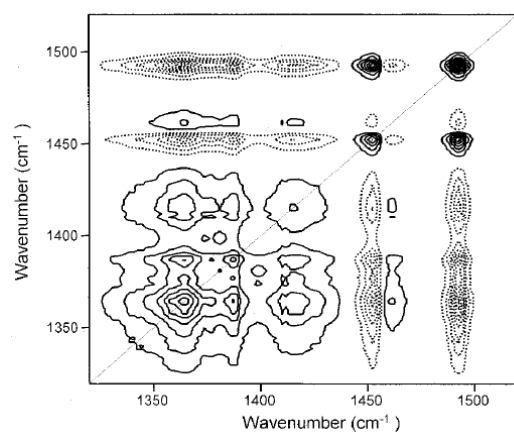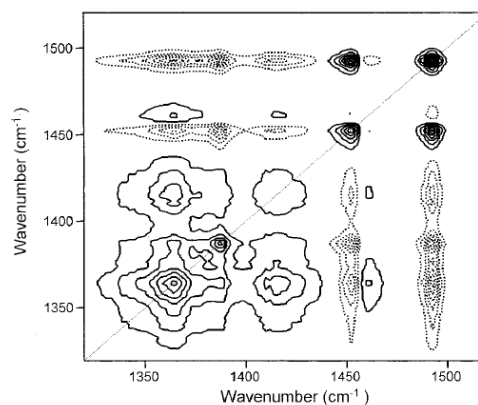
Figure 1-10. A) Synchronous 2D Correlation Spectra Constructed from the New Reconstructed Data Obtained by *m=2*; B) Synchronous 2D Correlation Spectrum Constructed from a Substantial Amount of Artificial Noise is Injected to the Time-Dependent FT-IR Spectra of a Mixture of Methyl Ethyl Ketone, Deuterated Toluene, and Polystyrene.[141]
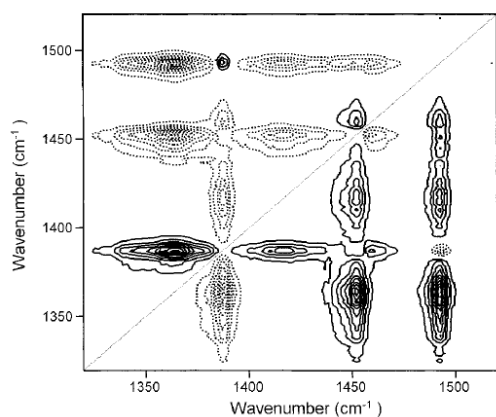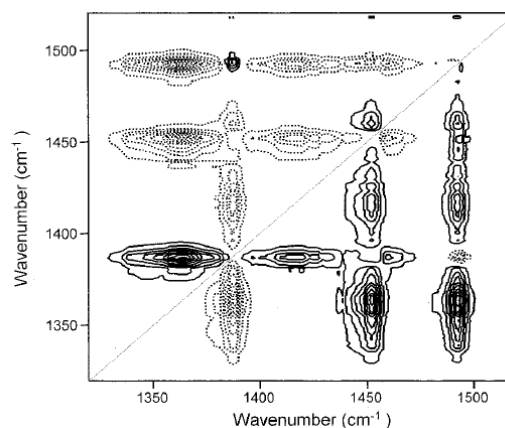
Figure 1-11. A) Asynchronous 2D Correlation Spectra Constructed from the New Reconstructed Data Obtained by *m=2*; B) Asynchronous 2D Correlation Spectrum Constructed from a Substantial Amount of Artificial Noise is Injected to the Time-Dependent FT-IR Spectra of a Mixture of Methyl Ethyl Ketone, Deuterated Toluene, and Polystyrene.[141]
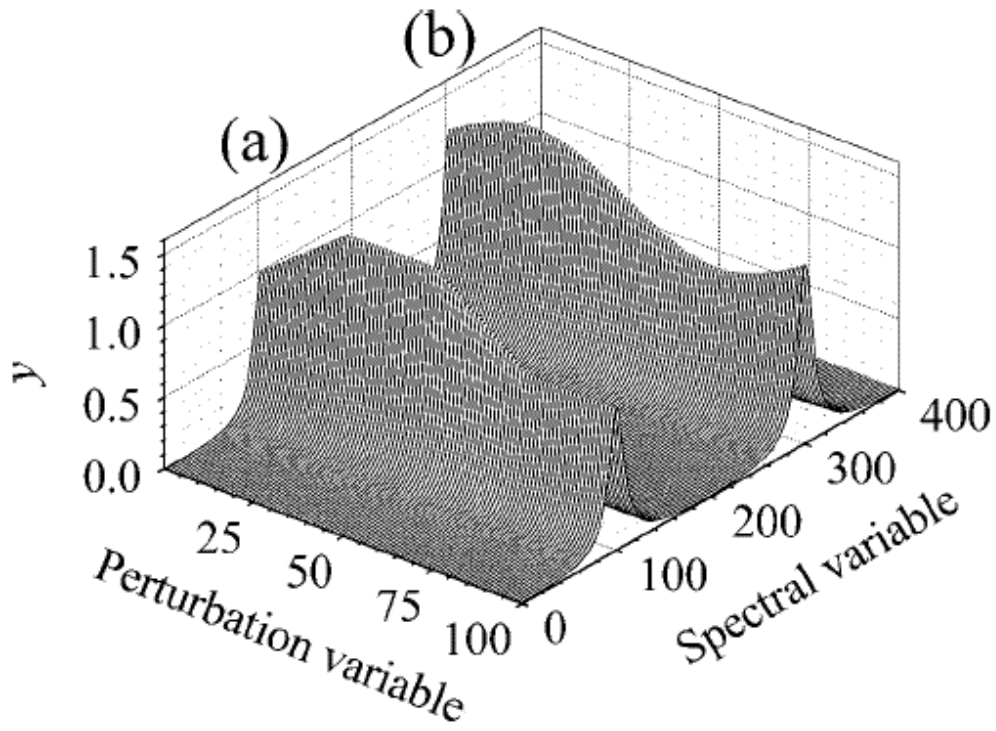
Figure 1-12. A Series of 1D Simulated Spectra.[148]
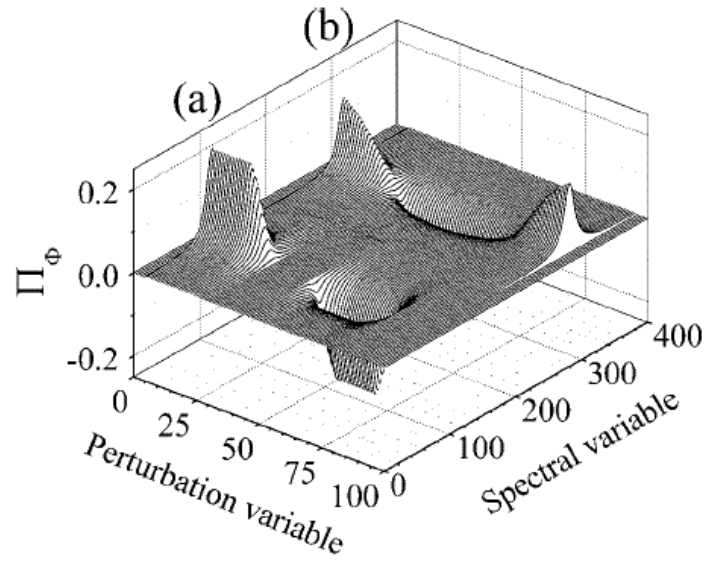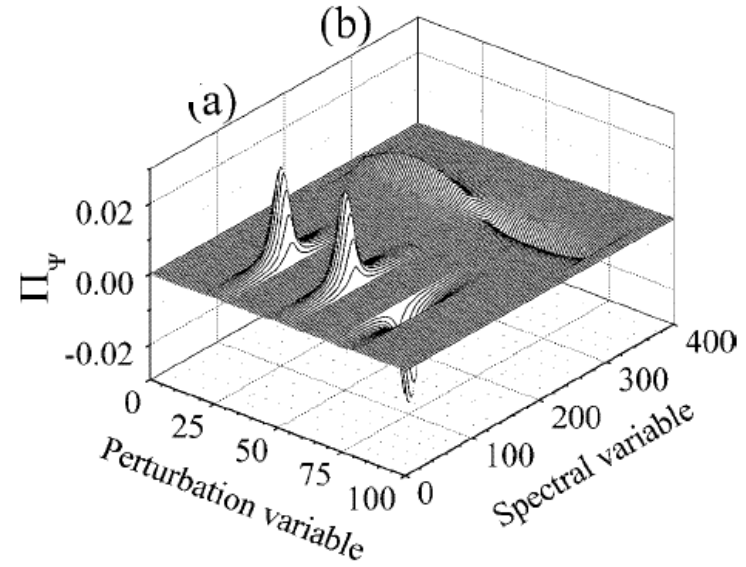
Figure 1-13. PCMW2D Correlation Spectra Calculated from the Series 1D Simulated Spectra (Figure. 1). A) Synchronous and B) Asynchronous PCMW2D Correlation Spectra. [148]
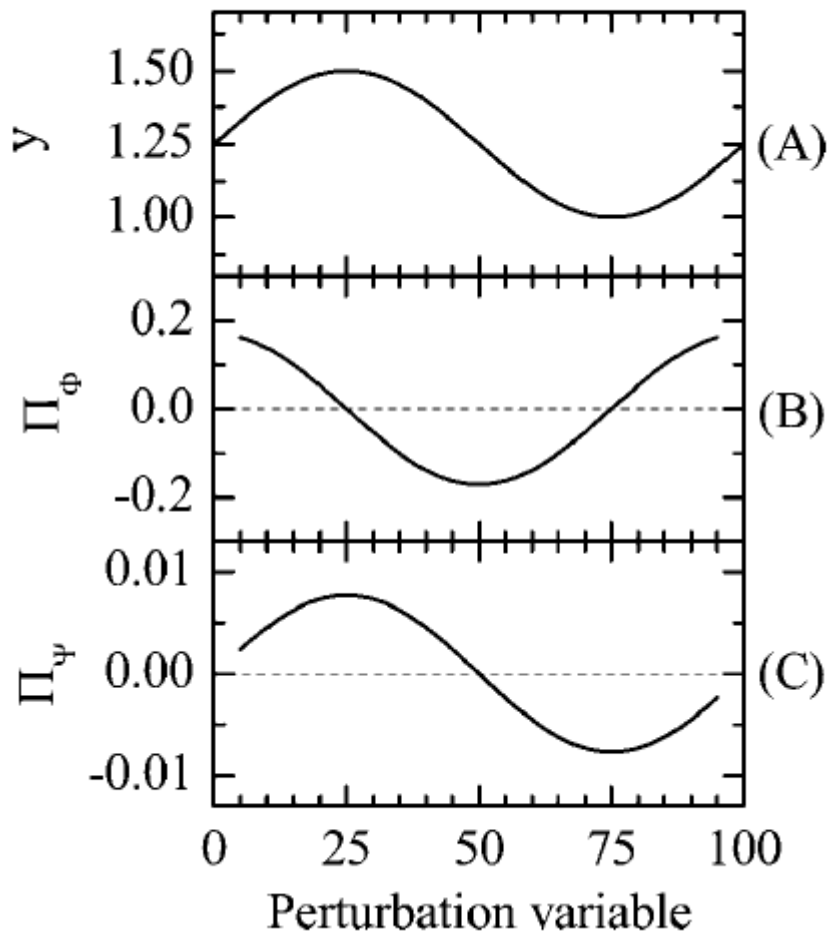
Figure. 1-14. Slice at $v=300$ of (A) Simulated Spectra and (B) Synchronous and (C) Asynchronous PCMW2D Correlation Spectrum.[148]
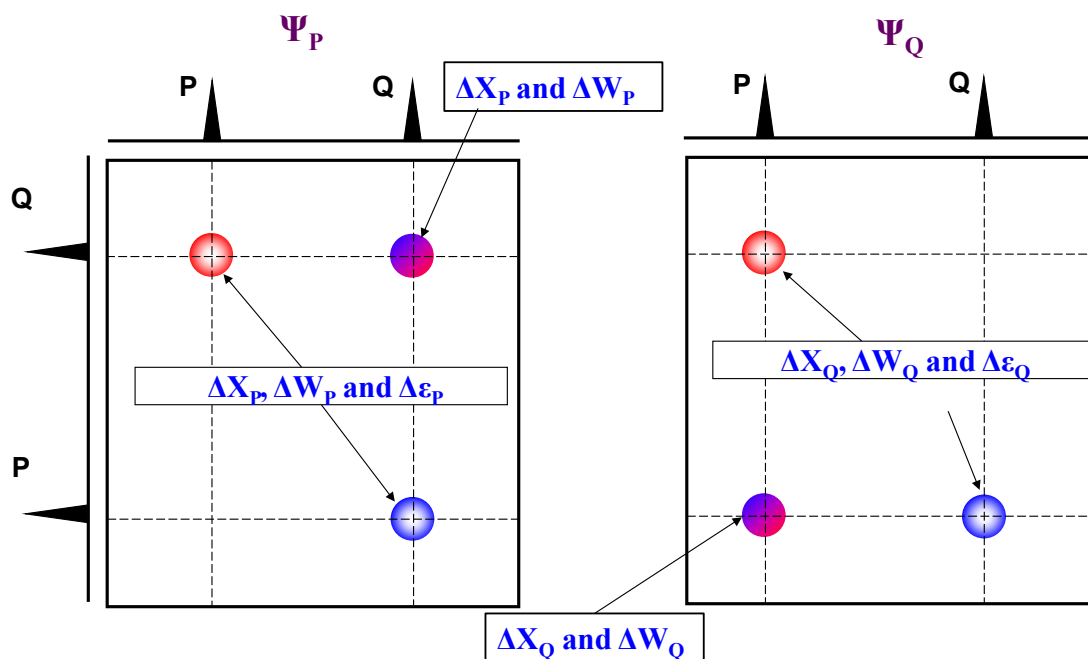
Scheme 1-1. Schematic Diagram that Illustrates the Relationship between the Cross Peaks in Six Spectral Regions and the Peak Variables.[103]

Chapter 1

A Novel Method of Constructing Two-Dimensional Correlation Spectra without Subtracting a Reference Spectrum

Significance of Enhancing Signal of Cross Peaks

In our previous work, we have developed orthogonal sample design scheme (OSD) and relevant techniques to reflect intermolecular interaction between two solutes in a reliable manner. [1-4] However, the limitation of these approaches is that the intensities of cross peaks are usually weak in comparison with typical cross peaks from 2D correlation spectra that are generated. Weak cross peaks are rather vulnerable to noise introduced during the spectral measurements. Consequently, it is still a challenge to study weak intermolecular interactions via cross peaks in 2D correlation spectrum generated by using the OSD and relevant techniques.

In order to enhance the signal of cross peaks, we tried to alter the sequence of sample spectra in the construction of 2D asynchronous spectrum.[5] In addition, we proposed a modified reference approach to increase the intensities of cross peaks.[6] However, above efforts are not always effective because of their own shortcomings. Thus, alternative approaches to enhance the intensities of cross peak are still needed.

In many situations, the research work may focus on a specific spectral region. In this spectral region, the component P possesses characteristic peaks at X_P. On the other hand, Q possesses no contribution in the spectra. We previously demonstrated that an interaction between P and Q can be reflected by the appearance of cross peaks near the main diagonal line around the spectral coordinate (X_P, X_P) in a 2D asynchronous spectrum. [7] We have utilized the results from this work on a couple of real chemical systems.[8-17] When we revisit this situation, we notice that near diagonal cross peaks around (X_P, X_P) have no interference portion that has nothing to do with intermolecular interaction. This realization confers us an opportunity to modify the procedure on the construction of 2D asynchronous spectrum so as to improve the performance of 2D asynchronous spectrum.

In this chapter, we propose that 2D asynchronous spectrum can be generated without the subtraction of a reference spectrum. Mathematical analysis and computer simulation on a model system demonstrate that: 1) near diagonal cross peaks around the coordinate (X_P, X_P) in 2D asynchronous spectrum generated by using the new method can reflect intermolecular interaction between P and Q reliably. 2) In comparison with conventional method, the intensities of cross peaks in the 2D asynchronous spectrum construct via the new method are significantly enhanced. In addition, we incorporated the new method with the DAOSD approach developed in our previous work. Then, we applied the modified DAOSD approach to study hydrogen bonding behavior in diethyl either/methanol/THF system. The appearance of cross peaks in 2D asynchronous spectrum with the new method demonstrate that THF competes with diethyl ether and combines to methanol via hydrogen bond. When 2D asynchronous spectrum is generated using the conventional method, the above cross peaks become too weak to be observed since the concentration range of THF is very narrow. These results demonstrate that the novel approach is very useful to enhance intensity of cross peaks, especially when the range of reactant concentration is very narrow.

Experimental

Methods

In the mathematical analysis and computer simulation on the model system, all the simulated 1D spectra were produced by using a program written in our lab using Matlab software (Mathworks, Inc.). 2D correlation spectra in both model system and real chemical system were constructed based on the algorithm developed by Noda via Matlab software.

Reagents

Diethyl ether was of AR grade and obtained from Beijing Chemical Company. Methanol (GR grade) was purchased from Beijing Tong Guang Fine Chemicals Company. Tetrahydrofuran (THF) of HPLC grade, was ordered from Xilong Chemical Co., Ltd.

A solvent purification system (MB-SPS-800) was used to treat diethyl ether and THF to remove trace amount on water. FTIR spectra of the diethyl ether, THF were recorded before and after treatment. No change was found in the corresponding FTIR spectra. That is to say, the interference of trace amount of water on FTIR spectra is negligible.

Instrument

FTIR spectra were collected on a Thermo-Fischer Nicolet 6700 Fourier transform infrared spectrometer equipped with an attenuated reflection accessory. All the spectra were recorded at a resolution of 4 cm^{-1} and 32 scans were co-added. During the experiment, the spectrometer was purged by dry air to remove the interference caused by water vapor.

Results and Discussion

1 Description of the Model System

The model system is composed of a series of solutions containing two solutes (P and Q). Under an intermolecular interaction, a small fraction of P undergoes a subtle structural variation and converts into another form denoted as U. Similarly, a small part of Q converts into another form (denoted as V). The inter-conversion can be described by a reaction shown in eq. 2-1.

$$P+Q \overset{K}{\leftrightarrow} U+V \tag{2-1}$$

where K is the equilibrium constant. We use concentrations of P and Q as external perturbations to construct 2D asynchronous spectra, so that the interaction between P and Q can be characterized by cross peaks in the resultant 2D asynchronous spectrum.

In the study, we focused on a specific spectral region. In the spectral region, solvent has not any contribution. Furthermore, neither Q nor V has an absorption band. P possesses a characteristic peak at X_P and U has a peak at X_U that is quite closed to X_P. We use Gaussian function shown in eq. 2-2 to model the absorption peak of P and that of U

$$f_j(x) = \varepsilon_j * e^{-(\ln 2)*[\frac{(x-X_j)^2}{W_j^2}]} \qquad (2-2)$$

where the index j refers to component P or U. Parameters ε_j, X_j, and W_j are the corresponding molar absorptivity, peak position and bandwidth (half-width at half-height, HWHH) of the characteristic band of the jth chemical species, respectively. The assumed values of absorptivity, peak position and bandwidth of the characteristic peaks of P and U are listed in **Table 2-1**.

To reflect the intermolecular interaction between P and Q, four solutions containing different amounts of P and Q are simulated. The initial concentrations of P and Q in the four solutions are listed in **Table 2-2**. In this case, the range of the initial concentration of P is quite narrow. Based on the above data, 1D spectra of the four solutions are simulated. Then 2D asynchronous spectrum is generated from the four 1D spectra.

Here, two methods to construct 2D asynchronous spectra are examined.

The first method is a conventional method, [31] where an average spectrum of the above four spectra is obtained and the used as a reference spectrum. The reference spectrum is subtracted from each of the four spectra. The resultant dynamic spectra are used to generate a 2D asynchronous spectrum. [31]

The second method is a new approach proposed in the present study. In this method, a 2D asynchronous spectrum is generated using the four spectra directly and no subtraction of a reference spectrum is carried out. First, we assume no intermolecular interaction occurs between P and Q, and this can be achieved by setting the value of K in eq. 2-1 to 0. The 2D asynchronous spectrum produced using the conventional method and the new method, respectively. No cross peak appears in the 2D asynchronous spectra constructed using both the conventional and new methods. Then, we assume that the interaction occurs between P and Q and the K value is now set as 0.01. The corresponding 2D asynchronous spectra produced using the two methods are depicted in **Figure 2-1A** and **Figure 2-1B**, respectively. This time, a group of cross peaks appears in **Figure 2-1A**. When we inspect **Figure 2-1B**, we find that a group of cross peaks can also be observed. Moreover, the pattern of cross peaks in **Figure 2-1B** is the exactly the same as those in **Figure 2-1A**. The results demonstrate that the near diagonal cross peaks around the coordinate (X_P, X_P) in the 2D asynchronous spectrum generated using the new method can also be used to reflect intermolecular interaction reliably.

Since the pattern of cross peaks of **Figure 2-1A** and **Figure 2-1B** are the same, we use the absolute value of cross peak at (88, 112) to reflect the intensities of cross peak in the two 2D asynchronous spectra. The absolute value of $\Psi_{conv}(88,112)$ and $\Psi_{mod}(88,112)$ are 2.26×10^{-6} and 1.89×10^{-2}, respectively. The intensity of cross peak in **Figure 2-1B** is about 8000 times larger than that in **Figure 2-1A**. Therefore, the intensity of cross peaks can be enhanced markedly if a 2D asynchronous spectrum is constructed without the subtraction of the reference spectrum defined as the average.

To understand the spectral behavior of 2D asynchronous spectra generated using the new method, a mathematical analysis is performed on the above model system. Firstly, the 1D spectra of the four solutions can be expressed as:

$$A^i(x) = C_P^{i(eq)} f_P(x) + C_U^{i(eq)} f_U(x) \tag{2-3}$$

where $i \in \{1,2,3,4\}$, x is the spectral variable, $f_P(x)$ and $f_U(x)$ are the spectral functions of P and U, and $C_P^{i(eq)}$ and $C_U^{i(eq)}$ are the equilibrium concentrations of P and U, respectively.

From eq. 2-1, we have

$$C_P^{i(eq)} = C_P^{i(init)} - C_U^{i(eq)} \tag{2-4}$$

Thus, eq. 2-3 changes into

$$A^i(x) = C_P^{i(eq)} f_P(x) + C_U^{i(eq)} \left(f_U(x) - f_P(x) \right) \tag{2-5}$$

In the conventional method of constructing 2D asynchronous spectrum estimated from the average, a reference spectrum is obtained as

$$R(x) = \frac{1}{4} \sum_{i=1}^{4} A^i(x) \tag{2-6}$$

Then, each spectrum is converted to dynamic spectrum via

$$\widetilde{A}(x) = A^i(x) - R(x) \tag{2-7}$$

After combining eq. 2-4-eq. 2-7, the expression of the dynamic spectrum can be expressed as

$$A^i(x) = \widetilde{C}_P^{i(eq)} f_P(x) + \widetilde{C}_U^{i(eq)} \left(f_U(x) - f_P(x) \right) \tag{2-8}$$

where

$$\widetilde{C}_P^i = C_P^{i(init)} - C_P^{init(av)}$$

$$\widetilde{C}_U^i = C_U^{i(eq)} - C_U^{eq(av)}$$

$$C_P^{init(av)} = \frac{1}{4} \sum_{i=1}^{4} C_P^{i(init)} \tag{2-9}$$

$$C_U^{eq(av)} = \frac{1}{4} \sum_{i=1}^{4} C_U^{i(eq)}$$

Afterward, a 2D asynchronous spectrum (denoted as $\Psi_{conv}(x,y)$) is generated from the dynamic spectra via

$$\Psi_{conv}(x,y) = \frac{1}{n-1} \vec{\widetilde{A}}^T(x) N \vec{\widetilde{A}}(y) \tag{2-10}$$

where $\vec{\widetilde{A}}(x) = \{ \widetilde{A}^1(x),\ \widetilde{A}^2(x),\ \widetilde{A}^3(x),\ \widetilde{A}^4(x) \}$, superscript T stands for transposition, and N is the Hilbert-Noda transformation matrix.

After combining eq. 2-10 with eq. 2-8, the expression of $\Psi_{conv}(x,y)$ is

$$\Psi_{\text{conv}}(x, y) = \sum_{i=1}^{4} \mathbf{M}_i(x, y) \tag{2-11}$$

where

$$\mathbf{M}_1(x, y) = f_P(x)f_P(y)\left(\vec{\tilde{C}}_P^{\text{init}}\right)^T \mathbf{N}\vec{\tilde{C}}_P^{\text{init}}$$

$$\mathbf{M}_2(x, y) = f_P(x)(f_U(y) - f_P(y))\left(\vec{\tilde{C}}_P^{\text{init}}\right)^T \mathbf{N}\vec{\tilde{C}}_U^{\text{eq}}$$

$$\mathbf{M}_3(x, y) = (f_U(x) - f_P(x))(f_U(y) - f_P(y))\left(\vec{\tilde{C}}_U^{\text{eq}}\right)^T \mathbf{N}\vec{\tilde{C}}_U^{\text{eq}} \tag{2-12}$$

$$\mathbf{M}_4(x, y) = (f_U(x) - f_P(x))f_P(y)\left(\vec{\tilde{C}}_U^{\text{eq}}\right)^T \mathbf{N}\vec{\tilde{C}}_P^{\text{init}}$$

Based on the mathematical property of Hilbert–Noda transformation matrix N listed in eq. 2-13,

$$\vec{B}^T\mathbf{N}\vec{B} = 0 \tag{2-13}$$

$\mathbf{M}_1(x, y)$ and $\mathbf{M}_3(x, y)$ are zero.

Additionally, $\mathbf{M}_2(x, y)$ and $\mathbf{M}_4(x, y)$ can be combined into one term according to another property of the Hilbert-Noda matrix shown in eq. 2-14.

$$\vec{A}^T\mathbf{N}\vec{B} = -\vec{B}^T\mathbf{N}\vec{A} \tag{2-14}$$

Therefore, the expression of the 2D asynchronous spectrum can be simplified as:

$$\Psi_{\text{conv}}(x, y) = [f_P(x)f_U(y) - f_U(x)f_P(y)]\left(\vec{\tilde{C}}_P^{\text{init}}\right)^T \mathbf{N}\vec{\tilde{C}}_U^{\text{eq}} \tag{2-15}$$

In the new method, all the 1D spectra are directly used to construct 2D asynchronous spectrum. The corresponding 2D asynchronous spectrum (denoted as $\Psi_{\text{mod}}(x, y)$) can be generated via:

$$\Psi_{\text{mod}}(x, y) = \frac{1}{n - 1}\vec{A}^T(x)\mathbf{N}\vec{A}(y) \tag{2-16}$$

The difference between eq. 2-10 and eq. 2-16 is that dynamic spectra vector $\vec{\tilde{A}}$ in eq. 2-10 is replaced by spectra vector $\vec{A}$ in eq. 2-16.

Via a similar procedure that is used to obtained eq. 2-16, $\Psi_{\text{mod}}(x, y)$ can be expressed as eq. 2-17.

$$\Psi_{\text{mod}}(x, y) = [f_P(x)f_U(y) - f_U(x)f_P(y)]\left(\vec{C}_P^{\text{init}}\right)^T \mathbf{N}\vec{C}_U^{\text{eq}} \tag{2-17}$$

When an intermolecular interaction is not present, the product of intermolecular interaction U between P and Q will not be produced. As a results, both $\vec{\tilde{C}}_U^{\text{eq}}$ and $\vec{C}_U^{\text{eq}}$ are zero vectors. According to eq. 2-15 and eq. 2-17, both $\Psi_{\text{conv}}(x, y)$ and $\Psi_{\text{mod}}(x, y)$ are zero. Thus, no cross peak is produced in 2D asynchronous spectra.

When an intermolecular interaction occurs between P and Q, U is produced and

neither $\vec{\tilde{C}}_U^{eq}$ nor $\vec{C}_U^{eq}$ is zero vector any more. Thus, cross peaks might be present in the corresponding 2D asynchronous spectra. According to eq. 2-15 and eq. 2-17, a 2D asynchronous spectrum can be regarded as a product of pattern factor and intensity factor (**Table 2-3**). The pattern factors for $\Psi_{conv}(x, y)$ and $\Psi_{mod}(x, y)$ are identical, i.e., $f_P(x)f_U(y) - f_U(x)f_P(y)$. Consequently, the pattern of cross peaks in **Figure 2-1A** is exactly the same as that of **Figure 2-1B**.

Then, we inspect the intensity factor, namely, $\left(\vec{C}_P^{init}\right)^T N\vec{C}_U^{eq}$ for $\Psi_{conv}(x, y)$ and $\left(\vec{C}_P^{init}\right)^T N\vec{C}_U^{eq}$ for $\Psi_{mod}(x, y)$.

According to eq. 2-9, $\left(\vec{C}_P^{init}\right)^T N\vec{C}_U^{eq}$ can be expressed as

$$\left(\vec{C}_P^{init}\right)^T N\vec{C}_U^{eq} = \left(\vec{\tilde{C}}_P^{init} + C_P^{init(av)}\vec{H}\right)^T N\left(\vec{\tilde{C}}_U^{eq} + C_U^{eq(av)}\vec{H}\right) \tag{2-18}$$

where $\vec{H} = \{1, 1, 1, 1\}$.

Equation 2-18 can be expanded as

$$\left(\vec{C}_P^{init}\right)^T N\vec{C}_U^{eq} = \left(\vec{\tilde{C}}_P^{init}\right)^T N\vec{\tilde{C}}_U^{eq} + C_P^{init(av)}\left(\vec{H}\right)^T N\vec{\tilde{C}}_U^{eq} + C_U^{eq(av)}\left(\vec{\tilde{C}}_P^{init}\right)^T N\vec{H}$$
$$+ C_P^{init(av)}C_U^{eq(av)}\left(\vec{H}\right)^T N\vec{H} \tag{2-19}$$

Based on the mathematical property of Hilbert–Noda transformation matrix **N** listed in eq. 2-13, the 4th term on the right of eq. 2-19 is zero. Moreover, we applied eq. 2-14 on eq. 2-19. Finally, eq. 2-18 can be simplified as

$$\left(\vec{C}_P^{init}\right)^T N\vec{C}_U^{eq} = \left(\vec{\tilde{C}}_P^{init}\right)^T N\vec{\tilde{C}}_U^{eq} + C_P^{init(av)}\left(\vec{H}\right)^T N\vec{\tilde{C}}_U^{eq} - C_U^{eq(av)}\left(\vec{H}\right)^T N\vec{\tilde{C}}_P^{init} \tag{2-20}$$

We define the first, second and third term on the right of eq. 2-20 as E, F and G, respectively. In addition, we define

$$^{norm}\vec{\tilde{C}}_P^{init} = \vec{\tilde{C}}_P^{init} / \left|\vec{\tilde{C}}_P^{init}\right|$$

$$^{norm}\vec{\tilde{C}}_U^{eq} = \vec{\tilde{C}}_U^{eq} / \left|\vec{\tilde{C}}_U^{eq}\right| \tag{2-21}$$

$$^{norm}\vec{H} = \vec{H}/|\vec{H}| = \left\{\frac{1}{2}, \frac{1}{2}, \frac{1}{2}, \frac{1}{2}\right\}^T$$

where $\left|\vec{\tilde{C}}_P^{init}\right|$, $\left|\vec{\tilde{C}}_U^{eq}\right|$ and $|\vec{H}|$ are the moduli of $\vec{\tilde{C}}_P^{init}$, $\vec{\tilde{C}}_U^{eq}$ and $\vec{H}$.

We have

$$|\vec{H}| = 2$$

$$\left|\vec{\tilde{C}}_P^{init}\right| = \sqrt{\sum_{i=1}^{4}\left(C_P^{i(init)} - C_P^{init(av)}\right)^2} = 2std\left(C_P^{init}\right) \tag{2-22}$$

$$\left|\vec{\tilde{C}}_U^{eq}\right| = \sqrt{\sum_{i=1}^{4}\left(C_U^{i(eq)} - C_U^{eq(av)}\right)^2} = 2std(C_U^{eq})$$

where std stands for standard deviation.

Thus E, F and G can be expressed as

$$E = \left(\vec{\tilde{C}}_P^{init}\right)^T N\vec{\tilde{C}}_U^{eq} = \left|\vec{\tilde{C}}_P^{init}\right|\left|\vec{\tilde{C}}_U^{eq}\right|\left(norm\vec{\tilde{C}}_P^{init}\right)^T N\left(norm\vec{\tilde{C}}_U^{eq}\right)$$

$$= 4std\left(C_P^{i(init)}\right)std\left(C_U^{i(eq)}\right)\left(norm\vec{\tilde{C}}_P^{init}\right)^T N\left(norm\vec{\tilde{C}}_U^{eq}\right) \tag{2-23a}$$

$$F = C_P^{init(av)}\left(\vec{\mathbf{H}}\right)^T N\vec{\tilde{C}}_U^{eq} = C_P^{init(av)}\left|\vec{\mathbf{H}}\right|\left|\vec{\tilde{C}}_U^{eq}\right|\left(norm\vec{\mathbf{H}}\right)^T N\left(norm\vec{\tilde{C}}_U^{eq}\right)$$

$$= 4C_P^{init(av)}std\left(C_U^{eq}\right)\left(norm\vec{\mathbf{H}}\right)^T N\left(norm\vec{\tilde{C}}_U^{eq}\right) \tag{2-23b}$$

$$G = -C_U^{eq(av)}\left(\vec{\mathbf{H}}\right)^T N\vec{\tilde{C}}_P^{init} = -C_U^{eq(av)}\left|\vec{\mathbf{H}}\right|\left|\vec{\tilde{C}}_P^{init}\right|\left(norm\vec{\mathbf{H}}\right)^T N\left(norm\vec{\tilde{C}}_P^{init}\right)$$

$$= -4C_U^{eq(av)}std\left(C_P^{init}\right)\left(norm\vec{\mathbf{H}}\right)^T N\left(norm\vec{\tilde{C}}_P^{init}\right) \tag{2-23c}$$

When the initial concentrations of P and Q are adopted as **Table 2-2**, the range of the initial concentration of P is very narrow, and thus, we have

$$\left|std\left(C_P^{init}\right)\right| \ll \left|C_P^{init(av)}\right| \tag{2-24}$$

Since the *K* value of eq. 2-1 is very small, only a very small fraction of P converts into U. Thus, we have

$$\left|C_U^{eq(av)}\right| \ll \left|C_P^{init(av)}\right| \tag{2-25}$$

Additionally, the range of initial concentration of Q is quite large, the range of the resultant equilibrium concentrations of U is larger than the range of the initial concentration of P. Thus, we have

$$\left|std\left(C_P^{init}\right)\right| < \left|std\left(C_U^{eq}\right)\right| \tag{2-26}$$

The values of $\left(norm\vec{\tilde{C}}_P^{init}\right)^T N\left(norm\vec{\tilde{C}}_U^{eq}\right)$, $\left(norm\vec{\mathbf{H}}\right)^T N\left(norm\vec{\tilde{C}}_U^{eq}\right)$ and

$\left(norm\vec{\mathbf{H}}\right)^T N\left(norm\vec{\tilde{C}}_P^{init}\right)$ are calculated to be 9.83×10^{-2}, -0.411 and -3.26×10^{-3}, when *k*

value of eq. 2-1 is 0.01. Thus:

$$\left|\left(norm\vec{\tilde{C}}_P^{init}\right)^T N\left(norm\vec{\tilde{C}}_U^{eq}\right)\right| \sim \left|\left(norm\vec{\mathbf{H}}\right)^T N\left(norm\vec{\tilde{C}}_U^{eq}\right)\right| \tag{2-27}$$

$$\gg \left|\left(norm\vec{\mathbf{H}}\right)^T N\left(norm\vec{\tilde{C}}_P^{init}\right)\right|$$

After combining formula. 2-24- formula 2-27, we have

$$\begin{aligned}\left|F\right| &\gg \left|E\right| \\ \left|F\right| &\gg \left|G\right|\end{aligned} \tag{2-28}$$

According to formula 2-27, eq. 2-20 changes into

$$\left| \left(\vec{C}_P^{init} \right)^T N \vec{C}_U^{eq} \right| = |E + F + G| \approx |F| \gg |E| = \left| \left(\vec{\tilde{C}}_P^{init} \right)^T N \vec{\tilde{C}}_U^{eq} \right| \tag{2-29}$$

The above analysis explains why the intensities of cross peak in the 2D asynchronous spectrum generated using the novel method described in this chapter are enhanced. Then, we investigate the spectrum behavior of 2D asynchronous spectrum generated using the new method. The initial concentrations of P and Q listed in **Table 2-2** are adopted while the K values of eq. 2-1 changes from 0.01 to 1.0×10^{-6}. We find eq. 2-24 to eq. 2-27 are still true. Thus, eq. 2-29 is still valid. Namely, the intensities of cross peaks are enhanced when the new method (constructing 2D asynchronous spectrum without subtracting a reference spectrum) is utilized to construct a 2D asynchronous spectrum.

In summary, we propose a novel approach to generate a 2D asynchronous spectrum without subtracting a reference spectrum during the constructing process. The resultant near diagonal cross peaks around (X_P, X_P) can be used to reflect intermolecular interaction in a reliable manner. Moreover, the intensities of cross peaks around the coordinate (X_P, X_P) in the 2D asynchronous spectrum generated using the new approach is much stronger than those in a 2D asynchronous spectrum generated using the conventional approach. It should be pointed out that the approach described in this chapter is very effective especially the range of initial concentrations of P is very narrow.

2 Application of novel method on a Real Chemical System

The approach described in this chapter can be incorporated into the now well-established DAOSD approach[31-41] to improve the performance of 2D asynchronous spectrum to probe the intermolecular interactions. In the DAOSD approach, a 2D asynchronous spectrum called $\Psi_P(x, y)$ is generated via the following procedure: a group of solutions containing P and Q are prepared. In a series of solutions, the initial concentration of P is constant. Then, 1D spectra of the series of solutions are recorded and used to construct a 2D asynchronous spectrum. The 2D asynchronous spectrum in the 2D spectral region around the coordinate (X_P, X_P) can be described via eq. 2-15.

Since the initial concentration of P is constant, $\vec{\tilde{C}}_P^{init}$ is a zero vector. That is to say, the intensity factor for $\Psi_P(x, y)$ is zero and $\Psi_P(x, y) = 0$ in the spectral region around (X_P, X_P). When the new approach is adopted, the intensity factor changes from $\left(\vec{\tilde{C}}_P^{init} \right)^T N \vec{\tilde{C}}_U^{eq}$ into $\left(\vec{C}_P^{init} \right)^T N \vec{C}_U^{eq}$. Since $\vec{\tilde{C}}_P^{init}$ is a zero vector, eq. 2-20 is simplified as

$$\left(\vec{C}_P^{init} \right)^T N \vec{C}_U^{eq} = C_P^{init(av)} \left(\vec{H} \right)^T N \vec{\tilde{C}}_U^{eq} \tag{2-30}$$

Thus, nonzero intensity factor can be produced and cross peaks appear near the diagonal line around the coordinate (X_P, X_P) in the resultant $\Psi_P(x, y)$.

Herein, we apply this approach on a real chemical system. The system is used a series of solutions. In these solutions, diethyl ether was utilized as a solvent. Methanol was used as one solute and tetrahydrofuran (THF) was employed as another solute. When methanol was dissolved in diethyl ether, hydrogen bonds are formed. FTIR spectra of the system were measured to characterize the hydrogen bonding behavior in the system. As shown in **Figure S2-1** in the **Supporting Information**, a single OH

stretching band appears at 3504 cm^{-1} when the concentration of methanol is below 4.61×10^{-4} mol/ml. Neither peak position nor band shape changes when the concentration of methanol is between 1.37×10^{-4} and 4.61×10^{-4} mol/ml. Thus, the band 3504 cm^{-1} is assigned to the OH stretching band of methanol that forms a methanol-diethyl ether complex via a hydrogen bond (**Scheme 2-1**). [57-60] As the concentration of methanol increases, the shape of the OH stretching band changes and undergo a red shift. (Please see the first part of **Supporting Information**) The reason for this change is that the OH groups of methanol play a dual role. On one hand, the OH group acts as a hydrogen bonding donor (the OH group marked in blue in **Scheme 2-2**); on the other hand, the oxygen atom of the OH group acts as hydrogen bonding acceptor (the OH group marked in red in **Scheme 2-2**). In this way, methanol may form (methanol)$_x$ (including dimer, trimer, tetramer or multimers) via hydrogen bonding among methanol molecules. The formation of (methanol)$_x$ makes the spectrum of OH stretching band rather complex. In this chapter, we focus on the diethyl ether solutions in which the concentration of methanol is below 4.61×10^{-4} mol/ml, so that (methanol)$_x$ will not be produced. Then, THF is now introduced into the solutions as a second solute. Upon introducing THF, THF may compete with diethyl ether on the formation of hydrogen bonding with methanol (**Scheme 2-3**). Namely, a small fraction of hydrogen bond between methanol and diethyl ether will break so that the resultant free methanol can form a hydrogen bond with THF. **Figure 2-2** depicts a typical FTIR spectrum of diethyl ether solution containing both methanol (2.47×10^{-4} mol/ml) and THF (7.40×10^{-4} mol/ml). For comparison, an FTIR spectrum of diethyl solution that contains only methanol (2.44×10^{-4} mol/ml) is also shown. However, no observable difference can be found for the OH stretching band between the two spectra shown in **Figure 2-2**. Moreover, the second derivative spectra (**Figure S2-4**) show that the OH stretching band of methanol does not split upon introduction of THF. The reason why no significant observable difference may be as follows: That the content of diethyl ether is overwhelmingly larger than that of THF. Alternately, the strength of hydrogen bond between methanol and diethyl ether may be similar to that between methanol and THF. As a result, the OH stretching band of methanol-diethyl ether may severely overlap with that of methanol-THF. The above reasons make it difficult to observe spectral changes on the OH stretching band even if a hydrogen bond is indeed formed between THF and methanol. Alternative approach should be adopted to address the problem.

The hydrogen bonding between methanol and THF dissolved in diethyl ether can be regarded as a form of intermolecular interaction (eq. 2-31), which might be revealed by cross peaks in a 2D asynchronous spectrum.

$$\text{Methanol-Diethyl Ether+THF} \overset{K}{\leftrightarrow} \text{Methanol-THF+Diethyl Ether} \qquad (2\text{-}31)$$

In this study, we try to use the near diagonal cross peaks around the coordinate (3504 cm^{-1}, 3504 cm^{-1}) in 2D asynchronous spectrum generated by using the DAOSD approach to probe whether Methanol-THF complex is formed or not. In the first experiment, three diethyl ether solutions were prepared with the initial concentrations of methanol and THF listed in **Table 2-4**. Their FTIR spectra were recorded and used to construct a 2D asynchronous spectrum (**Figure 2-3A**). Since the initial concentration

of THF is constant, the resultant 2D asynchronous spectrum is called Ψ_{THF}. According to the basic property of the DAOSD approach, cross peaks around the coordinate (3504 cm^{-1}, 3504 cm^{-1}) in the 2D asynchronous spectrum is expected to be useful in probing the peak position and bandwidth difference between the OH stretching band of methanol- diethyl ether and that of methanol-THF. As mentioned above, to prevent the formation of (methanol)$_x$ in the solution, the initial concentration of methanol has to be very low. As a result, the concentration ranges of methanol listed in **Table 2-4** is rather narrow. The narrow concentration ranges of methanol, in turn, make the intensities of cross peak rather weak. As a matter of fact, cross peaks in the resultant 2D asynchronous spectrum are so weak that they are completely covered by noise.

To address the problem, we adopt the new approach developed in the present study. Another series of diethyl ether solutions containing both methanol and THF are prepared. The initial concentration of methanol and THF are listed in **Table 2-5**. In these series of solutions, the initial concentrations of methanol are constant, while the initial concentrations of THF are variable. Then, FTIR spectra of the series of solution are collected. Afterward, the obtained FTIR spectra are used to generate a 2D asynchronous spectrum (denoted as $\Psi_{methanol}$) via a procedure without subtracting a reference spectrum. Because of the contribution of the extra term in eq. 2-30, cross peaks indeed appear around (3504 cm^{-1}, 3504 cm^{-1}) in the resultant $\Psi_{methanol}$ even if the initial concentration of methanol is constant (**Figure 2-3B**). The appearance of cross peak demonstrates that THF does take part in competition with diethyl ether in the formation of hydrogen bond with methanol. As a result, new OH stretching band is produced via the formation of methanol-THF complex. The new band that is buried under the congested envelop of the OH stretching band is revealed and manifested as cross peaks in the 2D asynchronous spectrum.

According to previous discussion, 2D asynchronous spectrum shown in **Figure 2-3B** can be described by

$$\Psi_{methanol}(x,y) = C_P^{init(av)}\left(\vec{\mathbf{H}}\right)^T \mathbf{N}\vec{C}_U^{eq}[f_P(x)f_U(y) - f_U(x)f_P(y)] \tag{2-32}$$

where $f_P(x)$ is the peak function of the OH stretching band of methanol-diethyl ether, and $f_U(x)$ is the peak function of the OH stretching band of methanol-THF, $C_P^{init(av)}$ is the average value of the initial concentration of methanol, and C_U^{eq} is the equilibrium concentration of methanol-THF complex.

The exact value of equilibrium concentrations of methanol-THF complex in the solution cannot be obtained since the *K* value of eq. 2-31 is not available. The sign of $C_P^{init(av)}\left(\vec{\mathbf{H}}\right)^T \mathbf{N}\vec{C}_U^{eq}$ is positive when the initial concentration of methanol and THF are set as **Table 2-5**. (Mathematical proof of this state can be found in the part 2 of **Supporting Information**). That is to say, the pattern of cross peaks (the number, position, shape and sign of cross peaks) can be represent by $f_P(x)f_U(y)-f_P(y)f_U(x)$ in $\Psi_{mod}(x, y)$. The pattern of $\Psi_{mod}(x, y)$ cannot reflect difference on absorptivity between the OH stretching band of methanol-diethyl ether complex and that of methanol-THF

complex. We try to find whether the peak position or bandwidth of the OH stretching band change when the methanol-diethyl ether complex is replaced by the methanol-THF complex. There are nine possible situations concerning the difference on the peak position and bandwidth. In part 3 of **Supporting Information**, the nine possible situation and corresponding pattern of $\Psi_{mod}(x, y)$ are listed in **Table S2-2**. A one-to-one correspondence can be set up. The pattern of cross peak in Situation II of **Figure S2-5** is the same as that shown in **Figure 2-3B**. Thus, the width of the OH stretching band of the methanol-THF complex is roughly the same as that of the methanol-THF complex. The OH stretching band of methanol-THF, in turn, undergoes a red shift in comparison with that of methanol-diethyl ether, even if the range of initial concentration of THF is only between 0 and 4.93 $\times 10^{-4}$ mol/ml.

The conclusions from the above 2D asynchronous spectra get additional support from the following experiment. Trace 1 of **Figure 2-4** shows an FTIR spectrum of THF solution containing methanol (2.78×10^{-4} mol/ml). In this case, all methanol molecules form methanol-THF complex. A single OH stretching band appears at 3484 cm^{-1}. For comparison, a spectrum of diethyl ether solution containing methanol (2.44×10^{-4} mol/ml) is shown as trace 2 of **Figure 2-4**. As mentioned above, all methanol molecules form methanol-diethyl complex and the corresponding OH stretching band occur at 3504 cm^{-1}. Therefore, the OH stretching band of the methanol-THF complex undergoes a red shift in comparison with the OH stretching band of the methanol-diethyl ether. Moreover, the widths of the OH stretching band in trace 1 and trace 2 in **Figure 2-4** are roughly the same. This example demonstrates that the approach described in this chapter is applicable in the real chemical system.

We suggest that this approach might be applicable in moving window analysis to enhance the intensities of cross peaks. Further work is still being performed.

Conclusion

A new method to construct 2D asynchronous spectrum without subtracting a reference spectrum is proposed. The resultant 2D asynchronous spectra are used to study intermolecular interaction between two solutes (P and Q, where P has a characteristic peak at X_P) dissolved in the same solvent. We focus on the spectral behavior of the near diagonal cross peaks around the coordinate (X_P, X_P) in the 2D asynchronous spectrum generated using the new method. Mathematical analysis and computer simulation on a model system demonstrate that cross peaks around (X_P, X_P) can reflect intermolecular interaction between P and Q in a reliable manner. Moreover, the intensities of cross peaks around (X_P, X_P) can be significantly enhanced in comparison with the corresponding 2D asynchronous spectrum produced with the conventional method. The new approach is especially effective in enhancing the intensities of weak cross peaks because of narrow variation range of the initial concentrations of P or Q. We incorporated the new method with the DAOSD approach developed in our previous work. Then we applied the modified DAOSD approach to study hydrogen bonding behavior in diethyl either/methanol/THF system. In diethyl

solution containing low concentration of methanol, only methanol-diethyl ether complex via a hydrogen bond exists. Upon introducing THF, THF breaks the methanol-diethyl ether hydrogen bond and forms methanol-THF complex via new hydrogen bond even if the content of diethyl is overwhelmingly larger than that of THF. This process can be revealed by the appearance of cross peak in 2D asynchronous spectrum using the modified DAOSD approach. Since the range of concentration of THF is very narrow, the cross peaks can only become observable using the new method.

References

1.   Qi, J.; Li, H. Z.; Huang, K.; Chen, H. H.; Liu, S. X.; Yang, L. M.; Zhao, Y.; Zhang, C. F.; Li, W. H.; Wu, J. G. et al. Orthogonal Sample Design Scheme for Two-Dimensional Synchronous Spectroscopy and its Application in Probing Intermolecular Interactions. *Appl. Spectrosc.* **2007**, *61*, 1359-1365.

2.   Li, X. P.; Pan, Q. H.; Chen, J.; Liu, S. X.; He, A. Q.; Liu, C. G.; Wei, Y. J.; Huang, K.; Yang, L. M.; Feng, J. et al. Asynchronous Orthogonal Sample Design Scheme for Two-Dimensional Correlation Spectroscopy (2D-COS) and its Application in Probing Intermolecular Interactions from Overlapping Infrared (IR) Bands. *Appl. Spectrosc.* **2011**, *65*, 901-917.

3.   Zhang, C. F.; Huang, K.; Li, H. Z.; Chen, J.; Liu, S. X.; Zhao, Y.; Wang, D. J.; Xu, Y. Z.; Wu, J. G.; Noda, I. et al. Double Orthogonal Sample Design Scheme and Corresponding Basic Patterns in Two-Dimensional Correlation Spectra for Probing Subtle Spectral Variations Caused by Intermolecular Interactions. *J. Phys. Chem. A* **2009**, *113*, 12142-12156.

4.   Chen, J.; Bi, Q.; Liu, S. X.; Li, X. P.; Liu, Y. H.; Zhai, Y. J.; Zhao, Y.; Yang, L. M.; Xu, Y. Z.; Noda, I. et al. Double Asynchronous Orthogonal Sample Design Scheme for Probing Intermolecular Interactions. *J. Phys. Chem. A* **2012**, *116*, 10904-10916.

5.   Li, X. P.; Liu, S. X.; Chen, J.; Yue, S. J.; Liu, C. G.; Wei, Y. J.; Huang, K.; Zhao, Y.; Xu, Y. Z.; Noda, I. et al. The Influence Of Changing the Sequence of Concentration Series on the 2D Asynchronous Spectroscopy Generated by the Asynchronous Orthogonal Sample Design (AOSD) Approach. *Vib. Spectrosc.* **2012**, *60*, 212-216.

6.   Li, X. P.; Bi, Q.; Liu, S. X.; Chen, J.; Yue, S. J.; Wei, Y. J.; Huang, K.; Zhao, Y.; Liu, H. Z.; Zhai, Y. J. et al. Improvement of the Sensitivity of the Two-Dimensional Asynchronous Spectroscopy Based on The AOSD Approach by using a Modified Reference Spectrum. *J. Mol. Struct.* **2013**, *1034*, 101-111.

7.   Li, X. P.; Fan, X. K.; Huang, K.; Liu, H. Z.; Zhao, Y.; Wei, Y. J.; Liu, C. G.; Xu, Y. Z.; Noda, I. et al. Characterization of Intermolecular Interaction Between Two Substances when One Substance does not Possess any Characteristic Peak. *J. Mol. Struct.* **2014**, *1069*, 127-132.

8.   Qi, J.; Huang, K.; Gao, X. X.; Li, H. Z.; Liu, S. X.; Zhao, Y.; Xu, Y. Z.;

Wu, J. G.; Noda, I. Orthogonal Sample Design Scheme for Two-Dimensional Synchronous Spectroscopy: Application in Probing Lanthanide Ions Interactions With Organic Ligands in Solution Mixtures. *J. Mol. Struct.* **2008**, *883*, 116-123.

9. Li, H. Z.; Tao, D. L.; Qi, J.; Wu, J. G.; Xu, Y. Z.; Noda, I. Dipole-Dipole Interactions in Solution Mixtures Probed by Two-Dimensional Synchronous Spectroscopy Based on Orthogonal Sample Design Scheme. *Spectrochim. Acta, Part A* **2014**, *124*, 697-702.

10. Bi, Q.; Chen, J.; Li, X. P.; Shi, J. J.; Wang, X. M.; Zhang, J.; Gao, D. Q.; Zhai, Y. J.; Zhao, Y.; Weng, S. F. et al. Investigation on the Dipole–Dipole Interactions between Tetramethylurea and Acetonitrile by Two-Dimensional Asynchronous Spectroscopy. *J. Mol. Struct.* **2014**, *1069*, 264-271.

11. Gao, Y. L.; Liu, J.; Liu, Y. H.; Shi, J. J.; Weng, S. F.; Yang, L. M.; Wen, X. D.; Kang, T. G.; Xu, Y. Z.; Noda, I. et al. Characterization of the Coordination between Nd^{3+} and Ester Groups by using Double Asynchronous Orthogonal Sample Design Approach. *J. Mol. Struct.* **2014**, *1069*, 205-210.

12. Liu, J.; Gao, Y. L.; Zheng, L. R.; Gao, D. Q.; He, A. Q.; Liu, Y. H.; Weng, S. F.; Zhao, Y.; Yang, Z. L. et al. Coordination between Cobalt (II) Ion and Carbonyl Group in Acetone Probed by using DAOSD Approach. *J. Mol. Struct.* **2014**, *1069*, 217-222.

13. Liu, Y. H.; Shi, J. J.; Gao, D. Q.; Gao, Y. L.; Guo, R.; Ling, X. F.; Weng, S. F.; Xu, Y. Z.; Noda, I.; Wu, J. G. Interactions between Pyridinium and Nd^{3+}. *Chin. Chem. Lett.* **2015**, *26*, 182-186.

14. Chen, M.; Guo, R.; Zhao, Y.; Weng, S. F.; Xu, Y. Z.; Noda, I.; Wu, J. G. Investigation on the Intermolecular Interaction between Diethyl Ether and Dichloromethane in Gaseous Phase by using the DAOSD Approach. *J. Mol. Struct.* **2016**, *1124*, 244-248.

15. Kang, X. Y.; He, A. Q.; Guo, R.; Zhai, Y. J.; Xu, Y. Z.; Noda, I.; Wu, J. G. A Simplified Concentration Series to Produce a Pair of 2D Asynchronous Spectra Based on the DAOSD Approach. *J. Mol. Struct.* **2016**, *1124*, 151-158.

16. Zhang, J.; Guo, R.; He, A. Q.; Weng, S. F.; Gao, X. X.; Xu, Y. Z.; Noda, I.; Wu, J. G. Investigation on the Relationship between Solubility of Artemisinin and Polyvinylpyrroli Done Addition by using DAOSD Approach. *Spectrochim. Acta, Part A* **2017**, *182*, 136-142.

17. He, A. Q.; Kang, X. Y; Xu, Y. Z.; Noda, I.; Ozaki, Y.; Wu, J. G. Investigation on Intermolecular Interaction between Berberine and β-Cyclodextrin By 2D UV–Vis Asynchronous Spectra. *Spectrochim. Acta, Part A* **2017**, *185*, 343–348.

Table 2-1 Spectral Parameters of P in the Model System when Intermolecular Interaction Occurs between P and Q

Spectral variable	Peak position (cm^{-1})	Bandwidth (cm^{-1})	Absorptivity
P	100	20	1.00
U	99	20	1.00

Table 2-2 The Initial Concentrations of P and Q in the Model System

Index	C_P (mol/ml)	C_Q (mol/ml)
1	1.48	17.4
2	1.47	4.93
3	1.46	2.47
4	1.45	0

Table 2-3 The Pattern Factor and Intensity Factor of the 2D Asynchronous Spectra Generated by Conventional Method and New Method described in this chapter

	$\Psi_{\mathrm{conv}}(x, y)$	$\Psi_{\mathrm{mod}}(x, y)$
Pattern factor	$f_{\mathrm{P}}(x)f_{\mathrm{U}}(y) - f_{\mathrm{U}}(x)f_{\mathrm{P}}(y)$	$f_{\mathrm{P}}(x)f_{\mathrm{U}}(y) - f_{\mathrm{U}}(x)f_{\mathrm{P}}(y)$
Intensity factor	$\left(\vec{\tilde{C}}_{\mathrm{P}}^{\mathrm{init}}\right)^{\mathrm{T}} \mathbf{N}\vec{\tilde{C}}_{\mathrm{U}}^{\mathrm{eq}}$	$\left(\vec{C}_{\mathrm{P}}^{\mathrm{init}}\right)^{\mathrm{T}} \mathbf{N}\vec{C}_{\mathrm{U}}^{\mathrm{eq}}$

Table 2-4 Initial Concentrations of Methanol and THF, which Meet the Requirement of the DAOSD Approach

Index	$C_{methanol}$ ($\times 10^{-4}$ mol/ml)	C_{THF} ($\times 10^{-4}$ mol/ml)
1	2.47	2.47
2	1.98	2.47
3	1.48	2.47

Table 2-5 Concentrations of Methanol and THF in the Group of Solutions

Index	$C_{methanol}$ $(\times 10^{-4} mol/ml)$	C_{THF} $(\times 10^{-4} mol/ml)$
1	2.47	4.93
2	2.47	2.47
3	2.47	0
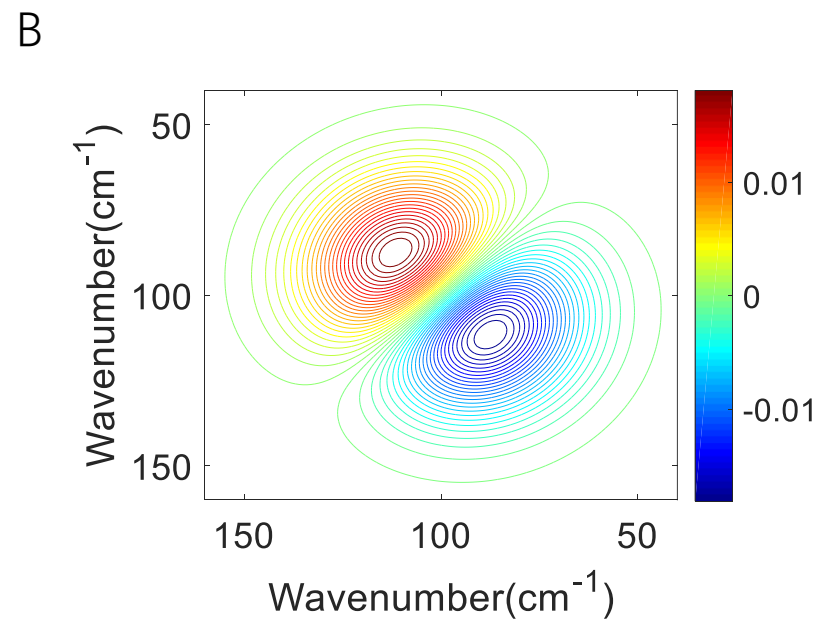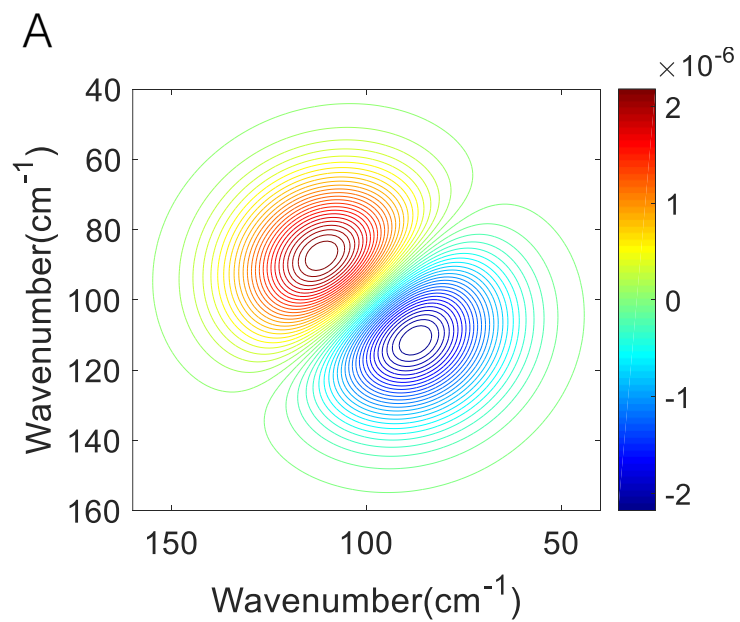
Figure 2-1 2D Asynchronous Spectra of the Model System. The Equilibrium Constant (*K*) of eq. 2-1 is set as 0.01.

A) 2D Asynchronous Spectrum is Generated using the Conventional Method.

B) 2D Asynchronous Spectrum is Generated using the New Method.
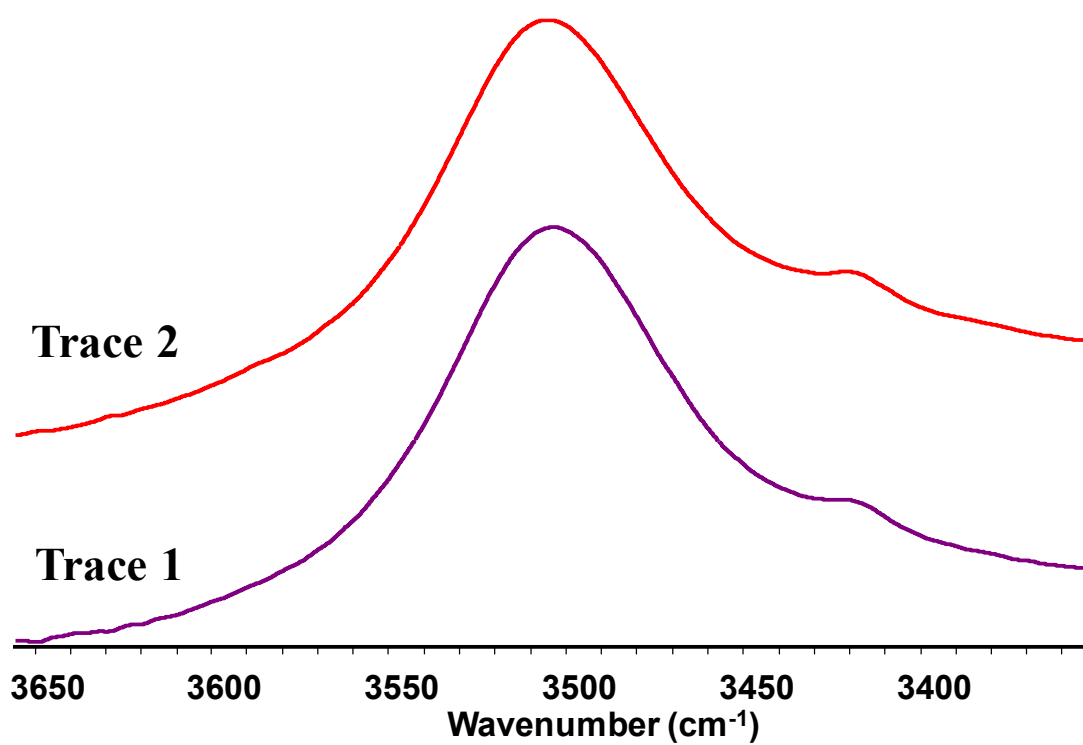
Trace 2

Trace 1

Figure 2-2 FTIR Spectrum of Diethyl Ether Solution Containing both Methanol $(2.47\times10^{-4}$ mol/ml) and THF $(7.40\times10^{-4}$ mol/ml) (Trace 1), FTIR Spectrum of Diethyl Solution Containing Methanol only $(2.4\times10^{-4}$ mol/ml) (Trace 2).
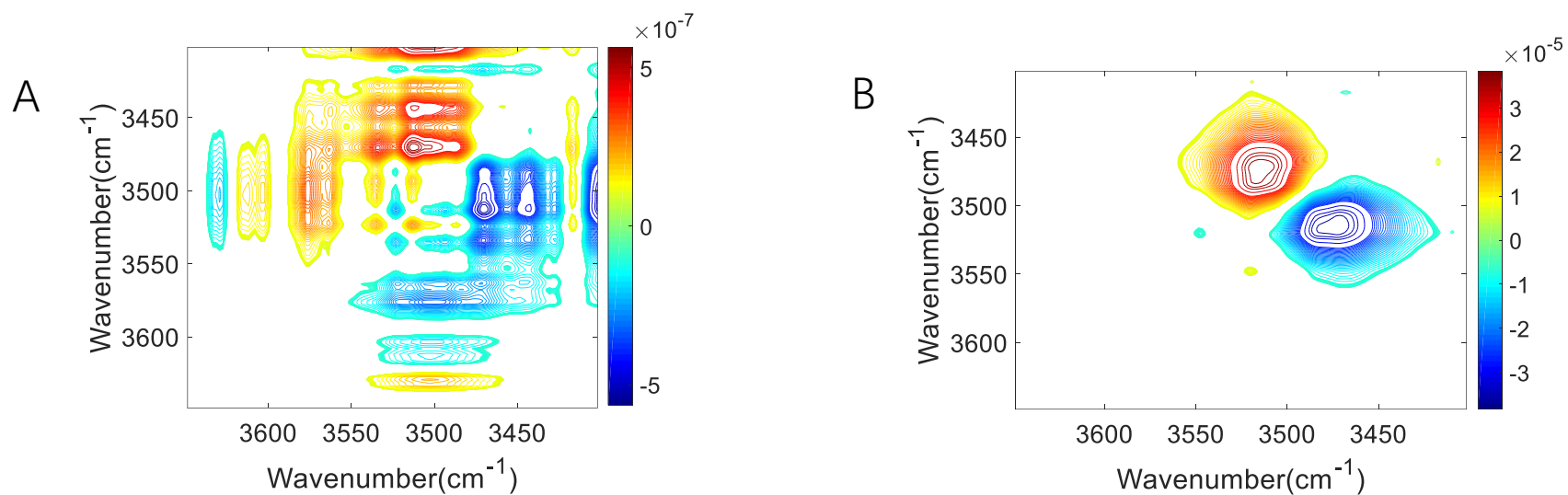
Figure 2-3 2D Asynchronous Spectrum of Methanol /THF/ Diethyl Ether System Generated by using the DAOSD Approach.

A) 2D Asynchronous Spectrum (Ψ_{THF}) is Generated from Three Solutions. The Concentrations of Methanol, THF in the Three Solutions are listed in **Table 2-4**.

B) 2D Asynchronous Spectrum ($\Psi_{methanol}$) using the New Approach is Generated from Three Solutions. The Concentrations of Methanol, THF in the Three Solutions are listed in **Table 2-5**.
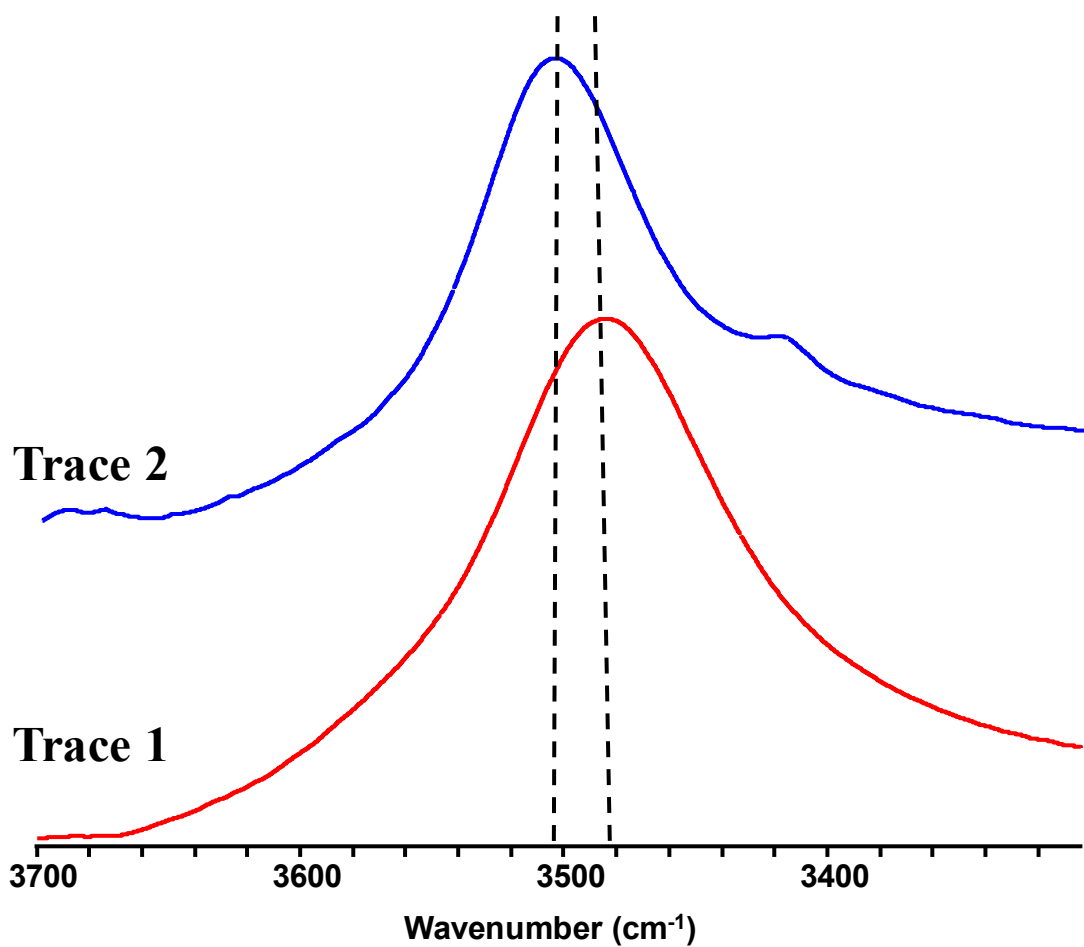
Figure 2-4 FTIR Spectrum of THF Solution Containing Methanol (2.78×10^{-4}mol/ml) (Trace 1); FTIR Spectrum Diethyl Ether Solution Containing Methanol (2.44×10^{-4}mol/ml) (Trace 2).
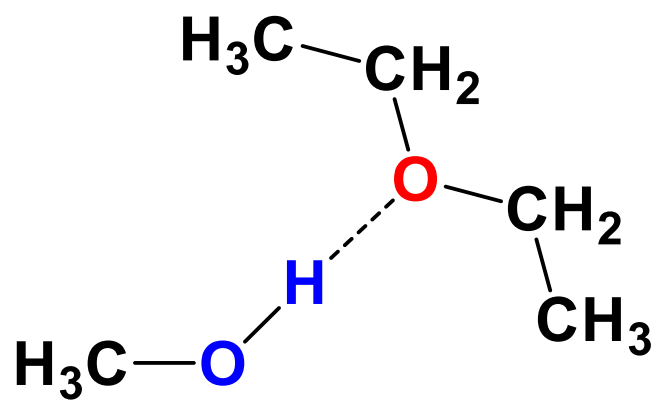
Scheme 2-1 The Methanol-Diethyl Ether Complex via a Hydrogen Bond.
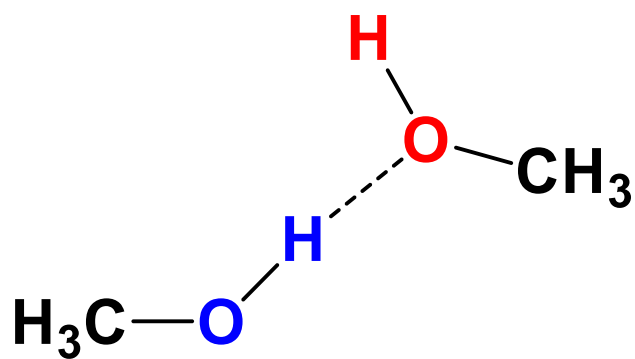
Scheme 2-2 The Methanol Aggregation via Hydrogen Bonding Among Methanol Molecules. The OH Group Marked in Blue Acts as a Hydrogen Bonding Donor; the OH Group Marked in Red Acts as a Hydrogen Bonding Acceptor.
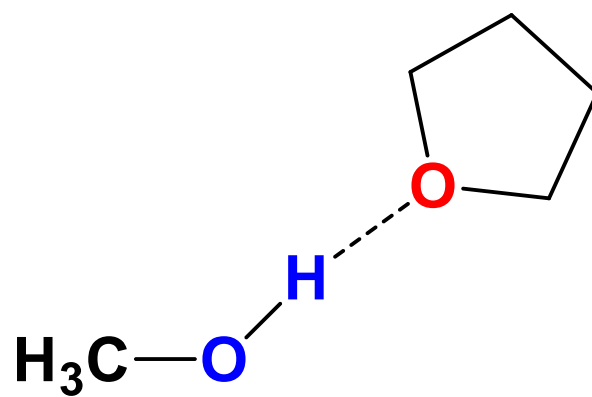
Scheme 2-3 The Methanol-THF Complex via a Hydrogen Bond.

Supporting Information 1

Part 1 FTIR Spectra of Diethyl Ether Solution containing Different Amounts of Methanol

Table S2-1 The Relationship between Molar Ratio of Methanol and OH Stretching Band

Index	$n_{methanol}:n_{diethyl\ ether}$
A	0.014
B	0.021
C	0.026
D	0.034
E	0.0489
F	0.0973
G	0.204
H	0.259
I	0.5770
J	2.321
K	5.109
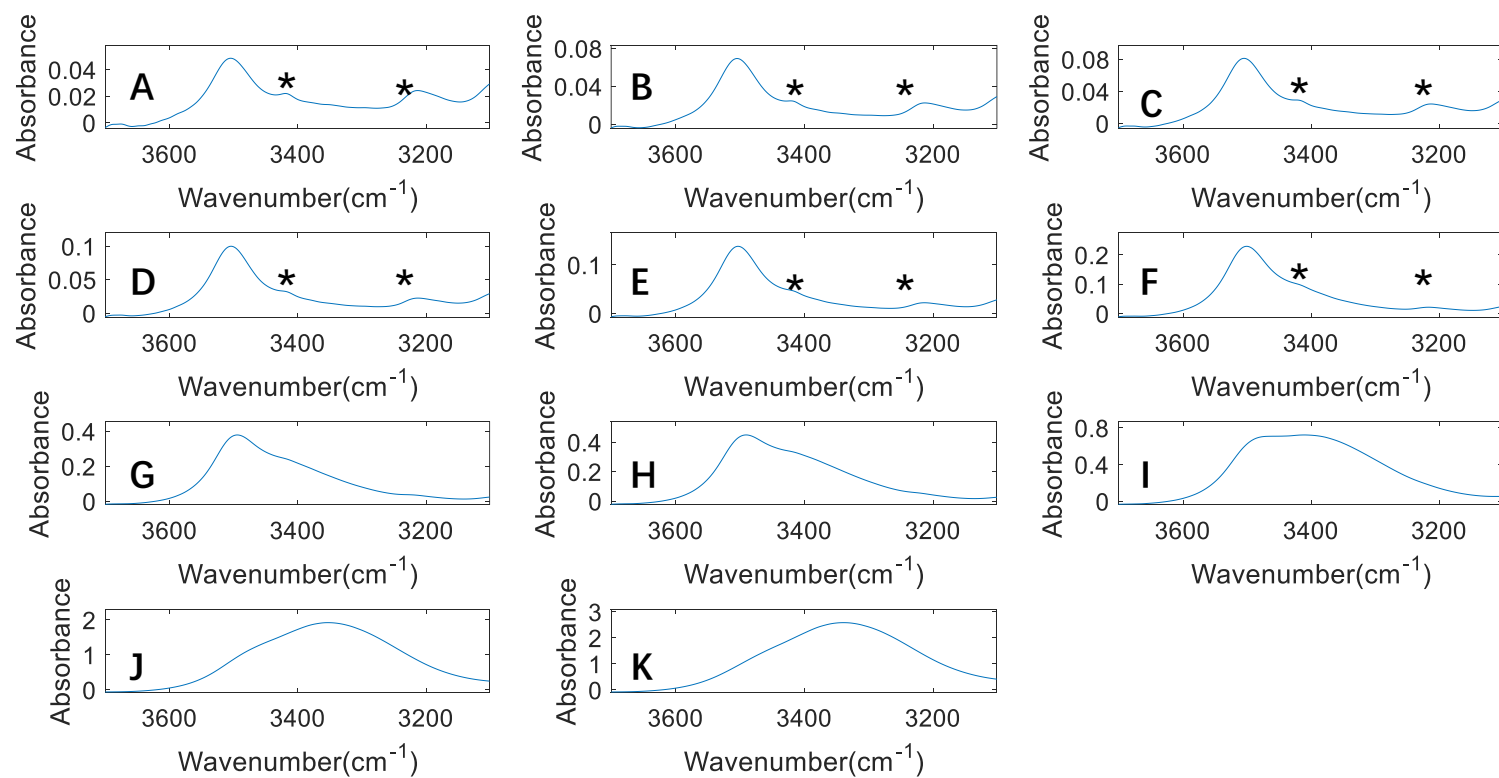
Figure S2-1 FTIR Spectra of Diethyl Ether Solutions Containing Different Amounts of Methanol. The Molar Ratios between Methanol and Diethyl Ether are Listed in **Table S2-1**.

* The peaks marked by * are from the overtone bands of diethyl ether.

Figure S2-2 shows an FTIR spectrum of hexane solution containing methanol(less than 1×10^{-4} mol/ml). The OH stretching band of methanol appears as a sharp single peak around 3654 cm^{-1}. In this case, the concentration of methanol is quite low, and thus methanol exists in a free state and no hydrogen bond is formed among methanol molecules.
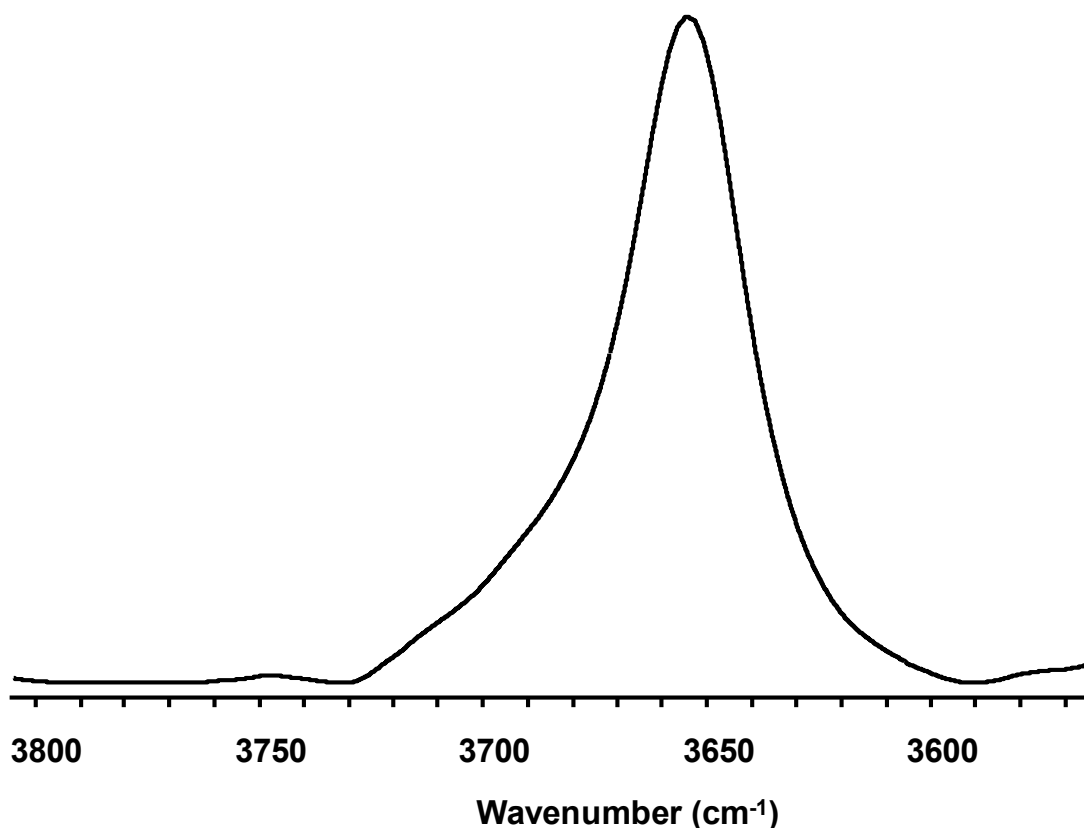
Figure S2-2 An FTIR Spectrum of Methanol in a Hexane Solution (The Concentration of Methanol is less than 1×10^{-4} mol/ml).

From **Figure S2-1**, we learn that: As the concentration of methanol is below 4.61×10^{-4} mol/ml, a single narrow OH stretching peak appear at 3504 cm^{-1}. In comparison with **Figure S2-2**, the OH stretching band of methanol dissolved in diethyl ether (the concentration is below 4.61×10^{-4} mol/ml) undergoes a red shift. That is to say, a hydrogen bond forms on the methanol molecules. Since the concentration of methanol is quite low and the content of diethyl ether is overwhelmingly larger than that of methanol, the OH stretching band around 3504 cm^{-1} can be assigned to the methanol whose OH group acts as a hydrogen bonding donor and form a single hydrogen bond with the oxygen atom so that a methanol-diethyl ether complex is formed (**Scheme 2-1** in the main text).

When the concentration of methanol is below 4.61×10^{-4} mol/ml, increasing the concentration does not bring about changes in the band shape of the OH stretching band. However, the intensities of the OH stretching band at 3504 cm^{-1} increases linearly with

the increment of the concentration of methanol (**Figure S2-3**). This phenomenon demonstrates that the concentration of the aforementioned methanol-diethyl ether increases with the concentration of methanol. Moreover, methanol molecules do not form other form of hydrogen bonding structure.
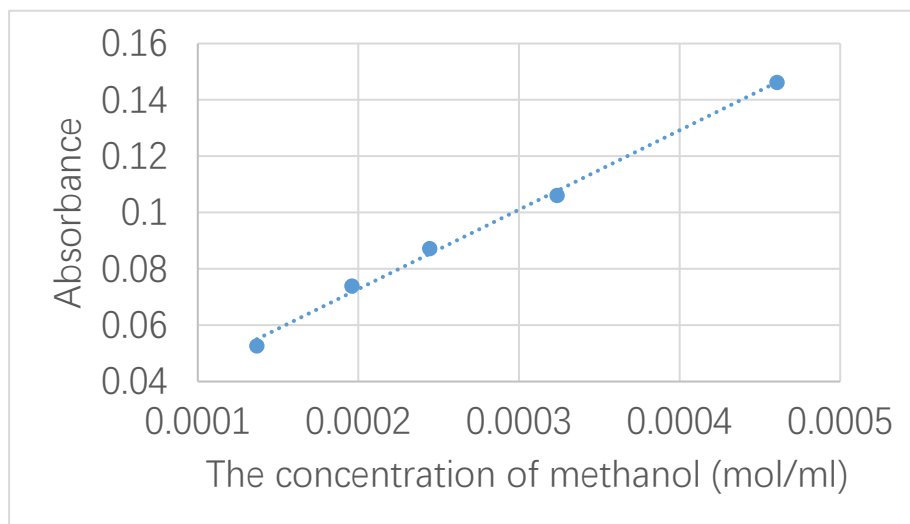
Figure S2-3 Linear Relationship between the Concentrations of Methanol and the Absorbance of the 3504 cm^{-1} Band in the FTIR Spectra.

As the concentration of methanol increases further, the OH stretching band becomes broad and exhibits a red shift. In addition, the intensity of the OH stretching band increases significantly. The reason for this phenomenon is that methanol molecules form dimer, trimer, tetramer and/or multimer via methanol-methanol hydrogen bond shown in **Scheme 2-2** in the main text. The formation of the above complex aggregation via hydrogen bonding among methanol molecules is out of the scope of this work.

In this chapter, we kept the concentration of methanol below 4.61×10^{-4} mol/ml. Under this condition, whether interconversion between methanol-diethyl ether complex (**Scheme 2-2** in the main text) and methanol-THF complex (**Scheme 2-3** in the main text) occur or not is investigated using 2D asynchronous spectra.

Part 2 Discussion on the Intensity Factor is $\left(\vec{\mathbf{C}}_{\mathrm{P}}^{\mathrm{init}}\right)^{\mathrm{T}}\mathbf{N}\vec{\mathbf{C}}_{\mathrm{U}}^{\mathrm{eq}}$

N is the M order Hilbert-Noda matrix as follows

$$\mathbf{N} = \begin{bmatrix} 0 & 1 & \dfrac{1}{2} & \dfrac{1}{3} & \cdots & \dfrac{1}{j-i} \\ -1 & 0 & 1 & \dfrac{1}{2} & \cdots & \cdots \\ -\dfrac{1}{2} & -1 & 0 & 1 & \cdots & \cdots \\ -\dfrac{1}{3} & -\dfrac{1}{2} & -1 & 0 & \cdots & \dfrac{1}{2} \\ \cdots & \cdots & \cdots & \cdots & 0 & 1 \\ -\dfrac{1}{j-i} & \cdots & \cdots & -\dfrac{1}{2} & -1 & 0 \end{bmatrix}_{\mathrm{M}} \tag{S2-1}$$

where $i, j \leq M$

The M order N matrix can be regarded as a summation of M(M-1)/2 sub-matrices $(\mathbf{N}_{i,j})$.

$$\mathbf{N} = \sum_{j=i+1}^{M} \sum_{i=1}^{M-1} \mathbf{N}_{i,j} \tag{S2-2}$$

The sub-matrices can be defined as:

$$\mathbf{N}_{ij} = \frac{1}{\pi} \begin{bmatrix} 0 & \cdots & 0 & \cdots & 0 & \cdots \\ \cdots & 0 & \cdots & \dfrac{1}{j-i} & \cdots & \cdots \\ 0 & \cdots & 0 & \cdots & 0 & \cdots \\ \cdots & -\dfrac{1}{j-i} & \cdots & 0 & \cdots & \cdots \\ 0 & \cdots & 0 & \cdots & 0 & \cdots \\ \cdots & \cdots & \cdots & \cdots & \cdots & 0 \end{bmatrix}_{\mathrm{M}} \tag{S2-3}$$

Intensity factor can be expressed as:

$$\left(\vec{\mathbf{C}}_{\mathrm{P}}^{\mathrm{init}}\right)^{\mathrm{T}}\mathbf{N}\vec{\mathbf{C}}_{\mathrm{U}}^{\mathrm{eq}} = \sum_{j=i+1}^{M} \sum_{i=1}^{M-1} V_{i,j} \tag{S2-4}$$

where:

$$V_{i,j} = \left(\vec{\mathbf{C}}_P^{\text{init}}\right)^{\text{T}} \mathbf{N}_{ij} \vec{\mathbf{C}}_U^{\text{eq}} = \begin{bmatrix} C_P^{1(\text{init})} & \cdots & C_P^{i(\text{init})} & \cdots & C_P^{j(\text{init})} & \cdots & C_P^{M(\text{init})} \end{bmatrix} \begin{bmatrix} 0 & \cdots & 0 & \cdots & 0 & \cdots \\ \cdots & 0 & \cdots & \dfrac{1}{j-i} & \cdots & \cdots \\ 0 & \cdots & 0 & \cdots & 0 & \cdots \\ \cdots & -\dfrac{1}{j-i} & \cdots & 0 & \cdots & \cdots \\ 0 & \cdots & 0 & \cdots & 0 & \cdots \\ \cdots & \cdots & \cdots & \cdots & \cdots & 0 \end{bmatrix}_M \begin{bmatrix} C_U^{1(\text{eq})} \\ \cdots \\ C_U^{i(\text{eq})} \\ \cdots \\ C_U^{j(\text{eq})} \\ \cdots \\ C_U^{M(\text{eq})} \end{bmatrix}$$

$$= \frac{1}{j-i}\left(C_P^{i(\text{init})} C_U^{j(\text{eq})} - C_U^{i(\text{eq})} C_P^{j(\text{init})}\right)$$

(S2-5)

As shown in **Table 2-5** in the main text, the initial concentration of P is constant. Thus, eq. S2-5 can be simplified as

$$V_{i,j} = \frac{C_P^{init}}{j-i}\left(C_U^{j(eq)} - C_U^{i(eq)}\right) \tag{S2-6}$$

In addition, the initial concentration of Q decreases with the increment of i.

Namely, $C_Q^{i(init)} > C_Q^{j(init)}$, when $i<j$.

Moreover, the initial concentration of P is constant. For the equilibrium reaction

shown in eq. 2-1 in the main text, we have: $C_U^{i(eq)} > C_U^{j(eq)}$, when $i<j$.

Thus, we have $V_{i,j}<0$. Since every $V_{i,j}$ is negative, the summation of all the $V_{i,j}$ terms are negative. Therefore, we come to the following conclusion: although we do not know the exact values of equilibrium concentration of U, the sign of the intensity

factor $\left(\left(\vec{C}_P^{init}\right)^T N \vec{C}_U^{eq}\right)$ is always negative when the initial concentrations of P and Q are

adopted as in **Table 2-5** in the main text.

Part 3 The Second Derivative Spectra in the OH Stretching Band of Diethyl Solutions Containing Methanol only and Methanol/THF
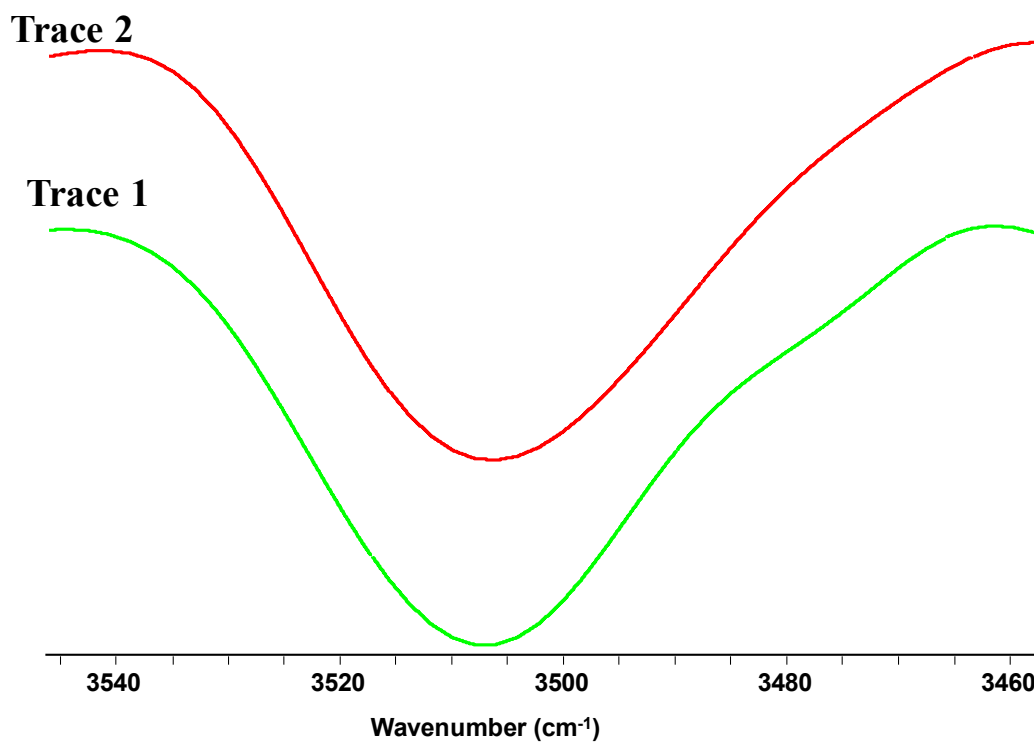
Figure S2-4 Second Derivative Spectrum of
Trace 1: The OH Stretching Band of Diethyl Ether Solution Containing Methanol $(2.47 \times 10^{-4}$ mol/ml)
Trace 2: The OH Streching Band of Diethyl Ether Solution Containing Methanol $(2.47 \times 10^{-4}$ mol/ml) and THF $(7.40 \times 10^{-4}$ mol/ml)

Part 4 The Relationship between the Patterns of Cross Peak in 2D Asynchronous Spectrum and Possible Changes of the Peak Parameters of the Characteristic Peak of U.

To explore what happens on the OH stretching band when the methanol-THF complexes is formed. We performed a computer simulate on a model system. Herein P stands for the OH stretching band of methanol-diethyl ether complex and U stands for the OH stretching band of the methanol-THF complex. Since the pattern of cross peaks around cannot be used to reflect the changes on the changes of the absorptivity of the band, the absorptivity of the peak of band U are all set the same as P. The qualitative difference on peak position, bandwidth can be classified into nine situations shown in **Table S2-2**.

Table S2-2 Nine Possible Situations Concerning the Changes on Peak Position and Bandwidth of the 100 cm^{-1} Band. The Peak Position and Bandwidth of P are 100 cm^{-1} and 20 cm^{-1}, respectively.

Model systems	Peak position (cm^{-1})	Bandwidth (cm^{-1})
1	99	19
2	99	20
3	99	21
4	100	19
5	100	20
6	100	21
7	101	19
8	101	20
9	101	21

The corresponding cross peak of pattern factor is shown in **Figure S2-3**. The pattern of **Figure 2-3B** in the main text is the same as **Situation System 2** in **Figure S2-5**. That is to say, the bandwidth of the OH stretching band of the methanol-THF complex is almost the same as that of the methanol-diethyl ether. Moreover, the OH stretching band of the methanol-THF complex exhibits a red shift in comparison with that of the methanol-diethyl complex.
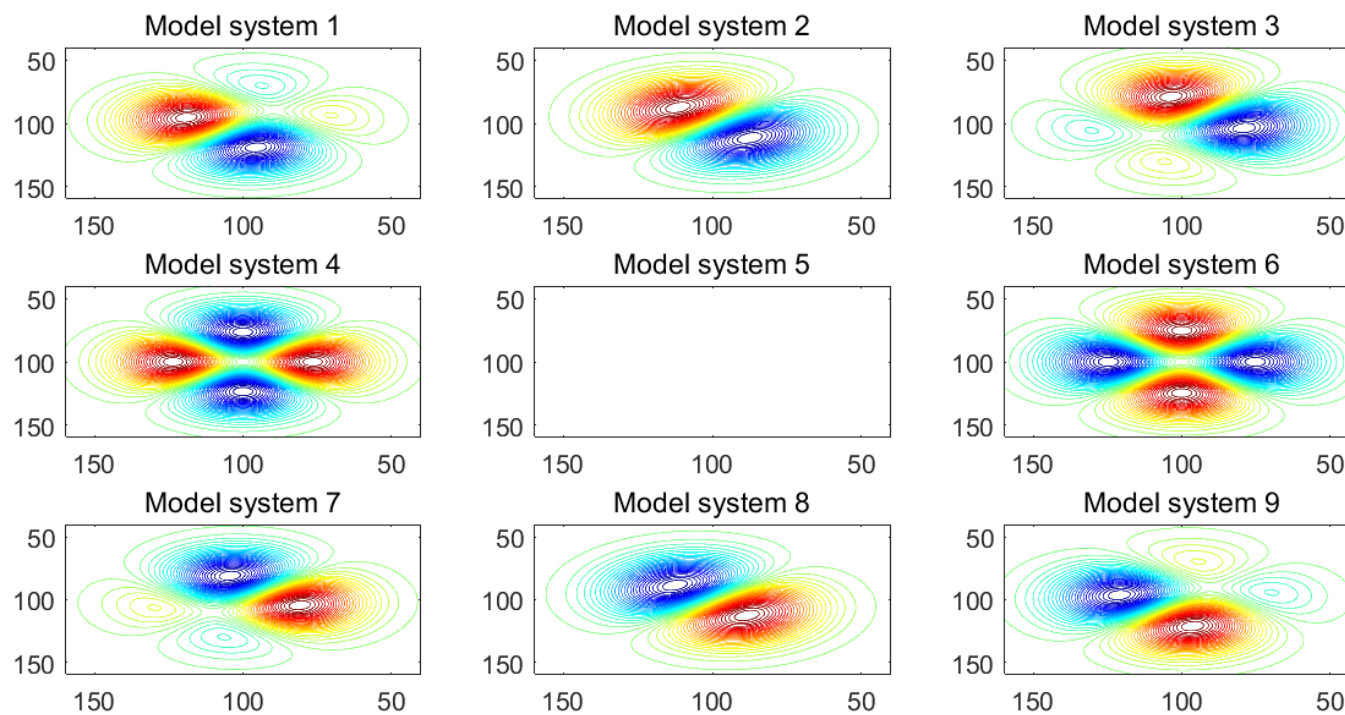
Figure S2-5 Cross Peaks Around (100, 100) in Ψ(*x*, *y*) of the Nine Model Systems, the Peak Parameter of U can be found in **Table S2-2.**

Chapter 2

Investigation on the Behavior of Noise in Asynchronous Spectra in Generalized Two-Dimensional (2D) Correlation Spectroscopy and Application of Butterworth filter in the Improvement of Signal-to-Noise ratio of 2D Asynchronous Spectra

Significance of reduction of noise

In the measurement of 1D spectra are used to construct 2D correlation spectra, there is always some amount of unpredictable noise. [1] The noise may arise from instrumental and environmental fluctuations, electrical signal contamination, truncation and other effects in digital processing, etc. Upon generation of 2D correlation spectra, the presence of such noise might bring about severe interference on the resultant 2D spectra. Thus, something should be done to extract useful information from 2D spectra, especially with heavily noisy background.

In the field of 2D correlation spectroscopy, several approaches have been implemented to improve the signal-to-noise ratio. [2-9] Smoothing on the original spectra has been extensively employed. In some cases, however, subtle spectral feature might be lost after smoothing process. Berry and Ozaki have demonstrated that denoising using a wavelets approach is superior to the conventional smoothing method. [2] Wu and co-workers have developed quadrature approaches, which have been proved to be quite effective in the suppression of noise. Additionally, reconstruction of the data based on principal component analysis with eigenvector manipulation is another promising approach in the improvement of signal-to-noise ratio of 2D correlation spectra. [9]

In OSD and related techniques, the occurrence of cross peaks in 2D spectra can be used as an unambiguous evidence of the existence of an intermolecular interaction. However, the cost of orthogonal sample design scheme and relevant techniques is that the intensity of cross peaks is significantly attenuated. As a consequent, the problem of noise becomes a challenge to interpreting resultant 2D spectra. To address the problem, we have proposed improvement of the quality of 2D asynchronous spectra by changing the sequence of 1D spectra. In addition, we use a modified reference spectrum in the generation of 2D asynchronous spectrum based on the AOSD approach. The above approaches may increase the absolute intensities of cross peaks in the resultant 2D correlation spectra by more than 100 times in some cases. As a result, the signal-to-noise ratio can be improved to some extent. [4-5] In our further work, the above approaches are indeed effective in improving the quality of the obtained 2D spectra. [4-5, 10-11] However, noise in 2D spectra can be magnified by accompanying signals in the cross peaks region of 2D spectra. As a consequence, it still becomes difficult to observe cross peaks that reflect intermolecular interaction when noise is severe in the original 1D spectra. Thus, something should be done to improve the quality of 2D spectra via an approach of effectively suppressing noise. There are many approaches to enhance the signal-to-noise ratio of 2D correlation spectra reported in the literature using noise suppressing methods. [2-9] However, the noise attenuation approaches may also bring about some signal distortion to the treated spectra. Uncontrolled signal distortion may produce artifactual interference in the resultant 2D spectra, which may result in misleading conclusions. Therefore, a useful approach on improvement of the quality of 2D spectra should satisfy the following requirements: The approach must effectively reduce the fluctuation of noise; on other hand, it should not bring about severe signal distortion on the treated spectra.

In the present study, we adopt a Butterworth filter, [12-14] which is extensively used

in the field of signal processing, [15-19] to improve the quality of 2D correlation spectra. The reason why we adopt this approach is that the Butterworth filter is a linear operator. Hence the effect of noise suppression and signal distortion produced by the Butterworth filter can be independently investigated and controlled. Herein, mathematical analysis on the statistic property of noise in 2D asynchronous spectrum and computer simulation on a model system are carried out to show the effectiveness of the Butterworth filter approach. Moreover, we apply the Butterworth filter on a real chemical system with added artificial noise. Experimental results demonstrate that the Butterworth filter is useful in the reduction of noise in real chemical systems.

Methods

In the investigation of the model system, all the simulated spectra were generated via a program written in our lab using Matlab software (Mathworks, Inc.). Two-dimensional correlation spectra were constructed based on the algorithm developed by Noda via Matlab software.

Results and Discussion

1 Description of the Model System

We establish a model system to study the behavior on the improvement of the quality of 2D asynchronous spectrum by a Butterworth filtering approach. The model chemical system is composed of six solutions containing two solutes (P and Q). In the spectral region investigated, the solvent has no absorption band. Under the intermolecular interaction between P and Q, a small fraction of P undergoes a subtle structural variation and converts into another form of solute denoted as U. Similarly, a part of Q changes into V. The interconversion caused by the intermolecular interaction can be modeled by a chemical reaction shown in eq. 3-1. The strength of the intermolecular interaction can be characterized by the equilibrium constant K that is set as 0.01 in this article.

$$P+Q \overset{K}{\leftrightarrow} U+V \qquad (3-1)$$

In the system, we assume that the characteristic peaks of P/U and Q/V are not overlapped, and thus we focus on the spectral region where only P and U possess absorptive peaks. The description of the spectral functions of P and U in detail can be found in the first part of the Supporting Information.

To construct a 2D asynchronous spectrum of the system, the spectra of six solution samples containing different amounts of P and Q are simulated. The initial concentrations of P and Q of the six sample solutions are listed in **Table 3-1**. The simulated 1D spectra are shown in **Figure 3-1A**. Based on the six 1D spectra, a 2D asynchronous spectrum is generated and is shown in **Figure 3-1B**.

Two independent cross peaks are observed around (283, 306), and (306, 330).

Another two cross peaks at (306, 283) and (330 306) are antisymmetric to the two cross peaks at (283, 306) and (306, 330) with respect to the diagonal. The pattern of cross peaks demonstrates that both peak position and bandwidth of the peak of the characteristic P and U are different. The cross peaks at (283, 306) and (330 306) are negative, indicating that the bandwidth of P is larger than that of U. Moreover, the intensity of cross peaks around (283, 306) is larger than that of cross peak at (330 306), demonstrating that the peak position of the characteristic peak of P is smaller than that of U. The above conclusions deduced from the pattern of cross peak are in accordance with the peak parameters listed in **Table S3-1** (please see the Supporting Information).

Then, noise is introduced into each 1D spectrum. The fluctuation of the noise is 1% of the maximum intensity of the each 1D spectrum. The simulated 1D spectra of the six samples are shown in **Figure 3-2A,** and the corresponding 2D asynchronous spectrum is shown in **Figure 3-2B**. In this model system, intermolecular interaction is not very strong (the corresponding K value is only 0.01). Consequently, the resultant cross peaks in the 2D asynchronous spectrum are not very strong. In this case, even noise whose fluctuation is not quite large can bring about a destructive effect. As shown in **Figure 3-2B**, all cross peaks are completely masked by the noise. This situation is different from denoise work reported in the literature. For example, the patterns of cross peaks are still observable even if the fluctuation of noise amounted to 5% (**Figure 7** of ref 2).

2 Analysis on the Behavior of Noise in a 2D Asynchronous Spectrum

To understand the influence of noise on a 2D asynchronous spectrum, mathematical analysis on noise in a 2D asynchronous spectrum is performed. First noise is introduced into a 1D spectrum, and the expression of the corresponding 2D asynchronous spectrum is listed in eq. 3-2. The details on how eq. 3-2 is obtained can be found in the second part of the **Supporting Information**.

$$\Psi(x, y) = \Psi_{signal}(x, y) + \Psi_{noise}(x, y) \tag{3-2}$$

As shown in eq. 3-2, $\Psi(x, y)$ can be classified into two parts; the first part is a signal part ($\Psi_{signal}(x, y)$), and the second part is a noise part ($\Psi_{noise}(x, y)$).

$$\Psi_{signal}(x, y) = \left(f_P(x)f_U(y) - f_U(x)f_P(y)\right) \left(\vec{\bar{C}}_P^{init}\right)^T N \vec{\bar{C}}_U^{eq} \tag{3-3A}$$

$$\Psi_{noise}(x, y) = \left(f_P(x) - f_P(y)\right)\left(\vec{\bar{C}}_P^{init}\right)^T N \left(\vec{\gamma}(y)\right) + \left(f_U(x) - f_P(x)\right.$$
$$\left. - f_U(y) + f_P(y)\right)\left(\vec{\bar{C}}_U^{eq}\right)^T N \left(\vec{\gamma}(y)\right) + \left(\vec{\gamma}(x)\right)^T N\left(\vec{\gamma}(y)\right) \tag{3-3B}$$

Figure 3-3A and **Figure 3-3B** depict $\Psi_{signal}(x, y)$ and $\Psi_{noise}(x, y)$, respectively. **Figure 3-3A** is actually the same as **Figure 3-1B**. For comparison, we select a 1D spectrum with the weakest intensity among the six spectra shown in **Figure 3-2A**. The signal part and noise part of the spectrum are shown in **Figure 3-3C** and **Figure 3-3D**, respectively. The absolute intensity of the strongest cross peak of $\Psi_{signal}(x, y)$ in **Figure 3-3A** is 2.077×10^{-3}. The intensity of the absorption peak of the 1D spectrum, which is the weakest among the six 1D spectra used to a generated 2D asynchronous spectrum, is 1.10. The intensity of signal in the 2D asynchronous spectrum is remarkably attenuated in comparison with the corresponding 1D spectrum. On the other hand, the

amplitude of noise in the 1D spectrum in **Figure 3-3D** is 5.5×10^{-3}. However, the maximum amplitude of noise in $\Psi_{noise}(x, y)$ is 5.27×10^{-2}. Thus, the noise part in the 2D asynchronous spectrum is significantly magnified compared with that of the 1D spectrum. Consequently, the attenuation of the signal part and magnification of the noise part in the 2D asynchronous spectrum deteriorate the quality of the resultant 2D asynchronous spectra. This is the reason why the cross peaks are completely masked by noise.

As shown in **Figure 3-3D**, the fluctuation level of noise is the same in every frequency in the 1D spectrum. However, the situation is dramatically different when we inspect the distribution of noise in the 2D asynchronous spectrum depicted in **Figure 3-3B**.

To describe the distribution behavior of noise, we first define the whole spectrum region in 1D spectrum as Ω. As shown in **Figure 3-1A**, Ω is composed of peak region (ν_1) and background region (ν_2). The definitions of ν_1 and ν_2 are given below:

$$\nu_1 = \{x \mid X_P - 4W_P \leq x \leq X_P - 4W_P \text{ or } X_U - 4W_U \leq x \leq X_U - 4W_U \}$$
$$\nu_2 = \{x \mid x \in \Omega \text{ and } x \notin \omega_1\}$$
$$\nu_1 \cup \nu_2 = \Omega \tag{3-4}$$
$$\nu_1 \cap \nu_2 = \varnothing$$

where $\varnothing$ is an empty set.

The corresponding spectral region of a 2D asynchronous spectrum ($\Omega \otimes \Omega$) can be classified into four regions.

Region I: For every point $[(x, y)]$ in Region I, we have $(x, y) \in \nu_1 \otimes \nu_1$. The shape of Region I is a square. As shown in **Figure 3-3B**, the fluctuation of noise is very large in this region.

Region II: For every point $[(x, y)]$ in Region II, we have $(x, y) \in \nu_2 \otimes \nu_1$. As shown in **Figure 3-3B**, Region II is composed of two disconnected rectangle subregions along the x axis. The fluctuation level of noise is significant but weaker than that of Region I. The noise in this region forms two horizontal ridges.

Region III: For every point $[(x, y)]$ in Region III, we have $(x, y) \in \nu_1 \otimes \nu_2$. As shown in **Figure 3-3B**, Region III is composed of two disconnected rectangle subregions. The fluctuation of noise is roughly the same as that of Region II. The noise in this region forms two vertical ridges.

Region IV: For every point $[(x, y)]$ in Region IV, we have $(x, y) \in \nu_2 \otimes \nu_2$. As shown in **Figure 3-3B**, Region IV is composed of four disconnected rectangle subregions. The fluctuation of noise is much weaker than those of Region I, Region II, and Region III.

Then, we calculate the expectation of noise of $\Psi_{noise}(x, y)$ ($E(\Psi_{noise}(x, y))$) and the standard deviation (STD) of $\Psi_{noise}(x, y)$ ($\sigma(\Psi_{noise}(x, y))$). The details of calculation can be found in the third part of the Supporting Information. The results indicate that $E(\Psi_{noise}(x, y))$ is always zero. Thus, $E(\Psi_{noise}(x, y))$ cannot be used to reflect the fluctuation level of noise in a 2D asynchronous spectrum. However, $\sigma(\Psi_{noise}(x, y))$ turns out to be nonzero.

To test whether $\sigma(\Psi_{noise}(x, y))$ can be used as a suitable index to reflect the fluctuation level of $\Psi_{noise}(x, y)$, a computer simulation is performed. In the simulation, 20000 groups of the 1D spectrum are generated. Each group is composed of six 1D

spectra. Each 1D spectrum is constructed according to eq. S3-8. $f_P(x)$ and $f_U(x)$ are calculated via eq. S3-1, and peak parameters used in eq. S3-1 are listed in **Table S3-1**.

The initial concentrations of P and Q used are listed in **Table 3-1,** and $C_U^{i(eq)}$ and $C_V^{i(eq)}$ are calculated via eq. 3-1. For each 1D spectrum, noise ($\gamma(x)$), whose fluctuation is 1% of the maximum intensity of the group 1D spectra, is independently simulated. One 2D asynchronous spectrum is constructed from every group of 1D spectra. Thus, 20000 2D asynchronous spectra ($\Psi(x, y)$) are generated. Then, $\Psi_{noise}(x, y)$ is extracted from each $\Psi(x, y)$. Afterward, the standard deviation of $\Psi_{noise}(x, y)$ is calculated and plotted in **Figure 3-4**.

After comparing $\Psi_{noise}(x, y)$ shown in **Figure 3-3B** with $\sigma(\Psi_{noise}(x, y))$ illustrated in **Figure 3-4**, we find that the level of noise fluctuation in $\Psi_{noise}(x, y)$ is roughly the same as that of $\sigma(\Psi_{noise}(x, y))$. Thus, $\sigma(\Psi_{noise}(x, y)$ is used to characterize the behavior of noise in a 2D asynchronous spectrum.

Based on the definition of ν_1 and ν_2, the expression of $\sigma(\Psi_{noise}(x, y))$ in Region I, Region II, Region III, and Region IV can be further simplified. The detail of analysis can be found in the third part of the Supporting Information, and the results are summarized in **Table 3-2**.

According to the results listed in **Table 3-2**, we learn that:

In the background region of a 2D asynchronous spectrum ($x \in \nu_2$ and $y \in \nu_2$), the noise level is quite low.

When $x \in \nu_1$ or $y \in \nu_1$, the fluctuation of noise is significantly enhanced. Thus, the noise in 2D asynchronous spectrum is actually magnified by cross peaks. This is the reason why the signal-to-noise level in 2D asynchronous spectrum is deteriorated when 2D asynchronous spectrum is constructed. Therefore, something should be done to suppress the noise level to improve the quality of 2D asynchronous spectrum.

We notice from eq. S3-29 that $\sigma[\Psi_{noise}(x, y)]$ is proportional to the standard deviation of noise of 1D spectrum ($\sigma[\gamma]$). Hence, reduction of the STD of noise of 1D spectrum is an effective way to improve the quality of 2D asynchronous spectra. A Butterworth filter may provide a feasible way to decrease the STD value of 1D spectrum. Herein, we develop an approach to use the Butterworth filter to improve the quality of 2D asynchronous spectrum.

The detailed description of the Butterworth filter can be found in the literature. [12-14] Herein we provide a brief introduction of the Butterworth filter. Any given 1D function can be regarded as the summation of sinusoidal components of different frequencies. Filtering is a process to change the relative contribution of different sinusoidal components in the function. Butterworth filter is a frequency selective filter, which is designed to selectively pass some frequencies without distortion and significantly attenuate or eliminate others. We already know that the actual signal only contains low frequencies (**Figure 3-3C**), while the noise component contains high frequencies (**Figure 3-3D**). Hence, we designed it as a low-pass filter. That is to say, Butterworth filter preserves sinusoidal components of the low frequencies and attenuates or rejects components of higher frequencies.

In this article, the Butterworth filter is designated as an operator $\widehat{\mathbf{B}}_{n,\omega}$, where n and ω are number of pole and cutting off frequency, respectively. Both n and ω are important parameters of a Butterworth filtering operator ($\widehat{\mathbf{B}}_{n,\omega}$). Treatment of a spectrum function (A(x), where x is spectral variable) by the Butterworth filter can be expressed as $\widehat{\mathbf{B}}_{n,\omega}A(x)$. First, we present a typical example on the application of the Butterworth filter. **Figure 3-5A** shows a noise whose fluctuation and standard deviation are $-5 \times 10^{-3} \sim 5 \times 10^{-3}$ and 2.8×10^{-3}, respectively Then a Butterworth filter whose n and ω values are 3 and 0.1, respectively is applied on the noise. The outcome is shown in **Figure 3-5B**. The fluctuation level of noise is significantly reduced and the standard deviation of noise is 7.51×10^{-4}. This result indicates that σ[γ] can be significantly reduced by a Butterworth filter (the reduction factor is 3.73 in this case).

The effect on the reduction of the standard deviation of noise by the Butterworth filter is also related to the selection on the number of poles and cutting off frequency of the filter. Herein a noise, whose fluctuation and standard deviation are $-0.015 \sim 0.015$ and 8.7×10^{-3}, respectively, is subjected to the Butterworth filter with different number of poles and cutting off frequency. **Figure 3-6** illustrates the variation of σ[γ] of the treated noise by a Butterworth filter whose cutting off frequency numbers of poles are variable. The results indicate that the value of σ[γ] decreases with decreasing of the cutting off frequency when the number of poles ranges from 1 to 6. Thus, decreasing the cutting off frequency is a very effective way in the reduction of the standard deviation of noise.

When a Butterworth filter is used to treat a 1D spectrum, the standard deviation of noise can be reduced. However, the treatment of the Butterworth filter may also bring about distortion on the signal part of the 1D spectrum. Uncontrolled distortion may produce interference cross peak and result in misleading outcome in the investigation. Thus, additional consideration is required to address the problem of signal distortion. For any give 1D spectrum A(x), where x is spectral variable, A(x) is composed of two parts as shown in eq. 3-5.

$$A(x)=S(x)+ \gamma(x) \tag{3-5}$$

where S(x) is the signal part of the spectrum and $\varepsilon(x)$ is the noise part of the spectrum.

When the Butterworth filter is applied to the spectrum, we have

$$\widehat{\mathbf{B}}_{n,\omega}A(x) = \widehat{\mathbf{B}}_{n,\omega}\big(S(x) + \gamma(x)\big) \tag{3-6}$$

Since the Butterworth filter is a linear operator (eq. 3-7).

$$\widehat{\mathbf{B}}_{n,\omega}(\alpha A_1(x) + \beta A_2(x)) = \alpha\widehat{\mathbf{B}}_{n,\omega}A_1(x) + \beta\widehat{\mathbf{B}}_{n,\omega}A_2(x) \tag{3-7}$$

Equation 4-6 can be expressed as

$$\widehat{\mathbf{B}}_{n,\omega}A(x) = \widehat{\mathbf{B}}_{n,\omega}S(x) + \widehat{\mathbf{B}}_{n,\omega}\gamma(x) \tag{3-8}$$

Thus, the outcome of the treatment of a spectrum by the Butterworth filter is composed of two parts. The first part is the result of the treatment of the Butterworth

filter on the signal part of spectrum and the second part is the result of the treatment of the Butterworth filter on the noise of spectrum. When $\hat{\mathbf{B}}_{n,\omega} S(x)$ is not equal to $S(x)$, distortion on the signal part by the Butterworth filter is produced. The distortion can be expressed as eq. 3-9.

$$\Delta(x) = \hat{\mathbf{B}}_{n,\omega} S(x) - S(x) \tag{3-9}$$

Figure 3-7 provides an example of distortion caused by a Butterworth filter. The original spectrum is a Gaussian peak whose peak position, bandwidth, and absorptivity are 300 nm, 20.0 nm, and 1.0, respectively(trace 1). When a Butterworth filter (the number of poles and cutting off frequency of the filter are 3 and 0.001, respectively) is applied to the signal, the results are shown as trace 2 in **Figure 3-7**. The distortion of the signal produced according to eq. 3-8 is illustrated as trace 3 in **Figure 3-7**.
When we use a Butterworth filter to treat the signal part of a 1D spectrum described by eq. S3-2, the expression of signal distortion can be expressed as eq. 3-10.

$$\begin{aligned}\Delta(x) = C_P^{i(\text{init})} \left(\hat{\mathbf{B}}_{n,\omega} f_P(x) - f_P(x) \right) \\ + C_U^{i(\text{eq})} \left(\hat{\mathbf{B}}_{n,\omega} \big(f_U(x) - f_P(x) \big) - \big(f_U(x) - f_P(x) \big) \right)\end{aligned} \tag{4-10}$$

Since $C_P^{i(\text{init})} \gg C_U^{i(\text{eq})}$, eq. 3-10 can be simplified as eq. 3-11

$$\Delta(x) = C_P^{i(\text{init})} \big(\hat{\mathbf{B}}_{n,\omega} f_P(x) - f_P(x) \big) \tag{4-11}$$

Because $f_P(x)$ is a Gaussian function, the signal distortion can be estimated from the Butterworth treatment on a Gaussian peak.

When a Gaussian peak is subjected to a Butterworth filter with fixed values of n and ω (for example, $n=3$ and $\omega=0.005$), the influence of peak parameter (peak position, bandwidth, and absorptivity) on the value of $\Delta(x)$ is estimated as discussed below. Herein we use the maximum value of $\Delta(x)$ to reflect the level of signal distortion. The maximum of the absolute value of $\Delta(x)$ is denoted as $\Delta_{\max}$. As shown in **Figure 3-8A**, variation on the peak position of a Gaussian peak does not have any influence on the value of $\Delta_{\max}$.

Then we consider the influence of absorptivity on the value of $\Delta_{\max}$. Since the Butterworth operator is a linear operator, we have

$$\Delta(x) = \gamma_P C_P^{i(\text{init})} \big(\hat{\mathbf{B}}_{n,\omega} e^{-(\ln2)*\left[\frac{(X-X_P)^2}{W_P^2}\right]} - e^{-(\ln2)*\left[\frac{(X-X_P)^2}{W_P^2}\right]} \big) \tag{3-12}$$

That is to say, $\Delta_{\max}$ is proportion to the absorptivity (**Figure 3-8B**).

Finally, we investigate that influence of bandwidth of the Gaussian peak on the signal distortion. The results are illustrated in **Figure 3-8C**. The results indicate that the profile of the distortion varies with the bandwidth of the peak.

On the other hand, the signal distortion for a given spectral function is also related to the parameters of the Butterworth filter (number of pole, cutoff frequency). We use a Gaussian peak as an example, whose peak position, bandwidth, and absorptivity are 300 nm, 20.0 nm and 1.0, respectively.

Figure 3-9 depicts the variation of Δ_{max} as a function of the cutoff frequency for different values of n of the Butterworth filter. No matter what *n* value is selected, the value of Δ_{max} increases with decrease of the cut-off frequency. Similar results are obtained for other spectra of the model system (data are not shown).

When we combine the results shown in **Figure 3-6** and **Figure 3-9** together, we found the following fact. As the cutoff frequency of the Butterworth filter decreases, the standard deviation of noise decreases while the value of Δ_{max} increases. The result is always true no matter what n value is selected. In the article, we propose a strategy that can take account of decreasing the standard deviation of noise and restriction of signal distortion together. Our strategy is to find suitable cutoff frequency of the Butterworth filter to make the value of Δ_{max} be below the standard deviation of noise. In this way, the signal distortion is buried by the treated noise, thereby avoiding the risk of being misleading results from signal distortion. In practice, the n value is fixed first. Then, both the standard deviation and the value of the distortion are drawn against the cutoff frequency so that the cross-section between the curves of the standard deviation-cutoff frequency and the curve of distortion-cutoff frequency is obtained. The cutoff frequency corresponding to the cross section is regarded as the optimized cutoff frequency for the Butterworth filter. Then we change the n values to acquire six optimized cutting off frequencies (**Figure 3-10**). Afterward, the optimized n value is selected from the six cross peak with lowest cutting off frequency.

We apply this approach on the model system mention in this article. For each 1D spectrum with noise, a Butterworth filter with optimized value of n and cutoff frequency is determined and then the spectrum is subjected to the treatment of the Butterworth filter. The obtained treated spectra are used to construct 2D asynchronous spectrum. The results are shown in **Figure 3-11**. In comparison with **Figure 3-2B**, noise in the 2D asynchronous spectrum is significantly reduced. As a result, cross peaks that are masked by the noise can be revealed. When we compare the treated 2D asynchronous spectrum in **Figure 3-11** with the 2D asynchronous spectrum of the system without noise (**Figure 3-1B**), we find that the patterns of cross peaks are faithfully regenerated. To quantitatively evaluate denoising effect of the Butterworth filter, we adopt the Carbo similarity metric expressed in eq. 3-13.

$$C_{AB} = \frac{\sum_{i,j}(P_A P_B)}{\sqrt{\left(\sum_{i,j} P_A^2\right)\left(\sum_{i,j} P_B^2\right)}} \tag{3-13}$$

where P_A is a data point from the original 2D asynchronous spectrum and P_B is a data point from another 2D-COS spectrum.

The C_{AB} value between **Figure 3-1B** and **Figure 3-2B** is 0.75. After application of the Butterworth filter on the 1D spectra shown in **Figure 3-2A**, the C_{AB} value between **Figure 3-1B** and **Figure 3-11** is 0.99. The remarkable changes on the C_{AB} values provide another evidence to show that the Butterworth filter is an effective approach to improve the quality of 2D asynchronous spectrum.

3 Application of Butterworth Filter on a Real Chemical System

In order to prove that the Butterworth filter is applicable to real chemical systems, we select the berberine/β-cyclodextrin system as an example. The details on the

investigation can be found in chapter 3.

In the study, we focused on the n-π* transition band of berberine around 420 nm in UV-vis spectra. In the experiment, three groups of aqueous solutions containing berberine chloride and β-cyclodextrin were prepared. Each group contains four solutions. The concentrations of berberine chloride and β-cyclodextrin are listed in **Table S3-2** in the Supporting Information. UV-Vis spectra of the three groups of solutions were recorded. The spectra of the solutions in group 1 were used to construct 2D asynchronous spectrum. The spectra of the solutions in group 2 and group 3 were utilized to generate a modified reference spectrum.

The obtained 2D UV-Vis spectrum is shown in **Figure S3-1** of the Supporting Information. Cross peaks around (420, 420) in 2D UV-vis asynchronous spectrum reflect intermolecular interaction between berberine and β-cyclodextrin. Then, we introduced artificial noise into each 1D spectrum. The fluctuation of noise is about 15% of the intensity of the absorption peak at 420 nm. The resultant 2D asynchronous spectrum is shown in **Figure 3-12**. In this case, noise brings about severe interference on the 2D asynchronous spectrum, and the cross peaks around (420, 420) are completely covered by the noise. The C_{AB} value between the 2D asynchronous spectrum shown in **Figure S3-1** and that shown in **Figure 3-12** is 0.65.

Subsequently, we applied the Butterworth filter on the 1D UV-vis spectra. The treated spectra are used to construct 2D asynchronous spectrum. The resultant 2D asynchronous spectrum is shown in **Figure 3-13**. In comparison with **Figure 3-12**, noise in the 2D asynchronous spectrum is significantly reduced. As a result, cross peaks around (420, 420) that are masked by the noise can be revealed. When the Butterworth filter is utilized, the C_{AB} value between 2D asynchronous spectrum shown in **Figure S3-1** and that shown in **Figure 3-13** is 0.95. The results on the C_{AB} values also demonstrated that the Butterworth filter is an applicable approach for real chemical systems.

Conclusion

Based on the investigation in this work, the following conclusions can be obtained.

1. Standard deviation of noise in 1D spectra turns out to be suitable to reflect the fluctuation of noise in 2D asynchronous spectrum.

2. Butterworth filter shows remarkable ability in the reduction of the standard deviation of noise. This confers the Butterworth filter with a good chance to improve the signal to noise level of 2D asynchronous spectrum by attenuation of noise in 1D spectra.

3. A strategy is proposed to obtain optimized parameter of the Butterworth filter by taking consideration of reducing the standard deviation of noise and restriction of signal distortion.

4. The result on a model system and a real chemical system demonstrate that our approach based on Butterworth filter is applicable in the improvement of the quality of 2D asynchronous spectrum.

References

1. Yu, Z. W.; Liu, J.; Noda, I. Effect of Noise on the Evaluation of Correlation Coefficients in Two-Dimensional Correlation Spectroscopy. *Appl. Spectrosc.* **2003**, *57*, 1605-1609.

2. Berry, R. J.; Ozaki, Y. Comparison of Wavelets and Smoothing for Denoising Spectra for Two-Dimensional Correlation Spectroscopy. *Appl. Spectrosc.* **2002**, *56*, 1462-1469.

3. Wu, Y.; Noda, I. Quadrature Orthogonal Signal Corrected Two-Dimensional Correlation Spectroscopy. *Appl. Spectrosc.* **2006**, *60*, 605-610.

4. Li, X. P.; Liu, S. X.; Chen, J.; Yue, S. J.; Liu, C. G.; Wei, Y. J.; Huang, K.; Zhao, Y.; Xu, Y. Z.; Noda, I. et al. The Influence Of Changing the Sequence of Concentration Series on the 2D Asynchronous Spectroscopy Generated by the Asynchronous Orthogonal Sample Design (AOSD) Approach. *Vib. Spectrosc.* **2012**, *60*, 212-216.

5. Li, X. P.; Bi, Q.; Liu, S. X.; Chen, J.; Yue, S. J.; Wei, Y. J.; Huang, K.; Zhao, Y.; Liu, H. Z.; Zhai, Y. J. et al. Improvement of the Sensitivity of the Two-Dimensional Asynchronous Spectroscopy Based on The AOSD Approach by using a Modified Reference Spectrum. *J. Mol. Struct.* **2013**, *1034*, 101-111.

6. Wu, Y.; Noda, I. Extension of Quadrature Orthogonal Signal Corrected Two-Dimensional (QOSC 2D) Correlation Spectroscopy: Principal Component Analysis and Partial Least Squares-Based QOSC 2D. *J. Mol. Struct.* **2008**, *883-884*, 149-154.

7. Jung, Y. M. Principal Component Analysis Based Two-Dimensional Correlation Spectroscopy for Noise Filtering Effect. *Vib. Spectrosc.* **2004**, *36*, 267-270.

8. Jung, Y. M.; Kim, S. B.; Noda, I. New Approach to Generalized Two-Dimensional Correlation Spectroscopy. II: Eigenvalue Manipulation Transformation (EMT) for Noise Suppression. *Appl. Spectrosc.* **2003**, *57*, 557-563.

9. Kramer, R. *Chemometric Techniques for Quanitative Analysis*; CRC Press: New York, USA, 1998.

10. Gao, Y. L.; Liu J.; Liu, Y. H.; Shi, J. J.; Weng, S. F.; Yang, L. M.; Wen, X. D.; Kang, T. G.; Xu, Y. Z.; Noda, I. et al. Characterization of the coordination between Nd^{3+} and ester groups by using double asynchronous orthogonal sample design approach. *J. Mol. Struct.* **2014**, *1069*, 205-210.

11. Liu, J.; Gao, Y. L.; Zheng, L. R.; Gao, D. Q.; He, A. Q.; Liu, Y. H.; Weng, S. F.; Zhao, Y.; Yang, Z. L. et al. Coordination between Cobalt (II) Ion and Carbonyl Group in Acetone Probed by using DAOSD Approach. *J. Mol. Struct.* **2014**, *1069*, 217-222.

12. Oppenheim, A. V.; Willsky A. S.; Nawab S. H. *Signals and Systems*; Prentice Hall: New Jersey, USA, 1996.

13. Butterworth, S. On the Theory of Filter Amplifiers. *Experimental Wireless and the Wireless Engineer* **1930**, *7*, 536-541.

14. Bianchi, G.; Sorrentino, R. *Electronic Filter Simulation & Design*; McGraw-Hill Professional: New York, USA, 2007.

15. Tsang, K.; Chan, W. L. Rapid Islanding Detection using Multi-Level Inverter for Grid-Interactive PV System. *Energy Convers. Manage.* **2014**, *77*, 278–286.

16. Watson, C. S.; Whtie, N. J.; Church J. A.; King, M. A.; Burgette R. J.; Legresy B. Unabated Global Mean Sea-Level Rise over the Satellite Altimeter Era. *Nat. Clim. Change.* **2015**, *5*, 565-568.

17. Patel, H. J.; Temple, M. A.; Baldwin, R. O. Improving ZigBee Device Network Authentication Using Ensemble Decision Tree Classifiers With Radio Frequency Distinct Native Attribute Fingerprinting. *IEEE Trans. Reliab.* **2014**, *64*, 221-233.

18. Lütkenhöner, B.; Patterson, R. D. Disruption of the Auditory Response to a Regular Click Train by a Single, Extra Click. *Exp. Brain Res.* **2015**, *233*, 1875-1892.

19. Widmann, A.; Schröger, E.; Maess, B. Digital Filter Design for Electrophysiological Data – a Practical Approach. *J. Neurosci. Methods* **2015**, *250*, 34-36

Table 3-1 Initial Concentrations of P and Q in the Model System, Which Meet the Requirement of the DAOSD Approach

index of the solutions	C_P	C_Q
1	3.00	2.10
2	2.50	2.10
3	2.20	2.10
4	1.80	2.10
5	1.40	2.10
6	1.10	2.10

Table 3-2 Expression of $\sigma[\Psi_{noise}(x, y)]$ in Different Region of a 2D Asynchronous Spectrum

Region	Expression of $\sigma[\Psi_{noise}(x, y)]$
I	$\sqrt{\dfrac{1}{n}\displaystyle\sum_{i=1}^{12}(H_i)^2}\,\sigma$
II	$\sqrt{\dfrac{1}{n}\displaystyle\sum_{i=7}^{12}(H_i)^2}\,\sigma$
III	$\sqrt{\dfrac{1}{n}\displaystyle\sum_{i=1}^{6}(H_i)^2}\,\sigma$
IV	0

A

B
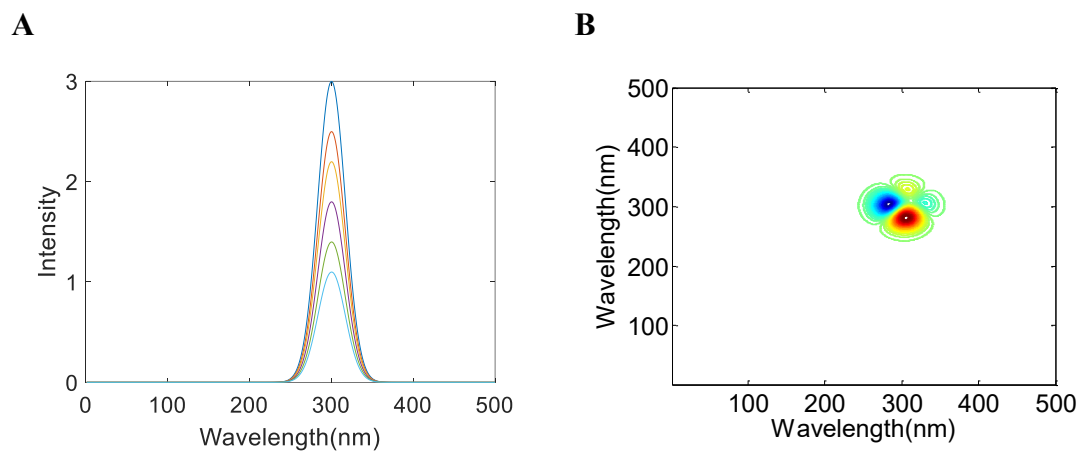
Figure 3-1. (A) Six Simulated 1D spectra of the Model System, in which Noise is not Present. (B) 2D Asynchronous Spectrum Generated from the six 1D Spectra shown in (A).
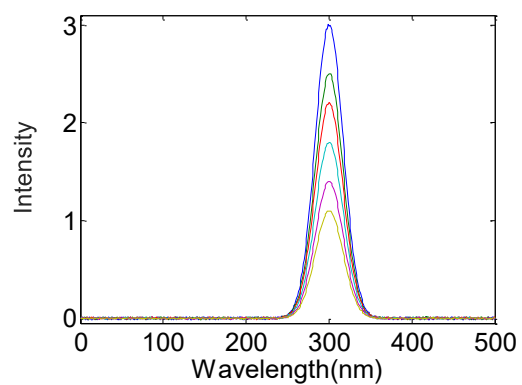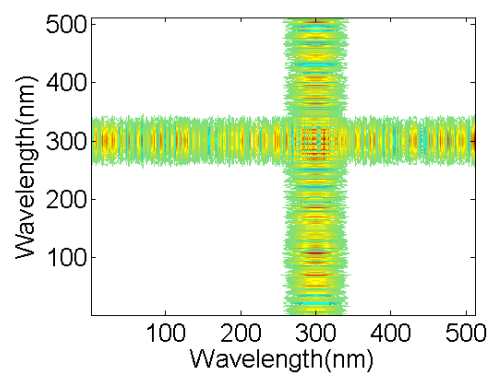
Figure 3-2. (A) Six Simulated 1D Spectra of the Model System, in which Noise is Present. (B) 2D Asynchronous Spectrum Generated from the Six 1D Spectra shown in (A). In this case, Cross Peaks are Completely Masked by Noise.
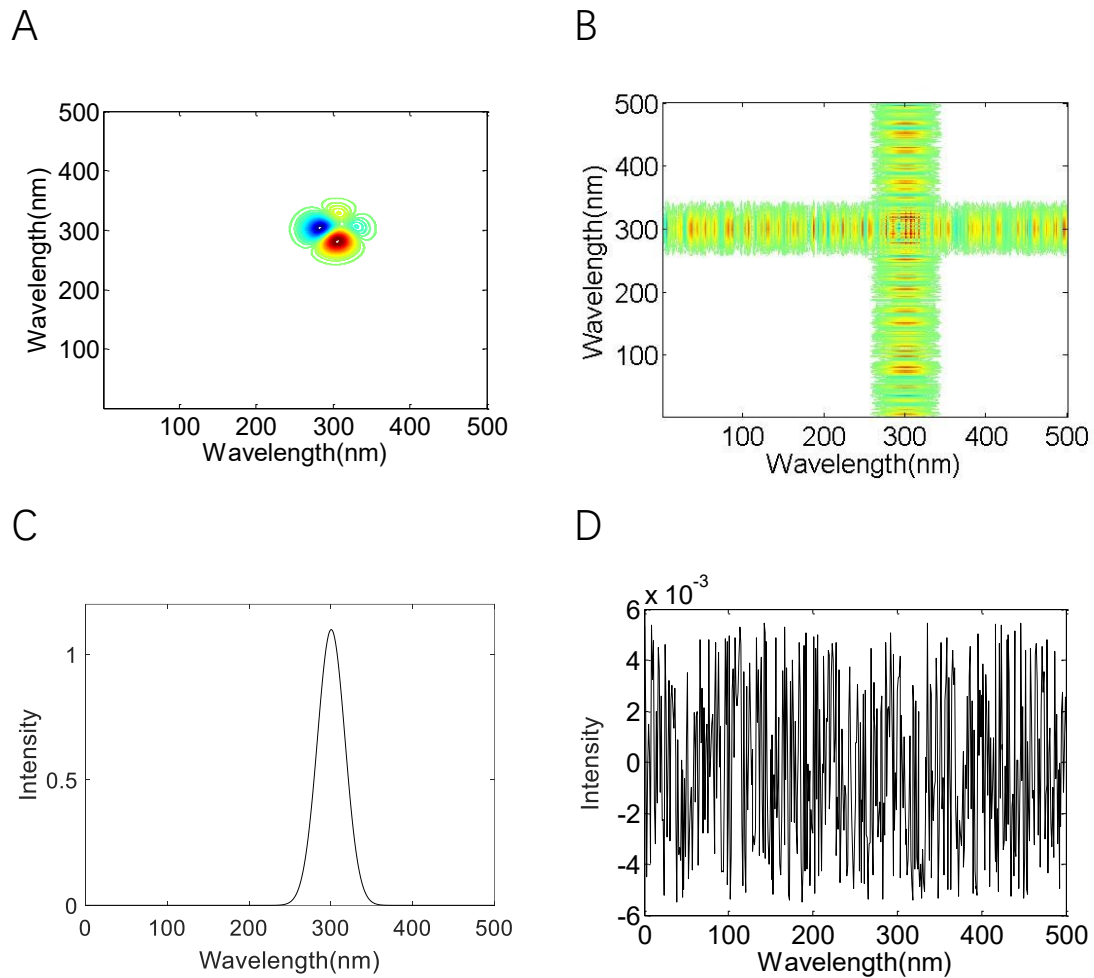
Figure 3-3. Decomposition of the 2D Asynchronous Spectrum shown in **Figure 3-2B** into Signal part and Noise part. For Comparison, the 1D Spectrum whose peak Intensity is the Weakest among the Six Spectra shown in **Figure 3-2A** is also Decomposed into Signal Part and Noise Part. (A) Signal Part of 2D Asynchronous Spectrum. (B) Noise Part of 2D Asynchronous Spectrum. (C) Signal Part of the 1D Spectrum. (D) Noise part of the 1D Spectrum.
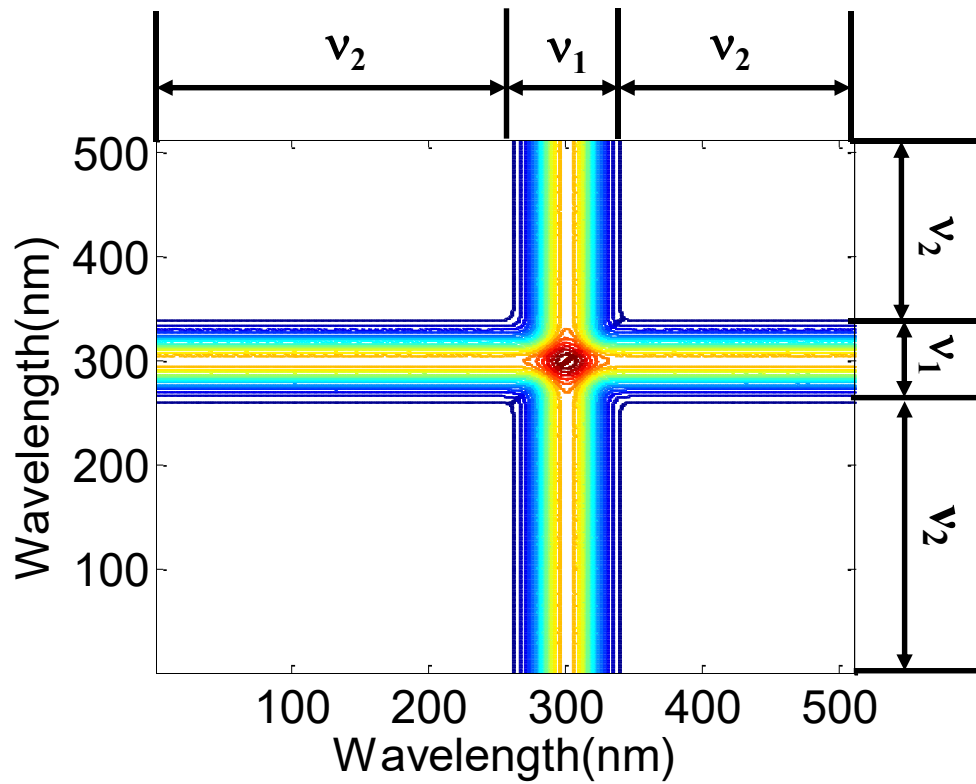
Figure 3-4. STD Values of Noise in the 2D Spectral Region. In this work, we Simulated 20000 2D Asynchronous Spectra. From each 2D Asynchronous Spectrum, the Noise part was Extracted. Then the Standard Deviation at each Spectral Point (x, y) over the 20000 Asynchronous Spectra is Calculated. Then the Obtained Standard Deviations of Noise as a Function of Spectral Variables x and y are Plotted here.
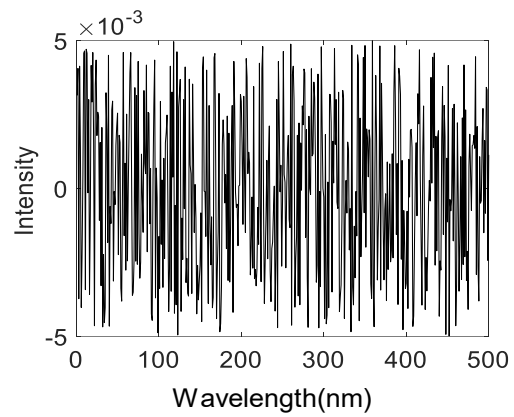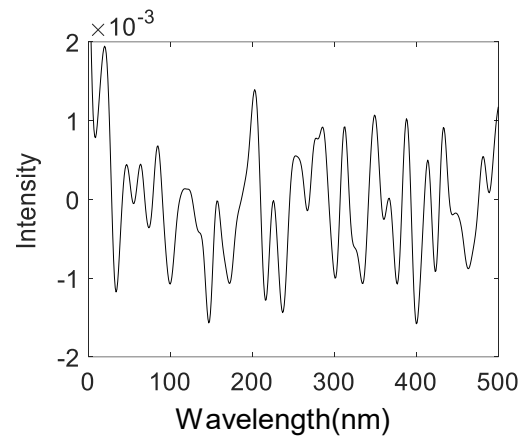
Figure 3-5. (A) Typical Example of Noise Extracted from 1D Spectrum. In this case the Standard Deviation of noise is 2.8×10^{-3}. (B) Result of the Treatment of Noise by the Butterworth Filter whose *n* and ω Values are 3 and 0.1, respectively. The Standard Deviation of Noise after the Treatment is 7.51×10^{-4}.
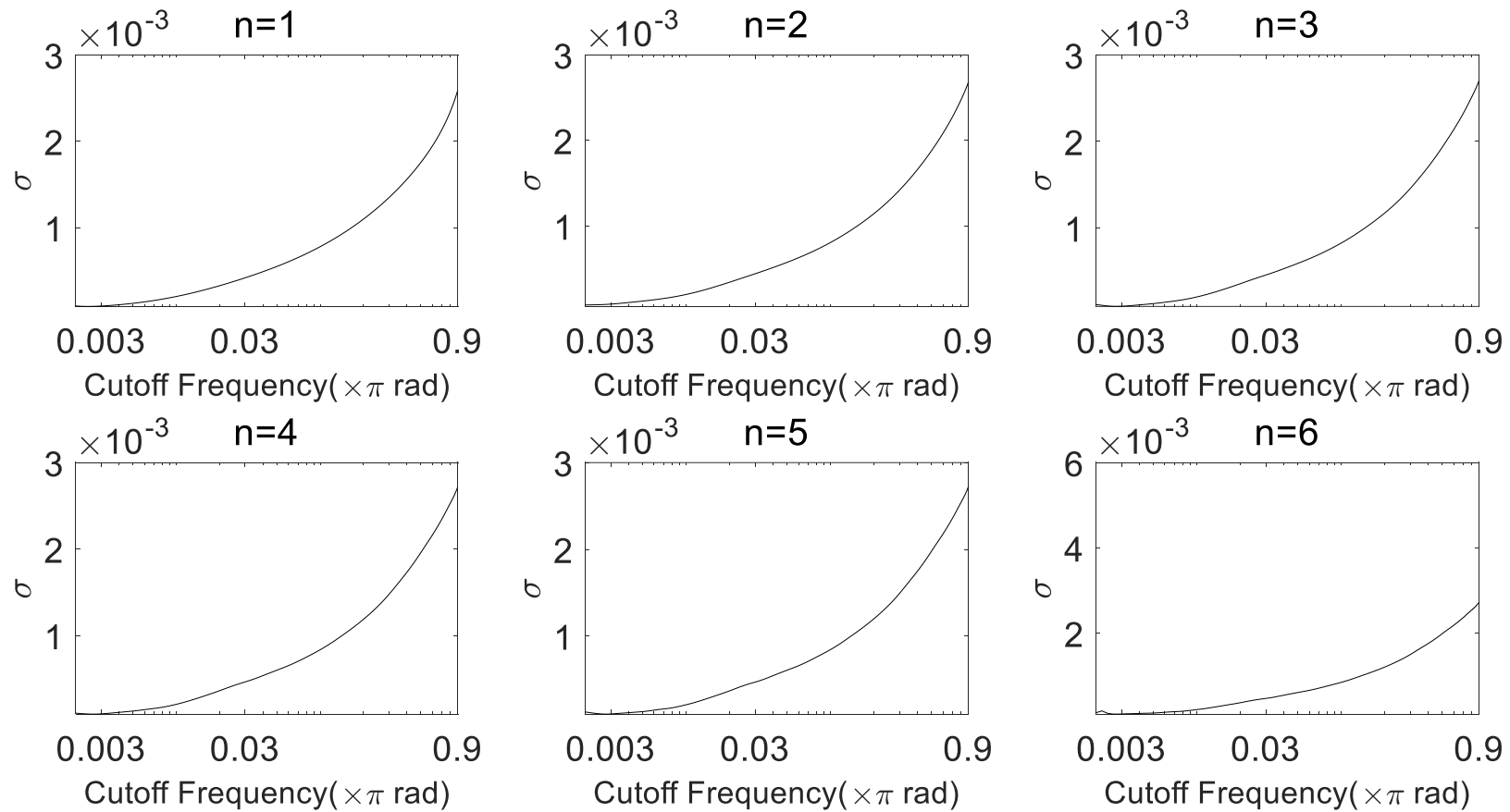
Figure 3-6. Relationship between STD of the Treated Noise in 1D Spectrum and Cutoff Frequency and Number of Poles of the Butterworth Filter. The Butterworth Filter is used in the Treatment of 1D Spectra Containing Noise.
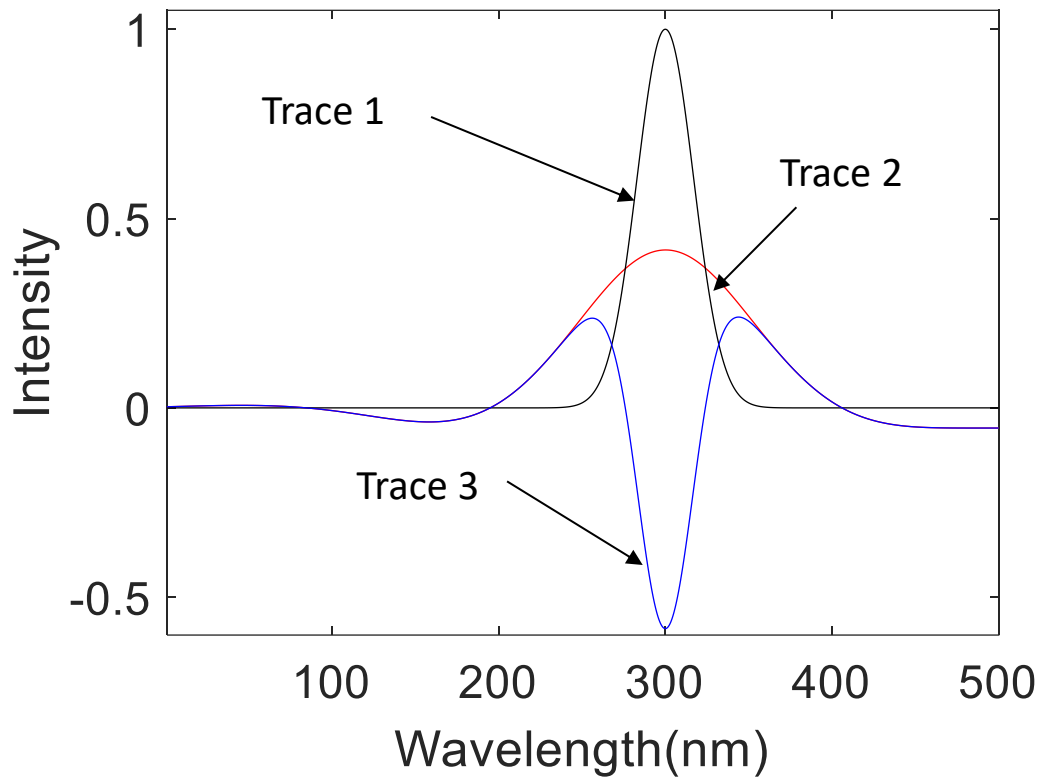
Figure 3-7. Example of Signal Distortion brought about by a Butterworth Filter on a 1D Spectrum without Noise. Trace 1: Original 1D Spectrum. Trace 2: Result of Butterworth Filter Treatment on the 1D Spectrum shown in trace 1. Trace 3: Difference between trace 2 and trace 1.
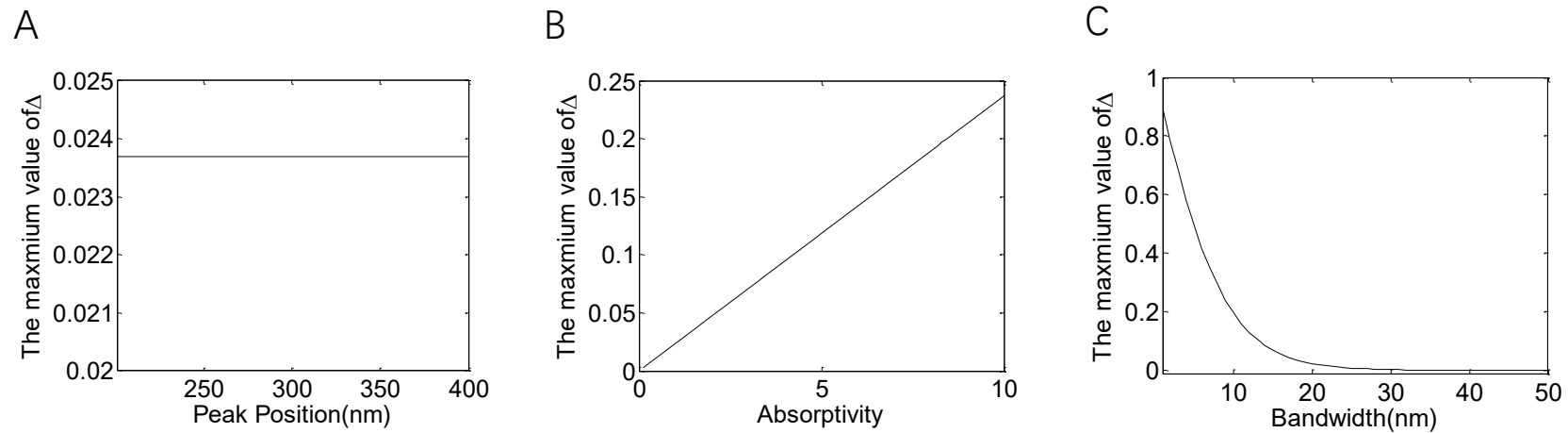
Figure 3-8. Variations of the Maximum Value of Signal Distortion versus the Parameters of the Gaussian Peak. A Butterworth Filter whose *n* and ω Values are 3 and 0.005, respectively, is used to Treat a Spectrum that is Composed of a Single Gaussian Peak. (A) Relationship between the Peak Position of the Gaussian Peak and the Maximum Value of Signal Distortion. (B) Relationship between the Absorptivity of the Gaussian peak and the Maximum Value of Signal Distortion. (C) Relationship between the Bandwidth of the Gaussian Peak and the Maximum value of Signal Distortion.
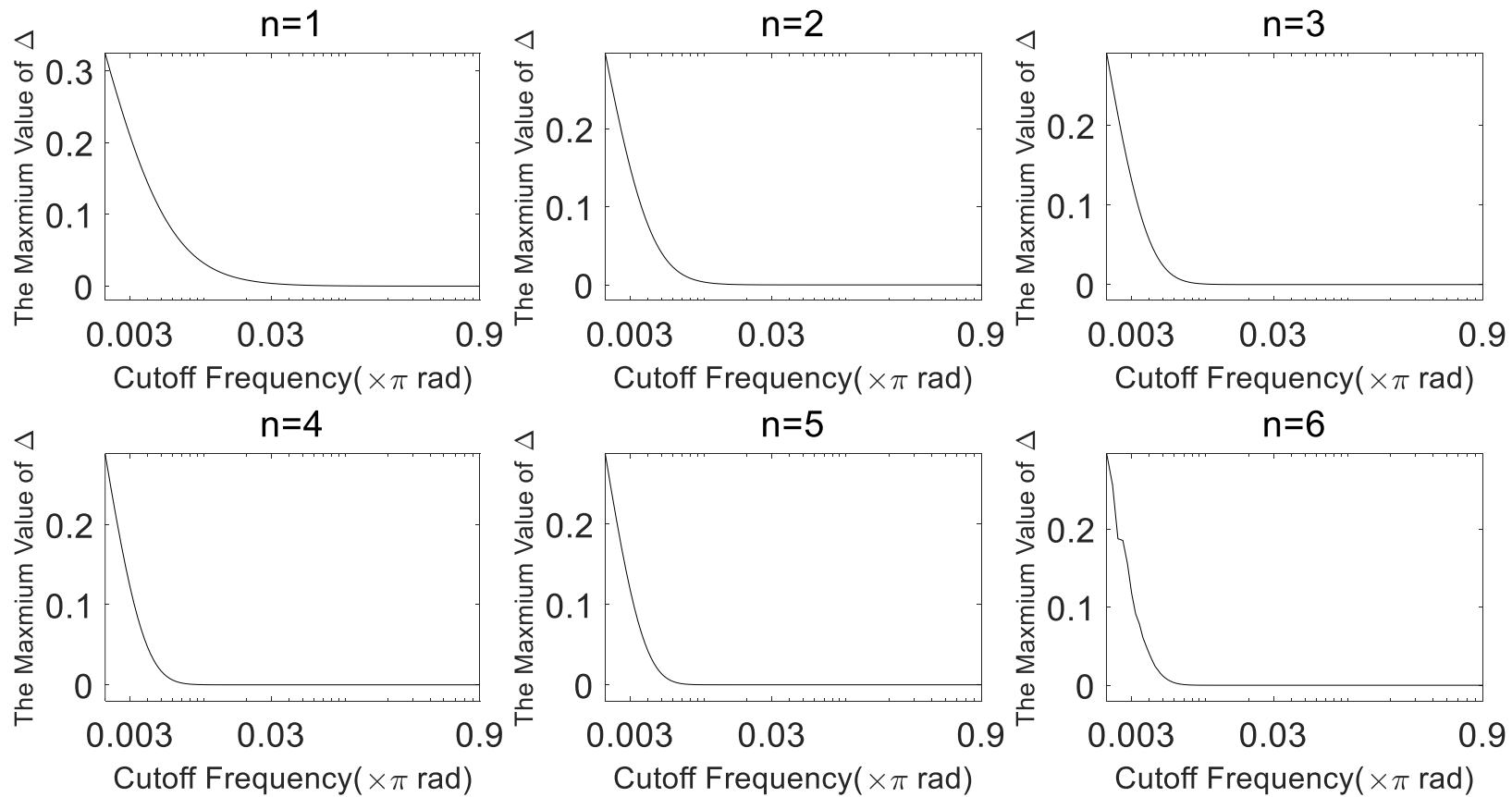
Figure 3-9. For a given Gaussian Peak with Fixed Peak Parameters, the Relationship between the Maximum value of Signal Distortion and Cutoff Frequency with Different Number of Poles.
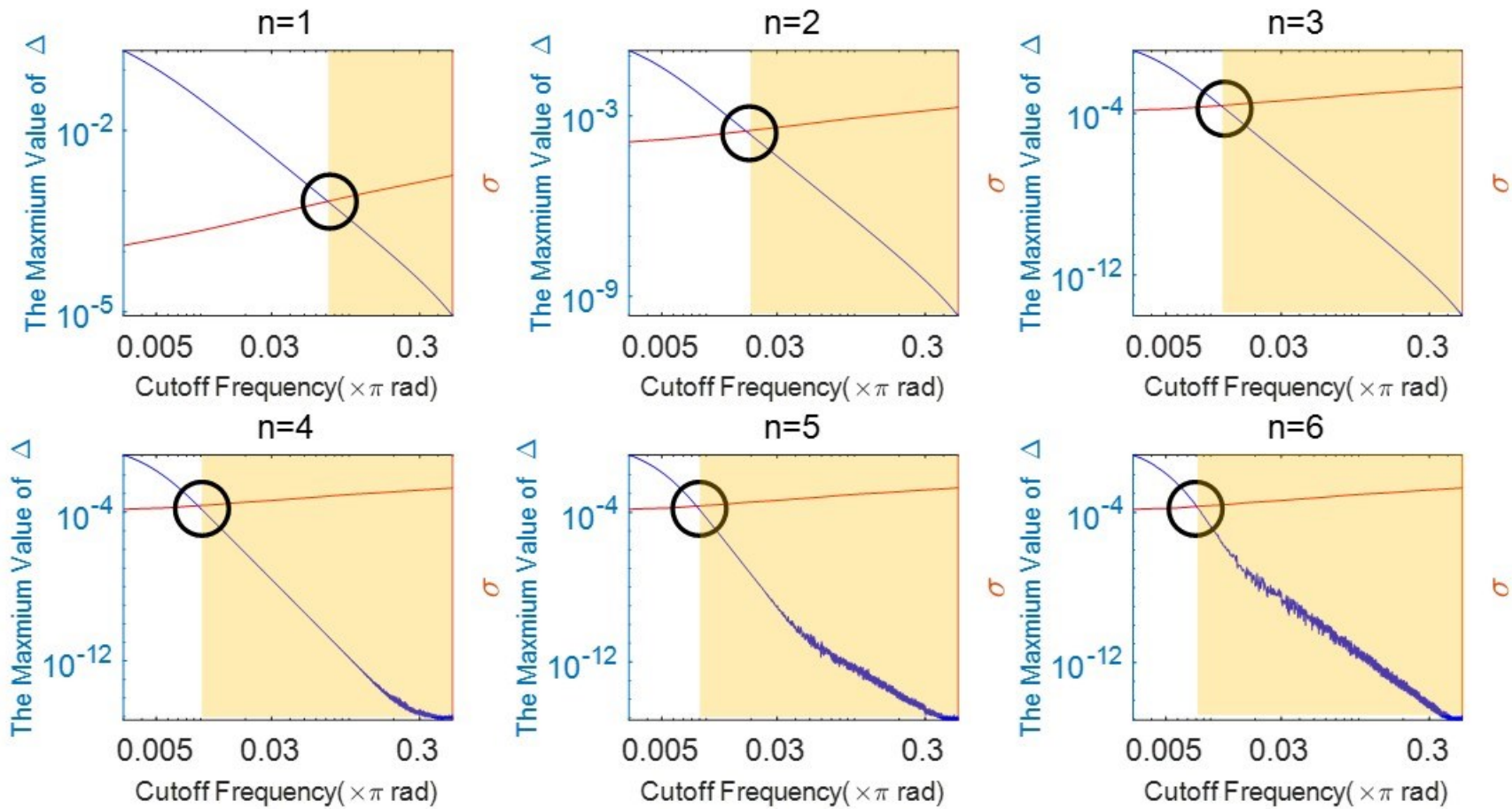
Figure 3-10. Combination of Standard Deviation of Noise Versus Cutoff Frequency of a Butterworth Filter Curve and Maximum Value of Signal Distortion Versus Cutoff Frequency of the Butterworth Filter for Different Numbers of Poles of the Filter. The Cross Section Corresponds To The Optimized Cutoff Frequency of the Butterworth Filter.
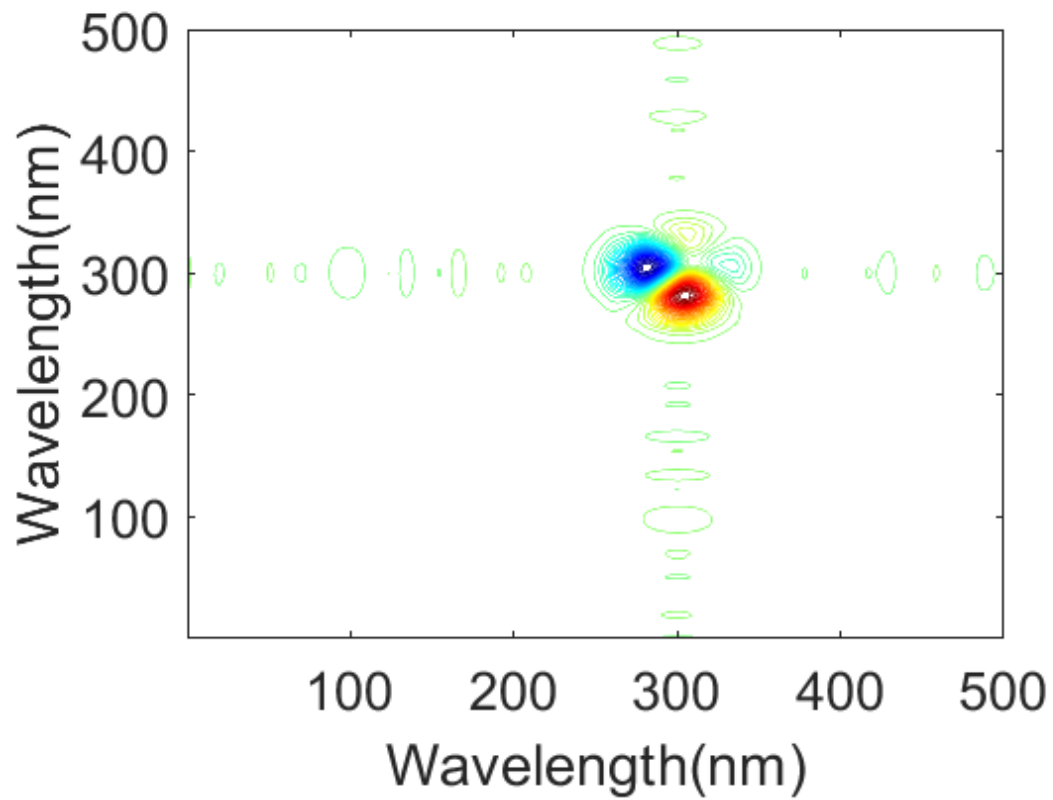
Figure 3-11. 2D Asynchronous spectrum. A Butterworth Filter with Optimized Parameters is Utilized on the 1D Spectra with Noise. Then the Treated 1D Spectra are used to Construct the 2D Asynchronous Spectrum that is shown here.
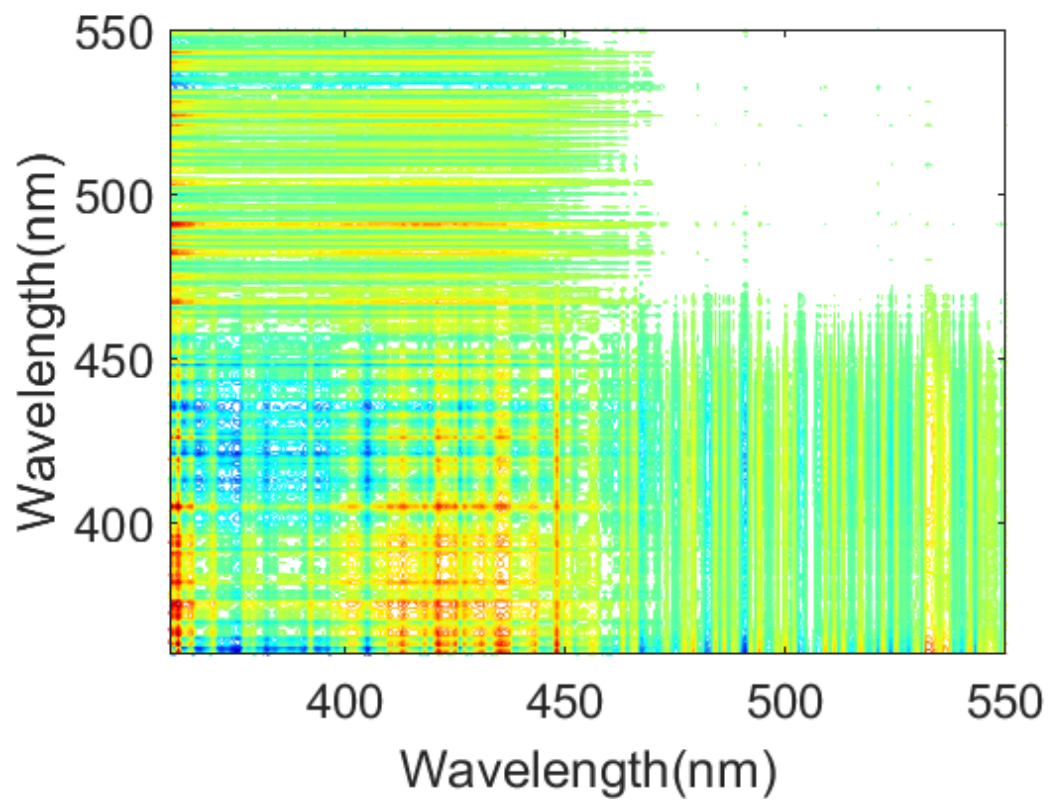
Figure 3-12. Two-Dimensional Asynchronous Spectrum of Berberine/β- Cyclodextrin System Constructed by a Series of 1D Spectra Containing Artificial Noise.
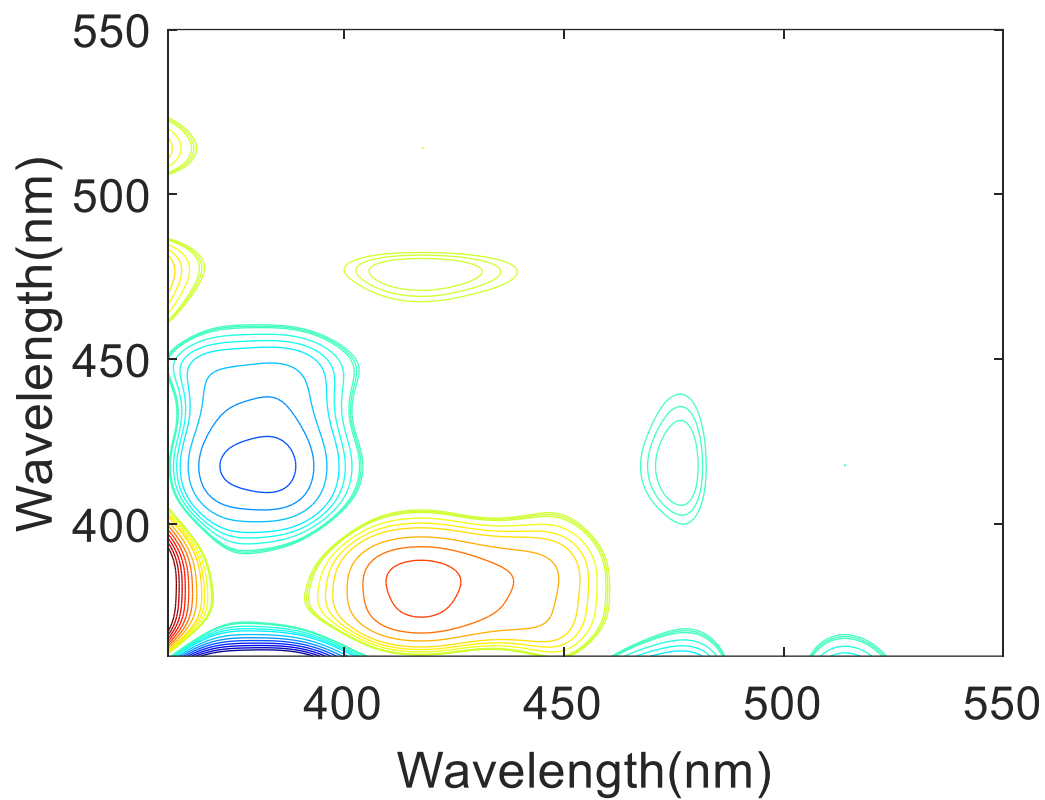
Figure 3-13. Two-Dimensional Asynchronous Spectrum Generated from Three Groups of 1D UV-vis Spectra that are Treated by using the Butterworth Filter.

Supporting Information 2

1. Description of the Model System

In the spectral region investigated, the spectral function of each substance (P, and U) possesses only one characteristic peak. The peak for each chemical species is represented by a Gaussian function as shown in eq. S3-1.

$$f_j(x) = \varepsilon_j * e^{-(\ln 2)*[\frac{(x-X_j)^2}{W_j^2}]} \tag{S3-1}$$

where j refers to chemical species, i.e., P or U; ε_j, X_j, and W_j are the corresponding molar absorptivity, peak position and bandwidth (half-width at half-height, HWHH) of the characteristic band of j. It should be pointed out that the characteristic peak of P is highly overlapped with that of U since the interaction is quite weak and only induces a subtle spectral variation. The peak parameters of P and U are listed in **Table S3-1**.

Table S3-1 Peak Parameters of P and U in the Model System.

Spectral variable	Peak position(nm)	Bandwidth(nm)	Absorptivity
M_P	300	20	1.0
M_U	302	18	1.0

For the ith solution, the simulated 1D spectrum is constructed by eq. S3-2 according to the Beer-Lambert's Law.

$$A^i(x) = C_P^{i(eq)} f_P(x) + C_U^{i(eq)} f_U(x) \tag{S3-2}$$

where $i \in \{1, 2, 3, 4, 5, 6\}$; $f_P(x)$ and $f_U(x)$ are spectral functions of P and U; $C_P^{i(eq)}$ and $C_U^{i(eq)}$ are equilibrium concentrations of P and U. For convenience, the path length is set as 1 and not appeared in eq. S3-2.

According to eq. 3-1, we have

$$C_P^{i(eq)} = C_P^{i(init)} - C_U^{i(eq)} \tag{S3-3}$$

Thus, eq. S3-2 can be converted as

$$A^i(x) = C_P^{i(eq)} f_P(x) + C_U^{i(eq)} \left(f_U(x) - f_P(x)\right) \tag{S3-4}$$

In the simulation, $C_U^{i(eq)}$ is calculated based on the initial concentrations of P, Q and equilibrium constant. The simulated 1D spectra are shown in **Figure 3-1A**. Subsequently, a reference spectrum of the above 6 spectra are generated according to eq. S3-5.

$$R(x) = \frac{1}{6} \sum_{i=1}^{6} A^i(x) \qquad\qquad \text{(S3-5)}$$

Afterwards, each sample spectrum is converted into dynamic spectrum using eq. S3-6.

$$\widetilde{A}(x) = A^i(x) - R(x) \qquad\qquad \text{(S3-6)}$$

Then, 2D asynchronous spectrum is constructed via eq. S3-7.

$$\Psi(x,y) = \frac{1}{n-1} \vec{\widetilde{A}}^{\mathrm{T}}(x) \mathbf{N} \vec{\widetilde{A}}(y) \qquad\qquad \text{(S3-7)}$$

The superscript $^{\mathrm{T}}$ denotes the transpose of the matrix, and $\mathbf{N}$ is the Hilbert-Noda transformation matrix.

2. Mathematical Analysis of 2D Spectra Containing Noise

When noise is introduced into a 1D spectrum, eq. S3-4 can be modified as eq. S3-8

$$A^i(x) = C_{\mathrm{P}}^{i(\mathrm{init})} f_{\mathrm{P}}(x) + C_{\mathrm{U}}^{i(\mathrm{eq})} \big(f_{\mathrm{U}}(x) - f_{\mathrm{P}}(x) \big) + \gamma_i(x) \qquad \text{(S3-8)}$$

where ε_i is noise, which is variable as the wavelength x is changed.

The corresponding dynamic spectrum can be expressed as eq. S3-9 after combining eq. S3-5, eq. S3-6 with eq. S3-8.

$$\widetilde{A}^i(x) = \widetilde{C}_{\mathrm{P}}^{i(\mathrm{init})} f_{\mathrm{P}}(x) + \widetilde{C}_{\mathrm{U}}^{i(\mathrm{eq})} \big(f_{\mathrm{U}}(x) - f_{\mathrm{P}}(x) \big) + \widetilde{\gamma}_i(x) \qquad \text{(S4-9)}$$

where

$$\begin{aligned}
\widetilde{C}_{\mathrm{P}}^i &= C_{\mathrm{P}}^{i(\mathit{init})} - C_{\mathrm{P}}^{\mathrm{init(av)}} \\
\widetilde{C}_{\mathrm{U}}^i &= C_{\mathrm{U}}^{i(\mathrm{eq})} - C_{\mathrm{U}}^{\mathrm{eq(av)}} \\
\widetilde{\gamma}_i(x) &= \gamma_i(x) - \gamma^{\mathrm{av}}(x)
\end{aligned} \qquad\qquad \text{(S3-10)}$$

and

$$\begin{aligned}
C_{\mathrm{P}}^{\mathrm{init(av)}} &= \frac{1}{6} \sum_{i=1}^{6} C_{\mathrm{P}}^{i(\mathit{init})} \\
C_{\mathrm{U}}^{\mathrm{eq(av)}} &= \frac{1}{6} \sum_{i=1}^{6} C_{\mathrm{U}}^{i(eq)} \\
\gamma^{\mathrm{av}}(x) &= \frac{1}{6} \sum_{i=1}^{6} \gamma_i(x)
\end{aligned} \qquad\qquad \text{(S3-11)}$$

When eq. S3-9 is combined with eq. S3-7, the resultant 2D asynchronous spectrum with noise can be expressed as eq. S3-12.

$$\Psi(x,y) = \sum_{i=1}^{9} \mathbf{M}_i(x,y) \qquad\qquad \text{(S3-12)}$$

where

$$\mathbf{M}_1(x,y) = f_{\mathrm{P}}(x) f_{\mathrm{P}}(y) \left(\vec{\widetilde{C}}_{\mathrm{P}}^{\mathrm{init}} \right)^{\mathrm{T}} \mathbf{N} \vec{\widetilde{C}}_{\mathrm{P}}^{\mathrm{init}} \qquad \text{(S3-13)}$$

$$\mathbf{M}_2(x,y) = f_P(x)(f_U(y) - f_P(y))\left(\vec{\tilde{C}}_P^{\,init}\right)^T \mathbf{N}\vec{\tilde{C}}_U^{\,eq}$$

$$\mathbf{M}_3(x,y) = f_P(x)(f_U(y) - f_P(y))\left(\vec{\tilde{C}}_P^{\,init}\right)^T \mathbf{N}(\vec{\tilde{\gamma}}(y))$$

$$\mathbf{M}_4(x,y) = (f_U(x) - f_P(x))f_P(y)\left(\vec{\tilde{C}}_U^{\,eq}\right)^T \mathbf{N}\vec{\tilde{C}}_P^{\,init}$$

$$\mathbf{M}_5(x,y) = (f_U(x) - f_P(x))(f_U(y) - f_P(y))\left(\vec{\tilde{C}}_U^{\,eq}\right)^T \mathbf{N}\vec{\tilde{C}}_U^{\,eq}$$

$$\mathbf{M}_6(x,y) = (f_U(x) - f_P(x))\left(\vec{\tilde{C}}_U^{\,eq}\right)^T \mathbf{N}(\vec{\tilde{\gamma}}(y))$$

$$\mathbf{M}_7(x,y) = f_P(y)(\vec{\tilde{\gamma}}(x))^T \mathbf{N}\vec{\tilde{C}}_P^{\,init}$$

$$\mathbf{M}_8(x,y) = (f_U(y) - f_P(y))(\vec{\tilde{\gamma}}(x))^T \mathbf{N}\vec{\tilde{C}}_U^{\,eq}$$

$$\mathbf{M}_9(x,y) = (\vec{\tilde{\gamma}}(x))^T \mathbf{N}(\vec{\tilde{\gamma}}(y))$$

According to the basic mathematical property of the Hilbert-Noda matrix shown in eq. S3-14:

$$\vec{B}^T \mathbf{N}\vec{B} = 0 \tag{S3-14}$$

We have

$$\mathbf{M}_1(x,y) = 0$$

$$\tag{S3-15}$$

$$\mathbf{M}_5(x,y) = 0$$

Thus, $\Psi(x, y)$ is composed of 7 terms. The 7 terms can be classified into two parts, the first part is a signal part ($\Psi_{signal}(x, y)$) and the second part is a noise part ($\Psi_{noise}(x, y)$). The expression of $\Psi_{signal}(x, y)$ and $\Psi_{noise}(x, y)$ are listed in eq. S3-16A and eq. S3-16B, respectively.

$$\Psi_{signal}(x, y) = \mathbf{M}_2(x, y) + \mathbf{M}_4(x, y) \tag{S3-16A}$$

$$\Psi_{noise}(x, y) = \mathbf{M}_3(x, y) + \mathbf{M}_6(x, y) + \mathbf{M}_7(x, y) + \mathbf{M}_8(x, y) + \mathbf{M}_9(x, y) \tag{S3-16B}$$

3. Mathematical Properties of Noise part in 2D asynchronous spectrum

According to eq. S3-16B, the expression of $\Psi_{noise}(x, y)$ is composed of five terms. The result of our simulation indicates that

$$|\mathbf{M}_3(x, y) + \mathbf{M}_6(x, y) + \mathbf{M}_7(x, y) + \mathbf{M}_8(x, y)| \gg |\mathbf{M}_9(x, y)| \tag{S3-17}$$

Thus, $\mathbf{M}_9(x, y)$ can be neglected.

According to the basic property of the Hilbert-Noda matrix shown in eq. S3-18.

$$\vec{A}^T \mathbf{N}\vec{B} = -\vec{B}^T \mathbf{N}\vec{A} \tag{S3-18}$$

$\Psi_{noise}(x, y)$ can be expressed as eq. S3-19.

$$\Psi_{noise}(x, y) = \vec{F}(x) \cdot \vec{\tilde{\gamma}}(y) - \vec{\tilde{\gamma}}(x) \cdot \vec{G}(y) \tag{S3-19}$$

where

$$\vec{F}(x) = \left[f_P(x)\left(\vec{\tilde{C}}_P^{\,init}\right)^T + (f_U(x) - f_P(x))\left(\vec{\tilde{C}}_U^{\,eq}\right)^T\right]\mathbf{N}$$

$$\vec{G}(y) = \left[f_P(y)\left(\vec{\tilde{C}}_P^{\,init}\right)^T + (f_U(y) - f_P(y))\left(\vec{\tilde{C}}_U^{\,eq}\right)^T\right]\mathbf{N} \tag{S3-20}$$

In this case, 2D asynchronous spectrum is constructed via spectra of six sample solutions. Thus eq. S3-19 can be expressed as

$$\Psi_{\text{noise}}(x, y) = \sum_{i=1}^{6} F_i(x)\tilde{\gamma}_i(y) - \sum_{i=1}^{6} \tilde{\gamma}_i(x)G_i(y) \tag{S3-21}$$

Herein, we define H_i and e_i where $i \in \{1, 2, 3, 4, 5, 6, 7, 8, 9, 10, 11, 12\}$
When $i \in \{1, 2, 3, 4, 5, 6\}$
$H_i = F_i(x)$
$e_i = \tilde{\gamma}_i(y)$
When $i \in \{7, 8, 9, 10, 11, 12\}$
$H_i = -G_i(y)$
$e_i = \tilde{\gamma}_{i-6}(x)$
Thus, eq. S3-21 can be expressed as eq. S3-22.

$$\Psi_{\text{noise}}(x, y) = \sum_{i=1}^{12} H_i e_i \tag{S3-22}$$

Then, a large number (m) of 2D asynchronous spectra are simulated. Noise portion of the 2D asynchronous spectrum ($\Psi_{\text{noise}}^{j}(x, y)$, where j=1, 2...., m) are extracted from each 2D asynchronous spectrum via eq. S3-22. Expectation and standard deviation of $\Psi_{\text{noise}}(x, y)$ are calculated.

Expectation of $\Psi_{\text{noise}}(x, y)$

According to eq. S3-22, the expectation of $\Psi_{\text{noise}}(x, y)$ is as follows:

$$E[\Psi_{\text{noise}}(x, y)] = \sum_{i=1}^{12} H_i E[e_i] \tag{S3-23}$$

Since $E[e_i]$ is zero. Thus, we have

$$E[\Psi_{\text{noise}}(x, y)] = 0 \tag{S3-24}$$

Standard deviation of $\Psi_{\text{noise}}(x, y)$

According to the definition of the standard deviation (STD), the STD of $\Psi_{\text{noise}}(x, y)$ can be calculated by using eq. S3-24

$$\sigma[\Psi_{\text{noise}}(x, y)] = \sqrt{\frac{1}{n} \sum_{m=1}^{n} (\Psi_{\text{noise}}^{m}(x, y) - E[\Psi_{\text{noise}}(x, y)])^2} \tag{S3-25}$$

Because of eq. S3-24, eq. S3-25 can be simplified as

$$\sigma[\Psi_{\text{noise}}(x, y)] = \sqrt{\frac{1}{n} \sum_{m=1}^{n} (\Psi_{\text{noise}}^{m}(x, y))^2} \tag{S3-26}$$

After combining eq. S3-22 with eq. S3-26, we have

$$\sigma[\Psi_{\text{noise}}(x,y)] = \sqrt{\frac{1}{n}\left(\sum_{i=1}^{12}(H_i)^2\sum_{j=1}^{n}(e_i^j)^2 + \sum_{k\neq l}^{k,l\leq12}(H_kH_l)\sum_{j=1}^{n}(e_k^je_l^j)\right)} \quad \text{(S3-27)}$$

Since

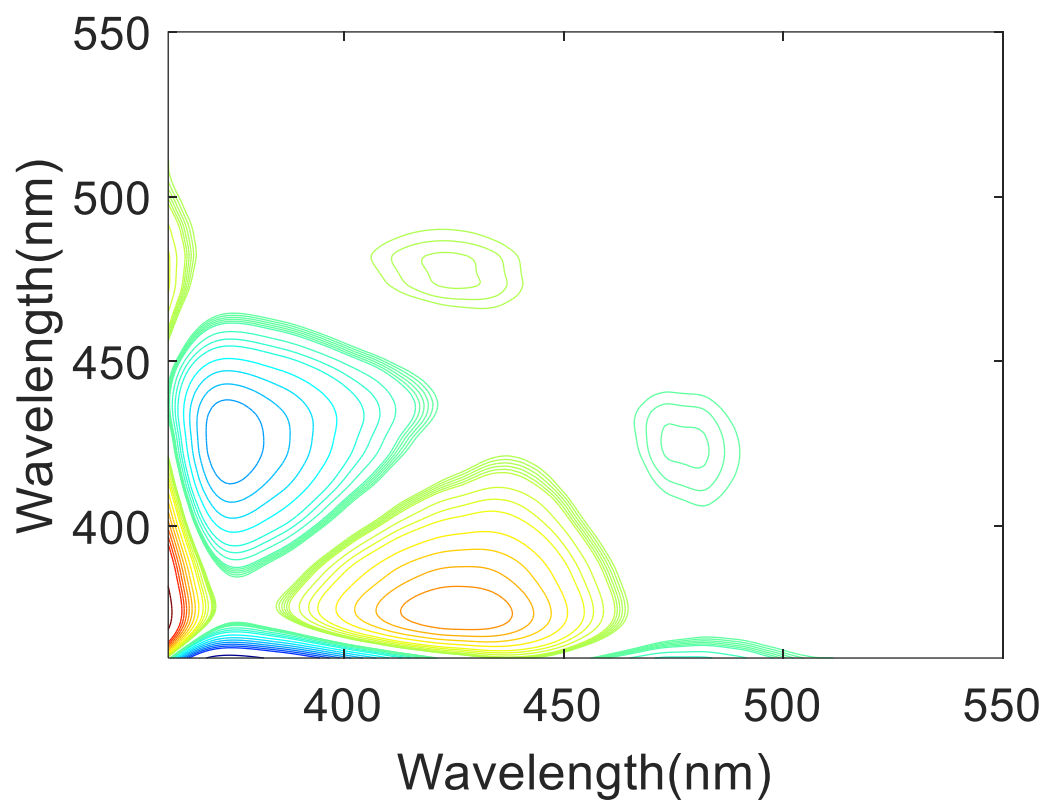$$\sum_{j=1}^{n}(e_k^je_l^j) = 0 \quad \text{(S3-28)}$$

Moreover, since $E[e_i^j]$ is zero, $\sum_{j=1}^{n}(e_i^j)^2$ is the standard deviation of e_i^j. Herein, the standard deviation of e_i^j is a constant, denoted as σ. Thus eq. S3-27 is simplified as

$$\sigma[\Psi_{\text{noise}}(x,y)] = \sqrt{\frac{1}{n}\sum_{i=1}^{12}(H_i)^2}\,\sigma \quad \text{(S3-29)}$$

4. Intermolecular Interaction between Berberine and β-Cyclodextrin

Table S3-2 Concentrations of berberine chloride and β- cyclodextrin in three groups of solutions

Index of the solutions	Group 1		Group 2		Group 3	
	$C_{berberine}$ $(\times 10^{-5}\text{g/ml})$	$C_{\beta\text{-cyclodextrin}}$ $(\times 10^{-4}\text{g/ml})$	$C_{berberine}$ $(\times 10^{-5}\text{g/ml})$	$C_{\beta\text{-cyclodextrin}}$ $(\times 10^{-4}\text{g/ml})$	$C_{berberine}$ $(\times 10^{-5}\text{g/ml})$	$C_{\beta\text{-cyclodextrin}}$ $(\times 10^{-4}\text{g/ml})$
1	3.97	7.05	0	7.05	3.97	0
2	2.98	7.05	0	7.05	2.98	0
3	1.98	7.05	0	7.05	1.98	0
4	0.99	7.05	0	7.05	0.99	0

Figure S3-1. Original 2D Asynchronous Spectrum of Berberine/β-Cyclodextrin System

Chapter 3

Investigation on Intermolecular Interaction between Berberine and β-cyclodextrin using 2D Asynchronous Spectra

Background

Berberine, a quaternary protoberberine isoquinoline alkaloid, is a well-known naturally occurring medicine obtained from the root and the stem bark of numerous clinically important medicinal plants such as coptidis rhizome and phellodendron.[1, 2] In traditional Chinese medicine, berberine has been extensively used in the treatment of diarrhea and gastroenteritis.[1, 3] In recent years, new pharmaceutical functions of berberine have also been found in medical researches. For example, oral intake of berberine by hypercholesterolemic patients can remarkably reduce the levels of serum cholesterol, triglycerides and low-density lipoprotein cholesterol.[4] In addition, berberine can reduce body weight, leading to the treatment of obesity, and bring about a significant improvement in glucose tolerance without altering food intake in animal models.[5, 6, 7] There are other applications of berberine serving as a drug, including anti-malaria, anti-arrhythmic, anti-tumor, anti-fungal, anti-oxidative, and cerebro-protective activities.[1, 8-11] Although berberine has wide-ranging therapeutic potential, the solubility is quite low in water (only 5.27 mM in aqueous solution at 25°C),[1] which poses a limitation to the broader application of berberine in medical practice. An effective way to increase its solubility is to introduce suitable excipient. Hence finding suitable excipient is of great importance in clinical application.

β-cyclodextrin (β-CyD) is a macrocyclic oligosugar composed of 7 glucosidic units in the $^4C_1$ conformation (**Figure 4-1**) .[12-14] It has an average structure of truncated cone with a cavity of hydrophobic character, while the exterior of β-CyD is of hydrophilic nature because it is covered by OH groups. The great significance of β-CyD lies in its ability to form inclusion compound. Various molecules, ions or radicals，whose sizes are suitable for the cavity of β-CyD, can be selectively clathrated.[15-20] In pharmaceutical field, β-CyD has been extensively applied to enhance the solubility, stability and bioavailability of many drug molecules.[21-22] According to the literature, the solubility of berberine in aqueous solution can be enhanced by β-CyD.[23]

The physico-chemical basis for the enhancement of the solubility of berberine by β-CyD is that significant intermolecular interaction occurs between berberine and β-CyD. In this chapter, we applied 2D correlation spectroscopic method to characterize the interaction between berberine and β-CyD.

We measured the UV-Vis spectra of a series aqueous solution containing different amounts of berberine chloride and β-CyD system. Then we construct 2D asynchronous UV-Vis spectra based on the obtained 1D spectra. Cross peaks in the 2D asynchronous spectrum are utilized to characterize intermolecular interaction between berberine and β-CyD. The reason we select UV-Vis spectra rather than other spectroscopic methods such as FTIR or NMR is: The characteristic peaks of solvent overlap severely with the characteristic peaks of berberine and β-CyD. Characteristic peaks of berberine overlap with the characteristic peaks of β-CyD. The above problems make it difficult to characterize intermolecular interaction between berberine and β-CyD via cross peak in 2D correaltion spectra in a reliable manner.

Experimental

Reagents

Berberine chloride with purity of 98% was purchased from J&K Scientific. β-CyD was of AR grade and obtained from Beijing Chemical Company.

Instrument

The UV–Vis spectra were recorded on a Lambda35 UV–vis spectrophotometer (Perkin Elmer) and the all the spectra were measured at a scanning rate of 480 nm/min.

Interference caused by solvent–solute interactions

When berberin is dissolved in the solvent, a solvating layer often occurs around the solute molecule. The berberin and its solvating layer can be regarded as separate entities. Under a suitable concentration range of the berberin, the complex of the separate entity remains virtually undisturbed. It also follows the Beer–Lambert Law. Hence, the intermolecular interactions between the solute and the solvent do not produce any interfering cross peaks in the 2D asynchronous spectrum.

Under this condition, a series of solutions containing different amount of berberin were prepared and UV–Vis spectra were recorded. A good linearity ($R^2 = 0.9990$) can be observed between the concentration of berberine chloride and absorbance at 420 nm in UV-Vis spectra when the suitable concentration of berberin is 0 to 4.96×10^{-5} g/ml (**Figure. S4-1**). Therefore, we select the concentration range to construct 2D asynchronous spectra, thereby excluding the possibility that the cross peaks are caused by solvent–solute interactions.

Procedure to generate 2D asynchronous spectra

To enhance the signal to noise ratio of the 2D asynchronous spectrum, the approach of using modified reference spectrum is adopted in the construction of 2D asynchronous spectrum. In the experiment, three groups of aqueous solutions containing berberine chloride, β-CyD are prepared. Each group contains 4 solutions. The concentrations of berberine chloride, β-CyD are listed in **Table 4-1**. UV-Vis spectra of the three groups of solutions were recorded.

The spectra of the solutions in group 1 were used to construct 2D asynchronous spectrum. The spectra of the solutions in group 2 and group 3 were utilized to generate a modified reference spectrum. Detail on utilizing a reference spectrum to produce a 2D asynchronous spectrum can be found in chapter 3.

Results and Discussion

Figure 4-2 shows the UV-Vis spectrum of aqueous solution of berberine chloride and the UV-Vis spectrum of aqueous solution of β-CyD. Since β-CyD does not have conjugated system, it has no absorption band in UV-Vis spectral region. From the molecular structure of berberine shown in **Figure 4-3**, we notice that berberine possesses a large conjugated system where both nitrogen and oxygen atoms are involved. Thus, both π-π* and n-π* transition bands are present in the UV-Vis spectra of berberin chloride. In the UV-Vis spectrum of berberine chloride, absorption band does occur. Based on our previous work,[57] we use cross peaks generated from the

characteristic peak of berberine chloride in 2D asynchronous spectrum to reflect interaction between berberine chloride and β-CyD.

Figure 4-4 displays a UV-Vis spectra of water (trace 1), berberine chloride (trace 2) and second derivative spectrum of the UV-Vis spectrum of berberine chloride (trace 3).   In the UV-Vis spectrum of berberine, four bands whose peak positions are 228 nm, 263 nm, 345 nm, 420 nm can be observed. The absorption band of berberine at 228 nm overlaps with the n-σ transition of water. Thus this band is not suitable to be used to reflect intermolecular interaction between berberine and β-CyD. Second derivative spectrum of berberine indicates that the band at 263 nm and 340 nm are not single bands. The 260 nm band is composed of two sub-band at 262 nm and 278 nm and the 340 nm band contains two highly overlapping sub-band at 334 nm and 351 nm. Upon interaction with β-CyD, the four sub-bands may undergo changes in peak position, bandwidth or absorptivity. These changes make the cross peak around (260, 260), (340,340) too complex, and it is difficult to predict what happens on the band of berberine under intermolecular interaction.

The band at 420 nm is not affected by the absorption band of the solvent. Moreover, the second derivative spectrum confirms that this band is a single peak. Thus, we use cross peaks from the 420nm band in 2D asynchronous spectrum to reflect the possible existence of intermolecular interaction between berberine and β-CyD.

The resultant 2D asynchronous spectrum is shown in **Figure 4-5**. The observation of cross peaks reveals that intermolecular interaction indeed occurs between berberine chloride and β-CyD. Moreover, the pattern of cross peak may provide additional information on the changes on the 420 nm band upon interaction with β-CyD.

Four cross peaks (Marked as cross peak A, B, C and D in **Figure 4-5**) appear in the spectral region around (420, 420) in 2D asynchronous spectrum. The four cross peaks is composed of two horizontal negative cross peaks (Cross peak A and D) and two vertical positive cross peaks (Cross peak B and C). These patterns suggest that both peak position and bandwidth of the 420 nm band change when berberine chloride interacts with β-CyD.

When we inspect 1D UV-Vis spectrum of berberine and 2D asynchronous spectrum, however, we found this situation is not that simple. In 1D UV-Vis spectrum, the 420 nm band is somewhat overlapped with the band at 340 nm.   In the corresponding 2D asynchronous spectrum, several groups of cross peaks in the spectral region around (420, 420), (340, 420), (420, 340) can be observed. The cross peaks A and B are also somewhat overlapped with cross peaks E, F G and H. The overlapping problem makes it impossible the measure the accurate intensities of cross peaks A and B. This complication makes it difficult to judge what happens on the 420 nm band under intermolecular interaction. Thus, careful analysis is performed on the pattern of cross peaks in the 2D asynchronous spectrum.

According to our previous work,[58] the pattern of cross peaks around (420, 420) in 2D asynchronous spectrum are relevant to the changes of peak position and bandwidth of the 420 nm band. Herein we define the peak position and bandwidth of the band around 420 nm of berberine that is dissolved in water alone as $X_{berberine}$ and $W_{berberine}$, respectively. When berberine interacts β-CyD, the corresponding peak position and

bandwidth of the band around 420 nm are denoted as $X_{berberine(\beta-CyD)}$ and $W_{berberine(\beta-CyD)}$, respectively. Then we define $\Delta X_{berberine}$ and $\Delta W_{berberine}$ as eq. 4-1

$$\Delta X_{berberine} = X_{berberine(\beta-CyD)} - X_{berberine}$$
$$\Delta W_{berberine} = W_{berberine(\beta-CyD)} - W_{berberine}$$

(4-1)

There are 9 possible situations listed in **Table 4-2**.

(1) The observation of cross peaks around (420, 420) precludes the possibility that both peak position and bandwidth remains unchanged. That is, situation 5 in **Table 4-2** is excluded.

(2) Second, although the measurement of the accurate intensity of cross peak A and B are affected cross peaks E, F, G and H, the result that four cross peaks occur in the cross peak group around (420, 420) is not affected. Thus, the possible situation that no changes on bandwidth of the 420 nm band upon intermolecular interaction is ruled out (i.e., situation 4 and situation 6 in **Table 4-2** are not possible.).

(3) The fact that cross peaks A and D are negative indicates that the bandwidth of the 420 nm band decreases under interaction with β-CyD. Thus, situations 7, 8 and 9 in **Table 4-2** are excluded.

(4) Then we consider whether the 420 nm band undergoes band shift under intermolecular interaction. According to our previous work,[58] cross peak with a diamond pattern appear when a band only undergoes change in bandwidth under intermolecular interaction. In this case, the pattern is composed of two horizontal cross peaks and two vertical cross peaks. The sign of two horizontal cross peaks are different from those of the two vertical cross peaks. However, the absolute intensities of the four cross peaks are the same. In the berberine/β-CyD system, cross peak A and B are affected by the cross peaks E, F, G and H. Thus, we cannot simply judge whether the 420 nm band undergoes band shift via the pattern of cross peaks around (420, 420). However, we notice that cross peak C and D are not affected by cross peaks E, F, G and H. If the 420nm band does not undergo band shift, the horizontal ordinate of cross peak C and vertical ordinate of cross peak D should be 420nm. This is not the case when we inspect **Figure 4-5**. As a matter of fact, the horizontal ordinate of cross peak C and vertical ordinate of cross peak D are 423 nm. Thus, the situation 2 in **Table 4-2** is excluded.

Up to now, there are only two possible situations are left (situation 1 and situation 3 in **Table 4-2**). The criterion is as follow:

If cross peak A is stronger than cross peak D, situation 3 is correct. If cross peak A is weaker than cross peak D, situation 1 is correct.

However, the problem is the intensity of cross peak A is affected by cross peak E and F because of band overlapping problem. This effect makes it difficult to judge whether cross peak A is stronger than cross peak D or not.

Fortunately, the sign of the cross peaks E and F is not the same as that of cross peak A.

To demonstrate this point, a horizontal slice is made at $y=420$ nm and the slice $f(x) = \Psi(x, 420)$ is shown in **Figure 4-6**. Two negative peak that located around 375 nm and 481 nm are marked as peaks A and D in **Figure 4-6**. Moreover, a positive peak around

350 nm is produced by cross peak E and F. Thus, the peak is labelled as E-F in **Figure 4-6**. **Figure 4-6** clearly indicates that the sign of peak A and peak E-F are opposite. Consequently, the observed intensity of cross peak A ($\Psi_{observed}(375, 425)$) is smaller than its actual value ($\Psi_{actual}(375, 425)$). Thus, we have

$$|\Psi_{actual}(375, 425)| > |\Psi_{observed}(375, 425)| \qquad (4\text{-}2)$$

In addition, we found that the observed the intensity of cross peak A is large than that of cross peak D ($\Psi_{observed}(481, 423)$). That is

$$|\Psi_{observed}(375, 425)| > |\Psi_{observed}(481, 423)| \qquad (4\text{-}3)$$

After combining Formula (3-2) and Formula (3-3), we have

$$|\Psi_{actual}(375, 425)| > |\Psi_{observed}(481, 423)| \qquad (4\text{-}4)$$

Therefore, we conclude that the 420 nm undergoes red shift and its bandwidth decreases upon interact with β-CyD.

The spectral behavior of the 420 nm band under the interaction with β-CyD is helpful for understanding why the solubility of berberine is improved when β-CyD is involved. According to its peak position, the 420 nm band can be safely assigned to the n-π* transition of berberine. Under the influence of β-CyD, the 420 nm band undergoes red shift. These results indicate the environment of the chromophore of berberine becomes more hydrophobic.[24] A plausible explanation to this phenomenon is that berberine come into the cavity of β-CyD, the hydrophobic nature of the cavity of β-CyD makes the n-π* transition band at 420 nm of berberine undergo a red-shift. Upon inspection of the molecular structure of berberine shown in **Figure 4-3**, we notice that most part of the chromophore is of hydrophobic nature. When berberine is dissolved in aqueous solution, π-π stacking takes place and results in reduction of the exposure of hydrophobic part in hydrophilic environment. However, the π-π stacking leads to aggregation of berberine and brings about the decreasing of the solubility of berberine in water. In the berberine/β-CyD system, berberine enter the hydrophobic cavity and form a berberine/β-CyD clusterate. The berberine/β-CyD clusterate can be solubilized via the hydrophilic surface of β-CyD, thereby increasing the solubility of berberine. Additionally, the environment of berberine becomes more homegenous when it is cluthrated by β-CyD. This is the reason the bandwidth of the 420 nm peak decreases under the interaction with β-CyD.

Conclusion

In this work, we investigated the interaction between berberine chloride and β-CyD by using 2D asynchronous UV-Vis spectrum. The observation of cross peaks around (420, 420) in 2D asynchronous spectrum confirms that a specific intermolecular interaction indeed occurs between berberine chloride and β-CyD. The difficulty in this system is that some cross peaks in the cross peak group around (420,420) overlap with the cross peaks in cross peak groups around (340, 420) and (420, 340). This overlap makes it difficult to judge what happen on the 420 nm band under intermolecular interaction. However, careful analysis demonstrate that the 420 nm band of berberine undergoes red-shift and its bandwidth decrease upon interacting with β-CyD. The red-shift of the 420 nm band that can be assigned to n-π* transition indicates the

environment of berberine become more hydrophobic. The above spectral behavior is helpful in understanding why the solubility of berberine is enhanced by β-CyD.

References

1. Battu, S. K.; Repka, M. A.; Maddineni, S.; Chittiboyina, A. G.; Avery, M. A.; Majumdar, S. Physicochemical Characterization of Berberine Chloride: A Perspective in the Development of a Solution Dosage Form for Oral Delivery. *Aaps. Pharmscitech.* **2010**, *11*, 1466-1475.

2. Zuo, F.; Nakamura, N.; Akao, T.; Hattori, M. Pharmacokinetics of Berberine and Its Main Metabolites in Conventional and Pseudo Germ-Free Rats Determined by Liquid Chromatography/Ion Trap Mass Spectrometry. *Drug Metab. Dispos.* **2006**, *34*, 2064-2072.

3. Taylor, C. T.; Winter, D. C.; Skelly, M. M.; O'Donoghue, D. P.; O'Sullivan, G. C.; Harvey, B. J.; Baird, A. W. Berberine Inhibits Ion Transport in Human Colonic Epithelia. *Eur. J. Pharmacol.* **1999**, *368*, 111-118.

4. Kong, W. J.; Wei, J.; Abidi, P.; Lin, M. H.; Inaba, S.; Li, C.; Wang, Y. L.; Wang, Z. Z.; Si, S. Y.; Pan, H. N.; Wang, S. K.; Wu, J. D. et al. Berberine is a Novel Cholesterol-Lowering Drug Working through a Unique Mechanism Distinct from Statins. *Nat. Med.* **2004**, *10*, 1344-1351.

5. Lee, Y. S.; Kim, W. S.; Kim, K. H.; Yoon, M. J.; Cho, H. J.; Shen, Y.; Ye, J. M.; Lee, C. H.; Oh, W. K.; Kim, C. T. et al. Berberine, a Natural Plant Product, Activates Amp-Activated Protein Kinase with Beneficial Metabolic Effects in Diabetic and Insulin-Resistant States. *Diabetes* **2006**, *55*, 2256-2264.

6. Yin, J.; Hu, R. M.; Chen, M. D.; Tang, J. F.; Li, F. Y.; Yang, Y.; Chen, J. L. Effects of Berberine on Glucose Metabolism in Vitro. *Metabolism* **2002**, *51*, 1439-1443.

7. Zhang, Z. G.; Zhang, H. Z.; Li, B.; Meng, X. J.; Wang, J. Q.; Zhang, Y. F.; Yao, S. S.; Ma, Q. Y.; Jin, L. N.; Yang, J. et al., Berberine Activates Thermogenesis in White and Brown Adipose Tissue. *Nat. Commun.* **2014**, *5,* 6493-6507.

8. Le Tran, Q.; Tezuka, Y.; Ueda, J. Y.; Nguyen, N. T.; Maruyama, Y.; Begum, K.; Kim, H. S.; Wataya, Y.; Tran, Q. K.; Kadota, S. In Vitro Antiplasmodial Activity of Antimalarial Medicinal Plants Used in Vietnamese Traditional Medicine. *J. Ethnopharmacol.* **2003**, *86*, 249-252.

9. Ko, W. H.; Yao, X. Q.; Lau, C. W.; Law, W. I.; Chen, Z. Y.; Kwok, W.; Ho, K.; Huang, Y. Vasorelaxant and Antiproliferative Effects of Berberine. *Eur. J. Pharmacol.* **2000**, *399*, 187-196.

10. Sanchez-Chapula, J. Increase in Action Potential Duration and Inhibition of the Delayed Rectifier Outward Current Ik by Berberine in Cat Ventricular Myocytes. *Br. J. Pharmacol.* **1996**, *117*, 1427-34.

11. Tsai, P. L.; Tsai, T. H., Hepatobiliary Excretion of Berberine. *Drug Metab. Dispos.* **2004**, *32*, 405-12.

12. Bilensoy, E. *Cyclodextrins in Pharmaceutics, Cosmetics, and Biomedicine: Current and Future Industrial Applications*, John Wiley & Sons, Inc., Hoboken, New Jersey, U.S.A., 2011.

13. Crini, G. Review: A History of Cyclodextrins. *Chem. Rev.* **2014**, *114*, 10940-75.

14. Szejtli, J. Introduction and General Overview of Cyclodextrin Chemistry. *Chem. Rev.* **1998**, *98*, 1743-1754.

15. Muller, B. W.; Brauns, U. Hydroxypropyl-Beta-Cyclodextrin Derivatives - Influence of Average Degree of Substitution on Complexing Ability and Surface-Activity. *J. Pharm. Sci.* **1986**, *75*, 571-572.

16. Yoshida, A.; Yamamoto, M.; Irie, T.; Hirayama, F.; Uekama, K. Some Pharmaceutical Properties of 3-Hydroxypropyl-Beta-Cyclodextrins and 2,3-Dihydroxypropyl-Beta-Cyclodextrins and Their Solubilizing and Stabilizing Abilities. *Chem. Pharm. Bull.* **1989**, *37*, 1059-1063.

17. Hirayama, F.; Usami, M.; Kimura, K.; Uekama, K. Crystallization and Polymorphic Transition Behavior of Chloramphenicol Palmitate in 2-Hydroxypropyl-Beta-Cyclodextrin Matrix. *J. Inclus. Phenom. Mol.* **1996**, *25*, 165-168.

18. Chowdary, K. P. R.; Reddy, G. K. Complexes of Nifedipine with β- and Hydroxypropyl-β-cyclodextrin in the Design of Nifedipine SR Tablets. *Indian J. Pharm. Sci.* **2002**, *64*, 142-146.

19. Cserhati, T.; Forgacs, E. *Cyclodextrins in Chromatography, The Royal Society of Chemistry*, Cambridge, U.K., 2003.

20. Hapiot, F.; Tilloy, S.; Monflier, E. Cyclodextrins as Supramolecular Hosts for Organometallic Complexes. *Chem. Rev.* **2006**, *106*, 767-781

21. Dodziuk, H. *Cyclodextrins and their Complexes*, WILEY-VCH Verlag GmbH&Co. KGaA: Weinheim, Germany, 2006.

22. Szejtli, J. *Cyclodextrin Technology*; Kluwer Academic Publishers: Dordrecht, U.S.A., 1988.

23. Kamigauchi, M.; Kawanishi, K.; Sugiura, M.; Ohishi, H.; Ishida, T. Gamma-Cyclodextrin as Inhibitor of the Precipitation Reaction between Berberine and Glycyrrhizin in Decoctions of Natural Medicines: Interaction Studies of Cyclodextrins with Glycyrrhizin and Glycyrrhetic Acid by H-1-Nmr Spectroscopy and Molecular-Dynamics Calculation. *Helv. Chim. Acta.* **2008**, *91*, 1614-1624.

24. Turro N. J.; Ramamurthy V.; Scaiano J. C.; *Modern Molecular Photochemistry of Organic Molecules* (in Chinese); Chemical Industry Press: Beijing, China, 2015.

**Table 4-1** Concentrations of Berberine Chloride and β-CyD in Three Groups of Solutions

Index of the solutions	Group 1		Group 2		Group 3	
	$C_{berberine}$ $(\times 10^{-5}g/ml)$	$C_{\beta\text{-CyD}}$ $(\times 10^{-4}g/ml)$	$C_{berberine}$ $(\times 10^{-5}g/ml)$	$C_{\beta\text{-CyD}}$ $(\times 10^{-4}g/ml)$	$C_{berberine}$ $(\times 10^{-5}g/ml)$	$C_{\beta\text{-CyD}}$ $(\times 10^{-4}g/ml)$
1	3.97	7.05	0	7.05	3.97	0
2	2.98	7.05	0	7.05	2.98	0
3	1.98	7.05	0	7.05	1.98	0
4	0.99	7.05	0	7.05	0.99	0

Table 4-2 Nine Possible Situations Concerning the Changes on Peak Position and Bandwidth of the 420 nm Band of Berberine

Situation	Spectral variable	
	$\Delta X_{berberine}$	$\Delta W_{berberine}$
1	$\Delta X<0$	$\Delta W<0$
2	$\Delta X=0$	$\Delta W<0$
3	$\Delta X>0$	$\Delta W<0$
4	$\Delta X<0$	$\Delta W=0$
5	$\Delta X=0$	$\Delta W=0$
6	$\Delta X>0$	$\Delta W=0$
7	$\Delta X<0$	$\Delta W>0$
8	$\Delta X=0$	$\Delta W>0$
9	$\Delta X>0$	$\Delta W>0$
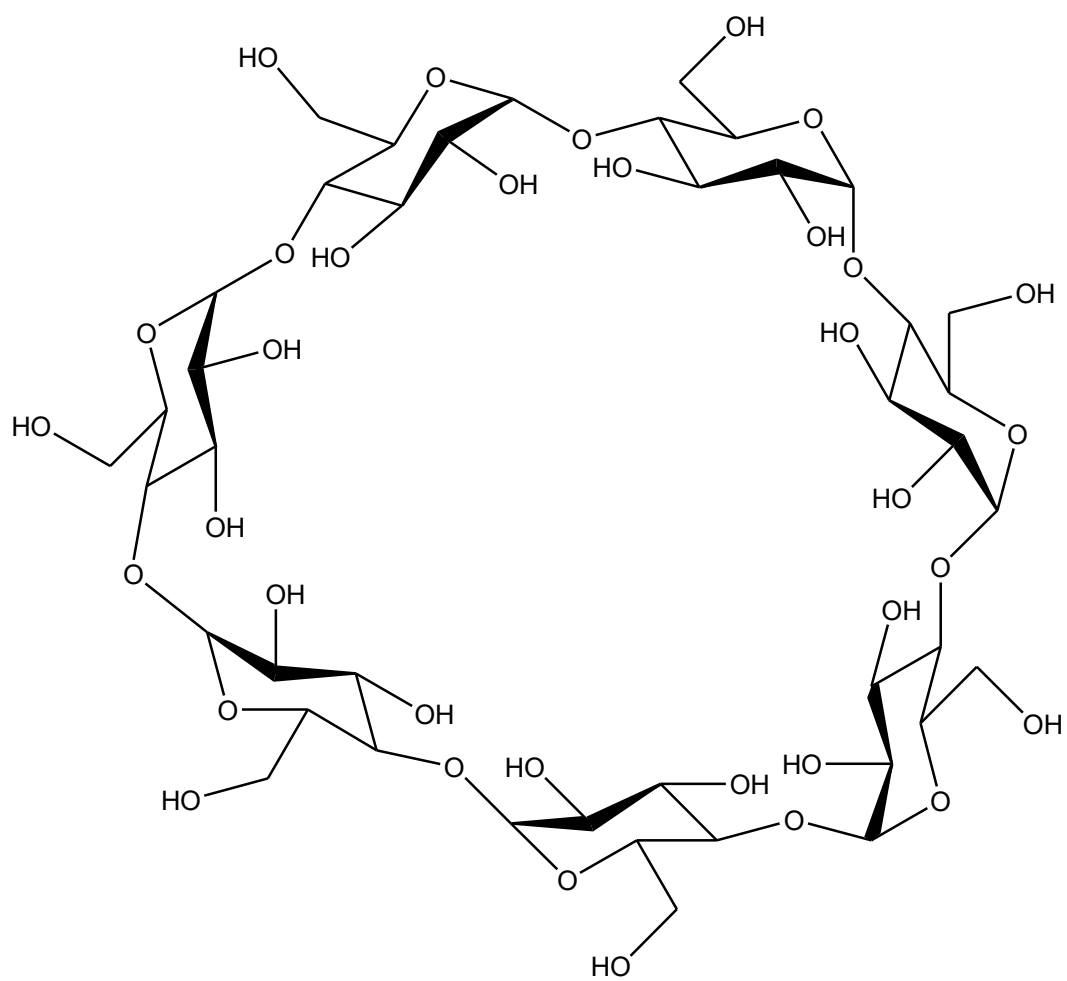
Figure 4-1 Molecular Structures of β-Cyclodextrin
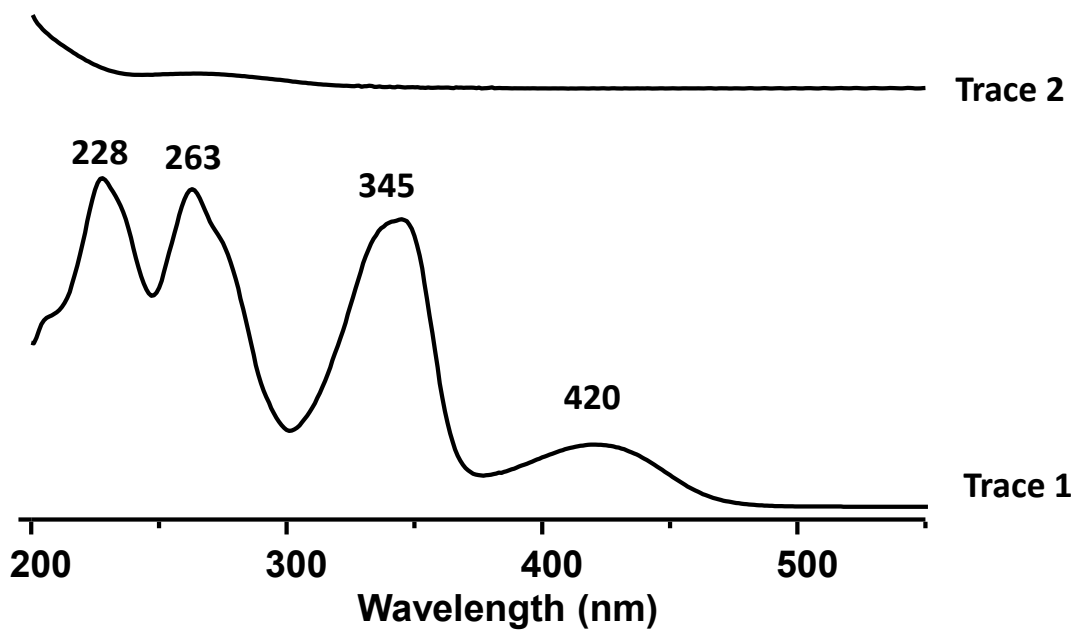
Figure 4-2 UV-Vis Spectra of Berberine Chloride (trace 1) and β-CyD (trace 2).
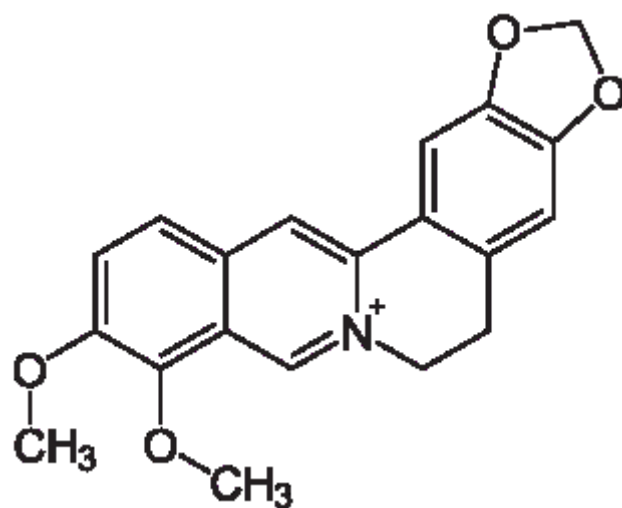
Figure 4-3 Molecular Structures of Berberine
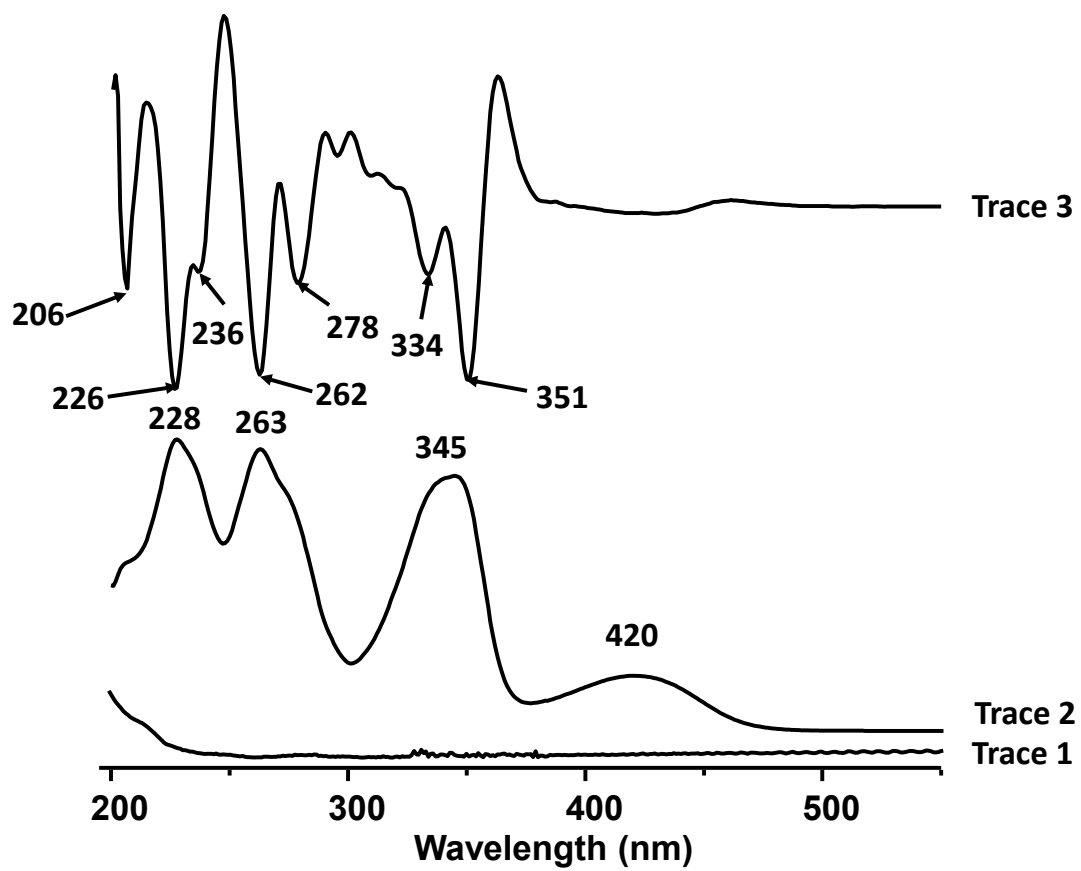
Figure 4-4 UV-Vis Spectra of Water (trace 1), Berberine Chloride (trace 2) and Second Derivative Spectrum of the UV-Vis Spectrum of Berberine Chloride (trace 3).
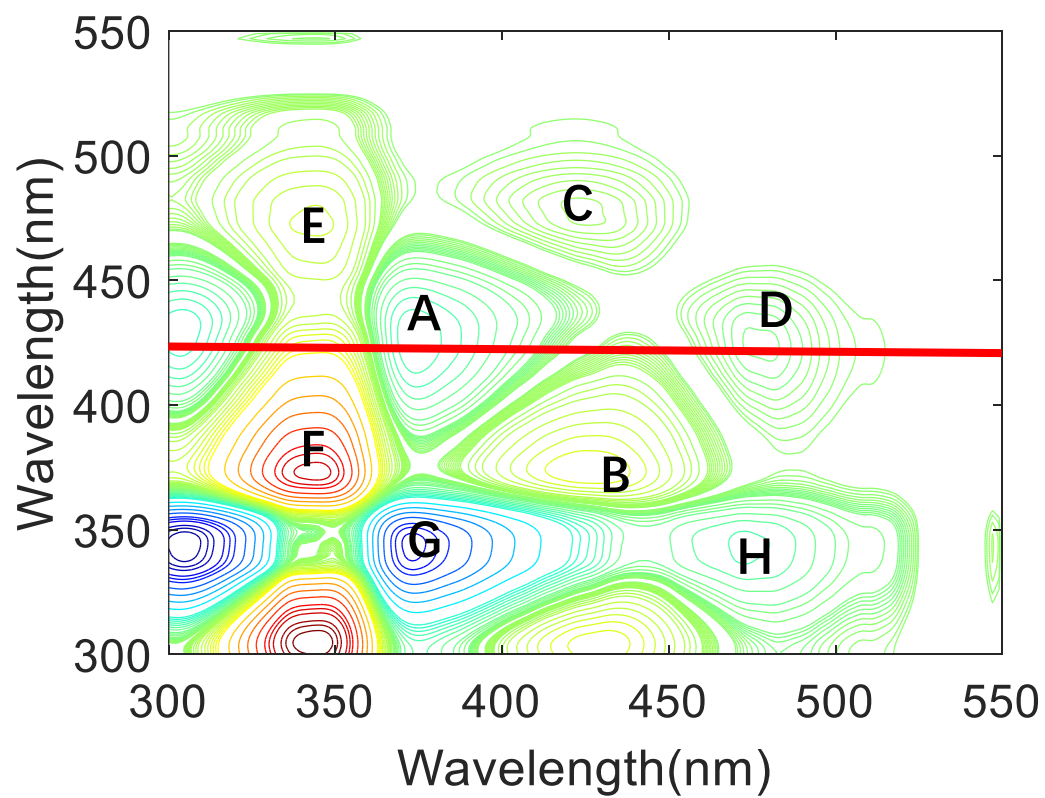
Figure 4-5 2D Asynchronous Spectrum of Berberine/β-CyD System. A Horizontal Slice was Made at y=420 nm (the Horizontal Red Line)
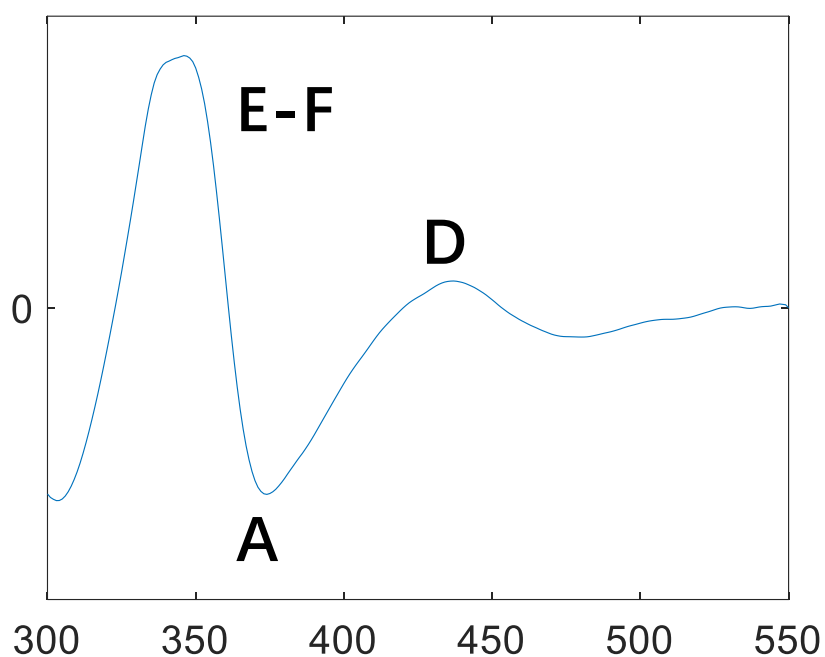
Figuere 2-6 Horizontal Slice from the 2D Asynchronous Spectrum at y=420 nm. Cross Peaks A and D in **Figure 4-5** Produce two Negative Peaks (marked as A and D). Because of Cross Peaks E and F in **Figure 4-5**, a Positive Peak Around 350 nm is Present and Marked as E-F. Peak A and peak E-F are Overlapped and the Signs of the Two Peaks are Opposite.

Supporting information 3
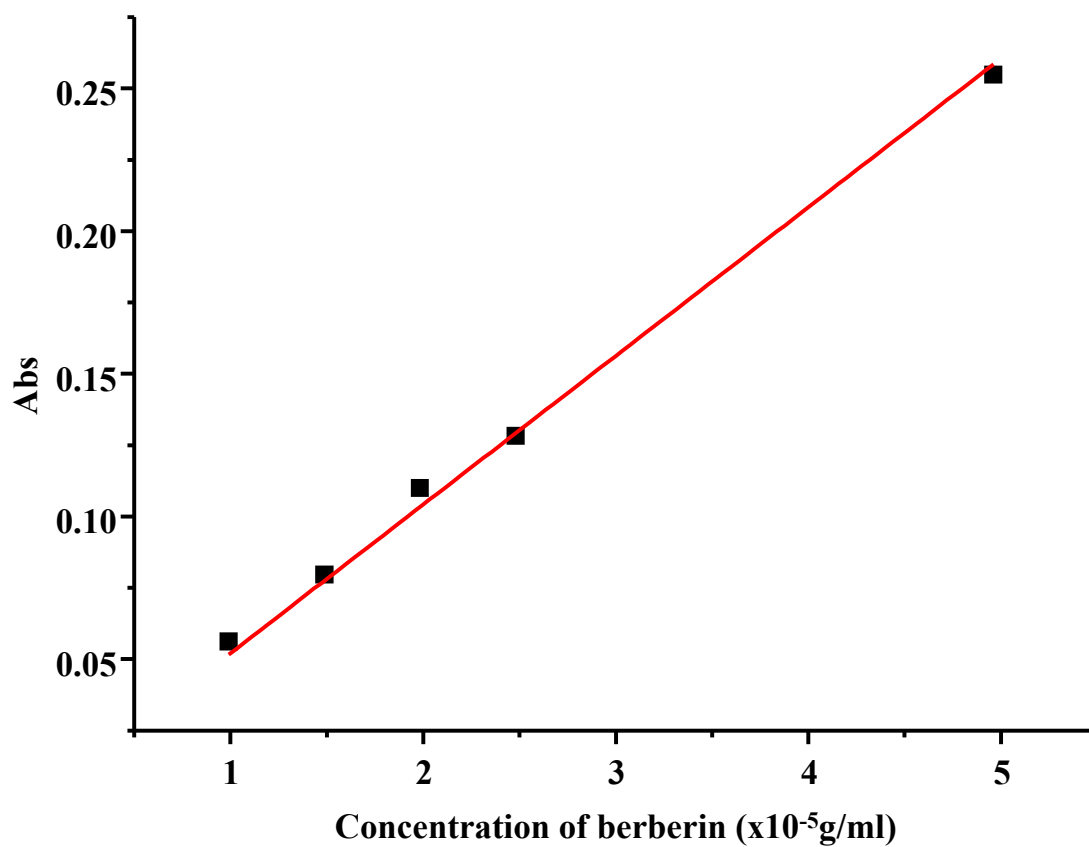
Figure S4-1 Linear Fitting Results of the Relationship between Concentration of Berberine and the Absorbance of the 420 nm Band in the UV-Vis Spectra of Berberine Chloride (R^2=0.9990).

Chapter 4

Investigation on Intermolecular Interaction between Two Solutes

where One Solute Occurs in Two States

Introduction

When intermolecular interaction between two solutes is investigated by using the OSD and relevant approaches, we assume that each of the solutes should be in a single state. However, many substances in the real world may occur in more than one state when they are dissolved in a solution. For example, equilibrium may set up between two distinct conformers as a solute is dissolved. In many cases, the solute may act as a weak base so that it may exist in different protonation states. Additionally, some solute molecules may undergo keto-enol tautomerism. In the above instances, additional complexity will be brought about when a second solute is introduced and intermolecular interactions occur between the first solute in different forms and the second solute. Understanding on the nature of the interactions in these systems are very important to enhance our research on molecular self-assembly and molecular catalysis. Upon to now, the use of OSD and relevant approaches on these multi-state systems has not been explored.

The DAOSD approach, developed in our previous work, is a powerful spectral analysis technique to reveal subtle spectral changes caused by intermolecular interaction. The full description of the DAOSD approach can be found in our previous work [41] and a brief introduction is provided in the first part of supporting information. In this chapter, mathematical analysis and computer simulation are carried out to study the spectral behaviors of a pair of 2D asynchronous spectra generated by using the DAOSD approach.

Establishment of a model system

The chemical system studied here is a series of solutions where two solutes (denoted as P and Q) are dissolved. In this system, P exists in two distinct inter-conversable states (denoted as P_1 and P_2, respectively). The inter-conversion is specified in terms of eq. 5-1 and the equilibrium constant is K_0.

$$P_1 \overset{K_0}{\leftrightarrow} P_2 \tag{5-1}$$

Under intermolecular interaction between P_1 and Q, part of P_1 undergoes subtle structure variation and converts into U_1 and part of Q converts into V_1. Similarly, part of P_2 converts into U_2 and part of Q converts into V_2 due to the interaction between P_2 and Q. These interactions could be specified in terms of eq. 5-2) and eq. 5-3 where the corresponding equilibrium constants are K_1 and K_2, respectively.

$$P_1 + Q \overset{K_1}{\leftrightarrow} U_1 + V_1 \tag{5-2}$$

$$P_2 + Q \overset{K_2}{\leftrightarrow} U_2 + V_2 \tag{5-3}$$
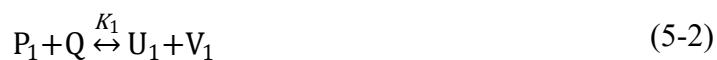
The spectral function of each substance (P_1, P_2, Q, U_1, U_2, V_1 and V_2) possesses only one characteristic peak. The peak for each chemical species is represented by a Gaussian function as shown in eq. 5-4.

$$f_j(x) = \varepsilon_j * e^{-(\ln2)*\left[\frac{(X-X_j)^2}{W_j^2}\right]} = \varepsilon_j g_j(x) \tag{5-4}$$

where j is the index of the seven chemical species, i.e., P_1, P_2, Q, U_1, U_2, V_1 and V_2; ε_j, X_j, and W_j are the corresponding molar absorptivity, peak position and bandwidth (half-width at half-height, HWHH) of the characteristic band of the jth chemical species; $g_j(x)$ is the peak shape function that is relevant to peak position and bandwidth.

To reflect the spectral behaviors of the 2D asynchronous spectra generated by using the DAOSD approach clearly, we assume that the characteristic peaks of P_1, P_2 and Q are not overlapped with one another. However, the peak of P_1 is highly overlapped with that of U_1 since interaction is quite weak and only induces subtle spectral variation. Similarly, the peak of P_2 is highly overlapped with that of U_2 and the peak of Q is overlapped severely with the peaks of V_1 and V_2. The peak parameters of P_1, P_2, Q, U_1, V_I, U_2 and V_2 are listed in **Table 5-1**. The subtle variations of peak parameters (i.e., absorptivity, bandwidth and peak position) of P_1, P_2 and Q are defined in **Table 5-2.**

Construction of a pair of 2D asynchronous spectra based on the DAOSD approach

According to the DAOSD approach, two groups of solutions are simulated. The initial concentrations of P and Q of the two groups of solutions are listed in **Table 5-3**.

For the ith solution, the simulated 1D spectrum is constructed by using eq. 5-5 according to the Beer-Lambert's Law.

$$A^i(x) = C_{P_1}^{i(eq)} lf_{P_1}(x) + C_{P_2}^{i(eq)} lf_{P_2}(x) + C_Q^{i(eq)} lf_Q(x) + C_{U_1}^{i(eq)} lf_{U_1}(x) +$$

$$C_{U_2}^{i(eq)} lf_{U_2}(x) + C_{V_1}^{i(eq)} lf_{V_1}(x) + C_{V_2}^{i(eq)} lf_{V_2}(x) \tag{5-5}$$

where $f_{P_1}(x)$, $f_{P_2}(x)$, $f_Q(x)$, $f_{U_1}(x)$, $f_{U_2}(x)$, $f_{V_1}(x)$ and $f_{V_2}(x)$ are spectral functions of P_1, P_2, Q, U_1, U_2, V_1 and V_2; l is the path-length and is set as 1 for convenience; $C_{P_1}^{i(eq)}$, $C_{P_2}^{i(eq)}$, $C_Q^{i(eq)}$, $C_{U_1}^{i(eq)}$, $C_{U_2}^{i(eq)}$, $C_{V_1}^{i(eq)}$ and $C_{V_2}^{i(eq)}$ are equilibrium concentrations of P_1, P_2, Q, U_1, U_2, V_1 and V_2. The method of obtaining the equilibrium concentrations of the above substances is discussed in second part of supporting information.

To construct 2D asynchronous spectra, dynamic spectrum of the ith solution is generated by using eq. 5-6

$$\tilde{A}^i(x) = \tilde{C}_{P_1}^{i(eq)} f_{P_1}(x) + \tilde{C}_{P_2}^{i(eq)} f_{P_2}(x) + \tilde{C}_Q^{i(eq)} f_Q(x) + \tilde{C}_{U_1}^{i(eq)} f_{U_1}(x) +$$

$$\tilde{C}_{U_2}^{i(eq)} f_{U_2}(x) + \tilde{C}_{V_1}^{i(eq)} f_{V_1}(x) + \tilde{C}_{V_2}^{i(eq)} f_{V_2}(x) \tag{5-6}$$

where

$$\tilde{C}_{P_1}^{i(eq)} = C_{P_1}^{i(eq)} - C_{P_1}^{eq(av)} \tag{5-7a}$$

$$\tilde{C}_{P_2}^{i(eq)} = C_{P_2}^{i(eq)} - C_{P_2}^{eq(av)} \tag{5-7b}$$

$$\tilde{C}_Q^{i(\text{eq})} = C_Q^{i(\text{eq})} - C_Q^{\text{eq(av)}} \tag{5-7c}$$

$$\tilde{C}_{U_1}^{i(\text{eq})} = C_{U_1}^{i(\text{eq})} - C_{U_1}^{\text{eq(av)}} \tag{5-7d}$$

$$\tilde{C}_{U_2}^{i(\text{eq})} = C_{U_2}^{i(\text{eq})} - C_{U_2}^{\text{eq(av)}} \tag{5-7e}$$

$$\tilde{C}_{V_1}^{i(\text{eq})} = C_{V_1}^{i(\text{eq})} - C_{V_1}^{\text{eq(av)}} \tag{5-7f}$$

$$\tilde{C}_{V_2}^{i(\text{eq})} = C_{V_2}^{i(\text{eq})} - C_{V_2}^{\text{eq(av)}} \tag{5-7g}$$

$\tilde{C}_{P_1}^{i(\text{eq})}$, $\tilde{C}_{P_2}^{i(\text{eq})}$, $\tilde{C}_Q^{i(\text{eq})}$, $\tilde{C}_{U_1}^{i(\text{eq})}$, $\tilde{C}_{U_2}^{i(\text{eq})}$, $\tilde{C}_{V_1}^{i(\text{eq})}$ and $\tilde{C}_{V_2}^{i(\text{eq})}$ are the dynamic equilibrium concentrations of P_1, P_2, Q, U_1, U_2, V_1 and V_2 in the ith solution. The average concentrations of P_1, P_2, Q, U_1, U_2, V_1 and V_2 of the group of solutions are defined in eq. 5-8.

$$C_{P_1}^{\text{eq(av)}} = \frac{1}{n}\sum_{i=1}^{n} C_{P_1}^{i(\text{eq})} \tag{5-8a}$$

$$C_{P_2}^{\text{eq(av)}} = \frac{1}{n}\sum_{i=1}^{n} C_{P_2}^{i(\text{init})} \tag{5-8b}$$

$$C_Q^{\text{eq(av)}} = \frac{1}{n}\sum_{i=1}^{n} C_Q^{i(\text{init})} \tag{5-8c}$$

$$C_{U_1}^{\text{eq(av)}} = \frac{1}{n}\sum_{i=1}^{n} C_{U_1}^{i(\text{eq})} \tag{5-8d}$$

$$C_{U_2}^{\text{eq(av)}} = \frac{1}{n}\sum_{i=1}^{n} C_{U_2}^{i(\text{init})} \tag{5-8e}$$

$$C_{V_1}^{\text{eq(av)}} = \frac{1}{n}\sum_{i=1}^{n} C_{V_1}^{i(\text{eq})} \tag{5-8f}$$

$$C_{V_2}^{\text{eq(av)}} = \frac{1}{n}\sum_{i=1}^{n} C_{V_2}^{i(\text{init})} \tag{5-8g}$$

Asynchronous correlation spectrum can be constructed via eq. 5-9.

$$\Psi(x,y) = \frac{1}{n-1}\vec{\tilde{A}}^{\text{T}}(x)\mathbf{N}\vec{\tilde{A}}(y) \tag{5-9}$$

where $\vec{\tilde{A}}(x)$ and $\vec{\tilde{A}}(y)$ are the dynamic spectral vector at the spectral coordination x and y, respectively; Superscript T stands for transposition; n is the number of solutions used to construct the 2D asynchronous spectrum; $\mathbf{N}$ is the Hilbert-Noda transformation

matrix. The above calculations were performed by using a program that is working under MATLAB.

Results and Discussion

1 Mathematical properties of 2D asynchronous spectrum generated by using the DAOSD approach on the model system

Based on the mathematical analysis described in the second part of supporting information, we have obtained the relationship among $\tilde{C}_P^{init}$, $\tilde{C}_Q^{init}$, $\tilde{C}_{P_1}^{i(eq)}$, $\tilde{C}_{P_2}^{i(eq)}$, $\tilde{C}_Q^{i(eq)}$, $\tilde{C}_{U_1}^{i(eq)}$, $\tilde{C}_{U_2}^{i(eq)}$, $\tilde{C}_{V_1}^{i(eq)}$ and $\tilde{C}_{V_2}^{i(eq)}$. In other words, the dynamic equilibrium concentrations of the six substances (P_1, P_2, Q, U_2, V_1, and V_2) can be expressed by $\tilde{C}_P^{init}$, $\tilde{C}_Q^{init}$ and $\tilde{C}_{U_1}^{i(eq)}$ quantitatively. Thus, the dynamic spectral function for the solution i can be expressed as eq. 5-10 after combining with eq. 5-6.

$$\widetilde{A}^i(x) = \tilde{C}_P^{i(init)}\left[sf_{P_1}(x) + sK_0f_{P_2}(x)\right] + \tilde{C}_Q^{i(init)}f_Q(x)$$

$$+ \tilde{C}_{U_1}^{i(eq)}\left\{f_{U_1}(x) + f_{V_1}(x) + d\left[f_{U_2}(x) + f_{V_2}(x)\right]\right. \tag{5-10}$$

$$\left. - (1+d)\left[sf_{P_1}(x) + sK_0f_{P_2}(x)\right] - (1+d)f_Q(x)\right\}$$

To simplify the expression, eq. 5-10 can be described as eq. 5-11.

$$\widetilde{A}^i(x) = \tilde{C}_P^{init}F(x) + \tilde{C}_Q^{init}f_Q(x) + \tilde{C}_{U_1}^{i(eq)}H(x) \tag{5-11}$$

where $F(x)$, $H(x)$, s and d are

$$F(x) = sf_{P_1}(x) + sK_0f_{P_2}(x) \tag{5-12}$$

$$H(x) = f_{U_1}(x) + f_{V_1}(x) + df_{U_2}(x) + df_{V_2}(x) - s(1+d)f_{P_1}(x) - sK_0(1+d)f_{P_2}(x) - (1+d)f_Q(x) \tag{5-13}$$

$$s = \frac{1}{1+K_0} \tag{5-14}$$

$$d = \sqrt{\frac{K_0 * K_2}{K_1}} \tag{5-15}$$

The corresponding 2D asynchronous spectrum is expressed as eq. 5-16.

$$\Psi(x,y) = \sum_{i=1}^{9} M_i(x,y) \tag{5-16}$$

where

$$M_1(x,y) = F(x)F(y)\left(\vec{\tilde{C}}_P^{init}\right)^T N\vec{\tilde{C}}_P^{init}$$

$$M_2(x,y) = f_Q(x)f_Q(y)\left(\vec{\tilde{C}}_Q^{init}\right)^T N\vec{\tilde{C}}_Q^{init} \tag{5-17}$$

$$\mathbf{M}_3(x,y) = F(x)f_Q(y)\left(\vec{\tilde{\mathbf{C}}}_P^{\text{init}}\right)^T \mathbf{N}\vec{\tilde{\mathbf{C}}}_Q^{\text{init}}$$

$$\mathbf{M}_4(x,y) = f_Q(x)F(y)\left(\vec{\tilde{\mathbf{C}}}_Q^{\text{init}}\right)^T \mathbf{N}\vec{\tilde{\mathbf{C}}}_P^{\text{init}}$$

$$\mathbf{M}_5(x,y) = F(x)H(y)\left(\vec{\tilde{\mathbf{C}}}_P^{\text{init}}\right)^T \mathbf{N}\vec{\tilde{\mathbf{C}}}_{U_1}^{\text{eq}}$$

$$\mathbf{M}_6(x,y) = H(x)F(y)\left(\vec{\tilde{\mathbf{C}}}_{U_1}^{\text{eq}}\right)^T \mathbf{N}\vec{\tilde{\mathbf{C}}}_P^{\text{init}}$$

$$\mathbf{M}_7(x,y) = f_Q(x)H(y)\left(\vec{\tilde{\mathbf{C}}}_Q^{\text{init}}\right)^T \mathbf{N}\vec{\tilde{\mathbf{C}}}_{U_1}^{\text{eq}}$$

$$\mathbf{M}_8(x,y) = H(x)f_Q(y)\left(\vec{\tilde{\mathbf{C}}}_{U_1}^{\text{eq}}\right)^T \mathbf{N}\vec{\tilde{\mathbf{C}}}_Q^{\text{init}}$$

$$\mathbf{M}_9(x,y) = H(x)H(y)\left(\vec{\tilde{\mathbf{C}}}_{U_1}^{\text{eq}}\right)^T \mathbf{N}\vec{\tilde{\mathbf{C}}}_{U_1}^{\text{eq}}$$

When there is no intermolecular interaction among P and Q, the products of intermolecular interaction (U_1, U_2, V_1 and V_2) will not be produced. That is to say, $\tilde{C}_{U_1}^{i(\text{eq})}$ should be zero. As a result, terms $\mathbf{M}_5(x,y) \sim \mathbf{M}_9(x,y)$ in eq. 5-17 should be zero.

Moreover, no cross peak should be produced when no intermolecular interaction occurs between P and Q if 2D asynchronous spectrum can reflect intermolecular interaction in a reliable manner. That is to say, the summation of $\mathbf{M}_1(x,y)$, $\mathbf{M}_2(x,y)$, $\mathbf{M}_3(x,y)$ and $\mathbf{M}_4(x,y)$ should be zero.

When the DAOSD approach is adopted, a pair of 2D asynchronous spectra, namely $\Psi_P(x,y)$ and $\Psi_Q(x,y)$, are constructed. The Hilbert-Noda matrix possesses the following property:

For any given n-dimensional vector $\vec{\mathbf{A}}$ $\vec{\mathbf{B}}$, eq. 5-18 and eq. 5-19 are always satisfied.

$$\vec{\mathbf{A}}^T\mathbf{N}\vec{\mathbf{B}} = 0 \tag{5-18}$$

$$\vec{\mathbf{A}}^T\mathbf{N}\vec{\mathbf{B}} = -\vec{\mathbf{B}}^T\mathbf{N}\vec{\mathbf{A}} \tag{5-19}$$

Thus, terms $R_1(x,y)$ and $R_2(x,y)$ are zero and can be naturally removed. In the generation of $\Psi_P(x,y)$, $\vec{\mathbf{C}}_P^{\text{init}}$ is a zero vector since the initial concentration of P is a constant. As a result, terms $R_3(x,y)$ and $R_4(x,y)$ are zero. Similarly, $\vec{\mathbf{C}}_Q^{\text{init}}$ is a zero vector in the generation of $\Psi_Q(x,y)$ so that the corresponding $R_3(x,y)$ and $R_4(x,y)$ are also zero. That is to say, the summation of $R_1(x,y)$, $R_2(x,y)$, $R_3(x,y)$ and $R_4(x,y)$ are zero in both $\Psi_P(x,y)$ and $\Psi_Q(x,y)$. When no intermolecular interaction occurs between P and Q, no cross peak will be produced in either $\Psi_P(x,y)$ or $\Psi_Q(x,y)$ even if P occurs in two exchangeable states.

The results of computer simulation confirm the above conclusion. In a model system, no intermolecular interaction occurs between P and Q which is achieved by

setting the values of K_1 and K_2 to be zero simultaneously. No cross peak is observed in either $\Psi_P(x, y)$ or $\Psi_Q(x, y)$ no matter what K_0 value is applied (The third part of supporting information).

When intermolecular interaction occurs between P and Q, which can be achieved by setting either of K_1 or K_2 to be nonzero, cross peaks are produced in the corresponding 2D asynchronous spectra. An example is provided in **Figure 5-1**. The initial concentrations of P and Q of the two groups of solutions are listed in **Table 5-3**.

Based on the above results, we come to a conclusion that the DAOSD approach can reflect intermolecular interaction between P and Q reliably even if P occurs in two exchangeable states.

General spectral properties of 2D asynchronous spectrum in the system

Based on the above result, we investigate the spectral properties of the pair of spectra generated by using the DAOSD approach. As described above, terms $\mathbf{M}_1(x, y)$ $\sim \mathbf{M}_4(x, y)$ in eq. 5-17 are zero. In addition, term $\mathbf{M}_9(x, y)$ is also zero according to the mathematical property of the Hilbert-Noda matrix shown in eq. 5-18.

When the spectra of the first group of solutions are used to generate Ψ_P, the dynamic initial concentration of P is zero since the initial concentration of P is a constant. As a result, terms $R_5(x, y)$ and $R_6(x, y)$ are zero. Thus we have

$$\Psi_P(x, y) = \mathbf{M}_7(x, y) + \mathbf{M}_8(x, y) \tag{5-20}$$

Accroding to Eq. (5-17), we have

$$\Psi_P(x, y) = f_Q(x)H(y)\left(\vec{\tilde{\mathbf{C}}}_Q^{init}\right)^T \mathbf{N}\vec{\tilde{\mathbf{C}}}_{U_1}^{eq} + H(x)f_Q(y)\left(\vec{\tilde{\mathbf{C}}}_{U_1}^{eq}\right)^T \mathbf{N}\vec{\tilde{\mathbf{C}}}_Q^{init} \tag{5-21}$$

Because of the property of the Hilbert-Noda matrix expressed by eq. 5-19, we have

$$\Psi_P(x, y) = \left[f_Q(x)H(y) - H(x)f_Q(y)\right]\left(\vec{\tilde{\mathbf{C}}}_Q^{init}\right)^T \mathbf{N}\vec{\tilde{\mathbf{C}}}_{U_1}^{eq} \tag{5-22}$$

In a similar manner, $\Psi_Q(x, y)$ can be expressed as eq. 5-23.

$$\Psi_Q(x, y) = \left[F(x)H(y) - H(x)F(y)\right]\left(\vec{\tilde{\mathbf{C}}}_P^{init}\right)^T \mathbf{N}\vec{\tilde{\mathbf{C}}}_{U_1}^{eq} \tag{5-23}$$

As is shown in **Scheme 5-1A**, absorption peaks appear in the following three regions (ω_1, ω_2, ω_3) in the 1D spectra. Accordingly, absorption peaks of the seven substances (P$_1$, P$_2$, Q, U$_1$, V$_1$, U$_2$ and V$_2$) and the corresponding values of H(x) and F(x) in different regions are summarized in **Table 5-4** and **Table 5-5**.

In the corresponding 2D asynchronous spectra, cross peaks may appear in the nine regions defined by $\omega_i \otimes \omega_j$ (where $i, j \in \{1, 2, 3\}$, shown in **Scheme 5-1B**). According to **Table 5-4** and **Table 5-5**, the expressions of $\Psi_P(x, y)$ or $\Psi_Q(x, y)$ in the nine regions are listed in **Table 5-6A** and **Table 5-6B,** respectively.

Based on the above results, we classify the eighteen regions in the pair of 2D asynchronous spectra ($\Psi_P(x, y)$ and $\Psi_Q(x, y)$) into six types.

Type 1: regions I, II, IV and V of $\Psi_P(x, y)$ and region IX of $\Psi_Q(x, y)$

If a point is in regions I, II, IV and V, $\Psi_P(x, y)$ is always zero according to **Table 5-6A**. That is to say, no cross peaks will be produced in these regions of Ψ_P. Similarly, $\Psi_Q(x, y) \equiv 0$ in region IX according to **Table 5-6B.** Thus, no cross peak occurs in region IX of Ψ_Q.

Type 2: regions I and V of $\Psi_Q(x, y)$

According **Table 5-6B**, the expressions of $\Psi_Q(x, y)$ in regions I and V are listed in eq. 5-24A and eq. 5-24B.

$$\Psi_Q(x, y) = s\left(f_{P_1}(x)f_{U_1}(y) - f_{U_1}(x)f_{P_1}(y)\right)\left(\vec{\tilde{C}}_P^{init}\right)^T N\vec{\tilde{C}}_{U_1}^{eq} \qquad (5\text{-}24A)$$

$$\Psi_Q(x, y) = sdK_0\left(f_{P_2}(x)f_{U_2}(y) - f_{U_2}(x)f_{P_2}(y)\right)\left(\vec{\tilde{C}}_P^{init}\right)^T N\vec{\tilde{C}}_{U_1}^{eq} \qquad (5\text{-}24B)$$

Since eq. 5-24A and eq. 5-24B are quite similar, we use the cross peaks in region I of $\Psi_Q(x, y)$ as an example. According to eq. 5-4, eq. 5-24A can be expressed as

$$\Psi_Q(x, y) = s\varepsilon_{P_1}(\varepsilon_{P_1}$$

$$+ \Delta\varepsilon_{U_1})\left[g_{P_1}(x)g_{U_1}(y) - g_{P_1}(y)g_{U_1}(x)\right]\left(\vec{\tilde{C}}_P^{init}\right)^T N\vec{\tilde{C}}_{U_1}^{eq} \qquad (5\text{-}25)$$

Equation 5-25 clearly demonstrates that $\Delta\varepsilon_{U_1}$ is only relevant to the intensity of cross peaks and has no influence on the pattern of cross peaks in this region. The pattern of cross peaks is related to $g_{P_1}(x)$ and $g_{U_1}(x)$, which are related to the peak position and bandwidth of the characteristic peaks of P_1 and U_1. That is to say, cross peaks in region I of $\Psi_Q(x, y)$ can be used to reflect ΔX_{U_1} and ΔW_{U_1}. In a similar manner, cross peaks in region V of $\Psi_Q(x, y)$ can be used to reflect ΔX_{U_2} and ΔW_{U_2}.

Type 3: region IX of $\Psi_P(x, y)$

As is shown in **Table 5-6A**, $\Psi_P(x, y)$ can be expressed as

$$\Psi_P(x, y) = \{f_Q(x)\left[f_{V_1}(y) + df_{V_2}(y)\right]$$

$$- \left[f_{V_1}(x) + df_{V_2}(x)\right]f_Q(y)\}\left(\vec{\tilde{C}}_Q^{init}\right)^T N\vec{\tilde{C}}_{U_1}^{eq} \qquad (5\text{-}26)$$

According to eq. 5-4, eq. 5-26 can be described as

$$\Psi_P(x, y) = \varepsilon_Q(\varepsilon_Q + \Delta\varepsilon_{V_1})\left[g_Q(x)g_{V_1}(y) - g_{V_1}(x)g_Q(y)\right]\left(\vec{\tilde{C}}_Q^{init}\right)^T N\vec{\tilde{C}}_{U_1}^{eq}$$

$$+ \varepsilon_Q(\varepsilon_Q + \Delta\varepsilon_{V_2})d\left[g_Q(x)g_{V_2}(y) - g_{V_2}(x)g_Q(y)\right]\left(\vec{\tilde{C}}_Q^{init}\right)^T N\vec{\tilde{C}}_{U_1}^{eq} \qquad (5\text{-}27)$$

The cross peaks are composed of two parts. The first part is relevant to ΔX_{V_1}, ΔW_{V_1} and $\Delta\varepsilon_{V_1}$. The second part is related to ΔX_{V_2}, ΔW_{V_2} and $\Delta\varepsilon_{V_2}$. The cross peaks in this region can be regarded as the linear combination of the two parts. $\Delta\varepsilon_{V_1}$ and $\Delta\varepsilon_{V_2}$, being part of the coefficient of the linear combination, may also affect the pattern of cross peak in this region. This is quite different from the spectral behavior of cross peaks in regions I and V of $\Psi_P(x, y)$.

Type 4: regions III, VI, VII, VIII of $\Psi_Q(x, y)$

The cross peaks in regions VII and VIII are anti-symmetric to those in regions III and VI in $\Psi_Q(x, y)$. Only the spectral features of cross peaks in regions III and VI will not be discussed. According to **Table 5-6B**, moreover, the expressions of $\Psi_Q(x, y)$ in regions III and VI are quite similar. Thus, we just discuss the cross peaks in region III.

As is shown in **Table 5-6B**, $\Psi_Q(x, y)$ can be expressed as

$$\Psi_Q(x,y) = s f_{P_1}(x)\big[f_{V_1}(y) + d f_{V_2}(y) - (1+d)f_Q(y)\big]\left(\vec{\tilde{C}}_P^{\text{init}}\right)^T \mathbf{N}\vec{\tilde{C}}_{U_1}^{\text{eq}} \qquad (5\text{-}28)$$

According to eq. 5-4, eq. 5-28 can be described as

$$\Psi_Q(x,y) = s f_{P_1}(x)\big\{(\varepsilon_Q + \Delta\varepsilon_{V_1})\big[g_{V_1}(y) - g_Q(y)\big] + g_Q(y)\Delta\varepsilon_{V_1}$$

$$+\, d(\varepsilon_Q + \Delta\varepsilon_{V_2})\big[g_{V_2}(y) - g_Q(y)\big] \qquad (5\text{-}29)$$

$$+\, d\Delta\varepsilon_{V_2} g_Q(y)\big\}\left(\vec{\tilde{C}}_P^{\text{init}}\right)^T \mathbf{N}\vec{\tilde{C}}_{U_1}^{\text{eq}}$$

Equation 5-29 clearly demonstrates that the cross peaks are relevant to ΔX_{V_1}, ΔW_{V_1}, $\Delta\varepsilon_{V_1}$, ΔX_{V_2}, ΔW_{V_2} and $\Delta\varepsilon_{V_2}$.

Type 5: regions III, VI, VII, VIII of $\Psi_P(x,y)$

The cross peaks in regions VII and VIII are anti-symmetric to those in regions III and VI of $\Psi_P(x,y)$. We only discuss cross peaks in regions III and VI of $\Psi_P(x,y)$.

As is shown in **Table 5-6A**, $\Psi_P(x,y)$ in regions III and VI can be expressed as

$$\Psi_P(x,y) = \big[f_{U_1}(x) - (1+d)s f_{P_1}(x)\big]f_Q(y)\left(\vec{\tilde{C}}_{U_1}^{\text{eq}}\right)^T \mathbf{N}\vec{\tilde{C}}_Q^{\text{init}} \qquad (5\text{-}30A)$$

$$\Psi_P(x,y) = \big[d f_{U_2}(x) - (1+d)s K_0 f_{P_2}(x)\big]f_Q(y)\left(\vec{\tilde{C}}_{U_1}^{\text{eq}}\right)^T \mathbf{N}\vec{\tilde{C}}_Q^{\text{init}} \qquad (5\text{-}30B)$$

After combining with eq. 5-4, eq. 5-30A and eq. 5-30B can be expressed as

$$\Psi_P(x,y) = (\varepsilon_{P_1} + \Delta\varepsilon_{U_1})\big[g_{U_1}(x) - g_{P_1}(x)\big]f_Q(y)\left(\vec{\tilde{C}}_{U_1}^{\text{eq}}\right)^T \mathbf{N}\vec{\tilde{C}}_Q^{\text{init}}$$

$$+\, g_{P_1}(x)\Delta\varepsilon_{U_1}f_Q(y)\left(\vec{\tilde{C}}_{U_1}^{\text{eq}}\right)^T \mathbf{N}\vec{\tilde{C}}_Q^{\text{init}} + \varepsilon_{P_1}g_{P_1}(x)(1-s \qquad (5\text{-}31A)$$

$$-\, sd)f_Q(y)\left(\vec{\tilde{C}}_{U_1}^{\text{eq}}\right)^T \mathbf{N}\vec{\tilde{C}}_Q^{\text{init}}$$

$$\Psi_P(x,y) = d(\varepsilon_{P_2} + \Delta\varepsilon_{U_2})\big[g_{U_2}(x) - g_{P_2}(x)\big]f_Q(y)\left(\vec{\tilde{C}}_{U_1}^{\text{eq}}\right)^T \mathbf{N}\vec{\tilde{C}}_Q^{\text{init}}$$

$$+\, d g_{P_2}(x)\Delta\varepsilon_{U_2}f_Q(y)\left(\vec{\tilde{C}}_{U_1}^{\text{eq}}\right)^T \mathbf{N}\vec{\tilde{C}}_Q^{\text{init}} + \varepsilon_{P_2}g_{P_2}(x)(d \qquad (5\text{-}31B)$$

$$-\, sK_0 - sK_0 d)f_Q(y)\left(\vec{\tilde{C}}_{U_1}^{\text{eq}}\right)^T \mathbf{N}\vec{\tilde{C}}_Q^{\text{init}}$$

According to eq. 5-31A, $\Psi_P(x,y)$ in region III is composed of three parts. The first part ($(\varepsilon_{P_1} + \Delta\varepsilon_{U_1})\big[g_{U_1}(x) - g_{P_1}(x)\big]f_Q(y)\left(\vec{\tilde{C}}_{U_1}^{\text{eq}}\right)^T \mathbf{N}\vec{\tilde{C}}_Q^{\text{init}}$) is relevant to ΔX_{U_1} and ΔW_{U_1}. The second part ($g_{P_1}(x)\Delta\varepsilon_{U_1}f_Q(y)\left(\vec{\tilde{C}}_{U_1}^{\text{eq}}\right)^T \mathbf{N}\vec{\tilde{C}}_Q^{\text{init}}$) is related to $\Delta\varepsilon_{U_1}$. The above two parts reflect the difference between $f_{P_1}(x)$ and $f_{U_1}(x)$ caused by intermolecular interaction. The third part reflects the difference on reactions shown in eq. 5-2 and eq. 5-3. Discussion on this issue can be found in next section of this chapter.

In a similar manner, $\Psi_P(x,y)$ in region VI is also composed of three parts. The first two parts are relevant to the differences between $f_{P_2}(x)$ and $f_{U_2}(x)$ caused by intermolecular interaction. Third part is related to the difference on reactions shown in eq. 5-2 and eq. 5-3.

Type 6: regions II and IV of $\Psi_Q(x, y)$

Since region IV is anti-symmetric to region II with the respect of the diagonal in $\Psi_Q(x, y)$, we focus on the spectral behavior of cross peak in region II.

As is shown in **Table 5-6B**, $\Psi_Q(x, y)$ can be expressed as

$$\Psi_Q(x, y) = \left[sd f_{P_1}(x) f_{U_2}(y) - s K_0 f_{U_1}(x) f_{P_2}(y)\right] \left(\vec{\tilde{C}}_P^{\text{init}}\right)^T \mathbf{N}\vec{\tilde{C}}_{U_1}^{\text{eq}} \tag{5-32}$$

According to eq. 5-4, eq. 5-32 can be described as

$$\begin{aligned}
\Psi_Q(x, y) = &\left\{ ds\varepsilon_{P_1}\left(\varepsilon_{P_2} + \Delta\varepsilon_{U_2}\right)\left[g_{P_1}(x)g_{U_2}(y)\right.\right. \\
&\left. - g_{U_1}(x)g_{P_2}(y)\right]\right\}\left(\vec{\tilde{C}}_P^{\text{init}}\right)^T \mathbf{N}\vec{\tilde{C}}_{U_1}^{\text{eq}} \\
&+ \left\{dsg_{U_1}(x)g_{P_2}(y)\left[\varepsilon_{P_1}\left(\varepsilon_{P_2} + \Delta\varepsilon_{U_2}\right)\right.\right. \\
&\left. - \left(\varepsilon_{P_1} + \Delta\varepsilon_{U_1}\right)\varepsilon_{P_2}\right]\right\}\left(\vec{\tilde{C}}_P^{\text{init}}\right)^T \mathbf{N}\vec{\tilde{C}}_{U_1}^{\text{eq}} \\
&+ \left[s\varepsilon_{P_2}\left(\varepsilon_{P_1} + \Delta\varepsilon_{U_1}\right)g_{U_1}(x)g_{P_2}(y)(d\right. \\
&\left. - K_0)\right]\left(\vec{\tilde{C}}_P^{\text{init}}\right)^T \mathbf{N}\vec{\tilde{C}}_{U_1}^{\text{eq}}
\end{aligned} \tag{5-33}$$

According to eq. 5-33, $\Psi_Q(x, y)$ is composed of three parts. The first part $\left\{ds\varepsilon_{P_1}\left(\varepsilon_{P_2} + \Delta\varepsilon_{U_2}\right)\left[g_{P_1}(x)g_{U_2}(y) - g_{U_1}(x)g_{P_2}(y)\right]\right\}\left(\vec{\tilde{C}}_P^{\text{init}}\right)^T \mathbf{N}\vec{\tilde{C}}_{U_1}^{\text{eq}}$ is related to the differences among the peak shape functions $g_{P_1}(x)$, $g_{P_2}(x)$, $g_{U_1}(x)$ and $g_{U_2}(y)$ caused by intermolecular interaction.

The second part $\left\{dsg_{U_1}(x)g_{P_2}(y)\left[\varepsilon_{P_1}\left(\varepsilon_{P_2} + \Delta\varepsilon_{U_2}\right) - \left(\varepsilon_{P_1} + \Delta\varepsilon_{U_1}\right)\varepsilon_{P_2}\right]\right\} *$ $\left(\vec{\tilde{C}}_P^{\text{init}}\right)^T \mathbf{N}\vec{\tilde{C}}_{U_1}^{\text{eq}}$ is relevant to the variations on the absorptivity of P_1, P_2, U_1 and U_2.

The third part $\left[s\varepsilon_{P_2}\left(\varepsilon_{P_1} + \Delta\varepsilon_{U_1}\right)g_{U_1}(x)g_{P_2}(y)(d - K_0)\right]\left(\vec{\tilde{C}}_P^{\text{init}}\right)^T \mathbf{N}\vec{\tilde{C}}_{U_1}^{\text{eq}})$ reflects the difference on reactions shown in eq. 5-2 and eq.5-3. Discussion on this issue can be found in the next section.

The spectral features of the pair of 2D asynchronous spectra generated by using the DAOSD approach on the system described in this chapter are summarized in **Scheme 5-2**.

Special spectral features of 2D asynchronous spectra generated using the DAOSD approach in the model systems

In our previous work, we have applied the DAOSD approach on many chemical systems in which the intermolecular interaction between the two solutes (denoted as P and Q) can be described by eq. 5-34.

$$P + Q \overset{K}{\leftrightarrow} U + V \tag{5-34}$$

In these cases, no cross peak appear on the corresponding $\Psi_P(x, y)$ or $\Psi_Q(x, y)$ if interaction does not bring about changes on the spectra of P and Q (i.e., $f_P(x) \equiv f_U(x)$

and $f_Q(x) \equiv f_V(x)$. Thus no changes on the spectra of solutes before and after interaction are equivalent to no intermolecular interactions.

However, the concept of no spectral change is not equivalent to that of no interaction when P occurs in two exchangeable states. Herein, we provide a typical example. The concentrations of P and Q in two groups of solutions are listed in **Table 5-3**. The peak parameters for P_1, P_2, Q, U_1, U_2, V_1 and V_2 are listed in **Table 5-7**. It should be pointed out that the peak parameters of P_1 are exactly the same as those of U_1. Similarly, the peak parameters of P_2 are the same as those of U_2 and the peak parameters of Q are the same as those of V_1 and V_2 (i.e., $f_{P_1}(x) \equiv f_{U_1}(x)$, $f_{P_2}(x) \equiv f_{U_2}(x)$, $f_Q(x) \equiv f_{V_1}(x) \equiv f_{V_2}(x)$). The values of K_0, K_1 and K_2 are set as 0.5, 0.01 and 0.01, respectively. The resultant $\Psi_P(x, y)$ and $\Psi_Q(x, y)$ are shown in **Figure 5-2A**.

In $\Psi_P(x, y)$, four cross peaks can be observed at (X_Q, X_{P_1}), (X_Q, X_{P_2}), (X_{P_1}, X_Q), (X_{P_2}, X_Q). The spectral regions for the four cross peaks are regions III, VI, VII and VIII. In $\Psi_Q(x, y)$, two cross peaks occur at (X_{P_1}, X_{P_2}) and (X_{P_2}, X_{P_1}). The spectral regions for the two cross peaks are regions II and IV, respectively.

Since cross peaks in regions III and VI are anti-symmetric to the cross peaks in regions VII and VIII with respect to the diagonal. Only cross peaks in regions III and VI are discussed.

As mentioned above, the expressions of cross peaks in regions III and VI are shown in eq. 5-31A and eq. 5-31B.

Since $f_{P_1}(x) \equiv f_{U_1}(x)$, $f_{P_2}(x) \equiv f_{U_2}(x)$, $f_Q(x) \equiv f_{V_1}(x) \equiv f_{V_2}(x)$, we have

$$X_{P_1} = X_{U_1}, \quad W_{P_1} = W_{U_1}, \quad \varepsilon_{P_1} = \varepsilon_{U_1}$$
$$X_{P_2} = X_{U_2}, \quad W_{P_2} = W_{U_2}, \quad \varepsilon_{P_2} = \varepsilon_{U_2}, \tag{5-35}$$
$$X_Q = X_{V_1} = X_{V_2}, \ W_Q = W_{V_1} = W_{V_2}, \ \varepsilon_Q = \varepsilon_{V_1} = \varepsilon_{V_2}$$

Thus, the first and second terms of eq. 5-31A and eq. 5-31B turn into zero. eq. 5-31A and eq. 5-31B can be expressed as

$$\Psi_P(x, y) = (1 - s - sd)\varepsilon_{P_1}g_{P_1}(x)f_Q(y)\left(\vec{\tilde{C}}_{U_1}^{eq}\right)^T N\vec{\tilde{C}}_Q^{init} \tag{5-36A}$$

$$\Psi_P(x, y) = (d - sK_0 - sK_0d)\varepsilon_{P_2}g_{P_2}(x)f_Q(y)\left(\vec{\tilde{C}}_{U_1}^{eq}\right)^T N\vec{\tilde{C}}_Q^{init} \tag{5-36B}$$

Equation 5-36A and eq. 5-36B can be nonzero, this is the reason why cross peak appears in in regions III and VI of $\Psi_P(x, y)$. The intensities of the cross peaks are affected by the values of s and d, which are the functions of K_0, K_1 and K_2. That is to say, cross peaks reflects the relationship among reaction shown in eq. 5-1, eq. 5-2 and eq. 5-3.

In a similar manner, the expression of cross peak in region II of $\Psi_P(x, y)$ is shown in eq. 5-33. According to eq. 5-35, the first and second terms of eq. 5-33 are zero. Thus, eq. 5-33 can be expressed as

$$\Psi_Q(x, y) = s(d - K_0)\varepsilon_{P_2}\varepsilon_{U_1}g_{U_1}(x)g_{P_2}(y)\left(\vec{\tilde{C}}_P^{init}\right)^T N\vec{\tilde{C}}_{U_1}^{eq} \tag{5-37}$$

Equation 5-37 can be nonzero, this is the reason why cross peak appears in region II of $\Psi_Q(x, y)$. The intensities of the cross peak are affected by the values of s and d,

which are the functions of K_0, K_1 and K_2. That is to say, cross peaks reflects the relationship among reaction shown in eq. 5-1, eq. 5-2 and eq. 5-3.

According to eq. 5-14, we learn that s cannot be zero. Thus, eq. 5-36A, eq. 5-36B and eq. 5-37 can be zero when eq. 5-38A, eq. 5-38B and eq. 5-38C are satisfied
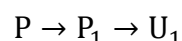
$$1 - s - sd = 0 \qquad (5\text{-}38\text{A})$$
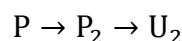$$d - sK_0 - sK_0 d = 0 \qquad (5\text{-}38\text{B})$$
$$d - K_0 = 0 \qquad (5\text{-}38\text{C})$$

According to eq. 5-14 and eq. 5-15. Equation 5-38A, eq. 5-38B and eq. 5-38C can be satisfied simultaneously when $K_0 = K_2/K_1$. That is to say, the relationship among different chemical species may be represented by a net-work graph shown in **Scheme 5-3**. The network is composed of two branches.

The first branch is

$$P \rightarrow P_1 \rightarrow U_1$$

The second branch is

$$P \rightarrow P_2 \rightarrow U_2$$

When $K_0 = K_2/K_1$ is not satisfied, the two branches of reaction are in an unbalance state and cross peaks can be observed. As $K_0 = K_2/K_1$ is satisfied, the two branches of reaction are in a balance state and cross peaks are removed. The above results are confirmed by computer simulation shown in **Figure 5-2A** and **Figure 5-2B**.

That is to say, the cross peaks can be used as a probe to reflect whether the two branches of interaction are in balance or not. This is the first time to find out that cross peak in 2D correlation spectra generated by using the DAOSD approach can reflect the interaction at a network level.

Conclusion

The DAOSD approach is applied to investigate intermolecular interaction between two solutes (P and Q) dissolved in the same solutions where P occurs in two exchangeable states. Results of mathematical analysis and computer simulation demonstrate that cross peaks are directly relevant to the interaction between P and Q. Thus, the DAOSD approach is applicable to investigate chemical system where one solute occurs in two exchangeable states. Subtle spectral variation on the characteristic peak of different chemical species can be reflected from different regions of the pair of 2D asynchronous spectra. In addition, the model systems provide the first example showing that no spectral change is conceptually different from no intermolecular interaction. In some special cases, the appearances of cross peaks in 2D asynchronous reflect intermolecular interaction at a network level from a chemical system.

Table 5-1 Spectral Parameters of P_1, P_2, Q, U_1, V_1, U_2 and V_2 in the Model System when Interaction Occurs between P and Q

Spectral variable	Peak position (nm)	Bandwidth (nm)	Absorptivity
P_1	100	20	1.0
P_2	300	20	1.0
Q	500	20	1.0
U_1	105	20	1.0
V_1	510	20	1.0
U_2	295	20	1.0
V_2	490	20	1.0

Table 5-2 A Series of Variables that are used to describe the Changes of the above Spectral Parameters

Spectral variable	Value
ΔX_{U_1}	$X_{U_1} - X_{P_1}$
ΔW_{U_1}	$W_{U_1} - W_{P_1}$
$\Delta \varepsilon_{U_1}$	$\varepsilon_{U_1} - \varepsilon_{P_1}$
ΔX_{V_1}	$X_{V_1} - X_Q$
ΔW_{V_1}	$W_{V_1} - W_Q$
$\Delta \varepsilon_{V_1}$	$\varepsilon_{V_1} - \varepsilon_Q$
ΔX_{U_2}	$X_{U_2} - X_{P_2}$
ΔW_{U_2}	$W_{U_2} - W_{P_2}$
$\Delta \varepsilon_{U_2}$	$\varepsilon_{U_2} - \varepsilon_{P_2}$
ΔX_{V_2}	$X_{V_2} - X_Q$
ΔW_{V_2}	$W_{V_2} - W_Q$
$\Delta \varepsilon_{V_2}$	$\varepsilon_{V_2} - \varepsilon_Q$

Table 5-3 Initial Concentrations of P and Q in the Model System, which meet the Requirement of the DAOSD Approach

Index of the solutions	C_P (arbitrary unit)	C_Q (arbitrary unit)
Group 1		
1	10	0
2	10	4
3	10	6
4	10	10
Group 2		
1	0	10
2	4	10
3	6	10
4	10	10

Table 5-4 Absorption Peaks of the Seven Substances (P$_1$, P$_2$, Q, U$_1$, V$_1$, U$_2$ and V$_2$) in Three Regions in the 1D Spectra

	ω1	ω2	ω3
$f_{P_1}(x)$	nonzero	0	0
$f_{P_2}(x)$	0	nonzero	0
$f_Q(x)$	0	0	nonzero
$f_{U_1}(x)$	nonzero	0	0
$f_{V_1}(x)$	0	0	nonzero
$f_{U_2}(x)$	0	nonzero	0
$f_{V_2}(x)$	0	0	nonzero

Table 5-5 Expression of F(x), f$_Q$(x) and H(x) in Different Regions

Region(x, y)	F(x)	f$_Q$(x)	H(x)	F(y)	f$_Q$(y)	H(y)
I (ω1, ω1)	$sf_{P_1}(x)$	0	$f_{U_1}(x) - (1+d)sf_{P_1}(x)$	$sf_{P_1}(y)$	0	$f_{U_1}(y) - (1+d)sf_{P_1}(y)$
II (ω1, ω2)	$sf_{P_1}(x)$	0	$f_{U_1}(x) - (1+d)sf_{P_1}(x)$	$sK_0f_{P_2}(y)$	0	$df_{U_2}(y) - (1+d)sKf_{P_2}(y)$
III (ω1,ω3)	$sf_{P_1}(x)$	0	$f_{U_1}(x) - (1+d)sf_{P_1}(x)$	0	$f_Q(y)$	$f_{V_1}(y) + df_{V_2}(y) - (1+d)f_Q(y)$
IV (ω2,ω1)	$sK_0f_{P_2}(x)$	0	$df_{U_2}(x) - (1+d)sK_0f_{P_2}(x)$	$sf_{P_1}(y)$	0	$f_{U_1}(y) - (1+d)sf_{P_1}(y)$
V (ω2,ω2)	$sK_0f_{P_2}(x)$	0	$df_{U_2}(x) - (1+d)sK_0f_{P_2}(x)$	$sK_0f_{P_2}(y)$	0	$df_{U_2}(y) - (1+d)sK_0f_{P_2}(y)$
VI (ω2,ω3)	$sK_0f_{P_2}(x)$	0	$df_{U_2}(x) - (1+d)sK_0f_{P_2}(x)$	0	$f_Q(y)$	$f_{V_1}(y) + df_{V_2}(y) - (1+d)f_Q(y)$
VII (ω3,ω1)	0	$f_Q(x)$	$f_{V_1}(x) + df_{V_2}(x) - (1+d)f_Q(x)$	$sf_{P_1}(y)$	0	$f_{U_1}(y) - (1+d)sf_{P_1}(y)$
VIII (ω3,ω2)	0	$f_Q(x)$	$f_{V_1}(x) + df_{V_2}(x) - (1+d)f_Q(x)$	$sK_0f_{P_2}(y)$	0	$df_{U_2}(y) - (1+d)sK_0f_{P_2}(y)$
IX (ω3,ω3)	0	$f_Q(x)$	$f_{V_1}(x) + df_{V_2}(x) - (1+d)f_Q(x)$	0	$f_Q(y)$	$f_{V_1}(y) + df_{V_2}(y) - (1+d)f_Q(y)$

Table 5-6A The Spectral Functions of $\Psi_\text{P}(x, y)$ in Different Regions

Region	$\Psi_\text{P}(x, y)$
I	0
II	0
III	$\left[f_{U_1}(x) - (1+d)sf_{P_1}(x)\right]f_Q(y)\left(\vec{\tilde{C}}_{U_1}^{\text{eq}}\right)^{\text{T}}\mathbf{N}\vec{\tilde{C}}_Q^{\text{init}}$
IV	0
V	0
VI	$[df_{U_2}(x) - (1+d)sK_0f_{P_2}(x)]f_Q(y)\left(\vec{\tilde{C}}_{U_1}^{\text{eq}}\right)^{\text{T}}\mathbf{N}\vec{\tilde{C}}_Q^{\text{init}}$
VII	$f_Q(x)\left[f_{U_1}(y) - (1+d)sf_{P_1}(y)\right]\left(\vec{\tilde{C}}_Q^{\text{init}}\right)^{\text{T}}\mathbf{N}\vec{\tilde{C}}_{U_1}^{\text{eq}}$
VIII	$f_Q(x)[df_{U_2}(y) - (1+d)sK_0f_{P_2}(y)]\left(\vec{\tilde{C}}_Q^{\text{init}}\right)^{\text{T}}\mathbf{N}\vec{\tilde{C}}_{U_1}^{\text{eq}}$
IX	$\left\{f_Q(x)\left[f_{V_1}(y) + df_{V_2}(y)\right] - \left[f_{V_1}(x) + df_{V_2}(x)\right]f_Q(y)\right\}\left(\vec{\tilde{C}}_Q^{\text{init}}\right)^{\text{T}}\mathbf{N}\vec{\tilde{C}}_{U_1}^{\text{eq}}$

Table 5-6B The Spectral Functions of $\Psi_Q(x, y)$ in Different Regions

Region	$\Psi_Q(x, y)$
I	$s\left(f_{P_1}(x)f_{U_1}(y) - f_{U_1}(x)f_{P_1}(y)\right)\left(\vec{\tilde{C}}_P^{\text{init}}\right)^{\text{T}} \mathbf{N}\vec{\tilde{C}}_{U_1}^{\text{eq}}$
II	$\left[sdf_{P_1}(x)f_{U_2}(y) - sK_0f_{U_1}(x)f_{P_2}(y)\right]\left(\vec{\tilde{C}}_P^{\text{init}}\right)^{\text{T}} \mathbf{N}\vec{\tilde{C}}_{U_1}^{\text{eq}}$
III	$sf_{P_1}(x)\left[f_{V_1}(y) + df_{V_2}(y) - (1+d)f_Q(y)\right]\left(\vec{\tilde{C}}_P^{\text{init}}\right)^{\text{T}} \mathbf{N}\vec{\tilde{C}}_{U_1}^{\text{eq}}$
IV	$\left[sdf_{U_2}(x)f_{P_1}(y) - sK_0f_{P_2}(x)f_{U_1}(y)\right]\left(\vec{\tilde{C}}_{U_1}^{\text{eq}}\right)^{\text{T}} \mathbf{N}\vec{\tilde{C}}_P^{\text{init}}$
V	$sdK_0\left[f_{P_2}(x)f_{U_2}(y) - f_{U_2}(x)f_{P_2}(y)\right]\left(\vec{\tilde{C}}_P^{\text{init}}\right)^{\text{T}} \mathbf{N}\vec{\tilde{C}}_{U_1}$
VI	$sK_0f_{P_2}(x)\ \left[f_{V_1}(y) + df_{V_2}(y) - (1+d)f_Q(y)\right]\left(\vec{\tilde{C}}_P^{\text{init}}\right)^{\text{T}} \mathbf{N}\vec{\tilde{C}}_{U_1}$
VII	$\left[f_{V_1}(x) + df_{V_2}(x) - (1+d)f_Q(x)\right]sf_{P_1}(y)\left(\vec{\tilde{C}}_{U_1}^{\text{eq}}\right)^{\text{T}} \mathbf{N}\vec{\tilde{C}}_P^{\text{init}}$
VIII	$sK_0\left[f_{V_1}(x) + df_{V_2}(x) - (1+d)f_Q(x)\right]f_{P_2}(y)\ \left(\vec{\tilde{C}}_{U_1}^{\text{eq}}\right)^{\text{T}} \mathbf{N}\vec{\tilde{C}}_P^{\text{init}}$
IX	0

Table 5-7 Spectral parameters of P_1, P_2, Q, U_1, V_1, U_2 and V_2 in a Special Model System. In this System, Intermolecular Interaction Occurs. However, the Peak Parameters of P_1 and P_2 are the Same as those of U_1 and U_2, respectively. The Peak Parameters of Q are the Same as those of V_1 and V_2.

Spectral variable	Peak position (nm)	Bandwidth (nm)	Absorptivity
P_1	100	20	1.0
P_2	300	20	1.0
Q	500	20	1.0
U_1	100	20	1.0
V_1	500	20	1.0
U_2	300	20	1.0
V_2	500	20	1.0
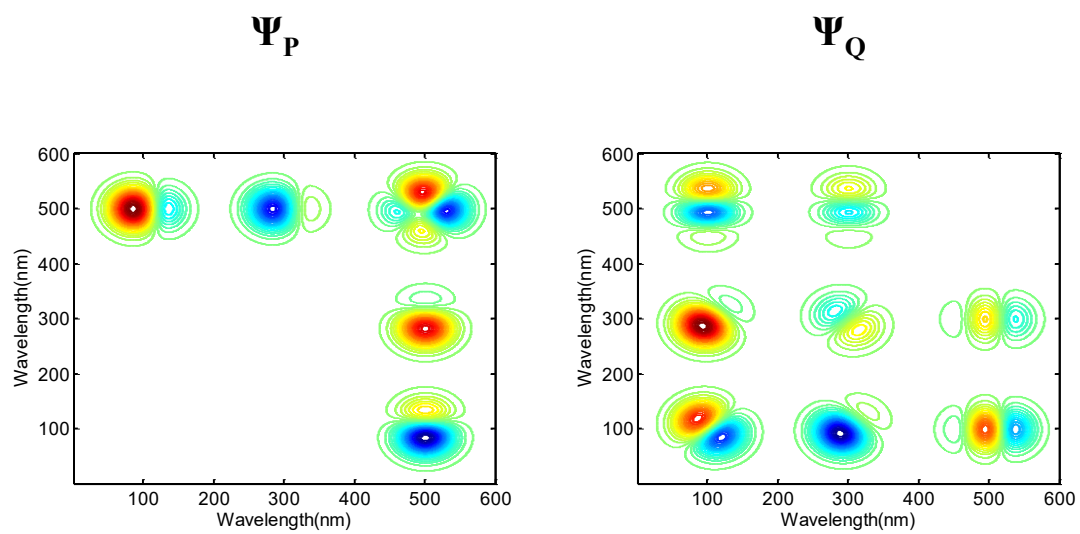
Figure 5-1. An Example of the Simulated 2D Spectra on a Model System where Intermolecular Interaction Occurs between P and Q.

Ψ_P Ψ_Q
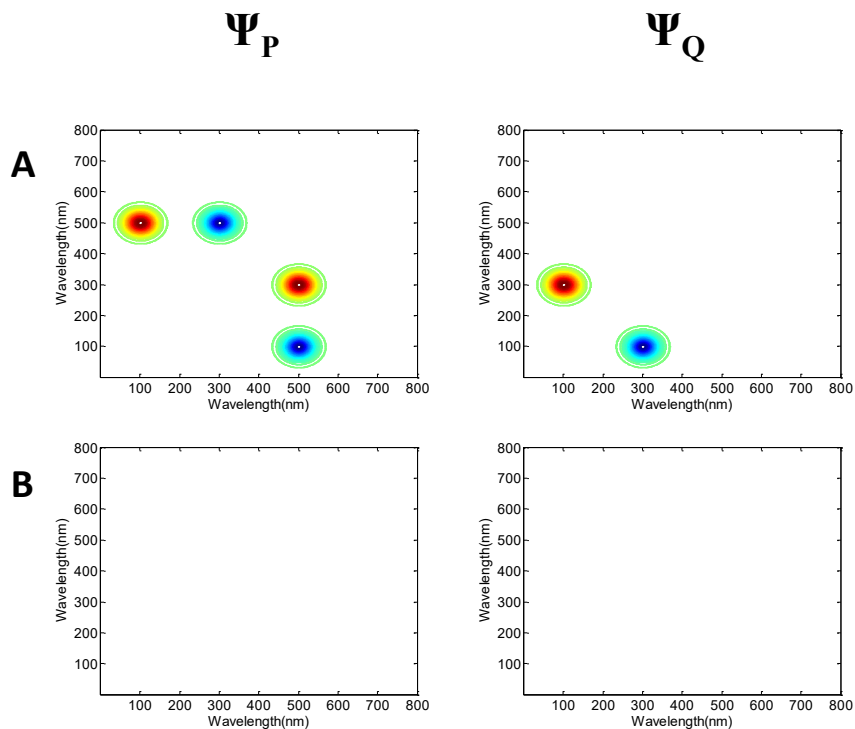
Figure 5-2 Two-Dimensional Asynchronous Spectra of a Special Model System where Intermolecular Interaction Occurs between P and Q. The Spectrum of U_1 is the Same as that of P_1, the Spectrum of U_2 is the Same as that of P_2 and the Spectrum of Q is the Same as those of V_1 and V_2.

A. $\Psi_P(x, y)$ and $\Psi_Q(x, y)$ of a Chemical System ($K_0=0.5$, $K_1=K_2=0.01$). Cross Peaks Appear in Region III, Region VI, Region VII and Region VIII of $\Psi_P(x, y)$. In addition, Cross Peaks Occur in Region II and Region IV of $\Psi_P(x, y)$

B. $\Psi_P(x, y)$ and $\Psi_Q(x, y)$ of a Chemical System ($K_0=1$, $K_1=K_2 =0.01$) Since $K_0=K_2/K_1$ is Satisfied, Cross peaks in Region III, VI, VII and VIII of $\Psi_P(x, y)$ and Region II and IV of $\Psi_Q(x, y)$ are Completely Removed.
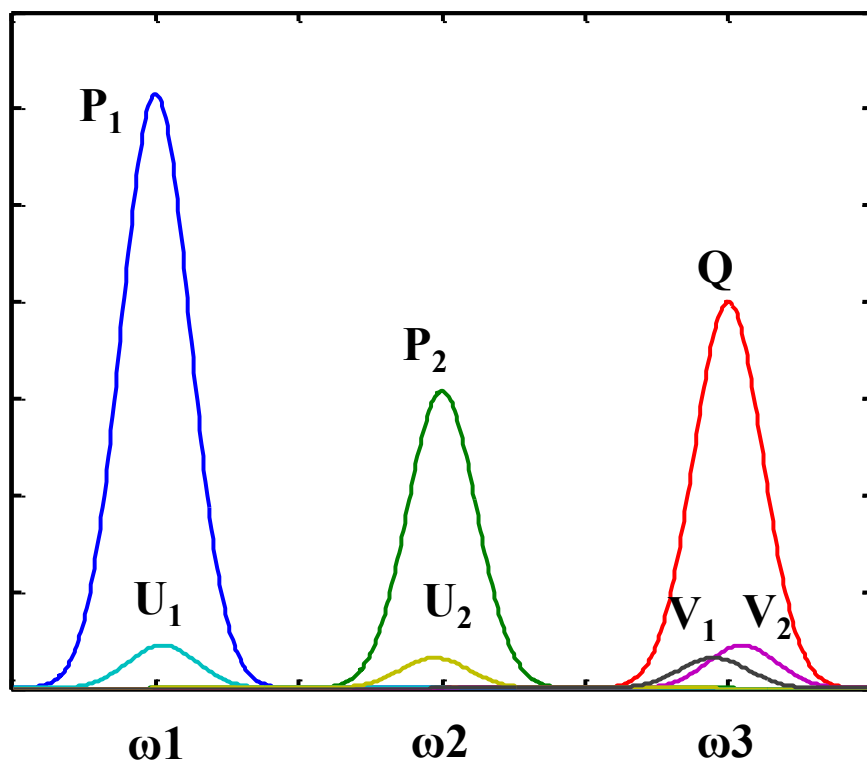
Scheme 5-1A. Schematic Diagram of 1D Spectra of the Model System.
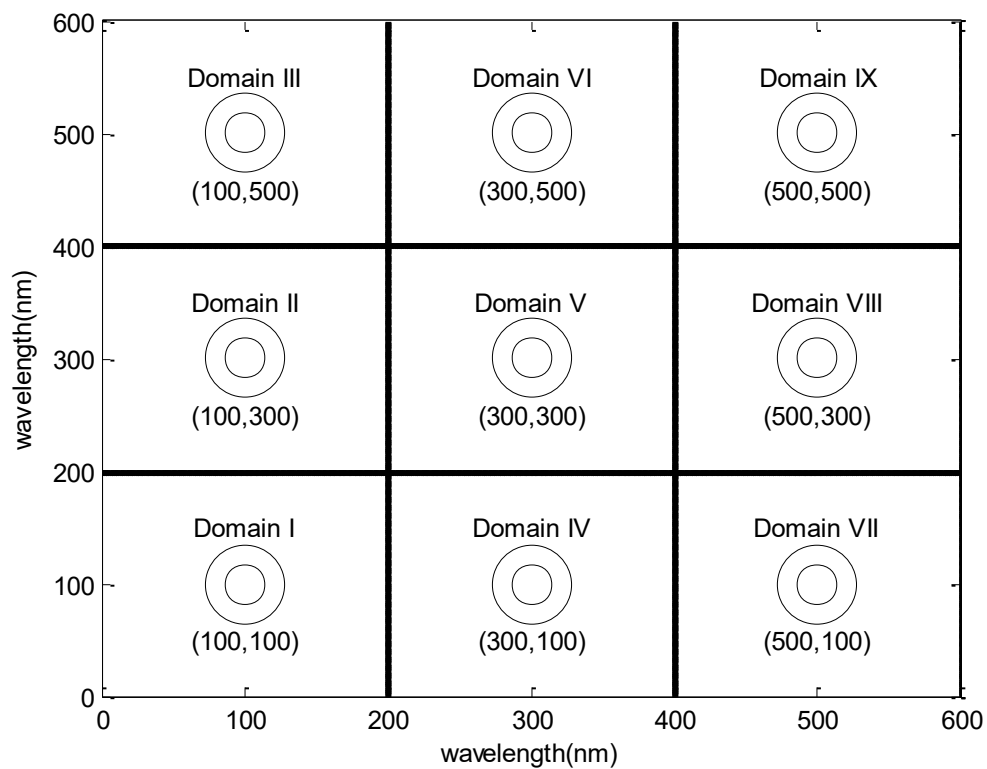
Scheme 5-1B. Schematic Diagram of the 2D Asynchronous Spectra, where the Contour Map Is Divided into Nine Spectral Regions.
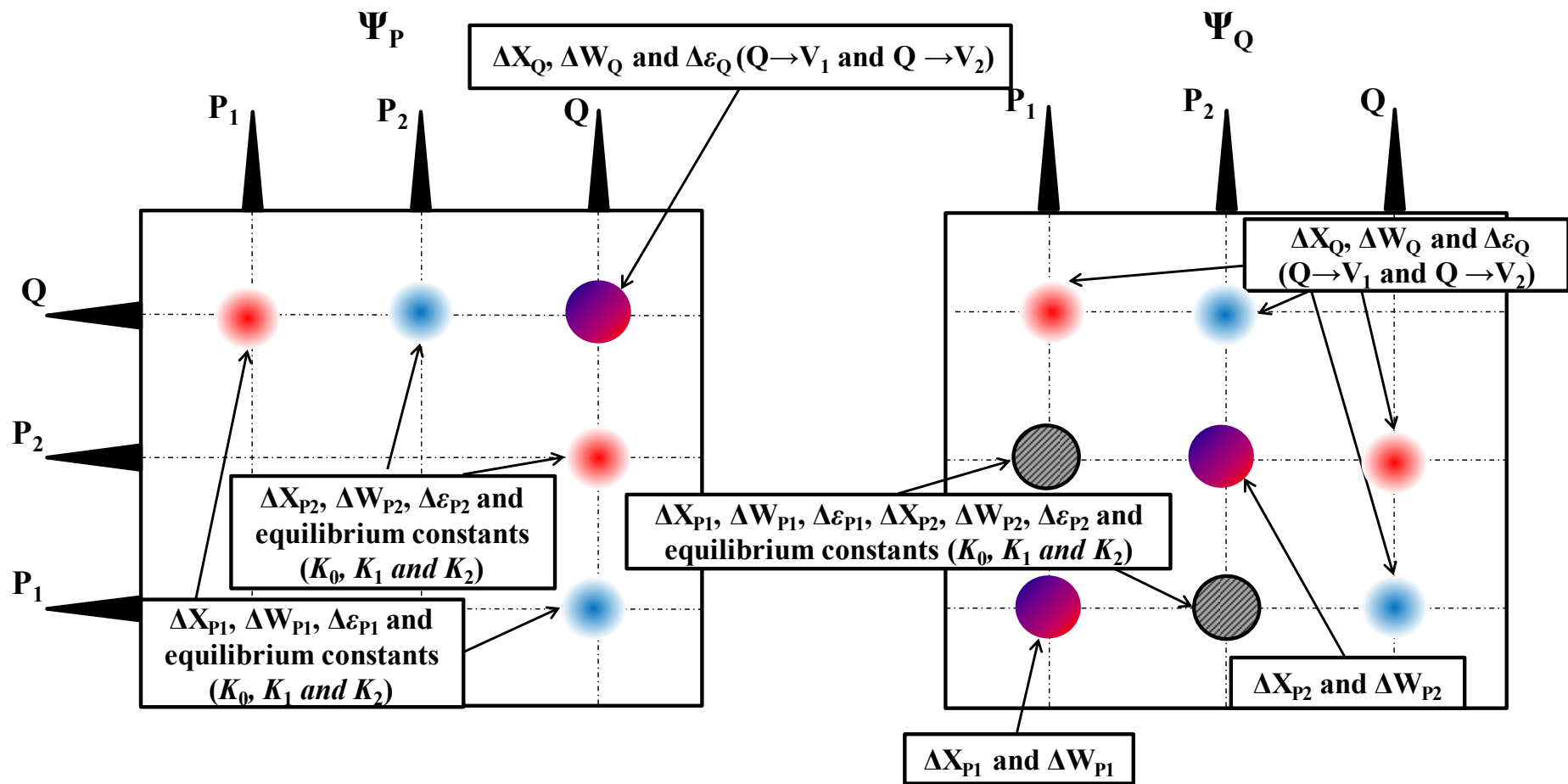
Scheme 5-2. Schematic Diagram of the Spectral Properties of the 2D Asynchronous Spectra Generated by the DAOSD Approach
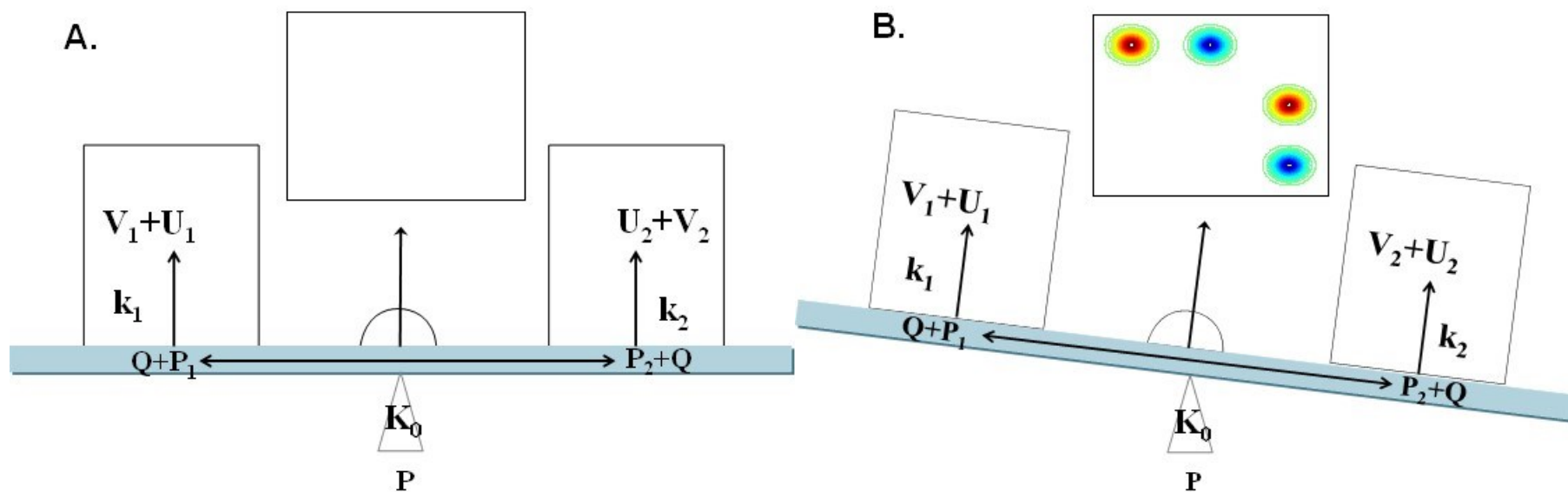
Scheme 5-3. Schematic Diagram of the Relationship among Different Chemical Species (Two Branches are formed from P. One is P→P$_1$→U$_1$, another is P→P$_2$→U$_2$).

A. Two Branches (P→P$_1$→U$_1$ and P→P$_2$→U$_2$) are in Balance. No cross Peak Appears in the 2D Asynchronous Spectrum.

B. Two Branches (P→P$_1$→U$_1$ and P→P$_2$→U$_2$) are out of Balance. Cross Peaks Appear in the 2D Asynchronous Spectrum.

Supporting Information 4

Part 1 Calculation of the Equilibrium Concentrations of P_1, P_2, Q, U_1, U_2, V_1 and V_2 in the Model System

Consider a solution i containing solutes P and Q, where the initial concentrations of P and Q are $C_P^{i(\text{init})}$ and $C_Q^{i(\text{init})}$, respectively. The equilibrium constant of eq. 5-1 can be expressed as eq. S5-1.

$$K_0 = \frac{C_{P2}^{i(\text{eq})}}{C_{P1}^{i(\text{eq})}} \tag{S5-1}$$

Based on eq. S5-1, the relationship between the equilibrium concentrations of P_1 and P_2 are expressed as eq. S5-2 and eq. S5-3.

$$C_{P_2}^{i(\text{eq})} = K_0 C_{P1}^{i(\text{eq})} \tag{S5-2}$$

$$C_{P_1}^{i(\text{eq})} = \frac{C_{P2}^{i(\text{eq})}}{K_0} \tag{S5-3}$$

The equilibrium constants of eq. 5-2 and eq. 5-3 in the main text can be expressed as eq. S5-4 and eq. S5-5.

$$K_1 = \frac{C_{U_1}^{i(\text{eq})} C_{V_1}^{i(\text{eq})}}{C_{P_1}^{i(\text{eq})} C_Q^{i(\text{eq})}} \tag{S5-4}$$

$$K_2 = \frac{C_{U_2}^{i(\text{eq})} C_{V_2}^{i(\text{eq})}}{C_{P_2}^{i(\text{eq})} C_Q^{i(\text{eq})}} \tag{S5-5}$$

According to eq. 5-2 and eq. 5-3, we have

$$C_{V_1}^{i(\text{eq})} = C_{U_1}^{i(\text{eq})} \tag{S5-6}$$

$$C_{V_2}^{i(\text{eq})} = C_{U_2}^{i(\text{eq})} \tag{S5-7}$$

Equation S5-4 and eq. S5-5 can be expressed as eq. S5-8 and eq. S5-9.

$$K_1 = \frac{\left(C_{U_1}^{i(\text{eq})}\right)^2}{C_{P_1}^{i(\text{eq})} C_Q^{i(\text{eq})}} \tag{S5-8}$$

$$K_2 = \frac{\left(C_{U_2}^{i(\text{eq})}\right)^2}{C_{P_2}^{i(\text{eq})} C_Q^{i(\text{eq})}} \tag{S5-9}$$

Here we assume that K_2 is nonzero. we have

$$\frac{K_1}{K_2} = \frac{\left(C_{U_1}^{i(\text{eq})}\right)^2 C_{P_2}^{i(\text{eq})}}{\left(C_{U_2}^{i(\text{eq})}\right)^2 C_{P_1}^{i(\text{eq})}} \tag{S5-10}$$

Equation S5-10 can be expressed by eq. S5-11 after combining eq. S5-2.

$$C_{U_2}^{i(eq)} = \sqrt{\frac{K_0 K_2}{K_1}}\, C_{U_1}^{i(eq)} \tag{S5-11}$$

Here we define

$$d = \sqrt{\frac{K_0 K_2}{K_1}} \tag{S5-12}$$

Because of the mass balance of the solution, we have

$$C_P^{i(init)} = C_{P_1}^{i(eq)} + C_{P_2}^{i(eq)} + C_{U_1}^{i(eq)} + C_{U_2}^{i(eq)}$$

$$C_P^{i(init)} = (1 + K_0)C_{P_1}^{i(eq)} + (1 + d)C_{U_1}^{i(eq)} \tag{S5-13}$$

Equation S5-13 can be expressed by eq. S5-14 after combining eq. S5-2 and eq. S5-11.

$$C_{P_1}^{i(eq)} = \frac{C_P^{i(init)} - (1 + d)C_{U_1}^{i(eq)}}{(1 + K_0)} \tag{S5-14}$$

Equation S5-12 also can be expressed by eq. S5-15 after combining eq. S5-3 and eq. S5-11.

$$C_{P_2}^{i(eq)} = \frac{K_0(C_P^{i(init)} - (1 + d)C_{U_1}^{i(eq)})}{(1 + K_0)} \tag{S5-15}$$

Because of the mass balance of the solution, we have

$$C_Q^{i(init)} = C_Q^{i(eq)} + C_{V_1}^{i(eq)} + C_{V_2}^{i(eq)}$$

$$C_Q^{i(init)} = C_Q^{i(eq)} + (1 + d)C_{U_1}^{i(eq)} \tag{S5-16}$$

The equilibrium concentration of Q can be described by

$$C_Q^{i(eq)} = C_Q^{i(init)} - (1 + d)C_{U_1}^{i(eq)} \tag{S5-17}$$

Equation 5-5 can be expressed by eq. S5-18 after combining eq. S5-6, eq. S5-7, eq. S5-11, eq. S5-14, eq. S5-15 and eq. S5-17.

$$A^i(x) = C_P^{i(init)}\left[sf_{P_1}(x) + sK_0 f_{P_2}(x)\right] + C_Q^{i(init)} f_Q(x)$$

$$+ C_{U_1}^{i(eq)}\left\{f_{U_1}(x) + f_{V_1}(x) + d\left[f_{U_2}(x) + f_{V_2}(x)\right]\right. \tag{S5-18}$$

$$\left. - (1 + d)\left[sf_{P_1}(x) + sK_0 f_{P_2}(x)\right] - (1 + d)f_Q(x)\right\}$$

where

$$s = \frac{1}{1 + K_0} \tag{S5-19}$$

Part 2 Computer Simulation on a Model System where Intermolecular Interaction does not occur between P and Q

$$\Psi_P \qquad\qquad\qquad \Psi_Q$$
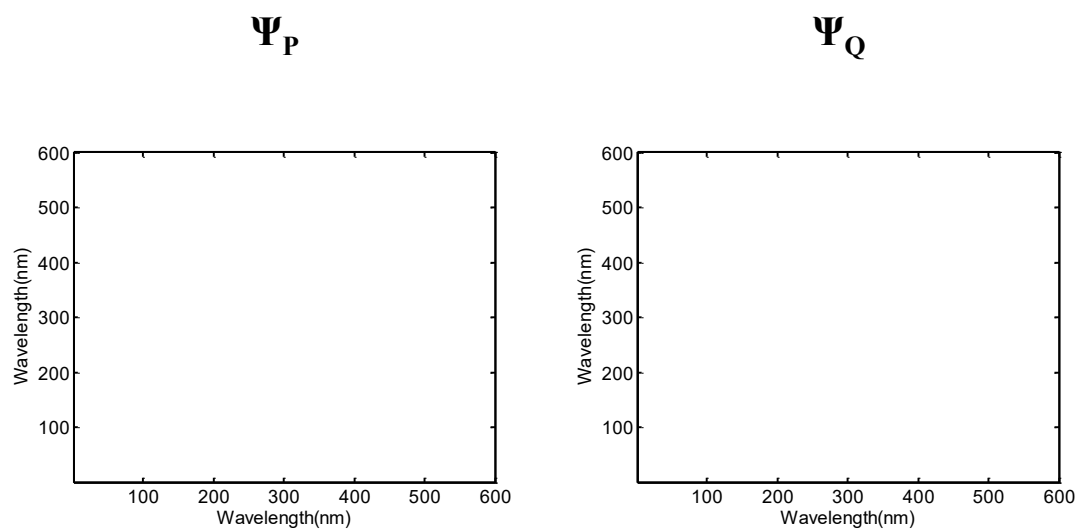
Figure S5-1. Simulated 2D Spectra of the Model System where no Intermolecular Interaction Occurs between P and Q.

When there is no intermolecular interaction between P and Q, no cross peak is produced in the pair of 2D asynchronous spectra even if P occur in two exchangeable states.

Chapter 5

Preparation and Characterization of Lanthanum Carbonate Octahydrate for the Treatment of Hyperphosphatemia

Introduction

Hyperphosphatemia is a complication of end stage renal failure. In healthy adults, the average daily intake of phosphate is around 1000–1500mg, which is balanced by faucal and urinary outputs.[1] For patients with renal failure, however, the phosphate excretion ability of kidneys reduces significantly. Consequently, the concentration of phosphate in the blood increases, leading to hyperphosphatemia.[2] Hyperphosphatemia causes secondary hyperparathyroidism and renal osteodystrophy and other diseases. Moreover, high concentration of phosphate in serum results in the formation of calcium phosphate precipitates. Large amount of calcium phosphate precipitates deposit in blood vessels may lead to fetal cardiovascular and cerebrovascular problem in the end stage renal failure patients.[3]

Current treatment of hyperphosphatemia involves dietary phosphate restrictions, dialysis, taking phosphate binder and vitamin D.[3] Most dietary phosphate is derived from protein, and the phosphate content has an almost linear correlation with protein intake. Dialysis patients have a higher dietary protein requirement than healthy persons.[4] It is difficult to rely on dietary restrictions to achieve control of phosphate. Moreover, dialysis provides inadequate removal of phosphate in serum. Therefore, renal failure patients have to take phosphate binders.[5]

The use of phosphate binder began in the early 1970s[5] and the earliest phosphate binders are aluminum-based compounds. The drug is highly effective and cheap.[1] However, aluminum may accumulate in bone, brain, heart and liver, causing aluminum toxicity in long-term use.[6, 7] Later a calcium-based phosphate binder was developed. However, the efficacy of the calcium-based drug turned out to be lower than that of the aluminum-based compound. Moreover calcium-based phosphate binder can cause hypercalcaemia and gastrointestinal adverse effects.[2] Therefore, ideal phosphate binders that are safe and high effective in binding phosphate are needed.[6]

Lanthanum carbonate is an ideal phosphate binder. It prevents adsorption of dietary phosphate by forming insoluble lanthanum phosphate. It has been reported that lanthanum carbonate binds phosphate optimally at pH 3–5, while retaining binding activity at pH 1–7.[8, 9] In *vitro* studies suggest that the efficacy of lanthanum phosphate is comparable to that of aluminium compounds in binding with phosphate[1]. FDA has approved that lanthanum carbonate can be utilized as phosphate binder for renal failure patients.

Concerning about the preparation of lanthanum carbonate, there are several approaches reported in the literatures.[10, 11] However, these methods have unresolved problems. For example, it has been reported that lanthanum carbonate can be prepared by a reaction between Na_2CO_3 and $LaCl_3$ in aqueous solutions. We notice that lanthanum ion possesses strong ability to bind hydroxide ion when the pH value of aqueous solution is high. On the other hand, the pH value of an aqueous solution of Na_2CO_3 is rather high. As a result, the reaction between Na_2CO_3 and $LaCl_3$ may produce undesirable $La(OH)CO_3$ as a side product with lanthanum carbonate.

Although it has been reported that $La(OH)CO_3$ can bind phosphate,[12] $La(OH)CO_3$ has not been approved by FDA for the treatment of hyperphosphatemia. It has not been

elucidated whether La(OH)CO₃ is safe in medical practice.

In this chapter, we proposed a new approach to prepare lanthanum carbonate via reactions between $NaHCO_3$ and $LaCl_3$ in aqueous solution under low pH environment. In addition, the prepared lanthanum carbonate was characterized by using FTIR, XRD, elemental analysis and titration methods. The ability of the lanthanum carbonate in binding phosphate was validated by spectrometric methods.

Experimental

Reagents

Lanthanum oxide (99.999% purity) was purchased from Jiaton technology company.

Hydrochloric acid (37 wt%, AR), sodium bicarbonate (AR), disodium salt of EDTA (AR), acetic acid (AR), sodium acetate (AR) were purchased from Beijing Chemical Plant.

Zinc oxide (reference materials) was purchased from Beijing Institute of Chemical Reagents.

Instrument

Elemental analyses (C, H, N) were performed on an Elementar Vario EL elemental analyzer.

X-ray powder diffraction(XRD) data were recorded on a Rigaku D/Max-2000 diffractometer at 40 kV, 100 mA for Cu Kα.

FTIR spectra of $La_2(CO_3)_3 \cdot 8H_2O$ and La(OH)CO₃ were collected on a Thermo-Fisher Nicolet iN10 MX FTIR spectrometer equipped with an IR microscope. The spectra were recorded under transmission mode at a resolution of 8 cm^{-1} and 64 scans were co-added.

Others FTIR spectra were recorded on a Fourier Transform Nicolet 6700 by using KBr pellets method. The spectra were recorded under transmission mode at a resolution of 2 cm^{-1} and 16 scans were co-added.

Quantitative analysis of phosphate was performed by using spectrophotometry (λ=700 nm) on a PE Lambda 35 UV-Vis spectrophotometer.

Preparation

Preparation of lanthanum carbonate

Lanthanum chloride was prepared via a reaction between lanthanum oxide and HCl solution. The initial concentration of La^{3+} was 1 mol/l and the initial pH value of the solution was below zero. $NaHCO_3$ was dissolved in deionized water and the concentration of $NaHCO_3$ of the obtained solution was 1 mol/l.

Lanthanum carbonate was prepared by adding $NaHCO_3$ solution into an aqueous solution of lanthanum chloride under stirring. Description and discussion on the experimental conditions in detail can be found in Result and Discussion part. During the reaction, the pH values of the reactive environment were measured by using a combination electrode. The data were converted into digital signal and collected into a desk-top computer via a cluster communication port (**Scheme 5-1**).

**Preparation of lanthanum carbonate hydroxide**

The obtained lanthanum carbonate was suspended in deionized water and the mixture was refluxed for 15 hours. Afterwards, the product was obtained via a filtration process.

Chemical analysis of the samples

The La^{3+} content of samples were measured by using EDTA titration. The concentration of the EDTA solution was calibrated by using zinc oxide.

Results and discussion

When the sodium bicarbonate solution is added into lanthanum chloride solution, the following two reactions co-occur in the system:

$$2La^{3+} + 3HCO_3^- = La_2(CO_3)_3\downarrow + 3H^+ \qquad (6\text{-}1)$$

$$H^+ + HCO_3^- = H_2O + CO_2\uparrow \qquad (6\text{-}2)$$
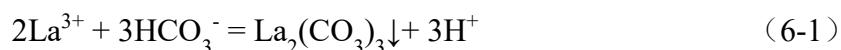
Reaction (6-1) is a precipitation reaction between HCO_3^- and La^{3+} and the products of the reaction are $La_2(CO_3)_3$ precipitates and proton. Reaction (6-2) is a neutralization reaction between HCO_3^- and H^+. The precipitation reaction cannot be initiated without lanthanum carbonate nuclei in the system while the acid-base neutralization reaction takes place as long as H^+ and HCO_3^- co-occur in the system. If the $NaHCO_3$ solution was slowly added into the lanthanum chloride solution, the precipitation reaction cannot be initiated since no lanthanum carbonate nuclei occur in the system. As a result, only the neutralization reaction takes place in the system. Thus, the pH value of system increases monotonically as more $NaHCO_3$ solution is added. As a result, lanthanum carbonate is prepared at high pH environment, the risk of producing lanthanum carbonate hydroxide increases considerably.

Herein, we propose an alternative approach to prepare lanthanum carbonate at lower pH environment. The approach is composed of three steps: (1) Preparation of lanthanum carbonate nuclei. (2) Preparation of lanthanum carbonate. (3) Termination of the reaction.

In the first step, small amount of $NaHCO_3$ solution was quickly added into the lanthanum chloride solution. The concentration of $NaHCO_3$ in local regions is high enough so that lanthanum carbonate precipitates are formed. The produced lanthanum carbonate can be used as nuclei center and hence the bottleneck of the lack of lanthanum carbonate nuclei is removed. During the reaction, the variation of pH value is monitored and shown in **Figure 6-1**. When aqueous solution of $NaHCO_3$ was quickly added, the pH value jumped around 3. In the meantime, white precipitates of lanthanum carbonate appeared. Since H^+ was released from the precipitation reaction between La^{3+} and HCO_3^-, decrease of pH can be observed in **Figure 6-1**. If no more $NaHCO_3$ was added, the produced lanthanum carbonate can be dissolved completely by the acid produced from the reaction. To preserve the lanthanum carbonate nuclei, $NaHCO_3$ solution was introduced into the system by using a ZDJ-400 multifunctional titrimeter so that the injecting rate can be accurately controlled. The speed of injection of $NaHCO_3$ solution was a kept at 0.2ml/s. During this process, more and more lanthanum carbonate precipitates were produced, while the pH value almost remained invariant. The reason

for this phenomenon is that $NaHCO_3$ plays a dual role in the system. On one hand, $NaHCO_3$ reacts with La^{3+} to produce lanthanum carbonate together with H^+. On the other hand, $NaHCO_3$ acts as a base that can neutralize H^+. Since both precipitation reaction and neutralization reaction co-occur in the system, a dynamic equilibration on the concentration of H^+ is established and the pH value remains a constant during the reaction. It should be pointed out that the reaction is carried out at lower pH environment (pH is below 4.5) and the risk of producing $La(OH)CO_3$ is much reduced.

When La^{3+} in the solution is completely consumed by the reaction, the precipitating reaction cannot be performed any more. However, the neutralization reaction can still be carried out. As a result, the pH value of the system jumped to 6 (**Figure 6-1**). To confirm La^{3+} is used up at this moment, we collected small amount of supernatant from the system and added several drops of NaOH solution (1 mol/l), no $La(OH)_3$ precipitate was observed, confirming that La^{3+} is completely consumed. Therefore, the reaction was stopped and the precipitate was collected as sample I.

The sample I was characterized by using XRD and the result is shown in **Figure 6-2** The XRD pattern of the product matches with the $La_2(CO_3)_3 \cdot 8H_2O$. in ICDD PDF2-2004 database (card number: 25-1400) with a matching degree of 92.0 %. This result indicated that the product of the above reaction is $La_2(CO_3)_3 \cdot 8H_2O$.

The sample I was added into deionized water and the mixture were refluxed for 15 hours. Afterwards, the product was obtained after a filtration process and denoted as sample II. XRD pattern of sample II is shown in Figure 6-**3**. The XRD pattern matches with the $La(OH)CO_3$ in ICDD PDF2-2004 database(card number: 26-0815) with a matching degree of 95.7%. Thus, the product is proved to be $La(OH)CO_3$.

Titration and elemental analysis results provide additional experimental evidence to support that the two samples are $La_2(CO_3)_3 \cdot 8H_2O$ and $La(OH)CO_3$, respectively. The contents of lanthanum in the two samples were measured by EDTA titration. The contents of carbon were obtained by elemental analysis. The results of the above analysis are summarized in **Table 6-1**. Good agreement is found between the theoretical content and experimental results. From the chemical formula, we find that lanthanum carbonate and lanthanum carbonate hydroxide show significant difference on the molar ratio between carbon and lanthanum (denoted as n_c/n_{La3+}). If the prepared sample is $La_2(CO_3)_3$, the n_c/n_{La3+} should be $3/2 = 1.5$. If the sample was $La(OH)CO_3$, the n_c/n_{La3+} should be $1/1 = 1$. The n_c/n_{La3+} values for sample I and sample II samples are 1.52, and 1.08 (**Table 6-1**), confirming that the products are lanthanum carbonate and lanthanum carbonate hydroxide, respectively.

Based upon the above result, we used FTIR spectroscopic method to establish a rapid and reliable approach to identify lanthanum carbonate and lanthanum carbonate hydroxide.

FTIR spectrum of $La_2(CO_3)_3 \cdot 8H_2O$ is given in **Figure 6-4**. For comparison, FTIR spectrum of $La(OH)CO_3$ is also shown. Significant difference between the spectrum of $La_2(CO_3)_3 \cdot 8H_2O$ and that of $La(OH)CO_3$ can be clearly observed in the fingerprint region (1000~600 cm^{-1}). $La_2(CO_3)_3 \cdot 8H_2O$ has sharp peaks at 850 cm^{-1}, 747 cm^{-1} and 679 cm^{-1}, while $La(OH)CO_3$ has absorption peaks at 872 cm^{-1}, 848 cm^{-1}, 778 cm^{-1} and 707 cm^{-1}. The above dramatically different spectral features make it possible to detect

La(OH)CO₃ impurity in lanthanum carbonates. Here, different amount of La(OH)CO₃ was mixed with La₂(CO₃)₃·8H₂O and FTIR spectra of the mixtures were collected by using KBr pellets method. Characteristic peak of La(OH)CO₃ at 872 cm⁻¹ can be observed when 5 wt% of La(OH)CO₃ was mixed with La₂(CO₃)₃·8H₂O (**Figure 6-5**). To improve the sensitivity of the FTIR method, second derivative spectra were utilized. In this case, characteristic peak of La(OH)CO₃ at 872 cm⁻¹ can be identified even if only 1 wt% of La(OH)CO₃ was mixed with La₂(CO₃)₃·8H₂O (**Figure 6-6**).

To characterize the ability of lanthanum carbonate on binding phosphate, the following experiment was conducted:

0.2 g KH_2PO_4 was dissolved in CH_3COOH-CH_3COONa solution (the concentration of CH_3COOH and CH_3COONa are both 1 mol/l) so that 100.0 ml KH_2PO_4 solution whose pH value is around 4.7 was prepared. 0.5 g $La_2(CO_3)_3 \cdot 8H_2O$ was added into the phosphate solution. Enough stirring was applied on the suspension. During the experiment, phosphate can be adsorbed by lanthanide carbonate so that the concentration of phosphate decreased with time. To monitor the decay of the concentration of phosphate, small amount of supernatant was collected at different time and the concentration of phosphate in the supernatant was analyzed by using the Mo-Sb anti-spectrophotometric method. **Figure 6-7** shows the variation of the concentration of phosphate in the solution as a function of time. 50% phosphate are removed from the solution within 30 min and more than 95% phosphate are adsorbed by lanthanum carbonate within 120 min. Considering the fact that food stay in stomach for 4 hours, Lanthanum carbonate is enough to bind most phosphate.

Conclusion

We proposed a new approach to prepare lanthanum carbonate via reactions between lanthanum chloride and $NaHCO_3$. In the reaction, small amount of $NaHCO_3$ solution was quickly added into the acidic lanthanum chloride solution to generate lanthanum carbonate nuclei. As a result, both precipitation reaction and neutralization reaction take place simultaneously. Lanthanum carbonate is produced at low pH environment (pH below 4.5) so that the risk of generating lanthanum carbonate hydroxide is significantly reduced. EDTA titration, elemental analysis and XRD characterization confirm that $La_2(CO_3)_2 \cdot 8H_2O$ are obtained by using the above method. In addition, we established a method to identify La(OH)CO₃ from $La_2(CO_3)_2 \cdot 8H_2O$. Small amount of La(OH)CO₃ can be identified from La(OH)CO₃/$La_2(CO_3)_2 \cdot 8H_2O$ mixture even if the content of La(OH)CO₃ is only 1 wt%. Lanthanum carbonate exhibits considerable ability to bind phosphate.


References

1   Albaaj, F.; Hutchison, A. J. Hyperphosphataemia in Renal Failure - Causes, Consequences and Current Management. *Drugs* **2003,** *63*, 577-596.

2   Schucker, J. J.; Ward, K. E. Hyperphosphatemia and Phosphate Binders. Am J Health-Syst Ph **2005,** *62*, 2355-2361.

3   Plagemann, T.; Prenzler, A.; Mittendorf, T. Considerations about the Effectiveness and Cost Effectiveness of Therapies in the Treatment of Hyperphosphataemia. *Health Economics Review* **2011,** *1*, 1-9.

4   Freitas, D. de; Donne, R. L.; Hutchison, A. J. Lanthanum Carbonate - A First Line Phosphate Binder?. *Semin Dialysis* **2007,** *20*, 325-328.

5   Coladonato, J. A. Control of Hyperphosphatemia among Patients with ESRD. *J. Am. Soc. Nephrol.* **2005,** *16*, S107-S114.

6   Tonelli, M.; Pannu, N.; Manns, B. Drug Therapy: Oral Phosphate Binders in Patients with Kidney Failure. *New Engl. J. Med.* **2010,** *362*, 1312-1324.

7   Malluche, H. H.; Mawad, H. Management of Hyperphosphataemia of Chronic Kidney Disease: Lessons From the Past and Future Directions. *Nephrol Dial. Transpl.* **2002,** *17*, 1170-1175.

8   Fricker, S. P. The Therapeutic Application of Lanthanides. *Chem. Soc. Rev.* **2006,** *35*, 524-533.

9   Murrer, B. A.; Powell, N. A. Pharmaceutical Composition Containing Selected Lanthanum Carbonate Hydrates. Patent US: 1999.

10 Murrer, B. A.; Powell, N. A. Pharmaceutical Composition Containing Selected Lanthanum Carbonate Hydrates. Patent CN: 1996.

11 Jeevanandam, P.; Koltypin, Y.; Palchik, O.; Gedanken, A. Synthesis of Morphologically Controlled Lanthanum Carbonate Particles using Ultrasound Irradiation. *J. Mater. Chem.* **2001,** *11*, 869-873.

12 Ferdinando, J.; Gilmour, D. Method of Treating Hyperphosphataemia using Lanthanum Hydroxycarbonate. Patent CN: 2005.

**Table 6-1** Results on the chemical analysis of sample I and sample II

	Content of Lanthanum		Content of Carbon		
	Experimental value $(\times10^{-3}\text{mol/g})$	Theoretical value $(\times10^{-3}\text{mol/g})$	Experimental value $(\times10^{-3}\text{mol/g})$	Theoretical value $(\times10^{-3}\text{mol/g})$	n_c/n_{La3+}
Sample I	3.293	3.322	4.98	4.98	1.52
Sample II	4.388	4.631	4.75	4.63	1.08
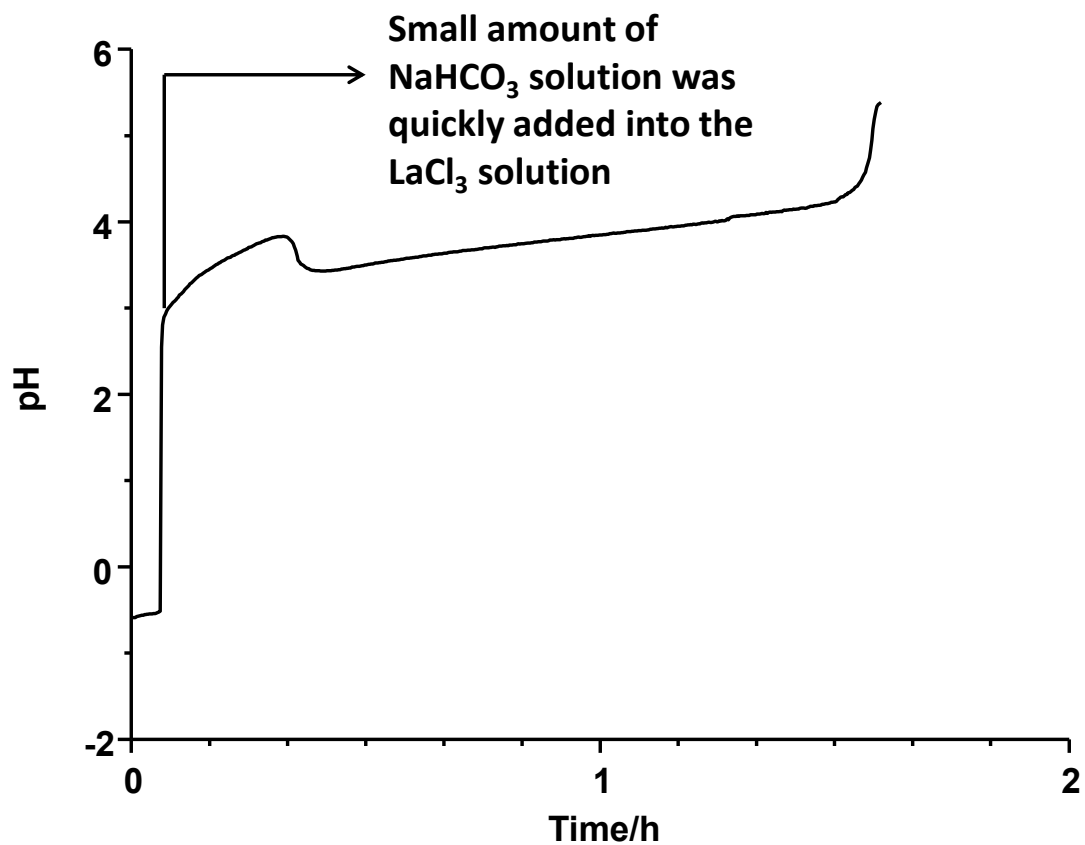
Figure 6-1 Variation of pH Value as a Function of Time when NaHCO₃ Solution is Added into LaCl₃ Solution at a Rate of 0.2 ml/s
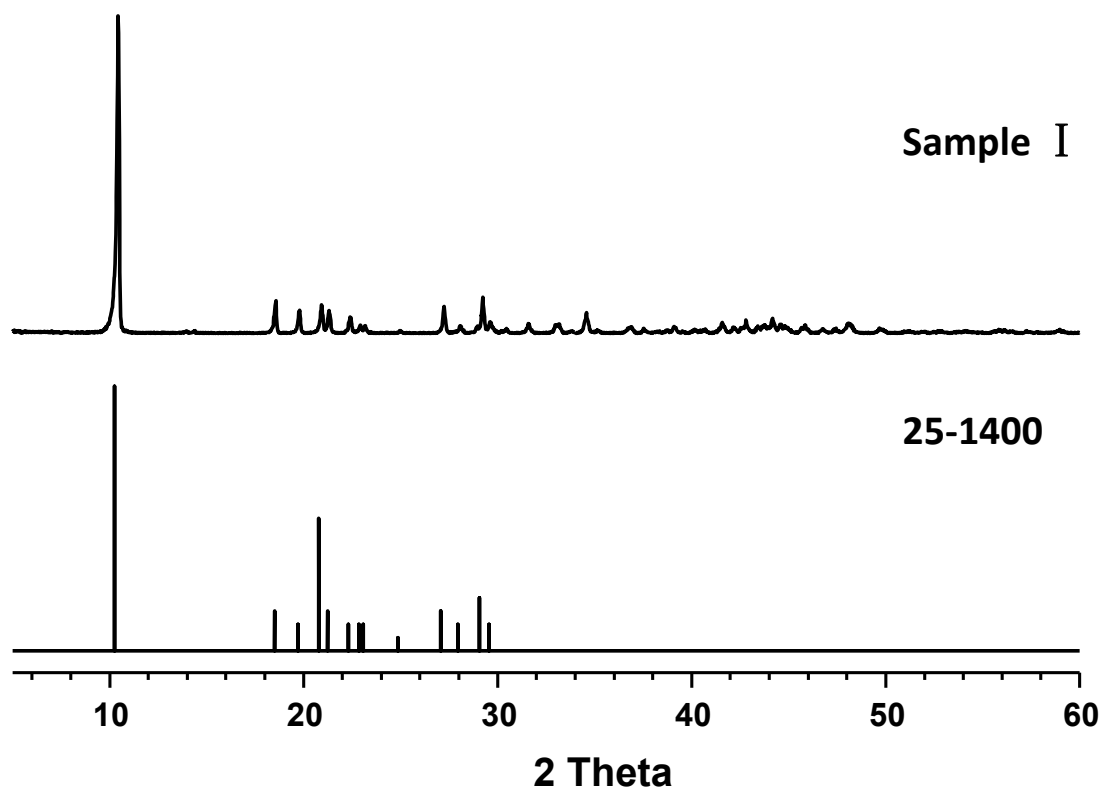
Figure 6-2 The XRD Patterns of Sample I and Standard $La_2(CO_3)_3 \cdot 8H_2O$ from ICDD PDF2-2004(card number: 25-1400). Match Degree: 92.0%
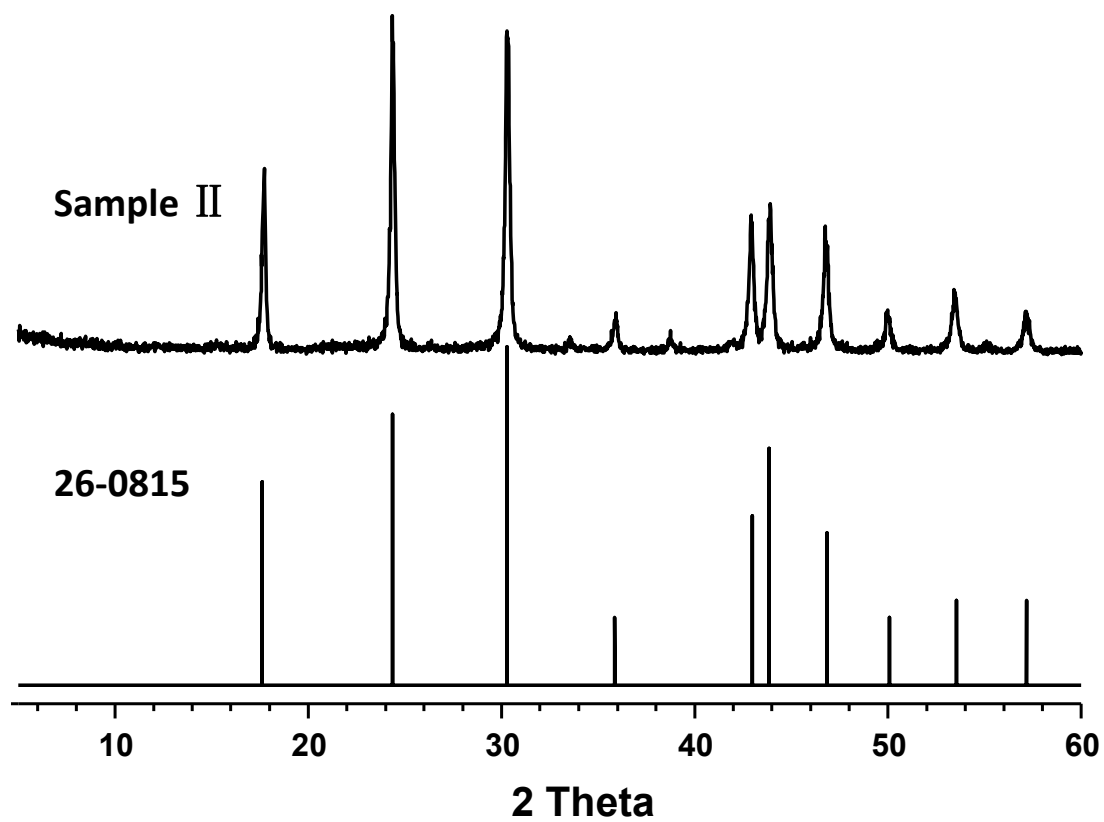
Figure 6-3 The XRD Patterns of Sample II and standard La(OH)CO$_3$ from ICDD PDF2-2004(Card Number: 26-0815). Match Degree: 95.7%
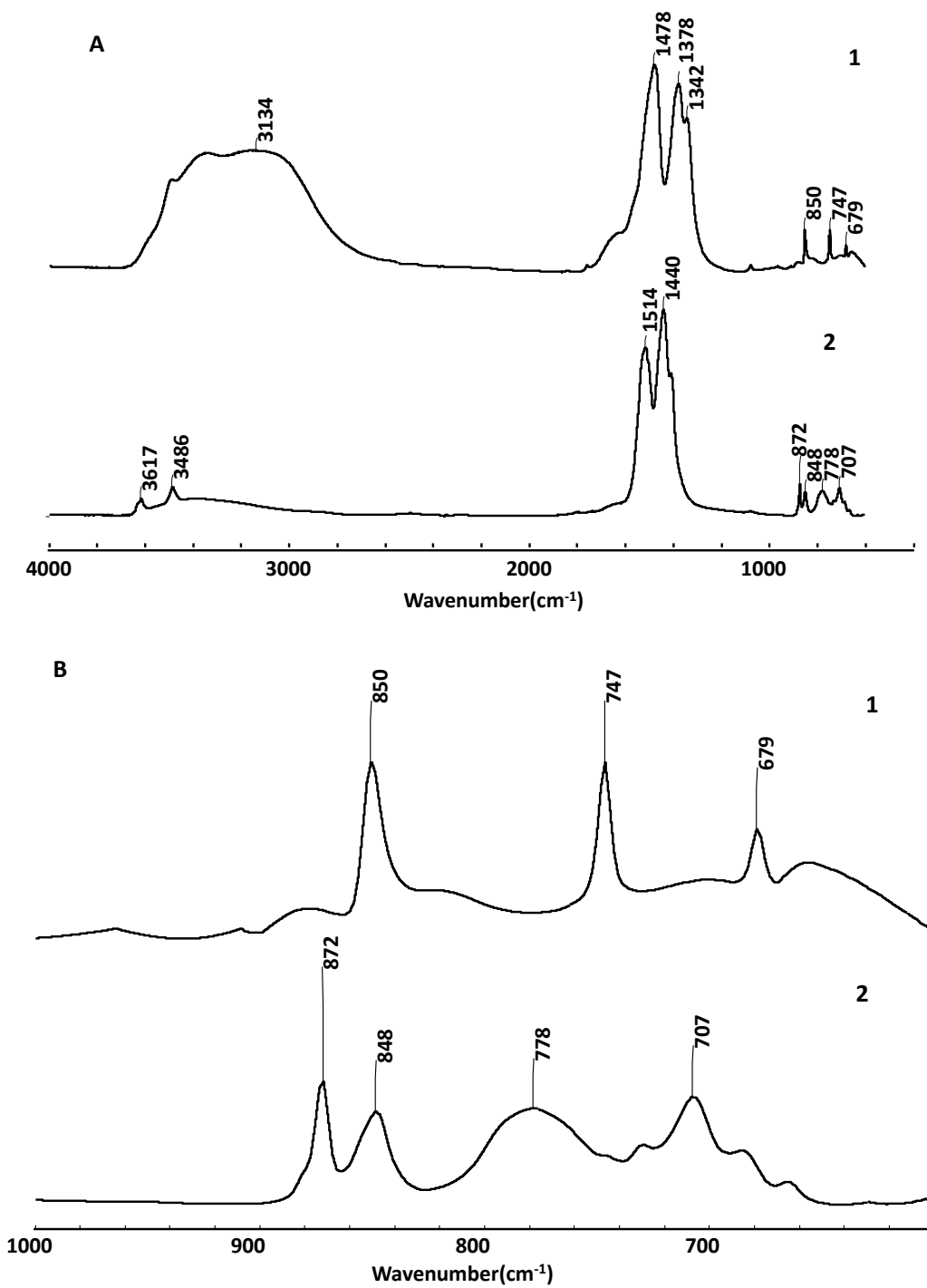
Figure 6-4 A) FTIR Spectra of $La_2(CO_3)_3 \cdot 8H_2O$ (line 1) and $La(OH)CO_3$ (line 2)
B) FTIR Spectra of $La_2(CO_3)_3 \cdot 8H_2O$ (line 1) and $La(OH)CO_3$ (line 2) in the
Fingerprint Region(1000-600cm^{-1}).
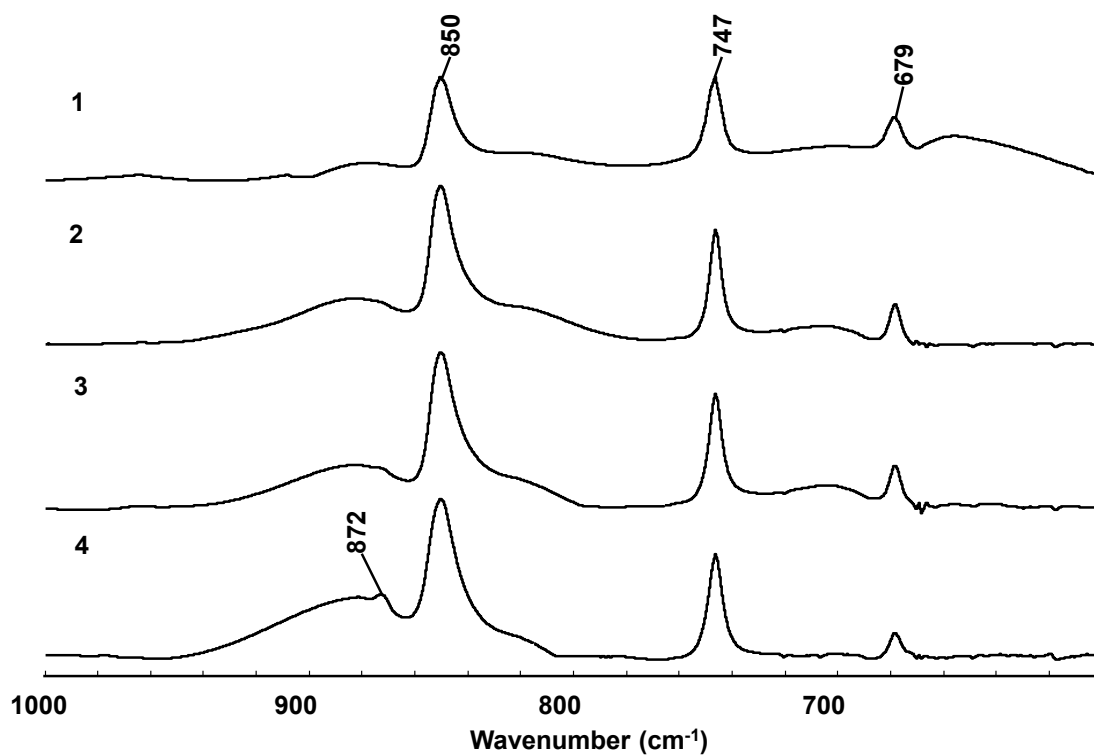
Figure 6-5 FTIR Spectra of $La_2(CO_3)_3 \cdot 8H_2O$ (line 1), and $La_2(CO_3)_3 \cdot 8H_2O$ Containing 1 wt% $La(OH)CO_3$ (line 2), $La_2(CO_3)_3 \cdot 8H_2O$ Containing 2 wt% $La(OH)CO_3$ (line 3) and $La_2(CO_3)_3 \cdot 8H_2O$ Containing 5 wt% $La(OH)CO_3$ (line 4) in the Fingerprint Region (1000-600cm^{-1}).
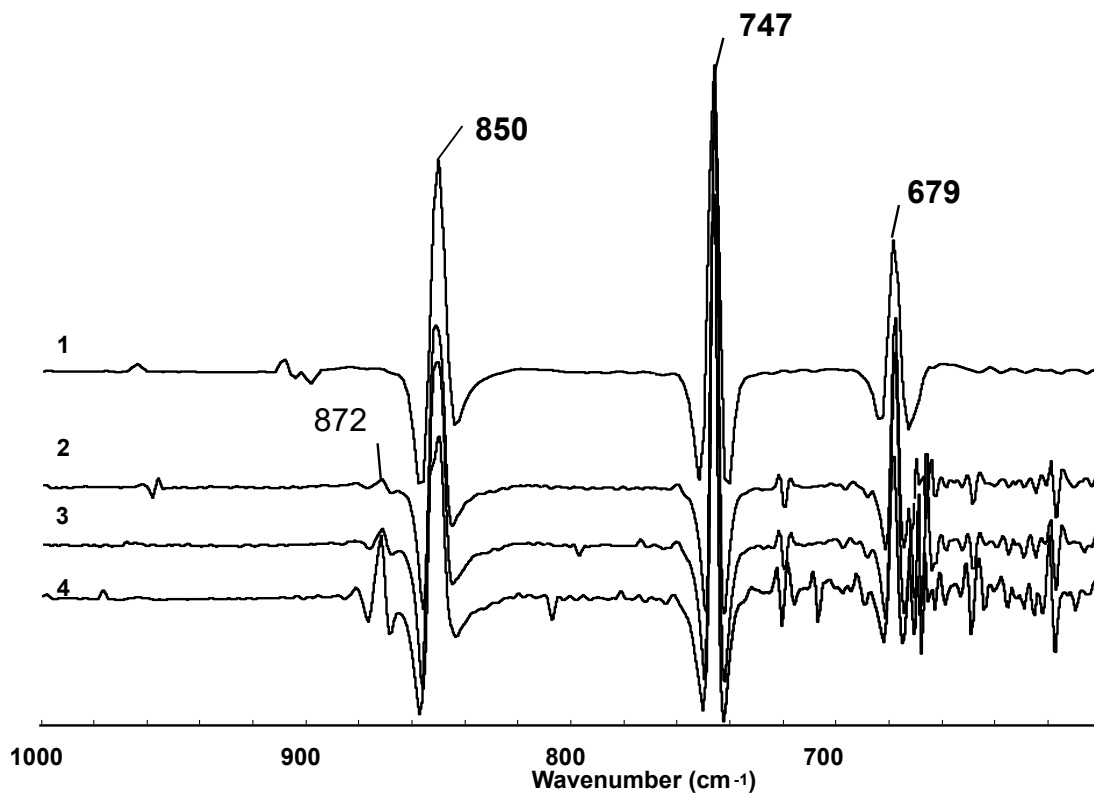
Figure 6-6 Second Derivative FTIR Spectra of $La_2(CO_3)_3 \cdot 8H_2O$ (line 1) , and $La_2(CO_3)_3 \cdot 8H_2O$ Containing 1 wt% $La(OH)CO_3$ (line 2), and $La_2(CO_3)_3 \cdot 8H_2O$ Containing 2 wt% $La(OH)CO_3$ (line 3), and $La_2(CO_3)_3 \cdot 8H_2O$ Containing 5 wt% $La(OH)CO_3$ (line 4) in the Fingerprint Region (1000-600cm^{-1}).
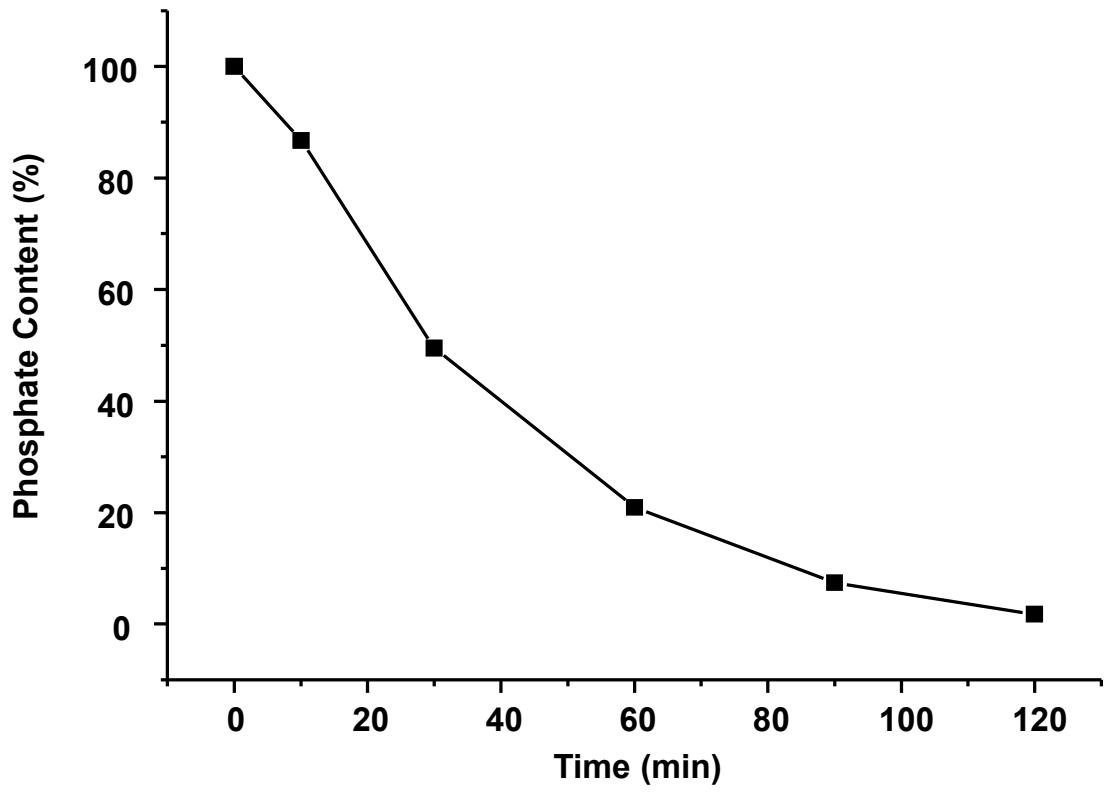
Figure 6-7 Variation of the Concentration of Phosphate in the Supernatant as a Function of Time.
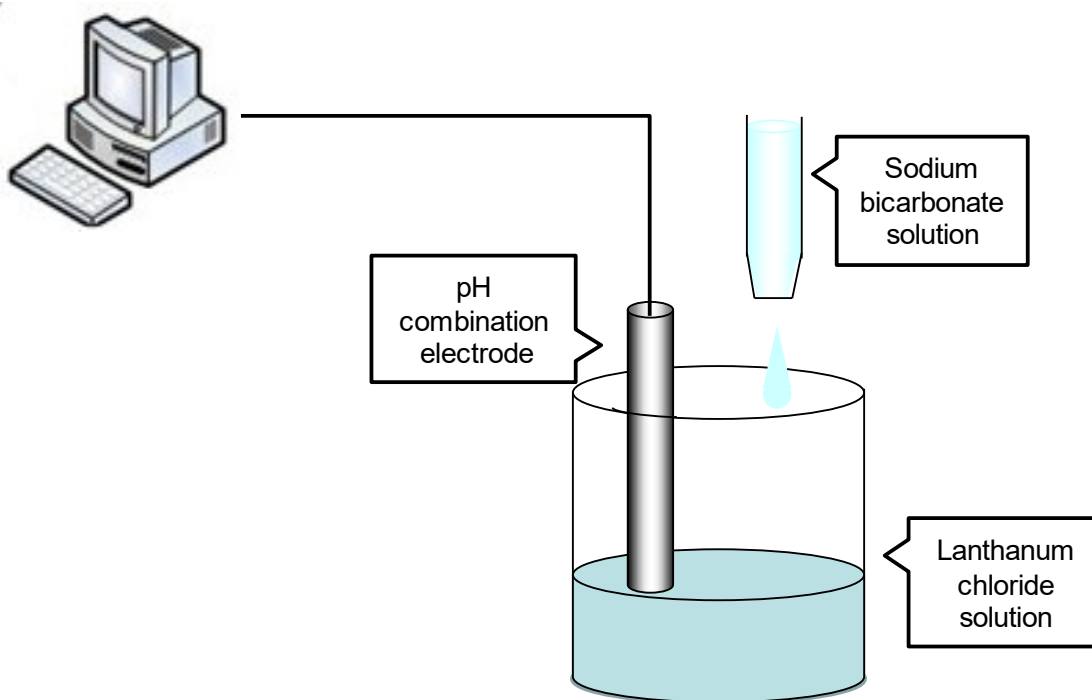
Scheme 6-1 Schematic Diagram of the Experimental Setup on the Reaction between Lanthanum Chloride and Sodium Bicarbonate.

Acknowledgments

During the evolution of this dissertation, I am deeply indebted to everyone who have guided and supported me in many ways.

I want to give my heartfelt gratitude to Prof. Yizhuang Xu from Peking University, who is undoubtedly the most important person for this dissertation. Thank you for recommending me to study in Japan and revising my papers. I will not forget the discussion with Prof. Xu, he answered every of my question patiently. All of the guidance from Prof. Xu were much helpful for my research, and will also continuously influence and help me in the future.

I am very grateful to Prof. Isao Noda from University of Delaware, USA, for providing guidance and advice on 2DCOS, and supporting my research work.

At the same time, I would like to express my utmost gratitude to Prof. Yukihiro Ozaki from Kwansei-Gakuin University, my supervisor, for his sincere and endless encouragement, selfless support, and kind advice throughout all the stages of my research in Ozaki Group. Moreover, I am so much appreciated that Prof. Ozaki provided me a very good research environment and strong supported every of my idea. He also devoted a considerable portion of his time to read my manuscript and gave me insightful suggestions for further revisions. It was him, who showed me what the real scientist is, made me truly grown up.

I also must thank Prof. Shigeaki Morita from Osaka Electro-Communication University, who spared their time to revise my paper and gave many professional comments to me.

I also want to thank to Dr. Ran Guo, Dr. Xiaoyan Kang and Dr. Yiwei Zeng, who are not only very important research partners but also good friends of mine. I also want to give my thanks to all Prof. Xu's group members.

The same thanks should also give to Dr. Takeyoshi Goto, Dr. Yasutaka Kitahama, Dr. Krzystof Beć, Mr. Koji Watari and other Prof. Ozaki's group members, who not only provided help and advice on the research, but also cared about my life in Japan.

Finally, but not the least, I want to express my great appreciation to my parents and all closest friends, for their selfless accompany and encouragement. Nothing can replace them in my heart.

List of Publications

1. **He, A. Q.**; Zeng, Y. W.; Kang, X. Y.; Morita, S.; Xu, Y. Z.; Noda, I.; Ozaki, Y.; Wu, J. G. A Novel Method of Constructing Two-dimensional Correlation Spectroscopy without Subtracting a Reference Spectrum. *J Phys. Chem. A* **2018**, *122*, 788-797. (**Chapter 1**)

2. **He, A. Q.**; Zeng, X. Z.; Xu, Y. Z.; Noda, I.; Ozaki, Y.; Wu, J. G. Investigation on the Behavior of Noise in Asynchronous Spectra in Generalized Two-Dimensional (2D) Correlation Spectroscopy and Application of Butterworth Filter in the Improvement of Signal-to-Noise Ratio of 2D Asynchronous Spectra. *J Phys. Chem. A* **2017**, *121*, 7524-7533. (**Chapter 2**)

3. **He, A. Q.**; Kang, X. Y; Xu, Y. Z.; Noda, I.; Ozaki, Y.; Wu, J. G. Investigation on Intermolecular Interaction between Berberine and β-Cyclodextrin by 2D UV–Vis Asynchronous Spectra. *Spectrochim. Acta, Part A* **2017**, *185*, 343–348. (**Chapter 3**)

4. Kang, X. Y.; **He, A. Q.**; Guo, R.; Chen, J.; Zhai, Y. J.; Xu, Y. Z.; Noda, I.; Wu, J. G. Investigation on Intermolecular Interaction between Two Solutes where one Solute Occurs in Two States. *J. Mol. Struct.* **2016**, *1124*, 228-237. (**Chapter 4**)

5. **He, A. Q.**; Zhou, F. S.; Ye, F.; Zhang, Y.; He, X. R.; Zhang, X.; Guo, R.; Zhao, X.; Sun, Y.; Huang, M.; Li, Q.; Yang, Z. L.; Xu, Y. Z.; Wu, J. G. Preparation and Characterization of Lanthanum Carbonate Octahydrate for the Treatment of Hyperphosphatemia. *J. Spectrosc.* **2013**, 593636. (**Chapter 5**)

List of related publications

6. Li, X. P.; Zeng, Y. W.; **He, A. Q.**; Bao, Y. N.; Wang, J. H.; Xu, Y. Z.; Ozaki, Y.; Noda, I.; Wu, J. G. A New Approach to Determine the Stoichiometric Ratio of Two Substances Involved in the Intermolecular Interactions. *Anal. Chem.* **submitted**

7. Wang J. D.; **He, A. Q.**; Guo, R.; Wei, Y. J.; Feng, J; Xu, Y. Z.; Noda, I.; Wu, J. G. Investigation on the Spectral Properties of 2D Asynchronous Fluorescence Spectra Generated by using Variable Excitation Wavelengths as a Perturbation. *J. Mol. Struct.* **2016**, *1124*, 221-227.

8. Kang, X. Y.; **He, A. Q.**; Guo, R.; Zhai, Y. J.; Xu, Y. Z.; Noda, I.; Wu, J. G. A Simplified Concentration Series to Produce a Pair of 2D Asynchronous Spectra Based on the DAOSD Approach. *J. Mol. Struct.* **2016**, *1124*, 151-158.

9. Li, X. P.; **He, A. Q.**; Huang, K.; Liu, H. Z.; Zhao, Y.; Wei, Y. J.; Xu, Y. Z.; Noda, I.; Wu, J. G. Two-Dimensional Asynchronous Spectrum With Auxiliary Cross Peaks in Probing Intermolecular Interactions. *RSC Adv.* **2015**, *5*, 87739–87749.

10. Zhao, W; **He, A. Q.**; Xu, Y. Z. Raman Second Hyperpolarizability Determination Using Computational Raman Activities and a Comparison with Experiments. *J Phys. Chem. A* **2013**, *117*, 6217-6223.

11. Zhao, W; **He, A. Q.**; Xu, Y. Z. Second Hyperpolarizability of C-H, C-D, and C≡N Stretch Vibrations Determined from Computational Raman Activities and a Comparison with Experiments. *J Phys. Chem. B* **2013**, *117,* 15812-15818.